Design Optimization of Permanent Magnet Machines Over a Target Operating Cycle Using Computationally Efficient Techniques

Alireza Fatemi
Marquette University

DESIGN OPTIMIZATION OF PERMANENT MAGNET MACHINES OVER A TARGET OPERATING CYCLE USING COMPUTATIONALLY EFFICIENT TECHNIQUES

By
Alireza Fatemi, A.S., B.S., M.S.

A Dissertation Submitted to the Faculty of the
Graduate School, Marquette University,
in Partial Fulfillment of the Requirements for the
Degree of Doctor of Philosophy

Milwaukee, Wisconsin
August 2016

ABSTRACT

DESIGN OPTIMIZATION OF PERMANENT MAGNET MACHINES OVER A TARGET OPERATING CYCLE USING COMPUTATIONALLY EFFICIENT TECHNIQUES

Alireza Fatemi, A.S., B.S., M.S.

Marquette University, 2016

The common practices of large-scale finite element (FE) model-based design optimization of permanent magnet synchronous machines (PMSMs) oftentimes aim at improving the machine performance at the rated operating conditions, thus overlooking the performance treatment over the entire range of operation in the constant torque and extended speed regions. This is mainly due to the computational complexities associated with several aspects of such large-scale design optimization problems, including the FE-based modeling techniques, large number of load operating points for load-cycle evaluation of the design candidates, and large number of function evaluations required for identification of the globally optimal design solutions.

In this dissertation, the necessity of accommodating the entire range of operation in the design optimization of PMSMs is demonstrated through joint application of numerical techniques and mathematical or statistical analyses. For this purpose, concepts such as FE analysis (FEA), design of experiments (DOE), sensitivity analysis, response surface methodology (RSM), and regression analysis are extensively used throughout this work to unscramble the correlations between various factors influencing the design of PMSMs. Also in this dissertation, computationally efficient methodologies are developed and employed to render unprohibitive the problems associated with large-scale design optimization of PMSMs over the entire range of operation of such machines. These include upgrading an existing computationally efficient FEA to solve the electromagnetic field problem at any load operating point residing anywhere in the torque-speed plane, developing a new stochastic search algorithm for effectively handling the constrained optimization problem (COP) of design of electric machines so as to reduce the number of function evaluations required for identifying the global optimum, implementing a k-means clustering algorithm for efficient modeling of the motor load profile, and devising alternative computationally efficient techniques for calculation of strand eddy current losses or characterization of the mechanical stress due to the centrifugal forces on the rotor bridges.

The developed methodologies in this dissertation are applicable to the wide class of sine-wave driven PM and synchronous reluctance machines. Here, they were successfully utilized for optimization of two existing propulsion traction motors over predefined operating cycles. Particularly, the well-established benchmark design provided by the Toyota Prius Gen. 2 V-type interior PM (IPM) motor, and a challenging high power density spoke-type IPM for a formula E racing car are treated.

ACKNOWLEDGEMENTS

Alireza Fatemi, A.S., B.S., M.S.

For any accomplishment, including my doctorate degree, I am grateful beyond words to my parents, Mr. Mohammad Fatemi and Mrs. Meymanat Shadkam, who gave me the gift of life, devoted their own lives to others' well-being, trusted in my abilities, encouraged me to have strong work ethics, and set me up for this journey. Yet, this dissertation would have not been possible without the guidance, encouragement, and support of a great number of other individuals whom I had the privilege to work with and learn from during the past four years, and to whom I will be indebted for the years to come.

First and foremost, I am thankful to Prof. Nabeel Aly Omar Demerdash, who, as an unparalleled academic advisor and pedagogue, supported me above and beyond that of any professor, throughout my Ph.D. studies, and mentored my scholarly, and intellectual development in numerous ways. The countless hours that he spent with me in person to teach me computational electromagnetics, discuss my research, read and evaluate my papers and dissertation word for word, and tell invaluable life stories and history lessons will for sure remain the most memorable moments of these years. For all he has done for me, Prof. Demerdash has expected nothing from me but to be as caring and supportive to my own students, should I choose an academic career path in the future, to whom I pledge my personal commitment.

I am very grateful to Prof. Dan M. Ionel, of the Department of Electrical and Computer Engineering of the University of Kentucky, for his instrumental role in every aspect of the research presented in this dissertation. In addition to his personal and close involvement, he established invaluable collaborations with renowned experts in this industry to pursue pragmatic research and to bridge academic scholarship and industrial practice. The depth and breadth of this work owes itself to Prof. Ionel's never-ending zest for research and its dissemination.

I am gratefully indebted to Dr. Thomas W. Nehl, of General Motors (GM) Global Research and Development, for all he did during these years from initiating the drive-cycle optimization project which lent itself to becoming the centerpiece of my Ph.D. research and dissertation, to providing the internship opportunity in his reputable team which led to starting my career at GM. His support has been essential during this time, and so have been his many contributions to the technical aspect of this work. I would have not embarked on this project, had it not been for Dr. Nehl's entrepreneurial initiatives.

I would like to also acknowledge the generous participation of Prof. Thomas M. Jahns, of the Department of Electrical and Computer Engineering of the University of Wisconsin-Madison, and Prof. Edwin E. Yaz and Prof. James E. Richie, of the Department of Electrical and Computer Engineering of Marquette University, in my Ph.D. Dissertation Committee. Particularly, Prof. Jahn's insightful commentary prompted mind-provoking discussions and substantially enriched the content of this dissertation, for which I am very much thankful.

I would like to express my special thanks to my dear friends and senior members of the Electric Machines and Drives Lab (EMDL) at Marquette University, Dr. Gennadi Y. Sizov, of Rockwell Automation, and Dr. Peng Zhang, of General Motors, for laying a solid foundation for the automated design optimization of permanent magnet machines, which served as the start point of my dissertation research. Their support in the initial stages of this project, and their encouragement in its continuation was exceptional.

Throughout my Ph.D. studies, I had the opportunity to collaborate with and learn from many experts in the field. During the early stages of this project, Mr. James R. Hendershot's instructions in recent advances in the design of brushless PM machines boosted my confidence to delve into this topic. Likewise, the instructive role of Dr. Dave A. Staton and Dr. Mircea Popescu, of Motor Design Ltd., in multiphysics analysis of PM machines was of great help and should be acknowledged. I also learned from, and enjoyed very much the collaborations with Mr. Steven J. Stretz, of Regal Beloit Company, and Dr. Rafal Wrobel and Dr. Yew C. Chong, of Motor Design Ltd. I am also thankful to Mr. Mark G. Solveson, of Ansys Inc., for his technical support for advanced use of Ansys software packages.

I would like to also thank the members of the Electric Drives and Power Electronics Systems Lab at GM R&D including Dr. Lei Hao, Dr. Chandra S. Namuduri, Dr. Rashmi Prasad, Dr. Suresh Gopalakrishnan, and Dr. Avoki Omekanda, for their mentorship and collegiality during summer 2015.

I would like to acknowledge the financial support of Marquette University's EECE Department, GM, M-WERC Consortium, and SEPMEED Consortium, which allowed me to work in this exciting and challenging field. The software support of Ansys Inc., and Motor Design Ltd. is also gratefully acknowledged.

I am also thankful to my present and former colleagues and friends at Marquette University's Electric Machines and Drives Lab, Dr. Gennadi Sizov, Dr. Peng Zhang, Dr. Jiangbiao He, Mr. Chad Somogyi, Mr. Andrew Strandt, Ms. Alia Strandt, and Mr. Muyang Li for creating a genuinely collegial learning and work environment. Also many thanks to my friends, Mr. Ahmadreza Baghaie, Dr. Benyamin Davaji, Dr. Marek Trawicki, Dr. Ahmed Sayed Ahmed, and Mr. Ramin Katebi for their encouragement and support.

Last but surely not least, I am eternally grateful to my most faithful companion, Nancy, whose love has inspired my life, and who is my home away from home.

Alireza Fatemi
August, 2016

TABLE OF CONTENTS

ACKNOWLEDGEMENTS . . . . . **i**

LIST OF TABLES . . . . . **viii**

LIST OF FIGURES . . . . . **x**

1 INTRODUCTION **1**

1.1 Significance of the Research Topic 1

1.2 Design Optimization of PM Machines Based on Computational Electromagnetics 5

1.2.1 Early Developments 5

1.2.2 Design Optimization for Rated Operation 10

1.2.3 Design Optimization for Entire Operating Range 14

1.3 Statement of the Problem 19

1.4 Dissertation Organization 21

1.5 Related Publications 22

2 DESIGN OPTIMIZATION FOR RATED OPERATING CONDITIONS **25**

2.1 Design Synthesis Using CE-FEA and DE 26

2.1.1 Overview of Computationally Efficient-Finite Element Analysis 26

2.1.2 Overview of Differential Evolution 35

2.2 Case Study Design Optimization of Toyota Prius Gen 2 Motor at Its Nominal Operating Point 39

2.2.1 Parametric CE-FEA Model 40

2.2.2 Optimization Procedure and Results 45

2.3 Summary 60

3 EFFECTS OF AMPERE LOADING LEVEL ON OPTIMAL DESIGN OF IPM MOTORS 61

3.1 Introduction 62

3.2 Benchmark Designs 65

3.2.1 Parametrized Cross Sections 65

3.2.2 Time-Stepping FE Models 67

3.3 Parallel Sensitivity Analysis at Different Ampere Loading Levels . . . 70

3.3.1 Methodology 70

3.3.2 Discussion of the Results of the Sensitivity Analysis 71

3.4 Parallel Statistical Analysis of the Optimized Designs at Different Ampere Loading Levels 76

3.4.1 Large-Scale Design Optimization 77

3.4.2 Scaling Rules of the Optimum Candidate Designs 79

3.5 Summary 85

4 MULTIOBJECTIVE CMODE-TYPE OPTIMIZATION OF ELECTRIC MACHINES 86

4.1 Introduction 87

4.2 CMODE Versus DE in the Design Optimization of Electric Machines 89

4.3 Benchmark Study- Application to IPM Motors 94

4.3.1 Parametrized FE Model 94

4.3.2 Optimization Fitness Functions 98

4.4 Comparative Study of the Results 100

4.5 Summary 114

5 DRIVE-CYCLE PERFORMANCE OPTIMIZATION 115

5.1 Introduction 116

5.2 Efficient Modeling of the Motor Load Profile 119

5.2.1 Energy Distribution Over the Torque-Speed Plane 119

5.2.2 Cyclic Representative Points 124

5.3 Performance Evaluation at Representative Points 128

5.4 Extended Speed Operation of PM Machines 136

5.5 Drive-Cycle Optimization 145

5.5.1 Algorithm 145

5.5.2 Computational Complexity of the Optimization Algorithm . . 149

5.6 Summary 150

6 CASE STUDY DRIVE-CYCLE OPTIMIZATION OF TRACTION MOTORS 151

6.1 Introduction 151

6.2 Optimization of the Prius IPM Motor Over a Compound Operating Cycle 152

6.2.1 Initialization 152

6.2.2 Optimization Results 157

6.3 Optimization of a Formula E Racing Car IPM Motor Over the Le Mans Operating Cycle 166

6.3.1 Initialization 168

6.3.2 Optimization Results 176

6.4 Summary 187

7 ADDITIONAL IMPLICATIONS OF PM MACHINES' DESIGN OPTIMIZATION 189

7.1 RSM-DE-ANN Sensitivity Analysis of Material Cost in PM Motors with Distributed and Concentrated Windings 191

7.1.1 FE-Based Machine Models 193

7.1.2 Effects of the Commodity Price on the Design Correlations . . 194

7.1.3 ANN-Based Design Optimization with Different Commodity Price Coefficients 198

7.1.4 Sensitivity of Optimal Design Values to Commodity Price Coefficients 202

7.2 A Computationally Efficient Method for Calculation of Strand Eddy Current Losses 206

7.2.1 Strand Eddy Current Loss Characterization 209

7.2.2 FE-Based Eddy Current Loss Estimation for Randomly Wound Stator Windings 211

7.2.3 Case-Study Analysis 217

7.3 Estimation of Tangential Mechanical Stresses on the Rotor Bridges . 223

7.3.1 Adopted Analytical Stress Estimation Method 225

7.3.2 Evaluation of the Accuracy of the Analytical Stress Estimation Method 227

7.4 Summary 232

8 CONCLUSIONS 235

8.1 Summary and Conclusion 235

8.2 Recommendation for Future Work 241

BIBLIOGRAPHY 243

APPENDIX I 264

APPENDIX II 267

APPENDIX III 272

LIST OF TABLES

1.1 Estimated annual savings resulting from the utilization of high-efficiency motor systems [1]. 2

2.1 Boundaries of the design variables defined over the parameterized cross-section of the Prius motor. 44

2.2 Geometric design parameters of the counterpart optimal designs obtained from the Prius motor design optimization at nominal load point. 48

2.3 Comparison of nominal performance between counterpart designs obtained from the Prius motor design optimization at nominal load point. 50

2.4 Distribution of power losses in the counterpart designs obtained from the Prius motor design optimization at nominal load point. 51

2.5 Mass of active components in the counterpart designs obtained from the Prius motor design optimization at nominal load point. 51

3.1 The independent design variables of the case study machines for sensitivity analysis and optimization at different ampere loading levels. 67

3.2 Typical current density ranges found in electric machines with different cooling systems. 69

3.3 Average design parameters of the optimized designs at different ampere loading levels. 82

3.4 Mean of the ratio of copper losses to core losses in the Pareto-optimal designs at different ampere loading levels. 82

3.5 Mean of the masses of the optimized designs normalized with respect to the values obtained for NC class. 83

4.1 Independent design variables of the parametric stator and rotor structures shown in Figs. 4.3 and 4.4. 98

4.2 Comparison of the number of the feasible Pareto optimal designs between DE and CMODE. 112

4.3 Comparison of the number of total feasible design candidates between DE and CMODE. 112

6.1 Cyclic representative points for the combined US driving cycle shown in Fig. 6.1. 156

6.2 Cyclic representative points of Le Mans driving cycle shown in Fig. 6.13.171

6.3 Independent design variables and their upper and lower bounds of the 18-slot 16-pole spoke-type machine. 172

6.4 The design characteristics of the counterpart spoke-type motors. . . . 180

6.5 The design characteristics of the optimized high power density "D3" motor. 182

LIST OF FIGURES

1.1 U.S. electricity use by sector, (million kWh/year 2006) [2]. 1

1.2 Required improvements in current electric drive systems to meet EV Everywhere requirements [3]. 3

1.3 Design optimization based on GA. 11

1.4 High level design flow of an electric machine. 20

2.1 Design optimization of PM machines based on CE-FEA and DE. . . . 27

2.2 Mapping the field values between typical sister elements in the CE-FEA method. 28

2.3 Reconstruction of mid-tooth flux densities using the CE-FEA method. 29

2.4 Reconstruction of mid-yoke flux densities using the CE-FEA method. 30

2.5 Reconstruction of stator winding flux linkages using the CE-FEA method. 31

2.6 Reconstruction of the torque profile using the CE-FEA method. . . . 32

2.7 Evolution model of DE from one generation to another. Multiple members of the current population can be processed simultaneously to decrease the computation time. 38

2.8 Cross-section of the Toyota Prius Gen 2 IPM motor. 40

2.9 Parametrized stator slot of the Prius motor. 42

2.10 Parametrized rotor layout of the Prius motor. 42

2.11 The parameterized cross-section of the Prius motor comprising 10 independent design variables, see Table 2.1. 45

2.12 Range of variation of the design parameters defined over the Prius motor topology. 46

2.13 Determination of current advanced angle for MTPA operation. 47

2.14 Results of the optimization of the Prius motor at the nominal load point expressed in terms of the designated objectives. 49

2.15 Cross-sections and rated field plots of the three counterpart designs obtained from the Prius motor design optimization at nominal load point. 53

2.16 Line to line back EMF of the counterpart designs obtained from the Prius motor design optimization at nominal load point (a) G59M12, (b) G20M62, and (c) Prius. 54

2.17 Harmonic content of the line to line terminal voltage of the counterpart designs obtained from the Prius motor design optimization at nominal load point. 55

2.18 Torque ripple of the counterpart designs obtained from the Prius motor design optimization at nominal load point. 56

2.19 Efficiency maps of the counterpart designs obtained from the Prius motor design optimization at nominal load point. 57

2.20 Load operating points of Toyota Prius propulsion PM motor obtained from ADVISOR. 58

2.21 Load operating points of Honda Insight propulsion PM motor obtained from ADVISOR. 59

3.1 The parametrized cross section of the case study machines for sensitivity analysis and optimization at different ampere loading levels. 66

3.2 Normalized regression coefficients from the sensitivity study indicating the effect of the design variables on, (a) active material cost, (b) copper loss, (c) core loss, (d) minimum PM flux density, and (e) torque ripple for the 48S8P machine. 72

3.3 Normalized regression coefficients from the sensitivity study indicating the effect of the design variables on, (a) active material cost, (b) copper loss, (c) core loss, (d) minimum PM flux density, and (e) torque ripple for the 12S10P machine. 73

3.4 Optimization results for the three case-study cooling systems. 78

3.5 The distribution of the design variables in the optimized designs for the three case study cooling systems. 80

3.6 Optimized cross sections derived based on the mean of the design variables in the 500 Pareto-optimal designs listed in Table 3.3, for the three current density levels. 82

4.1 Flowchart of the steps of the DE optimization algorithm. 90

4.2 Flowchart of the steps of the CMODE optimization algorithm. . . . 91

4.3 The parameterized stator structures used for constructing the example IPM motors for comparison between DE and CMODE. 96

4.4 The parameterized rotor structures used for constructing the example IPM motors for comparison between DE and CMODE. 97

4.5 The evolution of the optimization process using DE for the three case-study motors under the first scenario. 102

4.6 The evolution of the optimization process using CMODE for the three case-study motors under the first scenario. 103

4.7 The evolution of the optimization process using DE for the three case-study motors under the second scenario. 104

4.8 The evolution of the optimization process using CMODE for the three case-study motors under the second scenario. 105

4.9 Feasible Pareto optimal designs of the two optimization algorithms for scenario 1 of the fitness functions. 106

4.10 Feasible Pareto optimal designs of the two optimization algorithms for scenario 2 of the fitness functions. 107

4.11 Convergence of the feasible design candidates for the three case-study motors in terms of $loss \times AMC$ for scenario 1. 109

4.12 Convergence of the feasible design candidates for the three case-study motors in terms of $loss \times ripple$ for scenario 2. 110

4.13 The normalized hypervolumes of the Pareto fronts generated by DE and CMODE for the two scenarios of fitness functions. 111

4.14 Typical optimized cross-sections and the field plots of the studied motors for the two scenarios of fitness functions. 113

5.1 The Toyota Prius Gen 2. motor load profiles. 120

5.2 The Honda Insight Gen. 1 motor load profile. 121

5.3 Toyota Prius Gen. 2 motor output energy over torque-speed plane. . 122

5.4 Honda Insight Gen. 1 motor output energy over torque-speed plane. . 123

5.5 Cyclic representative points of Toyota Prius Gen. 2 motor output energy over torque-speed plane. 126

5.6 Cyclic representative points of Honda Insight Gen. 1 motor output energy over torque-speed plane. 127

5.7 The best sum of the distances of the load points to their corresponding cluster means versus the number of clusters. 129

5.8 Effects of saturation and cross-saturation in prediction of torque, and induced voltages over the full range of excitation current. 130

5.9 Developed method for derivation of the stator winding currents at every load point for time-stepping magneto-static FEA. Optimal control is ensured for constant torque and flux weakening operation. 133

5.10 Process of derivation of the excitation current for a typical load point. 134

5.11 PM demagnetization maps of a typical motor for PMs located with respect to the rotor motion for motoring operation. 135

5.12 Sampled flux contours of the three example motors with equal rated torque and rated current density. 138

5.13 Efficiency maps of the three example IPMs with infinite maximum speeds. 140

5.14 Loss ratio maps of the three example IPMs with infinite maximum speeds. 141

5.15 Current density maps of the three example IPMs with infinite maximum speeds. 142

5.16 Q-axis current density maps of the three example IPMs with infinite maximum speeds. 143

5.17 Negative d-axis current density maps of the three example IPMs with infinite maximum speeds. 144

5.18 Current density maps of the three example IPMs with infinite maximum speeds. 146

5.19 The flowchart of steps of the overall optimization algorithm. 147

6.1 Load profile of the Toyota Prius Gen. 2 IPM over a combined driving cycle. 153

6.2 Toyota Prius Gen. 2 motor output energy versus torque and speed for the combined US driving cycles. 154

6.3 Cyclic representative points with seven clusters for the combined US driving cycle. 155

6.4 Optimization results of Toyota Prius Gen .2 IPM motor over the combined US driving cycles. 158

6.5 Comparison of the selected designs obtained from drive-cycle optimization. 159

6.6 Efficiency maps of the selected designs obtained from drive-cycle optimization. 160

6.7 Tested efficiency map of the Toyota Prius Gen. 2 IPM motor reported by the research team at ORNL. 161

6.8 Lumped thermal network model of the motor cooling system developed in Motor-CAD. 162

6.9 The peak temperatures of the counterpart designs evaluated over US06 driving cycle. 163

6.10 Von-Mises stress throughout the rotor structure of the counterpart designs. 165

6.11 Formula E motor load profile for the Le Mans driving cycle. 168

6.12 Formula E motor energy consumption in the torque-speed plane. . . . 169

6.13 Le Mans driving cycle representative points obtained from k-means algorithm with seven clusters. 170

6.14 The parameterized FE model of the spoke-type PM motor, see Table 6.3. 172

6.15 The results of optimization of the spoke-type IPM over 3,400 design solutions. 174

6.16 Correlation of performance metrics with mass and power losses in the designs optimized for efficiency and high power density. 175

6.17 Distribution of the design parameters in the Pareto-optimal designs, and their correlation with total mass and power losses. 177

6.18 Equivalent machine model used for analytical investigation of the optimal design of spoke-type FSCWs. 178

6.19 Histogram of the distributions of (a) k_{si}, and (b) $k_{w_{pm}}$ in the 100 Pareto-optimal designs. 179

6.20 Flux lines distributions of the optimized designs at 6 000 r/min under rated load. 181

6.21 Efficiency maps of the optimized spoke-type designs. 183

6.22 Copper loss maps of the optimized spoke-type designs. 184

6.23 Core loss maps of the optimized spoke-type designs. 185

6.24 Identifying a design with higher power density and drive-cycle efficiency than the original design. 186

6.25 Flux lines distributions at 6000 r/min. 186

6.26 Efficiency maps of the high power density spoke-type designs. 187

7.1 Variation of the price of constructive commodities of Nd-based PM motors for three consecutive years leading the surge of the Nd price in 2011 [4, 5]. 191

7.2 Influence of the design parameters on AMC in the two case-study motors. 195

7.3 Change of the influences of the design parameters on AMC based on the value of the commodity price coefficients. 196

7.4 Developed procedure for sensitivity analysis of the optimal design values. 200

7.5 Estimation error of the ANN-based models when compared to FE-based machine models. 201

7.6 Optimization results of the 48S8P motor configuration for a typical set of commodity price coefficients. 203

7.7 Optimization results of the 12S10P motor configuration for a typical set of commodity price coefficients. 204

7.8 The sensitivity of the optimal design parameters to variation of the commodity price coefficients. 206

7.9 Slot leakage and fringing flux in a typical open-slot FSCW PM machine. 207

7.10 Alternative coil models for strand eddy current loss analysis. 212

7.11 Radial and tangential components of the field sections in Fig. 7.10(c) for a typical motor. 214

7.12 Determination of $s_{f,\max}$ and conductor positions by moving the slot geometry over a grid of conductors. 215

7.13 Slot fill factor and strand positions for example slot geometries as the net slot area increases. 216

7.14 Reconstruction of the field harmonics from the sample points using Delaunay triangulation method. 217

7.15 Mapped flux on each individual strand. 218

7.16 Distribution of strand eddy current losses under various loading levels. 219

7.17 Case-study investigation of strand eddy current losses. 220

7.18 Comparison of the accuracy of the loss calculation method over a wide range of frequencies and loading conditions. 221

7.19 Estimation error of the computationally efficient method of calculation of strand eddy current losses compared to the full-fledged time harmonic analysis with detailed coil modeling. 222

7.20 Variation of dc ohmic losses and strand eddy current losses with respect to loading level. 223

7.21 Ratio of ac to dc losses over a wide range of loading conditions. . . . 224

7.22 Modeling of the original layout on the left with the equivalent ring on the right. 226

7.23 Preparing the rotor geometry for structural FE analysis. 229

7.24 Comparison of the accuracy of the analytical stress estimation method through a sensitivity analysis. 230

7.25 Change of $k_{d_{pm}}$ ratio from lower to upper bound. 231

7.26 Change of k_{w_q} ratio from lower to upper bound. 231

CHAPTER 1
INTRODUCTION

1.1 Significance of the Research Topic

Electric motor driven systems are considered to be the largest consumers of electric energy, often accounting for up to one-third or more of the total electricity sold in industrialized countries [1]. In the U.S., electric motors account for 38% of the total electrical energy consumption [2, 6], see Figure 1.1. The financial and environmental incentives for energy savings are substantial, through improving the efficiency of the electric motor driven systems in the U.S., see Table 1.1 [1].

In this respect, two fundamental areas of opportunity are:

- improving the motor efficiency at the component level, and
- improving the device efficiency at the system level.

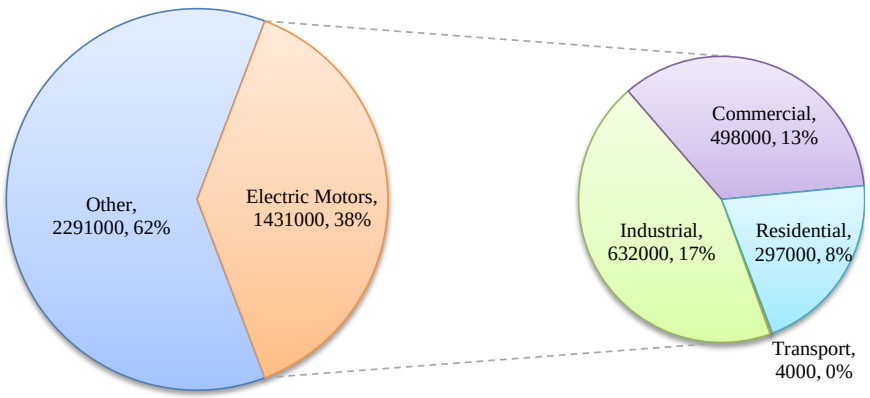

Figure 1.1: U.S. electricity use by sector, (million kWh/year 2006) [2].

Table 1.1: Estimated annual savings resulting from the utilization of high-efficiency motor systems [1].

Cost saved	\$3-5 billion
Energy saved	62-104 giga kWh
CO_2 emission	15-26 mega tons

The latter measure, which will not be addressed in this dissertation, covers a broad spectrum of strategies ranging from upgrading the system control technologies, to matching the type and size of the motor with the load requirements, better maintenance, etc.

Regarding the efficiency advancement of electric motors at the component level, recent trends have focused on [7]:

- the use of new materials for laminations, conductors, and permanent magnets (if applicable),
- the investigation of advanced concepts in design of the rotor, stator, and winding configurations, and
- perfecting the existing technology by fully exploring the design space for optimal sizing/shaping of the motor cross-section.

Owing to the Energy Policy and Conservation Act of 1992 (EPAct) and the subsequent NEMA Premium motors standard, which has been made mandatory since Dec. 2010, the penetration rate of high efficiency motors in the U.S. has been steadily rising in recent years [2]. Lately, the EV Everywhere Grand Challenge [3], which was initiated in March 2012 to render plug-in electric vehicles (PEVs) as affordable as gasoline-powered vehicles, introduced a new category of stringent requirements on

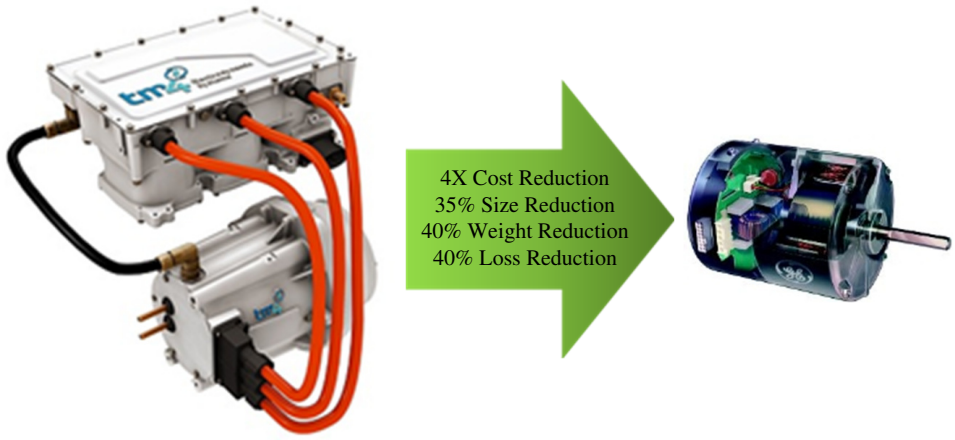

2012 Electric Drive System*

$30/kW, 1.1 kW/kg, 2.6 kW/L
90% system efficiency
55kW SYSTEM cost of $1650
* Today's electric drive systems use discrete components, silicon, semiconductors, and rare earth motor magnets.

2022 Electric Drive System**

$8/kW, 1.4 kW/kg, 4 kW/L
94% system efficiency
55kW SYSTEM cost of $440
** Future systems may meet these performance targets through advancements such as fully integrating motors and electronics, wide bandgap semiconductors, and non-rare earth motor.

Figure 1.2: Required improvements in current electric drive systems to meet EV Everywhere requirements [3].

electric drive systems in EV applications which should be realized by 2022, see Figure 1.2. Therefore, it is expected that performance enhancement of electric motors will remain a continuous challenge in future years.

There are a number of factors by which high performance electric motors are characterized and measured; amongst them are high efficiency, low torque ripple, high torque density, high power factor, sinusoidal back-emf waveform with low harmonic content, fast dynamics, mechanical robustness, low maintenance, manufacturability, cost effectiveness, and sustainability. As found in research studies by the American Council for an Energy-Efficient Economy (ACEEE) [8], the technical difficulties of performance improvement in induction motors are prohibitive due

to their associated mature technologies, thus promoting further research in other advanced commutatorless motors such as synchronous reluctance motors (SyRM), permanent magnet synchronous motors (PMSM), flux switching motors (FSM), switched reluctance motors (SRM), etc.

Due to the eliminated rotor copper losses in PMSMs, such machines can be designed to maintain high efficiency at higher torque densities, and yet with a less sophisticated cooling system [9]. With proper control, PMSMs can operate at high power factors similar to their counterpart wound-field synchronous machines with a separate controllable magnetic field source. However, as opposed to the wound-field synchronous machines, PMSMs have lower maintenance, better rotor structural integrity, and faster dynamics due to the absence of rotating field windings and elimination of the brushes or other complex brushless excitation systems. These characteristics have rendered PMSMs to represent a catagory of promising solutions to meet the stringent requirements of high performance applications.

In this regard, this dissertation will focus on performance improvements in sinewave drive brushless PMSM technology using computationally efficient and high fidelity simulations as will be discussed in the following sections.

1.2 Design Optimization of PM Machines Based on Computational Electromagnetics

1.2.1 Early Developments

Computational electromagnetics (CEM) began by applying the principles of highly developed finite difference (FD) discipline of mathematics to solving two-dimensional static field problems [10] in the works of Trutt [11], Erdelyi [12–15], and Demerdash [16–18]. From the very beginning, computer aided design optimization of electric machines based on CEM was pursued by many investigators. An example of pioneering numerical design optimization of synchronous machines was reported by Demerdash and Hamilton [16, 19], where finite difference models of two- and four-pole turbo-generators were developed and employed for determining asymmetric angular position of the rotor slots for reducing the eddy current losses in the stator strands. The model was capable of taking the complex geometry and the saturation phenomenon in to account.

As the finite element method (FEM) proved to be more effective, more accurate, and easier to implement in electromagnetic modeling of electric machines [20, 21], the tendency for application of FEM, as opposed to FD, in various types of electric machines grew rapidly in early works of many investigators such as Chari and Silvester [22–26], Brauer [27], Anderson [28], Demerdash and Nehl [21, 29–31], and others.

Some of the earliest FE-based design optimization efforts were conceived as "inverse field problems", as opposed to a "forward problem" in which the field

distribution and the magnetic vector potential is determined for given design specifications including the geometry, excitation, boundaries, and material properties. In an inverse problem, the flow of the design is reversed whereby a specific performance objective such as flux distribution is pursued by treating the parameters previously assumed to be known as unknowns [32, 33]. The first optimization attempts formulated as inverse problems were achieved by handling the coordinates of the boundary nodes of the FE model as additional unknowns in the Newton-Raphson iterations. In his work, Nakata [34–36] developed a simplified inverse model for one-at-a-time treatment of the dimensions of a group of permanent magnets to determine the optimal shape and size required for producing prescribed flux densities at desired points in the air-gap. As reported later, his developed method failed to produce meaningful results for relatively more complicated design cases [37]. This was in part due to the fact that the treatment of the boundary nodes as design variables results in piecewise linear structures, which in turn oftentimes led to undesirable spikes and edges in the structure of the optimized shapes [38–40], thus necessitating a subsequent manual smoothing with compromised performance [38]. In the following years, through a methodological analysis of different formulations for solving inverse electromagnetic problems, Guamieri et al. demonstrated that inverse problems can, in essence, be reduced to problems of numerical optimization [41].

In parallel with the formation of inverse field problems, some investigators formulated the design process as a classic optimization problem with two main segments: an "optimizer" to determine the direction of parameter adjustment; and an "analyzer" to calculate the performance criterion [42]. Armstrong et al. [42]

introduced a rudimentary automated approach for the design of electromagnetic components using 2-D magnetostatic integral field solutions in linear media. The investigators concluded that several attempts of user intervention in the design process is required to yield satisfactory results. With a similar perspective, Gitosusastro et al. [43] distinguished the two main segments of a systematic optimization procedure for the design of electromagnetic devices based on FE field computation methods. Also reported in their early investigations was the sensitivity analysis, which revealed, by way of direct differentiation of the FE matrices, how the performance characteristics of the machine are affected by changes in the design variables. In [44], Koh et al. studied magnetic pole optimization of a PM motor for the reduction of cogging torque. A similar sensitivity analysis was devised to study the correlation of the design variables with cogging torque. Park et al. fully elaborated this method of sensitivity analysis of 2-D magnetostatic problems in [45]. Hoole et al. [46] applied the same concepts to identify the magnetic systems through external measurements of the electromagnetic field.

Due to the limitations of computational power, early systematic design optimization methodologies tended to use deterministic, as opposed to stochastic, strategies/optimizers in their search algorithms [47]. Some early references on the application of deterministic methods in electromagnetic problems can be found in the works of Saldanha et al. [48, 49]. The deterministic algorithms are characterized with very fast convergence provided that the objective function is convex and differentiable. However, they face the risk of premature convergence to local minima in a practical optimization problem where such hypotheses cannot be made a priori. This

disadvantage of the deterministic approach led to popularity of stochastic algorithms in the design of non-linear and complex electromechanical devices, especially with the advent of more powerful computational systems. Stochastic methods are more reliable in finding the global minimum of non-differentiable non-convex functions because these methods do not rely on gradient calculations [50]. However, they require a large number of function evaluations, typically in the range of thousands, to locate global optimum. An early reference on comparative analysis of several search algorithms with zero, first, and second order characteristics including the Monte-Carlo iteration (MC), the steepest descent (SD), conjugate gradient, and quasi-Newton is a publication by Gottvald [51]. Gottvald's study was focused on a large class of magnetostatic optimization problems which can be extended to complex electromagnetic and electromechanical systems. He noticed that a multitude of the factors involved in design of these complex systems precludes the prescription of a fastest method, however, the zero-order methods such as MC are more effective not in terms of time-efficiency, but in terms of reliability, numerical stability, generality, and convergence to global minimum [52]. Gottvald also stressed the challenges in solving computational electromagnetics optimization problems such as the existence of local minima, and non-convex subdomains. In subsequent collaborations, Gottvald and Preis rigorously compared deterministic and stochastic optimization algorithms in computational electromagnetics design problems [53–55] to unequivocally conclude that the studied stochastic methods are far superior in terms of robustness and generality for complex applications, and that their convergence rates can be comparable to those of deterministic methods. A combination of stochastic

and deterministic techniques for taking advantage of desirable characteristics of each approach has also been suggested by some investigators, e.g. by Drago et al. in [56] or by Simkin and Trowbridge in [57].

Russenshuck [58] categorized the optimization of PM machines into constrained and unconstrained vector-optimization problems and comparatively studied the convergence of several optimization algorithms for these two types of problems using two different surface mounted PM machines as the benchmark designs. Russenshuck's work was also novel in other aspects such as the introduction of the concept of Pareto-optimality for design of PM machines in a multi-objective optimization problem, or the employment of global quantities (e.g. power density, torque, and magnet weight) as opposed to local quantities (e.g. flux distribution) in defining the objective functions. He pointed out the difficulties of incorporating higher order deterministic algorithms in optimization problems based on numerical field calculations which are subject to field discretization errors. This issue was further elaborated by Hoole et al. in [59]. They found out that the discontinuities in the objective function have no physical basis, yet they will persist regardless of the mesh accuracy. In a later work, the same investigators developed a structural mapping method for geometric parametrization to minimize these discontinuities [60], which was then used in the design optimization of salient pole synchronous machines [61].

In the early 1990s, several investigators reported the application of stochastic search algorithms in the design optimization of PM machines based on numerical field calculations. Preis et al. [62] utilized evolutionary algorithms for the design optimization of the pole shape of a dipole magnets using two- and three-dimensional

FE models. Some investigators, e.g. Schafer Jotter and Muller in [63] or Simkin and Trowbridge [64] reported a detailed step-by-step procedure for optimization of electromechanical devices using numerical techniques and systematic optimization algorithms.

1.2.2 Design Optimization for Rated Operation

Owing to the developments in electromagnetic FEM and the increase of processing power of computational resources, population-based design optimization of electric machines using high fidelity FE models has become an established practice. In [65], Uler et al. developed a population-based method for design optimization of electromagnetic devices using 2-D FE models as the analysis tool and genetic algorithms (GA) as the search algorithm. The investigators implemented the method in Fig. 1.3 for design optimization of the pole face of a motor to achieve sinusoidal magnetic flux density in the air-gap for one particular loading condition, i.e. a current density of $10A/mm^2$. Four design parameters each coded into 16-bit string segments of binary codes were incorporated in a large-scale design optimization with a population size of 30 members which was carried out over 24 iterations. In subsequent research, Mohammed [66] discussed the practical issues in the application of GA to design optimization of electromagnetics devices, with a particular emphasis on the issue of premature convergence.

In [67], Chun et al. developed an evolutionary strategy by combining genetic algorithm and simulated annealing for minimization of cogging torque of a closed slot PM servo motor. The FEM was used for performance evaluation of the design

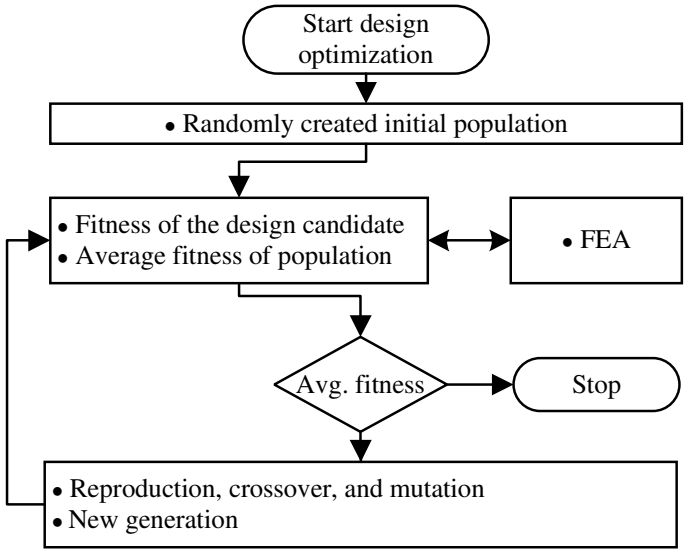

Figure 1.3: Design optimization based on GA.

candidates. A rated torque of 3 Nm and an ampere turn of 136 AT was considered. The optimization was performed over 900 generations each of 1 member to optimize the structure of the stator slot which was parameterized through 31 design variables. Also in [68], Chung et al. optimized the slot shape of a PM machine to reduce the cogging torque using FEM and a similar evolutionary algorithm. Their parametrized model consisted of 3 design variables.

In [69], Bianchi and Bolognani utilized GA to optimize a surface mounted PM motor using both analytical and FE models for analysis of the motor performance. The method could take global figures of merit such as torque, efficiency, and the material cost into account. Using the FE-based model, the investigators pursued two scenarios of optimization with different objectives, one with the objective of minimizing the PM mass for a rated torque of 10 Nm, and the other with the objective of maximizing torque density within confined stator outer diameter and axial stack

length. In both cases, the model consisted of five design parameters on the stator and PM structures. Furthermore, additional performance constraints on the winding temperature and the minimum air-gap flux density were defined. The optimization was performed with different population sizes to conclude that the best results are achieved with a population size of larger than 50 members. The investigators also performed the optimization using hill-climbing direct search method to observe that the optimized designs obtained using GA were slightly better than those produced by the hill-climbing direct-search method, indicating the presence of local minima in the search space. In a similar work, Bianchi and Canova [70] used the same GA-FEM large-scale design optimization methodologies to maximize the torque of an IPM machine for a given peak stator current of 70 A. In this case, the optimal values of five design parameters were pursued in a procedure consisting of 10 generations each of 100 members.

In early applications of FEM in the large-scale design optimization of PM machines, due to the computationally demanding nature of the FE models, typically a single magnetostatic solution would be performed to characterize the machine performance. In [71], Ohnishi and Takahashi included the rotor motion by taking into account the relative position of the rotor with respect to the stator through a nonconforming meshing technique, first introduced by Fouad et al. [72], which reduces the computation time required for mesh modification during the rotation. The investigators then used this technique in optimizing the rotor of an IPM machine with four design parameters. The optimization which was carried out over a large number of iterations, led to significant reductions of PM volume and torque ripple

under a rated current of 3 A(rms). Many other investigators have aimed to reduce the computational burden of the design optimization procedure by incorporating alternative modeling techniques, including analytical models as in [73], lumped parameter models as in [74], and artificial intelligence models as in [75]. However, as studied in [76–78] for a broad range of modeling techniques, there is always a trade-off between accuracy and execution time of the model-based design and analysis.

In the case of sinusoidally excited three-phase PM synchronous machines, as was observed by some investigators in [72, 79–81], in addition to the magnetic periodicity, the existing electrical symmetry enables estimation of various performance metrics of the machine by only analyzing a sixth of an electrical period. This idea was fully elaborated by Sizov et al. in [82] as the computationally efficient-finite element analysis (CE-FEA). The CE-FEA approach was subsequently utilized in the parametric study and later-on in large-scale design optimizations of several PM machines using only a regular desktop workstation, as opposed to using high performance computing (HPC) systems as reported in [83]. Although the CE-FEA method does not provide an estimation of the rotor core losses, these losses are usually smaller than the stator core losses due to the unvarying field in the stator of synchronous machines. In [84], five case-study machines with different pole-slot combinations and power ratings were optimized using CE-FEA and DE. Each case-study was fully parameterized to allow variations of the rotor and stator structures. The optimization involved thousands of design evaluations each incorporating multiple magnetostatic solutions to take into account the rotor motion. The designs were optimized to maximize the torque density, and to minimize the

torque ripple and power losses at the rated load operating point. In [85], Zhang et al. reported the optimization of a fault-tolerant 12-slot 10-pole IPM machine using the CE-FEA and DE design synthesis package. The motor model, which was parameterized through 9 independent design variables, was optimized for minimized losses and active material cost, subject to several performance constraints on torque ripple, induced voltage THD, and degree of PM demagnetization, all at the rated load point corresponding to a torque of 42 Nm and a speed of 1800 r/min. For a large number of design candidates, i.e. 50 generations of 70 members each, the optimization took only 28 hours on a PC workstation. The same design methodology was employed by Brown et al. [86], for optimization, comparison, and prototyping of two IPM topologies for use in a commercial heat pump. The investigators concluded that the CE-FEA optimization methodology was successfully tested in designing the high-efficiency prototypes. Duan et al. in [87], Zhang et al. in [85, 88], and Wang et al. in [89, 90] reported several other successful implementations of the CE-FEA design optimization methodology for improving the rated performance of various types of PM or SyR machines.

1.2.3 Design Optimization for Entire Operating Range

One of the major merits of salient pole synchronous machines is their efficient operation in the extended speed range. This is due to the contribution of the reluctance torque in this mode of operation, which can be overlooked if not directly evaluated in the optimization fitness function. However, the common practice is to assess the fitness function at the rated load point.

In [91], Sibande et al. implemented an FE-based design optimization algorithm to improve the field weakening performance of a synchronous reluctance machine (SyRM) which was equipped with additional sheets of PM in between the rotor flux barriers resulting in a PM-assisted SyRM. The goal of the optimization was to minimize the volume of the rotor PMs while realizing the performance constraints on minimum required torque and maximum allowed supply voltage under rated and maximum speeds. The design parameters were limited to the thickness of the magnet sheets in the rotor flux barriers, leaving the stator and the rotor structures unchanged. An optimal design was achieved and was shown to outperfom the original SyRM in terms of torque and terminal voltage characteristics. The efficiency during the extended speed operation was not investigated.

Zarko et al. first introduced a systematic optimization algorithm for simultaneously minimizing the rotor volume and maximizing the power capability in the flux weakening regime in [92] based on the idea of equality of the rated current and the characteristic current [93], i.e. the ratio of magnet flux linkage to d-axis inductance. The investigators utilized FE-based models and a DE optimizer for maximizing the characteristic current and minimizing the active volume of the example two- and three-layer IPM motors. An additional performance constraint was imposed on the back emf to limit it to 400 V at maximum 6 000 r/min speed. A relatively large number of design parameters, 13 and 15 variables depending on the number of the magnet layers, and a relatively large number of design candidates, 8 000 and 10 000 designs, were evaluated. Although a minimum efficiency of 0.8 was considered as a design constraint, maximizing efficiency was not pursued. Another

pioneering model-based design optimization study for improving the field weakening performance of IPM machines was developed by Quyang et al. [94], where Monte Carlo and DE algorithms were coupled to FE-based models to optimize two IPM motors with modular and regular stator structures. In the optimization of the conventional stator design, similar to Zarko's work in [92], the motor was optimized for maximum electromagnetic torque at base speed, and maximum normalized characteristic current for improved field weakening operation.

Similarly, the idea of equality of the characteristic current, I_{CH}, with the rated current, I_R, was introduced as an additional objective for optimization of IPM motors for enhanced field weakening performance. In [95], Pellegrino and Cupertino adopted this criterion to optimize the rotor structure of an IPM motor with three PM layers using a genetic algorithm optimizer coupled to a static FE-based model. Through performing four sets of optimizations with different objectives, it was asserted that there is a trade-off between the constant power range and torque production capability. In [96], Zhang et al. developed an optimization algorithm based on CE-FEA coupled to a DE optimizer to minimize the difference between the values of I_{CH} and I_R, in order to achieve a wide constant power range of operation. Minimization of material cost and stator losses at the rated load point were simultaneously pursued. Based on these objectives, it was concluded that for the two studied IPM motors with single-layer and double-layer PMs, when extended speed operation is considered, high efficiency, high power factor, and saliency increase the material cost.

The equality of I_{CH}, and I_R improves the torque production capability of the machine [93]. However, from the efficiency standpoint, congruity of I_{CH}, and I_R

cannot be the ideal criterion for constant power operation. By definition, maximizing I_{CH} results in either stronger magnets or lower d-axis inductance. Accordingly, when the non-linear and lossy nature of the machine is considered, for machines with larger I_{CH}, a larger magnitude of negative d-axis current is required to demagnetize the magnet flux and maintain controllability in the extended speed range. This results in higher copper losses and diminishes the energy efficiency of the field weakening regimen [97, 98].

In some studies, the field weakening performance of the machine is directly investigated by evaluating two critical load points: maximum torque at base and maximum speeds. In [99], Parasiliti used an FE-based model with a controlled random search optimizer to realize three objectives: maximize the torque at base speed, maximize the torque at maximum speed, and minimize the weight of the motor. Although the equality of I_{CH}, and I_R is not directly introduced in the optimization fitness function, overlooking efficiency in the definition of the objectives resulted in an optimized design in which the two currents are equal. Alternatively, in [100] in lieu of minimizing the weight, maximizing the torque and efficiency at the base and maximum speeds were considered as the objectives by Lee and Kwon. In this reference [100], an FE-based model in conjunction with a so-called Kriging approximation method were used to simultaneously improve the efficiency and operation range of a concentrated flux IPM motor. One limitation of the proposed method in [100], is the estimation of the stator winding excitation current using inductance-based motor models. Also in [101], Yamazaki et al. optimized the rotor design of an IPM motor through FE-based models to minimize the iron losses for maximum torque operation

at base and maximum speeds. However, the rotor geometry was only subjected to limited variations with some additional assumptions regarding the current advance angle which were not fully substantiated. The same investigators carried out another fine-tuning optimization of the rotor shape of IPM motors for reducing the iron losses in the field weakening region in [102].

In a different approach [103], Cupertino et al. suggested a three-stage FE-based optimization with genetic algorithm optimizer, for achieving desirable field weakening performance in a PM assisted SyR motor. In the first stage, the SyR motor with three flux barriers is optimized for maximum torque, and minimum torque ripple at the rated load point. Upon finding an optimal solution, a second optimization is carried out with constrained design parameters close to those obtained in the first stage plus or minus 15%. In the final stage of the design, PMs are introduced in the rotor structure. The grades of the PMs are so chosen to achieve the required flux weakening operation. Another study on PM assisted SyR motor by Barcaro et al. in [104] analyzed the influence of the PM volume on the field weakening performance using FEM. Subsequently, the relationships between PM remnant flux density and efficiency at two load points residing at base and corner speeds were investigated.

In more recent studies, researchers have attempted to optimize the machine performance over the entire driving cycle. In [105, 106], Wang et al. proposed a method known as the cyclic representative points to efficiently model a target driving cycle, specifically the New European Driving Cycle (NEDC) and the Artemis Urban Driving Cycle, by a finite number of torque versus speed points. These points were derived based on the energy distribution function specifically calculated for the vehicle

model and the target driving cycle. The investigators subsequently performed the optimization over these cyclic representative points. However, these studies do not fully address the following two issues:

1. The selection criterion for the representative points is relatively subjective, requiring a systematic approach for identification of the high-energy-throughput zones of the machine energy distribution function.

2. As opposed to a large-scale optimization algorithm, the method undertaken in those studies is a comparative study of a few designs with limited number of design variables.

In [107] the second shortcoming of [105, 106] was addressed in optimizing a PM assisted SyR motor using a FE-based model with genetic algorithm optimizer by Carraro et al. However, only two representative points, which were selected in a relatively subjective manner, were considered. This limited number of points cannot effectively represent the driving cycle. In the case study, both of the two representative points resided in the constant torque range. Therefore, the objectives which were defined as minimization of the torque ripple and motor losses over these points do not necessarily hold through the entire operating range.

1.3 Statement of the Problem

A typical traditional design procedure of an electric machine is shown in Figure 1.4. When an initial design is obtained, further improvements are possible through numerical optimization.

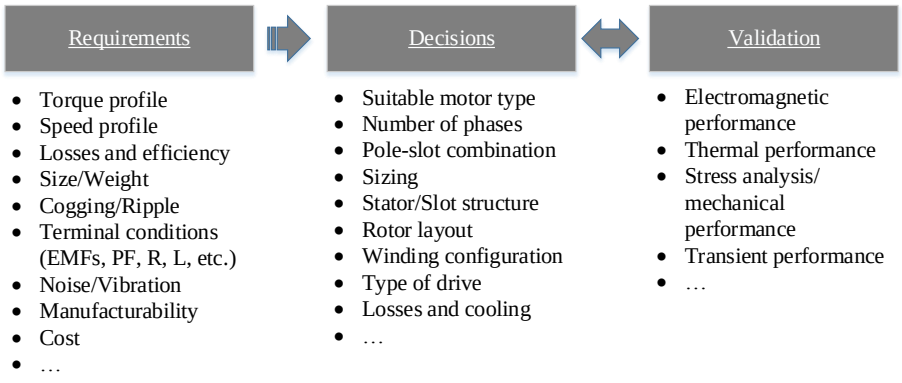

Figure 1.4: High level design flow of an electric machine.

In the light of the literature review, the common practice in large-scale design optimization of electric machines is to improve the desired performance metrics under the rated operating conditions. This is most suitable for applications in which the load profile is constant over the majority of the operation period, e.g. classes S1-S3, and S6 of standard rotating electrical machines according to IEC 60034-1. However, in many applications, the motor torque and speed profiles experience wide variations, e.g. electric motors in traction applications, or classes S4, S5, and S7-S10 of standard electric machines according to IEC 60034-1. Many impediments exist in taking the entire range of operation into account, of which the most notable is the computationally demanding nature of various stages of the optimization procedure. Accordingly, this dissertation addresses the challenges in the design optimization of high performance electric machines with non-constant operating cycles where an optimal design is to maintain high performance under wide loading conditions.

1.4 Dissertation Organization

In view of the problem background and the literature search, Chapter 2 discusses the essence of a recently introduced computationally efficient approach for large-scale design optimization of electric machines under rated operating conditions. This automated design package, which serves as the starting point of the topics investigated in this dissertation, is utilized in Chapter 2 to optimize the performance of the well-established benchmark design represented by Toyota Prius Gen 2 IPM motor for one particular operating condition. The necessity of including the entire range of operation into the optimization procedure is highlighted by this example. To mathematically corroborate the importance of design optimization over the motor operating cycle, the variations of optimal design rules of PM machines with respect to ampere loading level are systematically investigated in Chapter 3. For this purpose, two IPM motors with different cooling systems and winding configurations are studied. As the first step for increasing the computational efficiency of the design optimization procedure, a fast stochastic search algorithm for large-scale design optimization of electric machines is introduced in Chapter 4. By reducing the computational burden of the searching process, the developed algorithm enables adopting more complicated models with larger number of load operating points. In Chapter 5, the drive-cycle design optimization procedure, consisting of several stages, is developed, followed by optimization of two benchmark traction motors in Chapter 6. Chapter 7 is dedicated to additional implications of design of PM machines, including a sensitivity analysis of active material cost with respect to commodity price changes,

a computationally efficient method for calculation of strand eddy current losses, and a method for estimation of tangential mechanical stresses on the rotor bridges. The conclusions, and future works are provided in Chapter 8.

1.5 Related Publications

So far the topics discussed in this dissertation are published, or are in press in various IEEE publications, as follows:

[108] A. Fatemi; D. M. Ionel; N. A. O. Demerdash; T. W. Nehl, "Optimal Design of IPM Motors with Different Cooling Systems and Winding Configurations," in IEEE Transactions on Industry Applications , vol.PP, no.99, pp.1-1 (Early Access)

[109] A. Fatemi; N. Demerdash; T. Nehl; D. Ionel, "Large-scale Design Optimization of PM Machines Over a Target Operating Cycle," in IEEE Transactions on Industry Applications , vol.PP, no.99, pp.1-1 (Early Access)

[110] A. Fatemi; D. M. Ionel; N. A. O. Demerdash; T. W. Nehl, "Fast Multi-Objective CMODE-Type Optimization of PM Machines Using Multicore Desktop Computers," in IEEE Transactions on Industry Applications , vol.PP, no.99, pp.1-1 (Early Access)

[111] A. Fatemi, D. M. Ionel, M. Popescu, and N. A. O. Demerdash, "Design Optimization of Spoke-Type PM Motors for Formula E Racing Cars," Accepted for 2016 IEEE Energy Conversion Congress and Exposition (ECCE),

Milwaukee, WI, 2016.

[112] A. Fatemi, D. M. Ionel, N. A. O. Demerdash, S. Stretz, and T. M. Jahns "RSM-DE-ANN Method for Sensitivity Analysis of Active Material Cost in PM Motors," Accepted for 2016 IEEE Energy Conversion Congress and Exposition (ECCE), Milwaukee, WI, 2016.

[113] A. Fatemi, D. M. Ionel, N. A. O. Demerdash, D. Staton, R. Wrobel, and Y. C. Chong, "Computationally Efficient Method for Calculation of Strand Eddy Current Losses in Stator Windings of Electric Machines," Accepted for 2016 IEEE Energy Conversion Congress and Exposition (ECCE), Milwaukee, WI, 2016.

[114] A. Fatemi, N. A. O. Demerdash, D. M. Ionel and T. W. Nehl, "Large-scale Electromagnetic Design Optimization of PM Machines Over a Target Operating Cycle," 2015 IEEE Energy Conversion Congress and Exposition (ECCE), Montreal, QC, 2015, pp. 4383-4390.

[115] A. Fatemi, D. M. Ionel, N. A. O. Demerdash and T. W. Nehl, "Fast Multi-Objective CMODE-type Optimization of Electric Machines for Multicore Desktop Computers," 2015 IEEE Energy Conversion Congress and Exposition (ECCE), Montreal, QC, 2015, pp. 5593-5600.

[116] A. Fatemi, D. M. Ionel and N. A. O. Demerdash, "Identification of Design Rules for Interior PM Motors with Different Cooling Systems," 2015 IEEE International Electric Machines & Drives Conference (IEMDC), Coeur d'Alene,

ID, 2015, pp. 1228-1234.

[98] A. Fatemi, N. A. O. Demerdash and D. M. Ionel, "Design Optimization of IPM Machines for Efficient Operation in Extended Speed Range," Transportation Electrification Conference and Expo (ITEC), 2015 IEEE, Dearborn, MI, 2015, pp. 1-8.

CHAPTER 2

DESIGN OPTIMIZATION FOR RATED OPERATING CONDITIONS

In this chapter, an automated design package for optimization of sine-wave driven permanent magnet synchronous machines (PMSMs) and synchronous reluctance machines (SyRM) is reviewed. The presented design optimization methodology was previously developed by Dr. Gennadi Sizov [117] and Dr. Peng Zhang [118] at the Electric Machines and Drives Laboratory at Marquette University over the past few years. This design package, which on par with the common practice was developed for improving the machine rated performance, serves as the starting point of the research conducted in this dissertation. First, the essence of this design optimization approach including its two main segments, one for computationally efficient FE-based performance evaluation of the design members, and another for fast convergence to the globally optimal design solutions, is reviewed. Subsequently, a typical traction propulsion motor represented by the well-established/well-documented Toyota Prius Gen 2 interior PMSM design will be optimized for its peak operating condition. Through this case study, the principles of the automated design package developed by the team at Marquette University are reviewed. Furthermore, the shortcomings of the common optimization techniques in overlooking the performance requirements throughout the entire range of operation are delineated.

2.1 Design Synthesis Using CE-FEA and DE

The design synthesis of electric machines is a classical optimization problem which aims at realizing a set of objectives under a set of constraints. Either global performance metrics such as torque, losses and efficiency, terminal conditions, and material cost, or local quantities such as air-gap flux distribution, and PM local demagnetization can constitute the set of objectives. The constraints can also be either geometry-related, such as those imposed by mechanical design considerations, or performance-related, such as maximum permissible torque ripple, or degree of PM demagnetization.

A recently developed large-scale design optimization approach [119], which features FE-based performance evaluation of thousands of design members within a reduced time, is composed of two main parts, see Fig. 2.1. The first part is a computationally efficient-finite element analysis (CE-FEA) [80] which is utilized for performance evaluation of the design members with high fidelity. The second part is a stochastic differential evolution (DE) [120] search algorithm which is employed for finding the globally optimal solutions. In this section, the principles of CE-FEA and DE are reviewed.

2.1.1 Overview of Computationally Efficient-Finite Element Analysis

The CE-FEA approach fully exploits the existing electric symmetry and magnetic periodicity of PMSMs with sinusoidal current excitation. It is based on a sequence

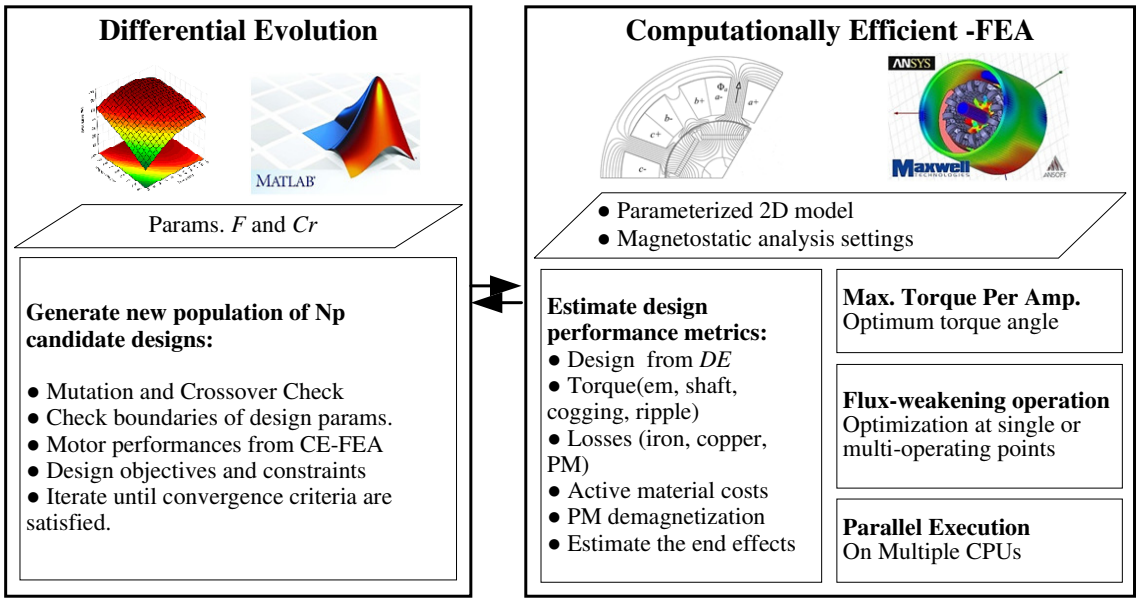

Figure 2.1: Design optimization of PM machines based on CE-FEA and DE.

of two-dimensional (2D) magnetostatic FE solutions at successive rotor positions covering one sixth of an electrical revolution/cycle. Compared to full-fledged transient time-stepping FEA, analyzing the motor performance using the CE-FEA approach can lead to significant savings in the modeling time, up to two orders of magnitude as stated in [119]. The principles of this modeling approach are briefly explained as given next.

2.1.1.1 Reconstruction of Field Waveforms

The steady-state 2D magnetostatic FEA of a PM machine in xy-plane is expressed by the Poison's equation given below:

$$\frac{\partial}{\partial x}\left(\nu\frac{\partial A}{\partial x}\right)+\frac{\partial}{\partial y}\left(\nu\frac{\partial A}{\partial y}\right)=-J-J_{PM} \tag{2.1.1}$$

where ν is the material reluctivity, A is the magnetic vector potential (mvp), J is the excitation current density, and J_{PM} is the equivalent current density for modeling

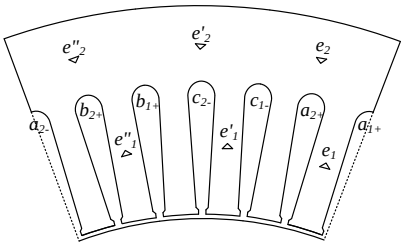

(a) 48-slot 8-pole configuration

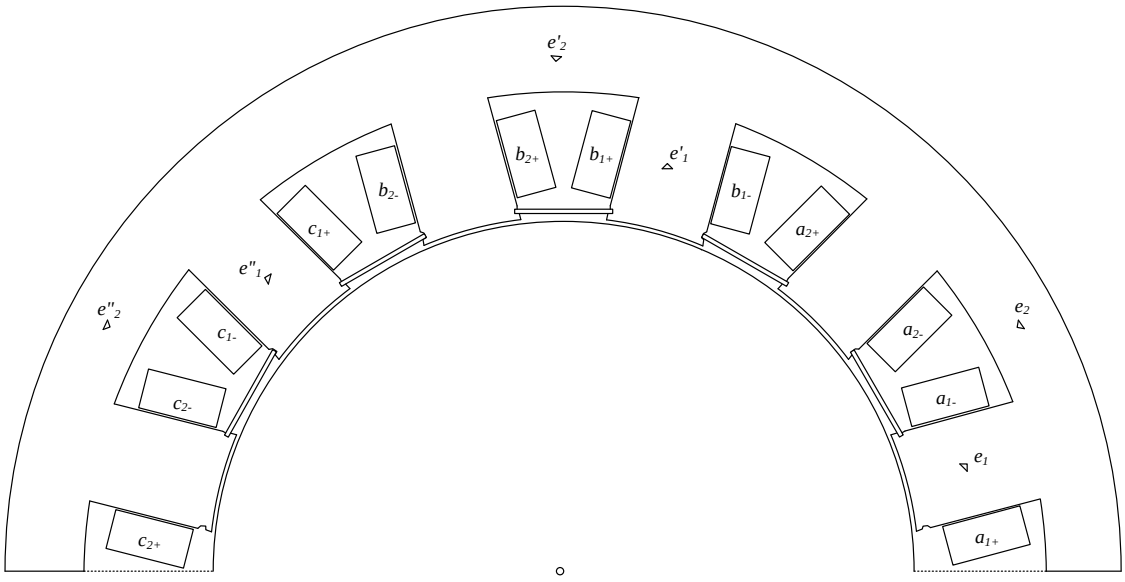

(b) 12-slot 10-pole configuration

Figure 2.2: Mapping the field values between typical sister elements in the CE-FEA method.

the permanent magnets. Equation (2.1.1) is solved at successive rotor positions for obtaining the unknown mvps according to a predefined excitation, J and J_{PM}. The instantaneous values of J are determined from the rotor position, θ_m, and loading condition of the machine.

If a balanced three-phase sinusoidal current excitation is assumed, the electric symmetry in the stator geometry can be used to map the tangential, f_T, and radial, f_R, field values between sister elements throughout the stator periodicity span, as

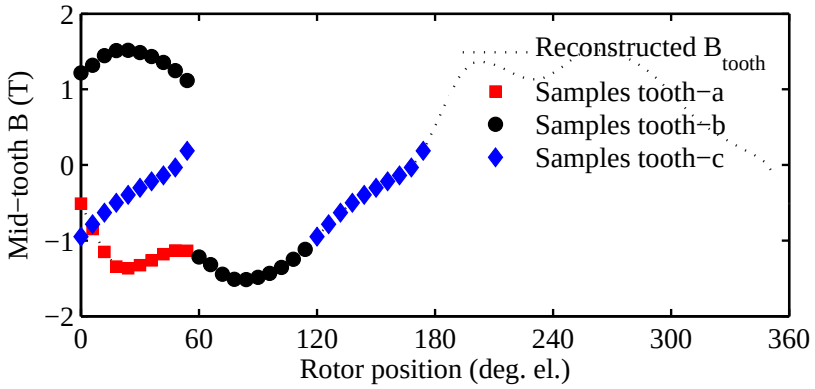

(a) 48-slot 8-pole configuration

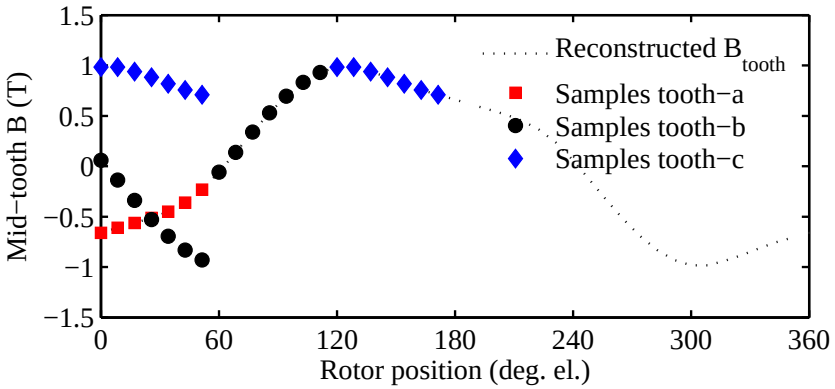

(b) 12-slot 10-pole configuration

Figure 2.3: Reconstruction of mid-tooth flux densities using the CE-FEA method.

given below:

$$f_{R,T}(t + \frac{k\alpha_s P}{2\omega}, r, \theta) = f_{R,T}(t, r, \theta + k\alpha_s) \tag{2.1.2}$$

where, k is the index that depends on the slot-pole combination and winding layout, P is the number of poles, ω is angular frequency, and α_s is the slot pitch in mechanical measure.

Typical sister elements for two different pole-slot combinations, i.e. a 48-slot 8-pole, and a 12-slot 10-pole configuration are graphically illustrated in Fig. 2.2 (a) and (b). As shown Fig. 2.2, in the CE-FEA method, the field values are mapped

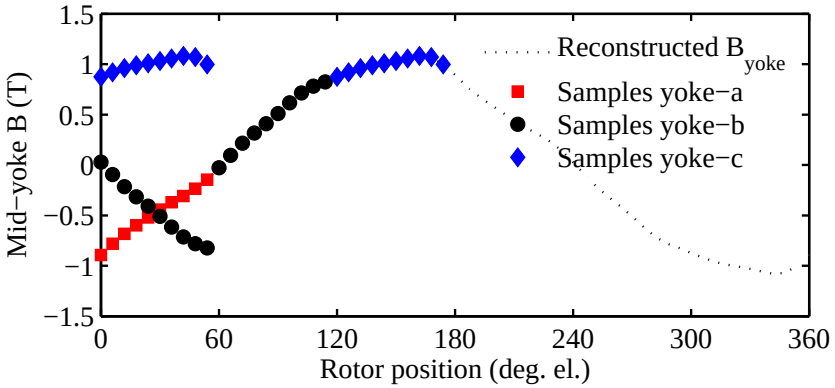

(a) 48-slot 8-pole configuration

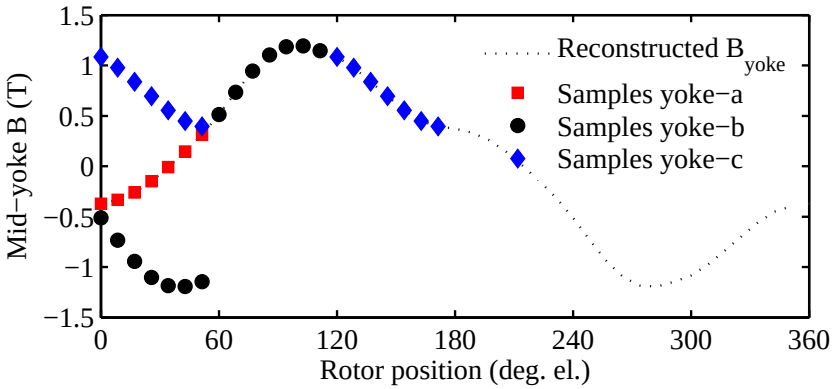

(b) 12-slot 10-pole configuration

Figure 2.4: Reconstruction of mid-yoke flux densities using the CE-FEA method.

between typical sister elements such as e_1 , e_1', and e_1'' or e_2 , e_2', and e_2''. It should be pointed out that the relative location of the sister elements is independent of the rotor PM layout as long as the number of the poles is fixed.

The aforementioned existing symmetry in the stator structure of sinusoidally excited PMSMs is fully utilized in the CE-FEA method to reconstruct the entire field waveforms through multiple snapshots of magnetostatic FE solutions over a time span corresponding to 60 electrical degrees.

In Fig. 2.3, the reconstruction of the mid-tooth flux densities using CE-FEA

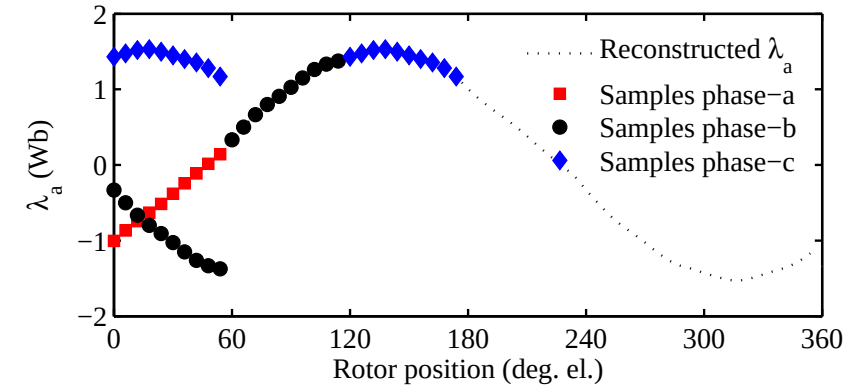

(a) 48-slot 8-pole configuration

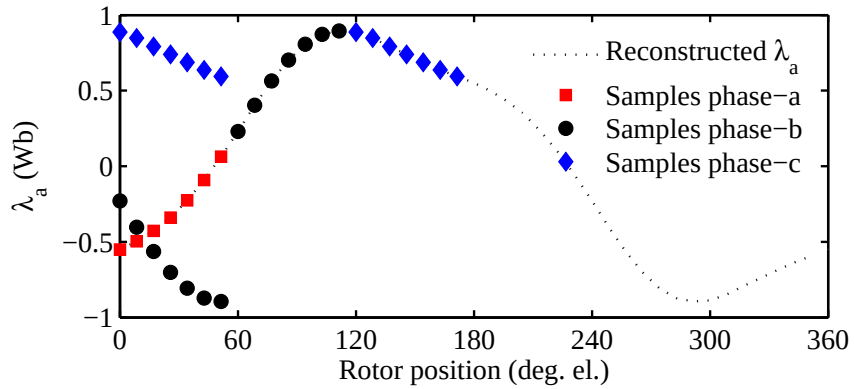

(b) 12-slot 10-pole configuration

Figure 2.5: Reconstruction of stator winding flux linkages using the CE-FEA method.

approach are illustrated for the two example machines previously shown in Fig. 2.2, respectively using 10 and 7 static solutions for the 48-slot 8-pole, and 12-slot 10-pole machine configurations.

As shown in Fig. 2.4 for the same machine configurations, a similar procedure can be employed for reconstruction of the mid-yoke flux density waveforms. It should be pointed out that for illustration purposes in Figs. 2.3 and 2.4, the "virtual search coils" [118] for collecting the flux density values are located perpendicular to the main flux path. Otherwise, the tangential and radial components of elemental flux densities

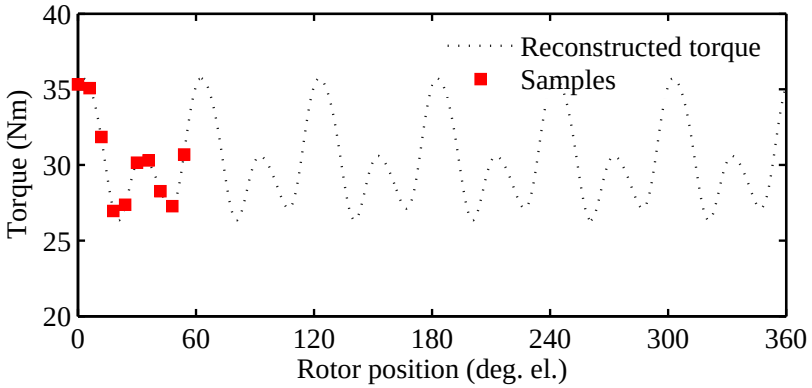

(a) 48-slot 8-pole configuration

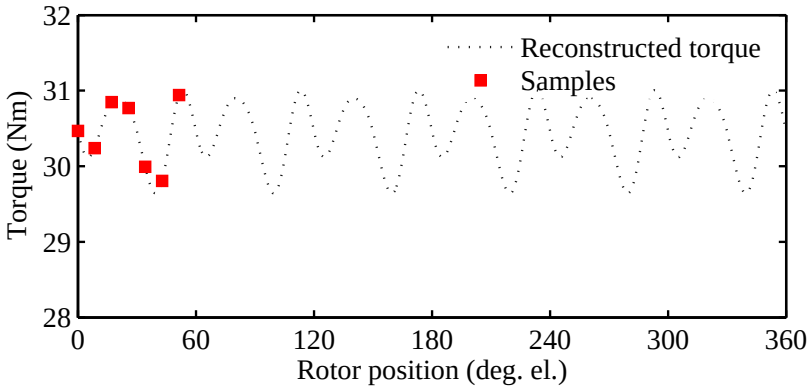

(b) 12-slot 10-pole configuration

Figure 2.6: Reconstruction of the torque profile using the CE-FEA method.

should be treated separately.

In addition to the elemental flux density values in the stator core, the same symmetry rules can be found in the waveforms of the stator winding flux linkages. This is illustrated in Fig. 2.5(a) and (b) for the two previously discussed example machines. The waveforms of the induced voltages can be subsequently obtained from the differentiation of the flux linkage waveforms.

2.1.1.2 Reconstruction of Torque

In the CE-FEA method, the torque values, which can be calculated using the virtual work method [121] or the Maxwell stress tensor, are obtained at the sample points within the first 60 electrical degrees of the fundamental cycle. Subsequently, these sample points are replicated over the entire cycle to reconstruct the torque profile. A Fourier analysis on the resultant torque profile is then conducted to extract the average torque in Eq. (2.1.3) and the torque ripple in Eq. (2.1.4) [118]:

$$T_{em} = T_{avg} + \sum_{n=6,12} T_n \cos\left(n\omega t + \phi_n\right) \tag{2.1.3}$$

$$T_r = (T_{max} - T_{min})/T_{ave} \times 100 \tag{2.1.4}$$

The process of reconstruction of the torque profile in the CE-FEA method is illustrated in Fig. 2.6 for the two previously discussed 48-slot 8-pole, and 12-slot 10-pole machines.

2.1.1.3 Estimation of Core Losses

Upon deriving the waveform profiles of the field quantities, a subsequent Fourier analysis should be performed according to Eq. 2.1.5 to determine their harmonics expressions:

$$f(\theta) = \sum_{n=1}^{n_{max}} F_n \cos(n\theta + \phi_n) \tag{2.1.5}$$

where F_n and ϕ_n are the magnitude and the phase angle of the n^{th} harmonic, respectively.

The Fourier series of the stator core flux densities is of special interest for calculation of the hysteresis losses, P_h, and eddy-current losses, P_e, which constitute

the total core losses, P_{Fe}, of the stator laminations. Throughout this work, the CAL2 loss model introduced by Ionel et al. in [122], which features accurate estimation of core loss components at individual frequencies, is used:

$$P_{Fe} = k_h(B,\omega)\omega B^2 + k_e(B,\omega)(\omega B)^2 \tag{2.1.6}$$

According to the loss model in Eq. (2.1.6), the hysteresis, k_h, and eddy-current, k_e, core loss coefficients, are expressed as functions of the peak flux density, B, and angular frequency, ω, i.e. $k_h(B,\omega)$, and $k_e(B,\omega)$. It has been previously demonstrated [123–125] that the frequency dependency in these functions can be considered at multiple non-overlapping frequency ranges, thus simplifying the expressions for core loss coefficients, as given in Eq. (2.1.7).

$$\begin{cases} k_h(B) = k_{h3}B^3 + k_{h2}B^2 + k_{h1}B + k_{h0} \\ k_e(B) = k_{e3}B^3 + k_{e2}B^2 + k_{e1}B + k_{e0} \end{cases} \tag{2.1.7}$$

Accordingly, the hysteresis and eddy current loss components can be separately expressed based on Fourier series derivations of the stator core flux densities using the CE-FEA method:

$$P_h = \sum_{n=1}^{n_{max}} k_h(B_n)(n\frac{\omega}{2\pi})B_n^2, (W/kg) \tag{2.1.8}$$

$$P_e = \sum_{n=1}^{n_{max}} k_c(B_n)(n\frac{\omega}{2\pi})^2 B_n^2, (W/kg) \tag{2.1.9}$$

The CE-FEA method does not provide an indication of the rotor losses, i.e. core and magnet losses. Nonetheless, these losses are expected to be smaller, as opposed to the stator core losses, due to the non-varying (non-pulsating) fundamental field in the rotor laminations. Whenever high frequency fluctuations (pulsations) of the rotor

field are significant, which is more likely to occur in PM machines with fractional slot concentrated winding configurations [126], the rotor losses can be taken into account by using alternative surrogate methods such as response surface methodology [80, 119].

2.1.1.4 Estimation of Ohmic Losses

The dc copper losses, P_{dc}, are obtained by Eq. (2.1.10) provided below:

$$P_{dc} = v_{Cu}\rho \cdot J^2, (W) \tag{2.1.10}$$

where v_{Cu} is the volume of the copper including the end-turns, J is the excitation current density, and ρ is the copper resistivity which is calculated for a given temperature, $Temp$, by using a reference temperature of $20°C$ in Eq. (2.1.11).

$$\rho = 1.724 \times 10^{(-8)}[1 + 0.00393(Temp - 20)], (\Omega \cdot m) \tag{2.1.11}$$

2.1.2 Overview of Differential Evolution

Finding the globally optimal design solutions requires incorporation of a search algorithm, aka optimizer. The optimizer utilized in the design synthesis package developed by the team at Marquette University is the differential evolution (DE) algorithm [120].

Similar to other evolutionary algorithms, the DE algorithm is a stochastic optimizer. That is, there is a degree of uncertainty involved in the evolution model of the "non-dominated" designs. Yet, the DE algorithm is characterized by its unique method for the generation of trial design members, $\vec{u}$, which are the designs

that compete with the parent population members, $\vec{x}_g$, to determine the offspring population, $\vec{x}_{g+1}$. The DE algorithm with adaptations for electric machinery design optimization problems is explained in the following discussion.

2.1.2.1 Initialization

In a typical 2-D design problem, the cross section of the given machine configuration can be parametrized by defining a certain number, p, of design parameters establishing the strongest correlations with the machine performance metrics. Accordingly, each design member, $\vec{x}$, is a vector consisting of p design parameters, $\vec{x} = [x_1, x_2, ..., x_p]$. Each generation of the DE optimization algorithm is composed of N_p distinct designs which constitute the current population, $\vec{P}_g = [\vec{x}_{g,1}, \vec{x}_{g,2}, ..., \vec{x}_{g,N_p}]$. The first generation of the design members is randomly generated by considering the predefined upper, $x_{i,\max}$, and lower, $x_{i,\min}$, bounds of the design parameters as given below:

$$x_i = x_{i,\min} + rand(0,1)(x_{i,\max} - x_{i,\min}) \tag{2.1.12}$$

The number of the design parameters p is determined by the machine model, whereas the population size, N_p, is determined heuristically to yield the fastest rate of convergence to the globally optimum solution. The population size, N_p, is recommended to be at least 5-10 times greater than p for optimization of PM machines using the classical DE approach [117, 118].

2.1.2.2 Generation of Trial Designs

Upon identification of the design members of the parent population, and calculation of their performance metrics, the offspring population needs to be determined by

comparing the performance of the design members in the parent population with that of a corresponding trial design. Each parameter of the trial design, $\vec{u}_k$, is created in reference to a corresponding design member, $\vec{x}_k$, in addition to three randomly selected design members from the current population, $\vec{x}_{r0}$, $\vec{x}_{r1}$, and $\vec{x}_{r2}$, through the mutation and crossover operations expressed below:

$$u_i = \begin{cases} x_{r0} + F(x_{r1} - x_{r2}) \text{ if } rand(0,1) \leq C_r, \\ x_i \text{ otherwise} \end{cases} \tag{2.1.13}$$

where F is a positive scale factor, $F > 0$, and C_r is the crossover probability, $C_r \in [0, 1]$, i.e. $0 \leq C_r \leq 1.0$. Although similar to N_p, the specific values of F and C_r are not known, it is recommended that $F < 1$ for better reliability and convergence rate [120]. Furthermore, a lower limit of $F_{\min}$ for enhanced diversity of the population is suggested in [120] as given in Eq. 2.1.14 below:

$$F_{\min} = \sqrt{\frac{(1 - C_r/2)}{N_p}} \tag{2.1.14}$$

If the lower or upper bounds of the design parameters are violated in the trial member, either Eq. (2.1.12) or the "bounce-back" method in Eq. (2.1.15) given below can be used to recreate the trial member.

$$u_i = \begin{cases} x_i + rand(0,1)(x_{i,\min} - x_i) \text{ if } u_i < x_{i,\min} \\ x_i + rand(0,1)(x_{i,\max} - x_i) \text{ if } u_i > x_{i,\max} \end{cases} \tag{2.1.15}$$

2.1.2.3 Selection

After the performance metrics of the trial designs are identified, in this case through utilization of CE-FEA, a competition takes place between corresponding pairs of members to determine the winning offspring design. This competition is based on

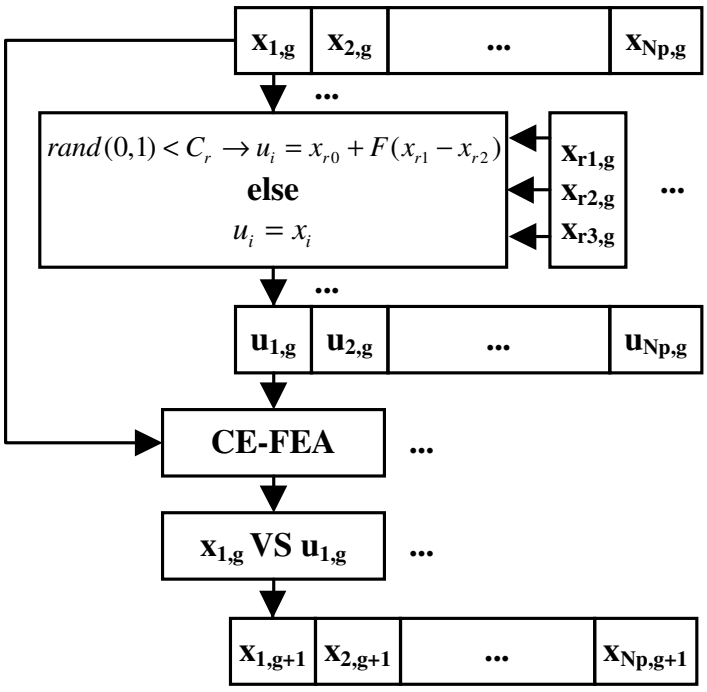

Figure 2.7: Evolution model of DE from one generation to another. Multiple members of the current population can be processed simultaneously to decrease the computation time.

minimizing/maximizing a set of objectives, and satisfying a set of equality/inequality constraints defined in the optimization fitness function. In a typical electric machinery design problem, the minimization of active material cost and power losses are common objectives, subject to performance constraints on maximum torque ripple or maximum degree of PM demagnetization.

According to the Lampinen method of constraint handling which is specifically recommended for DE algorithms [120], the trial vector $\vec{u}$ wins the competition if:

- it has better or equal objectives and satisfies all the constraints, or
- it does not violate the constraints whereas the current design does, or
- its constraint violation is less severe than the current member.

In the case of a multiobjective design optimization, the Pareto optimality can be used to determine the non-dominated design members. According to the Pareto criterion, in a minimization problem, a design is non-dominated if none of its objectives are higher and at least one of its objectives is lower compared to the other design members.

The evolution model of DE coupled to CE-FEA for two consecutive generations is illustrated in Fig. 2.7.

2.1.2.4 Termination

Although there is not a specific rule for termination of the optimization iterations, a few possible stop criteria for the DE algorithm are discussed in [77, 127, 128]. The general idea is that the optimization needs to be carried out until the changes in the value of the objective functions between two consecutive generations are small. From this point on, the optimization can be continued to add to the density or diversity of the optimal designs in the optimal solution region, which is in the form of a Pareto front in case the number of objectives is greater than one.

2.2 Case Study Design Optimization of Toyota Prius Gen 2 Motor at Its Nominal Operating Point

In this section, the 48-slot 8-pole IPM machine topology shown in Fig. 2.8 which was used in the Toyota Prius Gen 2 Hybrid Synergy Drive (HSD), is optimized at

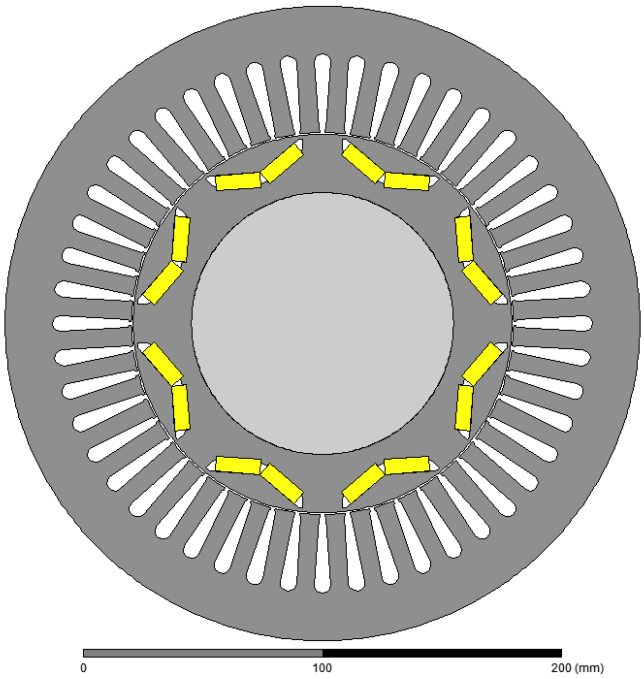

Figure 2.8: Cross-section of the Toyota Prius Gen 2 IPM motor.

the nominal operating point using the design optimization package described in the previous section. The purpose of this case study design is twofold: (a) to examine the steps involved in a sample case study using CE-FEA and DE, and (b) to illustrate the shortcomings of the existing approach in performance improvement for the entire range of operation.

2.2.1 Parametric CE-FEA Model

The details concerning the general nature of a finite element non-linear magnetic field computation, such as setting up the geometries, winding parameters, material types, operating conditions, meshing, boundary conditions, etc., are available in the literature [21–31] and, therefore, will not be discussed here. In addition to the fundamental procedures involved in solving a magnetostatic solution, which in

this case is carried out in Ansys Maxwell, another important step in an automated design optimization package is creating a well-defined parametric model which can be implemented to reliably explore the entire design space.

In this case study design optimization, based on the overall shapes of the stator and rotor structures, they can be parametrized as follows:

2.2.1.1 Parametrized Stator Structure

The stator geometry of the Prius propulsion motor is composed of common parallel tooth and rounded slot bottom structures, which can be parametrized using the geometric variables shown in Fig. 2.9.

Assuming the center of the machine axis to be the origin of the coordinate system, the equations governing the principal nodes in this stator structure are expressed as follows, see Fig. 2.9 for description of the parameters:

$$
\begin{cases} x_{p1} = \sqrt{r_{si}^2 - (w_{so}/2)^2} \\ y_{p1} = w_{so}/2 \end{cases}
$$

$$
\begin{cases} x_{p2} = x_{p1} + d_{t2} \\ y_{p2} = y_{p1} \end{cases}
$$

$$
\begin{cases} x_{p3} = x_{p2} + d_{t3} \\ y_{p3} = y_{p2} + d_{t3}/\tan(\beta) \end{cases}
$$

$$
\begin{cases} x_{p4} = r_{si} + d_s - r_{sb} \\ y_{p4} = r_{sb}, \text{ where, } r_{sb} = \dfrac{(r_{si}+d_s)\tan\left(\frac{\alpha_s}{2}\right) - \frac{w_t}{2\cos\left(\frac{\alpha_s}{2}\right)}}{1+\tan\left(\frac{\alpha_s}{2}\right)} \end{cases}
$$

$$
\begin{cases} x_{p5} = r_{si} + d_s \\ y_{p5} = 0 \end{cases}
$$

(2.2.1)

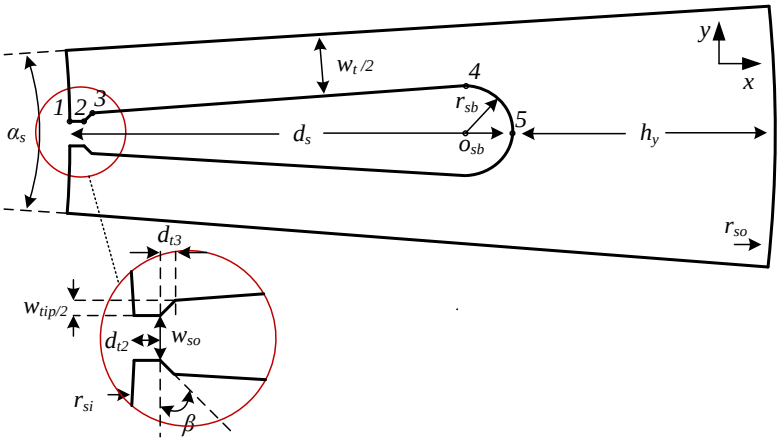

Figure 2.9: Parametrized stator slot of the Prius motor.

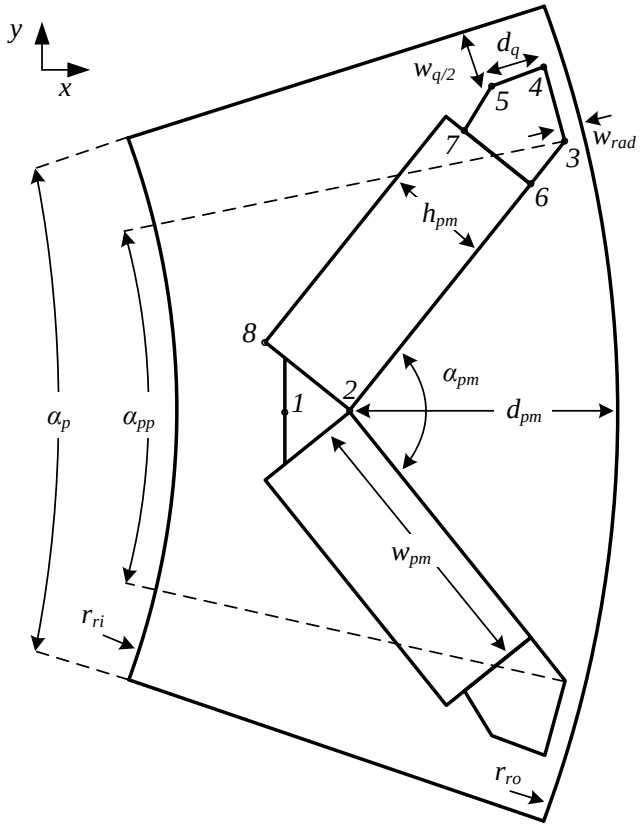

Figure 2.10: Parametrized rotor layout of the Prius motor.

2.2.1.2 Parametrized Rotor Structure

The rotor structure of the Prius Gen 2 propulsion motor is also a common configuration with single-layer V-type PM layouts. Assuming the center of the machine axis as the origin of the coordinate system, the parametrized structure shown in Fig. 2.10 can be defined by following nodes:

$$
\begin{cases} x_{q1} = x_{q2} - 0.75 h_{pm} \sin\left(\alpha_{pm}/2\right) \\ y_{q1} = 0 \end{cases}
$$

$$
\begin{cases} x_{q2} = r_{ro} - d_{pm} \\ y_{q2} = 0 \end{cases}
$$

$$
\begin{cases} x_{q3} = (r_{ro} - w_{rad}) \cos(\alpha_{pp}/2) \\ y_{q3} = (r_{ro} - w_{rad}) \sin(\alpha_{pp}/2) \end{cases}
$$

$$
\begin{cases} x_{q4} = (r_{ro} - w_{rad}) \cos\left(\alpha_p/2 - \arcsin\left(\frac{w_q}{2(r_{ro} - w_{rad})}\right)\right) \\ y_{q4} = (r_{ro} - w_{rad}) \sin\left(\alpha_p/2 - \arcsin\left(\frac{w_q}{2(r_{ro} - w_{rad})}\right)\right) \end{cases}
$$

$$
\begin{cases} x_{q5} = x_{q4} - d_q \cos(\alpha_p/2) \\ y_{q5} = y_{q4} - d_q \sin(\alpha_p/2) \end{cases}
$$

$$
\begin{cases} x_{q6} = x_{q2} + 2 w_{pm} \cos(\alpha_{pm}/2) \\ y_{q6} = y_{q2} + 2 w_{pm} \sin(\alpha_{pm}/2) \end{cases}
$$

$$
\begin{cases} x_{q7} = x_{q6} - h_{pm} \sin(\alpha_{pm}/2) \\ y_{q7} = y_{q6} + h_{pm} \cos(\alpha_{pm}/2) \end{cases}
$$

$$
\begin{cases} x_{q8} = x_{q2} - h_{pm} \sin(\alpha_{pm}/2) \\ y_{q8} = y_{q2} + h_{pm} \cos(\alpha_{pm}/2) \end{cases}
$$

(2.2.2)

Table 2.1: Boundaries of the design variables defined over the parameterized cross-section of the Prius motor.

Parameter(x_i)	Description	$x_{i,min}$	$x_{i,max}$
k_{si}	r_{si}/r_{so}	0.6	0.7
h_g	Fig. 2.11	0.7 mm	2.5 mm
k_{w_t}	w_t/α_s	0.35	0.75
$k_{w_{tt}}$	$w_{tip}/(w_{so}+w_{tip})$	0.3	0.8
$k_{d_{pm}}$	$d_{pm}/d_{pm,max}$	0.25	0.50
$k_{w_{pm}}$	$w_{pm}/w_{pm,max}$	0.80	0.93
k_{w_q}	$w_q/w_{q,max}$	0.5	0.9
h_{pm}	Fig. 2.11	3.8 mm	9.0 mm
α_{pm}	Fig. 2.11	20 deg.	32 deg.
h_y	Fig. 2.11	13 mm	25 mm

2.2.1.3 Final Parametrized Model

The final parameterized cross-section of the Toyota Prius 48-slot 8-pole IPM motor is constructed based on the parameterized stator and rotor cross-sections, see Fig. 2.11. Ten independent design variables are defined in its structure, 4 pertaining to the stator geometry, 5 pertaining to the rotor geometry, in addition to the airgap height. The geometric parameters are rationalized and confined according to Table 2.1 so as to avoid surface interference between the structures of various components of the motor. As depicted in Fig. 2.12, the wide variations of the geometric design parameters, from the lower to upper bounds is crucial for full exploration of the design space.

With reference to the original design, the stator outer and the rotor inner diameters are fixed to 260mm and 111mm, respectively. The active stack length of the laminations and rotor PMs of each design candidate are scaled to produce the nominal torque at the rated stator winding current density.

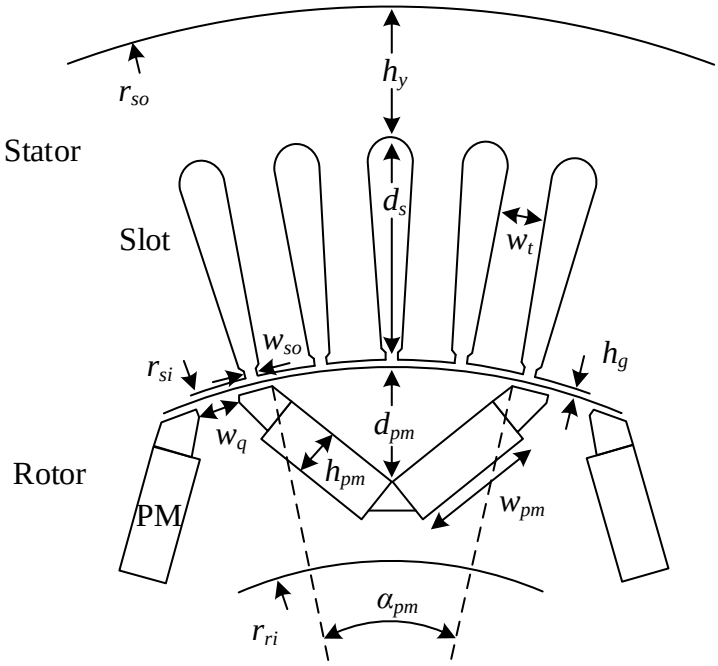

Figure 2.11: The parameterized cross-section of the Prius motor comprising 10 independent design variables, see Table 2.1.

The calculation of the nominal torque is performed under maximum torque per ampere (MTPA) operation for the given rated current density. The angle of the current phasor for MTPA operation is determined by sampling the average torque using a reduced number of static solutions, followed by interpolation of the average torque profile versus the advance angle [129] of the current phasor as shown in Fig. 2.13. The MTPA operation is achieved at the angle where the torque reaches its peak.

2.2.2 Optimization Procedure and Results

The optimization was carried out over 60 generations each consisting of 80 members. Two objectives were defined:

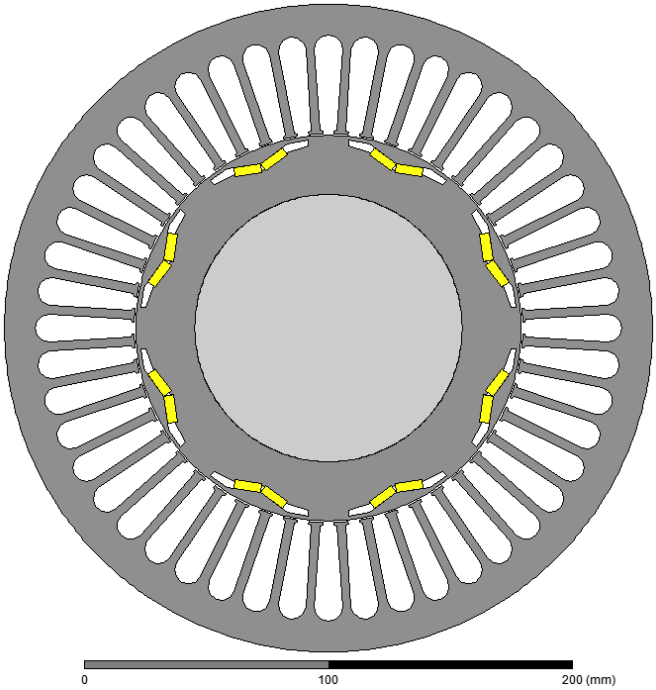

(a) Lower bounds of the design variables

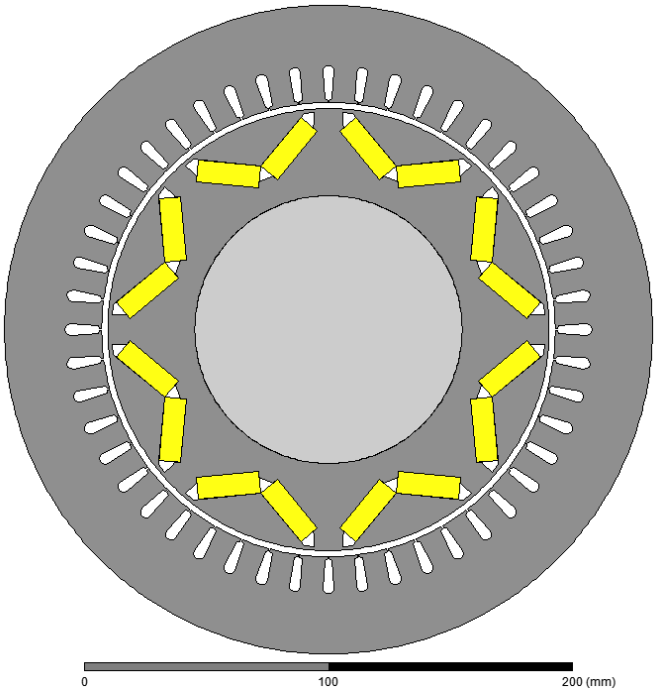

(b) Upper bounds of the design variables

Figure 2.12: Range of variation of the design parameters defined over the Prius motor topology.

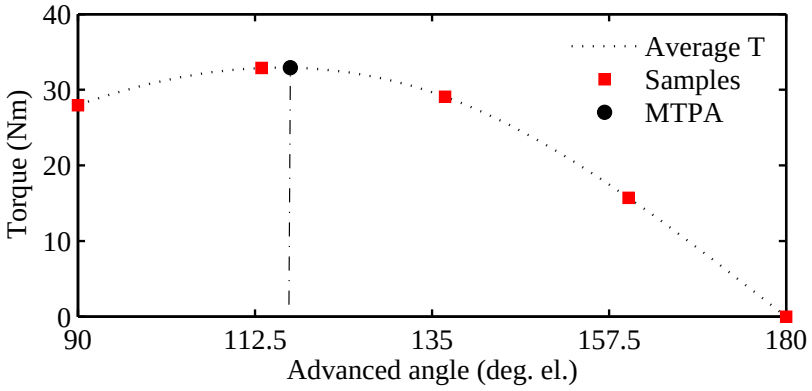

Figure 2.13: Determination of current advanced angle for MTPA operation.

- Minimize the active material cost, AMC, as formulated in Eq. (2.2.3).

$$AMC = 24 \cdot m_{pm} + 3 \cdot m_{copper} + m_{steel} \tag{2.2.3}$$

  where the mass, m, is in kg and the steel cost is considered as the one-unit reference in this normalized/per-unit formulation. It can be assumed that the AMC is an approximate indication of the total cost of each motor configuration, given that the manufacturing expenses of the same motor topology with identical winding configuration is usually comparable for different design solutions.

- Minimize the power losses consisting of the stator core and copper losses.

Furthermore, the two following constraints were considered for this optimization case study to:

- Limit the torque ripple to less than 15%.

- Limit the degree of PM demagnetization to less than 70% of the retentivity/remnant B_r.

Table 2.2: Geometric design parameters of the counterpart optimal designs obtained from the Prius motor design optimization at nominal load point.

Parameter	G59M12	G20M62	Prius
k_{si}	0.66	0.64	0.60
h_g (mm)	0.71	0.71	0.73
k_{w_t}	0.72	0.69	0.72
$k_{w_{tt}}$	0.34	0.47	0.36
$k_{d_{pm}}$	0.43	0.25	0.44
$k_{w_{pm}}$	0.93	0.93	0.88
k_{w_q}	0.66	0.73	0.86
h_{pm} (mm)	4.22	5.55	6.50
α_{pm}	31.67	25.24	30.15
h_y (mm)	22.11	21.77	20.10
Stack length	106	95	84

The machine performance was optimized at a load point corresponding to a torque of $400Nm$ and a rotational speed of $1\,500r/min$. A current density of $23A/mm^2$ and a slot fill factor of 0.47 has been reported for the original Prius design at this load point [130, 131], which were maintained the same for all the design candidates throughout this optimization process.

The optimization results are plotted in terms of objectives, and are color-coded with respect to three performance metrics, namely torque ripple, minimum flux density of the PMs, and power factor in Fig. 2.14(a) through (c), respectively. Some observations could be made regarding the existing trade-offs between the objectives and constraints in this specific case study. Aside from the conflicting relationship between the active material cost and power losses, it can be seen that the machines with higher costs tend to have a lesser PM demagnetization, and higher power factor. This can be attributed to the larger amount of expensive magnet material used in their constructions.

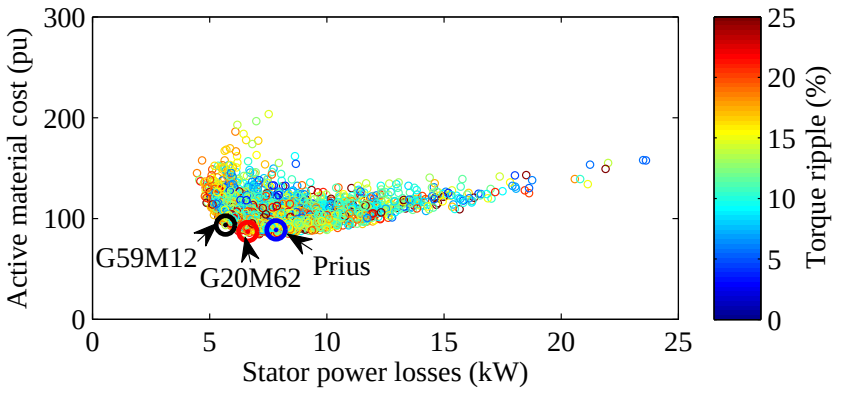

(a) Color-coded for torque ripple

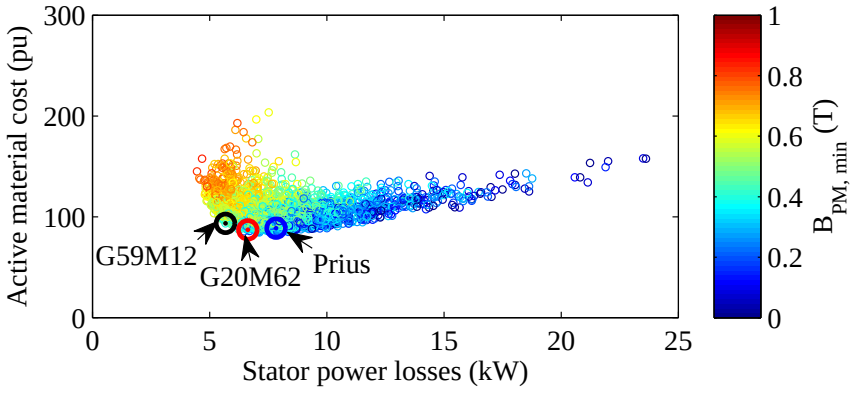

(b) Color-coded for PM minimum flux density

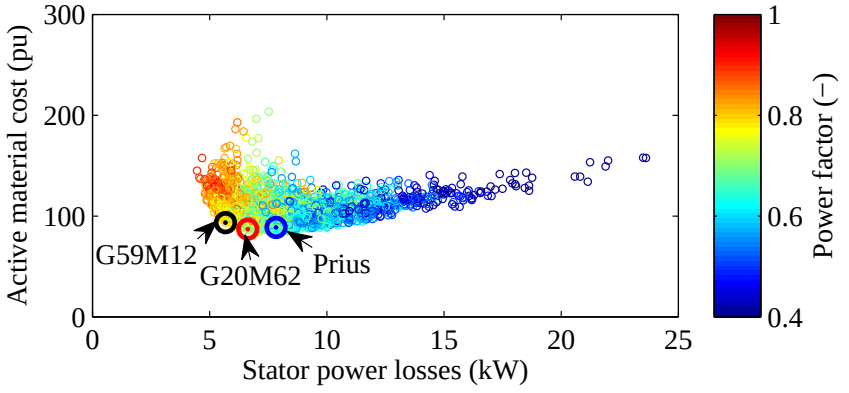

(c) Color-coded for power factor

Figure 2.14: Results of the optimization of the Prius motor at the nominal load point expressed in terms of the designated objectives.

Table 2.3: Comparison of nominal performance between counterpart designs obtained from the Prius motor design optimization at nominal load point.

Index	G59M12	G20M62	Prius
Harmonic Distortion Line-Line Terminal Voltage (%)	5.5	7.6	12.8
Harmonic Distortion Phase Terminal Voltage (%)	16.2	14.6	20.0
Torque Ripple (%)	10	13	18
Total Losses (W)	5763	6857	8148
Efficiency (%)	90.84	89.58	87.81
Power Factor (-)	0.82	0.76	0.69
Torque Per Rotor Volume (kNm/m^3)	142.1	174.5	223.72
Rotor Peripheral Velocity (m/s)	13.85	13.41	12.60
Peak Airgap Flux Density (T)	1.95	1.91	1.96
Peak Stator Tooth Flux Density (T)	1.84	2.00	1.97
Peak Stator Yoke Flux Density (T)	1.55	1.61	1.68
Peak Rotor Yoke Flux Density (T)	1.00	1.08	1.78
Minimum PM Flux Density (T)	0.4	0.38	0.41

In Fig. 2.14, two optimized designs, "G59M12" and "G20M62" are marked, the number after G indicates the generation and the number after M indicates the member candidate design. Using the same simulation tools, the performance of the Prius motor is also computed at this load operating point, and is compared with respect to the design space in Fig. 2.14.

Accordingly, the Prius design can be recognized as an optimal design in terms of active material cost. However, the efficiency is further improved in the other two selected design candidates. In fact, design G20M62 exhibits both lower losses and lower costs compared to the Prius design.

The three counterpart designs and their performance metrics are thoroughly compared in Tables 2.2 through 2.5 , and Figs. 2.15 through 2.18. These metrics are obtained using full-fledge time-stepping 2-D FEA in Motor-CAD for the same operating point and at a temperature of $100°C$ for all components as was the case

Table 2.4: Distribution of power losses in the counterpart designs obtained from the Prius motor design optimization at nominal load point.

Index	G59M12	G20M62	Prius
Copper Loss (W)	5126	6204	7477
Magnet Loss (W)	5	6	6
Stator Back Iron Hysteresis Loss (W)	268	255	249
Stator Back Iron Eddy Loss (W)	24	22	22
Stator Tooth Hysteresis Loss (W)	196	231	252
Stator Tooth Eddy Loss (W)	38	39	42
Rotor Back Iron Hysteresis Loss (W)	18	29	26
Rotor Back Iron Eddy Loss (W)	0	0	0
Rotor Magnet Pole Hysteresis Loss (W)	85	66	70
Rotor Magnet Pole Eddy Loss (W)	5	4	3

Table 2.5: Mass of active components in the counterpart designs obtained from the Prius motor design optimization at nominal load point.

Index	G59M12	G20M62	Prius
Stator Lamination (kg)	21.2	19.3	17.6
Winding (kg)	4.1	5.0	6.0
Rotor Lamination (kg)	10.1	7.8	4.7
Magnet (kg)	1.28	1.13	1.25

throughout the optimization process.

According to Table 2.2, the split ratios, i.e. the ratio of stator inner to outer diameter, of the optimized designs are higher than the original design, which, in addition to the longer stack lengths of the optimized designs, has resulted in a lower torque per rotor volume in the optimized designs, as listed in Table 2.3.

If the machine length has to be confined within a predefined value, the maximum stack length can be introduced as an additional constraint in the optimization fitness function. Yet, since the volume of the machine is oftentimes directly related to the efficiency, the conflicting relationship between limitation of stack-length and minimization of power losses will further narrow down the feasible design space.

The higher rotor peripheral velocity of the optimized designs in Table 2.3, necessitates structural analysis of the rotor body to ensure that the bridges can withstand the centrifugal stresses at the maximum operating speed. This mechanical aspect of the design will be addressed in the last Chapter of this dissertation where an analytical procedure is presented for calculation of these centrifugal stresses and subsequent adjustment of the rotor bridges.

From Table 2.4 whereby the distributions of the losses are indicated for the counterpart designs, it can be seen that the contribution of the rotor core losses and PM losses to the overall core losses is marginal compared to that of the stator core losses.

The masses of the main active components in the counterpart designs are listed and compared in Table 2.5. It is interesting to note that the proportion of the mass of the lamination steel to the masses of copper and PM is higher in the optimized designs, whereas the copper masses and the PM masses are comparable to those obtained for Prius.

The cross-sections of the three counterpart designs as well as the field plots under the rated operating conditions are provided in Fig. 2.15, according to which a higher degree of saturation is evident throughout the cross-section of the Prius design.

The waveforms of the line to line back EMF of the three counterpart designs are shown in Fig. 2.16. Also the harmonic distribution of the back EMF waveforms and the induced voltages are provided in Fig. 2.17(a) and (b), respectively. It is interesting to note that the three designs have comparable distortions in their no-load back EMF waveforms. However, the high order harmonics, namely 7^{th}, 11^{th},

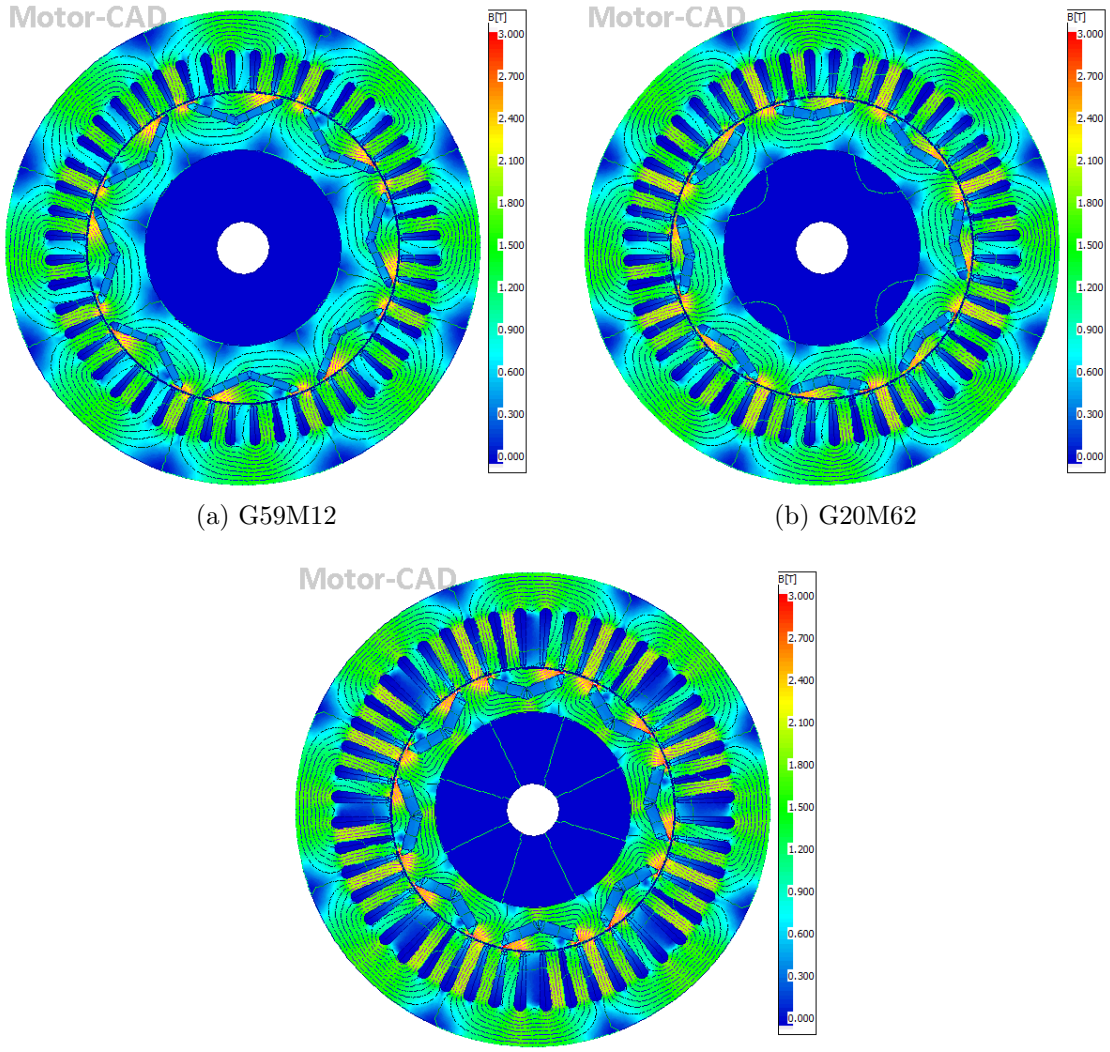

(a) G59M12

(b) G20M62

(c) Prius

Figure 2.15: Cross-sections and rated field plots of the three counterpart designs obtained from the Prius motor design optimization at nominal load point.

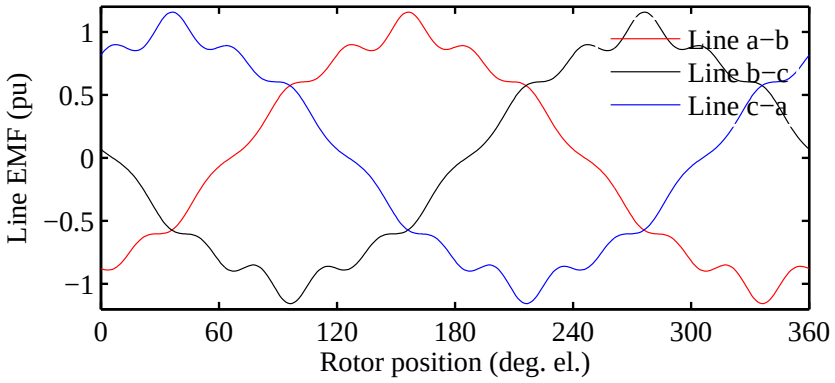

(a)

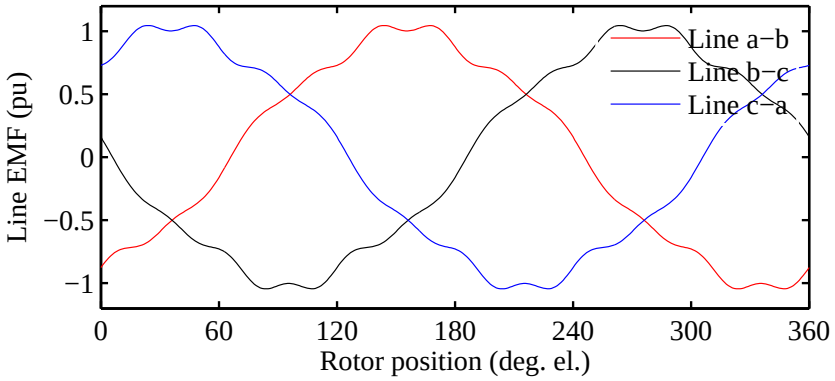

(b)

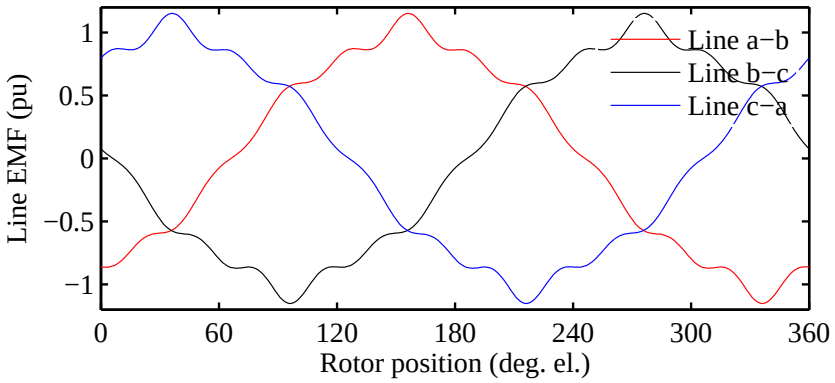

(c)

Figure 2.16: Line to line back EMF of the counterpart designs obtained from the Prius motor design optimization at nominal load point (a) G59M12, (b) G20M62, and (c) Prius.

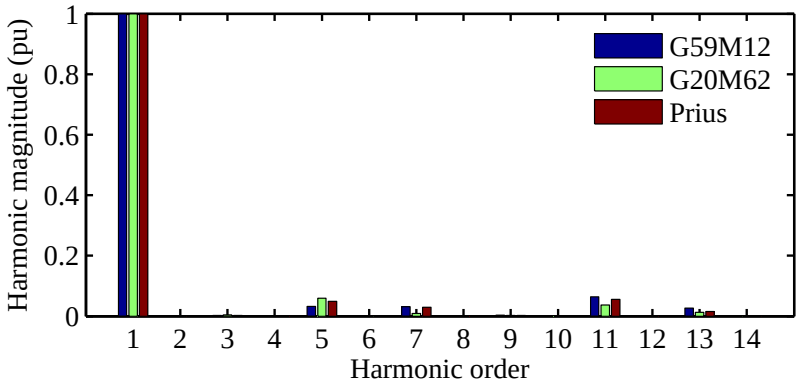

(a) No-load (back EMF)

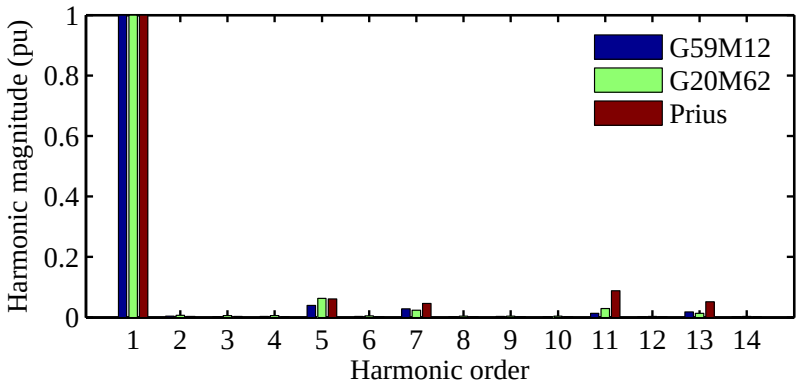

(b) Full load

Figure 2.17: Harmonic content of the line to line terminal voltage of the counterpart designs obtained from the Prius motor design optimization at nominal load point.

and 13^{th}, are introduced to the induced voltage waveform of the Prius design to a larger extent.

Similar to the back EMF waveforms, according to Fig. 2.18(a) the cogging torque profiles of the two optimized designs are inferior to that of the Prius design. However, as can be seen in Fig. 2.18(b), the optimized designs demonstrate a lower value of peak torque ripple under rated operating conditions when compared to Prius design.

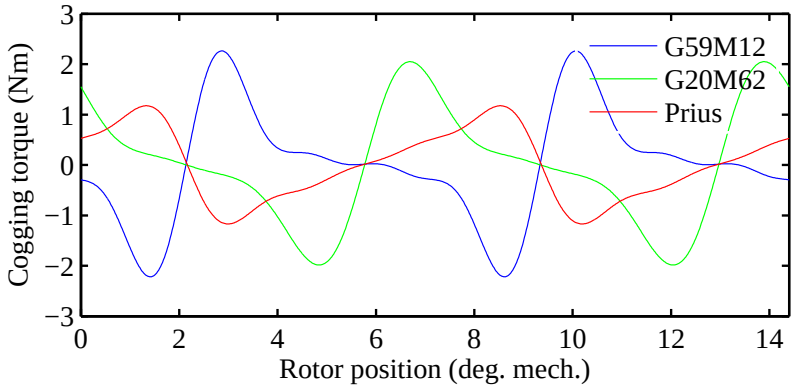

(a) Cogging

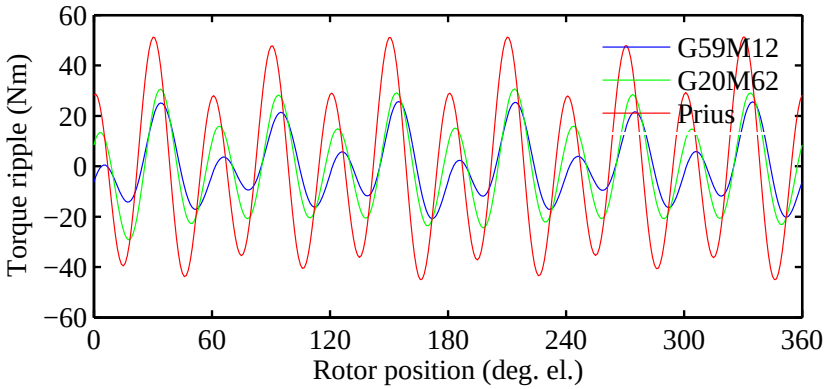

(b) Full load

Figure 2.18: Torque ripple of the counterpart designs obtained from the Prius motor design optimization at nominal load point.

As can be seen in the metrics shown in Tables 2.2 through 2.5 , and Figs. 2.15 through 2.18, the selected optimized designs outperform the original Prius design at the nominal load point. However, when the power losses throughout the entire range of operation are considered, as shown in Fig. 2.19, the Prius design features higher efficiency in the extended speed region.

The procedure for calculation of the efficiency maps provided in Fig. 2.19, which are obtained through 1 600 performance evaluations over sample load points

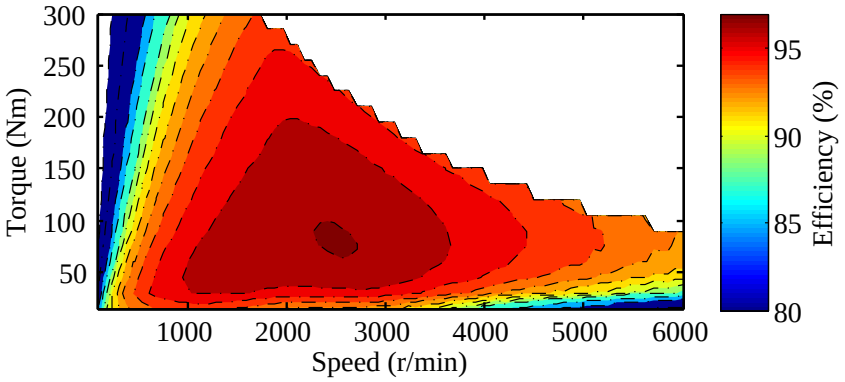

(a) G59M12

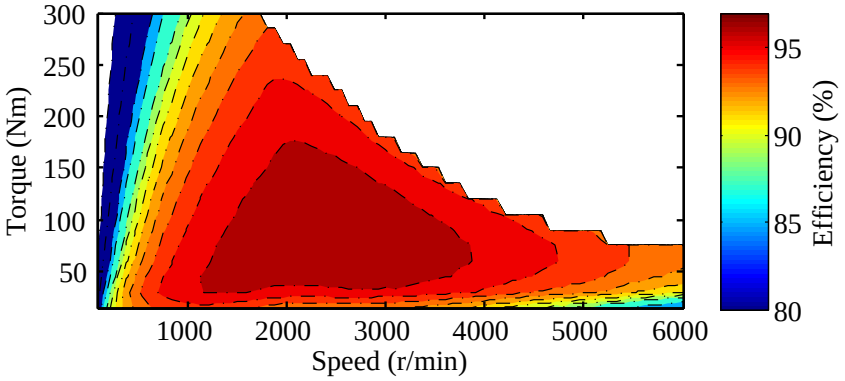

(b) G20M62

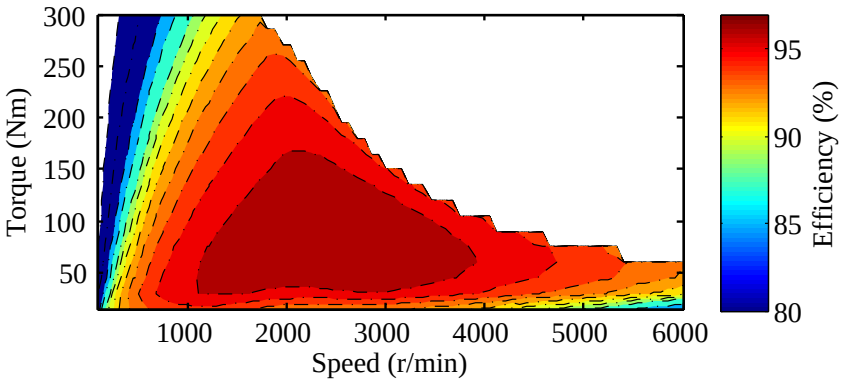

(c) Prius

Figure 2.19: Efficiency maps of the counterpart designs obtained from the Prius motor design optimization at nominal load point.

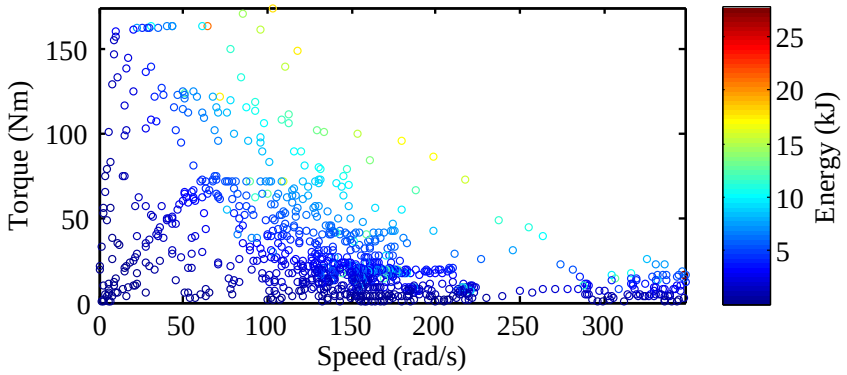

(a) UDDS

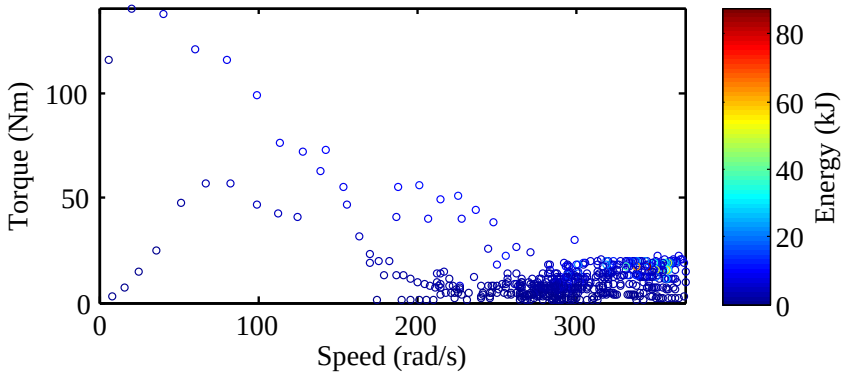

(b) HWFET

Figure 2.20: Load operating points of Toyota Prius propulsion PM motor obtained from ADVISOR.

equidistantly distributed in the torque speed plane, will be described in Chapter 5. Here, the purpose of this comparison is to recognize the fact that although the nominal efficiencies of the optimized designs are higher than that of the Prius design, the high efficiency contours of the optimized designs retract faster as the speed increases.

In many applications, including traction propulsion motors, maintaining high performance throughout the entire operating range is imperative. Specifically in the example case, the electric machine undergoes a wide range of speed and torque variations both in constant torque and constant speed regions.

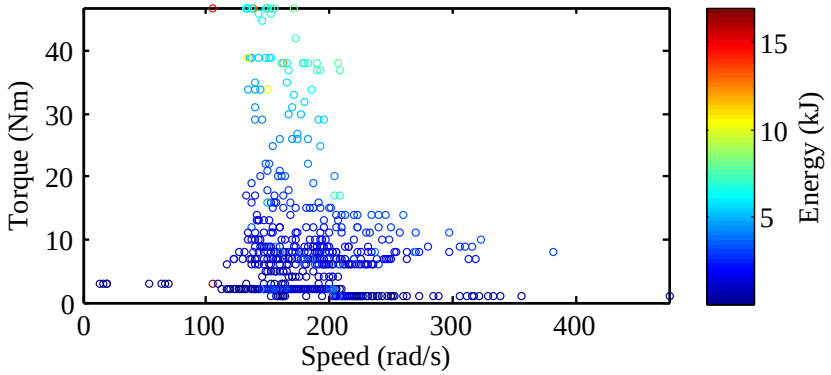

(a) UDDS

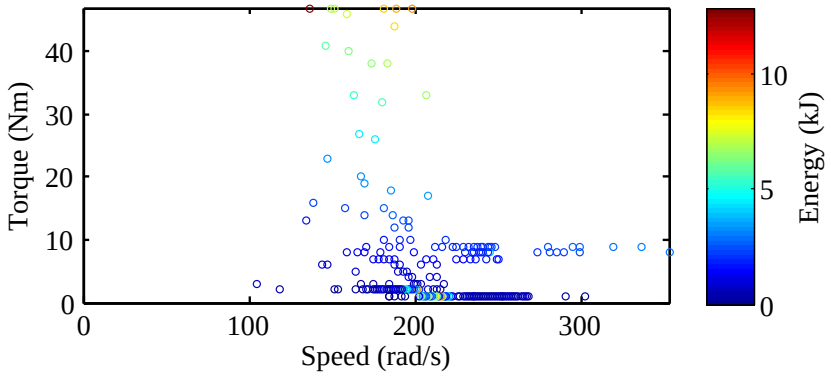

(b) HWFET

Figure 2.21: Load operating points of Honda Insight propulsion PM motor obtained from ADVISOR.

To further illustrate this argument, the operating points of two traction propulsion motors, Toyota Prius and Honda Insight are derived by modeling the two vehicles in Advanced Vehicle Simulator (ADVISOR). Two US driving cycles, urban dynamometer driving schedule (UDDS), and highway driving schedule (HWFET) are considered to also underscore the variations of the operation conditions in reference to the driving cycle.

It can be seen in Fig. 2.20 and Fig. 2.21 that not only do these motors operate at a multitude of load points, but depending on the driving cycle, these operating points

can be far away from the rated/nominal load point. Even including the efficiency improvement at the maximum torque of the corner speed in the fitness function, as reported by some investigators [100], cannot accommodate the swarm of the load operating points which can be located anywhere on the torque-speed plane.

In light of the above discussion, a high fidelity design optimization practice for motors with wide ranges of operation requires accounting for the performance over all load points. The realization of this goal is the main objective of the research presented in this dissertation.

2.3 Summary

In this chapter, the fast and high fidelity design synthesis methodology using CE-FEA and DE for large-scale design optimization of PM machines for rated operation was reviewed. The principles of CE-FEA and DE were discussed and were implemented in the design optimization of the Toyota Prius 2004 IPM motor. It was illustrated that the design optimization at rated operation does not guarantee optimal performance for the entire range of operation.

CHAPTER 3

EFFECTS OF AMPERE LOADING LEVEL ON OPTIMAL DESIGN OF IPM MOTORS

In the previous chapter, the Toyota Prius Gen 2 interior permanent magnet (IPM) motor was optimized for nominal (or peak) load point operation. It was shown that although the losses of the selected optimized designs were reduced for the targeted load point, the efficiency during the extended speed operation was degraded. The question still remains as to whether and how the optimal design rules vary for different loading conditions. Provided that the machine operating condition is characterized by the magnitudes and rate of change of flux and ampere loading in the core and in the windings, further clarifications concerning this matter can be made by investigating the optimal design rules at various ampere loading levels. Indeed, the design optimization of PM motors for a specific loading condition, which leads to derivation/interpretation of optimal scaling rules for that particular loading condition, has been widely investigated in the literature [87]. This chapter demonstrates how these derivations vary with respect to the machine ampere loading and ferrous core saturation level. For this purpose, a two-fold approach is adopted. First, a parallel sensitivity analysis is carried out on three machines with three levels of ampere loading. This is in order to gain an understanding as to how the correlation between the design parameters and performance metrics vary under different ampere loading conditions. Subsequently, a large-scale design optimization based on evolutionary

algorithms (EA), is pursued in order to identify how the optimal ranges of the design variables are influenced by the Ampere loading and magnetic core saturation levels. In this respect, ampere loading levels prevalent in three common cooling systems, that is naturally cooled (NC), fan-cooled (FC), and liquid-cooled (LC) machines are investigated. To fully account for the complex geometry, magnetic core nonlinearities, and stator and rotor losses, a full-fledge time-stepping finite element(FE)-based simulation platform is developed. Furthermore, to distinguish the intrinsic loss and ripple characteristics of distributed and fractional slot concentrated winding machines, in addition to the Toyota Prius 48-slot 8-pole configuration which was introduced in the previous chapter, a 12-slot 10-pole configuration is also analyzed in this chapter.

3.1 Introduction

The design and modeling of PM motors has consistently been a subject of special interest in the literature due to the distinctive features of such machines, including but not limited to high efficiency, and high power density, which makes them suitable for high performance applications [132, 133]. Recent design trends rely on large-scale design optimization techniques based on electromagnetic (EM) finite element (FE) analysis of design candidates for high fidelity calculation of their performance metrics/characteristics [77]. In some studies, coupled EM/thermal models have been utilized to accurately model the multi-physics nature of the design problem [89, 134–136]. In many others, a fixed current density corresponding to the machine's cooling system, and accordingly an educated engineering guess of the operating temperatures

of various components are assumed [70, 137–141]. Although the coupled EM/thermal models offer relatively reasonable predictions of temperature distributions inside such machines, which can be used either to update the material properties for a subsequent iteration of the EM FE analysis until a convergence is reached [89], or to determine the maximum current density limit based on the winding temperatures [134], the uncoupled approach is considerably faster. The uncoupled optimization approach can also be as effective, provided that the design problem is well-defined and that the thermal performances of the optimal designs are examined at the final stages of the design process. The post-design optimization thermal modeling [142] is usually done in order to identify the parameters of the cooling system such as the type of surfaces or the coolant flow rate [143]. Since more efficient designs are achieved through the design optimization, the cooling system is anticipated to remove lesser magnitudes of losses than those associated with motors constructed on the basis of traditional design methods which may yield suboptimal designs.

The design optimization practice is often accompanied by establishing the optimal scaling rules for achieving a particular improvement in the machine performance. Accordingly, design recommendations for mitigation of torque ripples, minimization of power losses, and reducing dependency on rare-earth PMs, have been often reported in the literature for naturally cooled machines [70, 85, 88, 138, 139]. Nevertheless, increasing the stator winding current density or the machine's ampere loading elevates the flux level, and hence the saturation level throughout the machine's magnetic circuit. This not only affects the machine performance, but also alters the correlation

between them and the geometric design parameters associated with the machine cross-section. In reference [144], the influence of ampere loading and magnetic saturation on the cogging torque, back-emf and torque ripple of PM machines was investigated. However, the impacts of the geometric design parameters on these performance metrics was not considered. In reference [87], nonlinear scaling rules for low power density brushless PM synchronous machines were developed without taking the effects of ampere loading and magnetic core saturation into account.

This chapter contains further contribution through a parallel investigation of the relations between the geometric design parameters and the performance metrics of IPM motors for a wide range of ampere-loading levels determined by the machine's cooling system. This is accomplished through a systematic sensitivity analysis and large scale design optimization. Accordingly, it will be demonstrated that one set of design rules, such as those derived in [87], cannot be generalized to all three classes of cooling systems.

In order to account for the distinctive performance characteristics of the integral and fractional winding IPM machines, two mainstream case-study industrial IPM machine configurations with distributed and fractional slot concentrated windings (FSCW) are considered. In essence, while FSCW machines offer reduced copper losses owing to shorter end windings [126, 145], they suffer from higher core losses as a result of the space harmonics introduced by the more "discrete" nature of the stator mmf waveform [146]. Furthermore, FSCW machines are less susceptible to torque ripple due to their intrinsically lower cogging torque. This will lead to different correlations of the geometric design parameters with these performance metrics as will

be discussed in this chapter.

3.2 Benchmark Designs

The parametric cross-sections of the studied machines and their full-fledged 2-D time-stepping FE (TSFE) models are discussed in this section.

3.2.1 Parametrized Cross Sections

Two generic industrial IPM motor configurations with similar rotor layouts, though with different slot-pole combinations are considered:

1. The first case-study is the 48-slot, 8-pole motor with a single-layer distributed winding configuration, see Fig. 3.1(a). This is the same design configuration as the Toyota Prius introduced and parametrized in the previous chapter. For brevity, this design will be referred to as the 48S8P machine.

2. The second case study is a 12-slot, 10-pole motor with a so-called "double-layer" concentrated winding configuration, see Fig. 3.1(b). The parametrization of the stator design of this open-slot configuration is different than the 48-slot stator design, and is elaborated in Appendix I. Hereafter, this design will be denoted as the 12S10P machine.

The design parameters in Fig. 3.1 are rationalized according to Table 3.1 in order to avoid geometric conflicts between the structures of various components of the two motors. The parameterized FE model of the 48S8P motor is comprised of a total of 10 independent design variables, 5 residing in the rotor, 4 residing in the stator, in

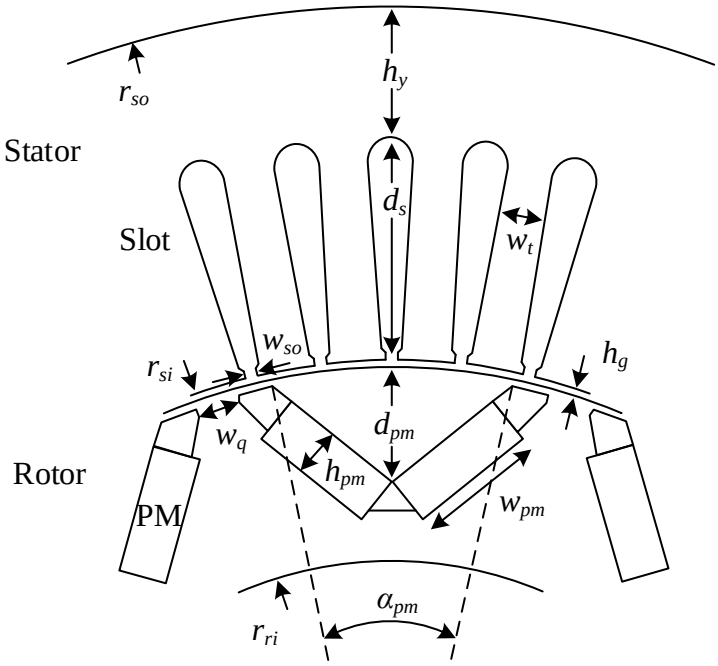

(a) The 48-slot 8-pole machine configuration

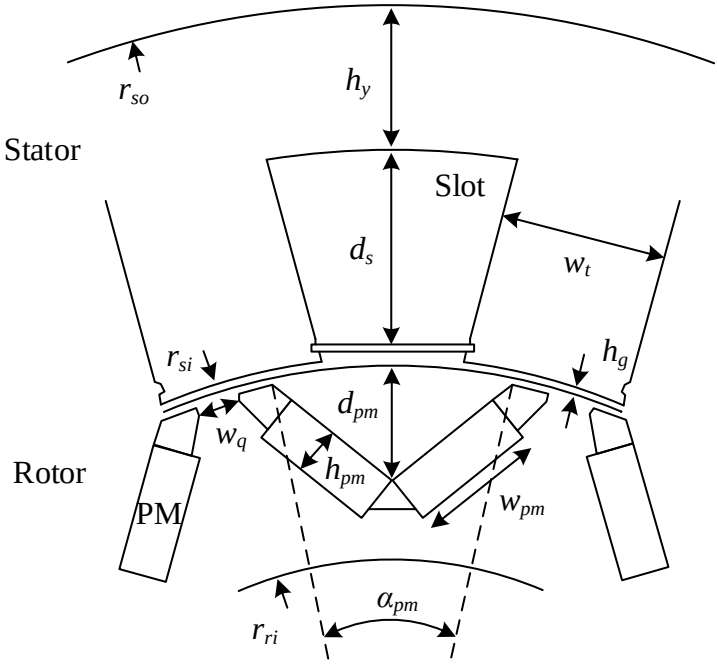

(b) The 12-slot 8-pole machine configuration

Figure 3.1: The parametrized cross section of the case study machines for sensitivity analysis and optimization at different ampere loading levels.

Table 3.1: The independent design variables of the case study machines for sensitivity analysis and optimization at different ampere loading levels.

Parameter(x_i)	Description	48S8P		12S10P	
		$x_{i,min}$	$x_{i,max}$	$x_{i,min}$	$x_{i,max}$
k_{si}	r_{si}/r_{so}	0.60	0.70	0.60	0.70
h_g (mm)	Fig. 3.1	0.70	2.50	0.70	2.50
k_{w_t}	w_t/α_s	0.35	0.75	0.35	0.75
$k_{w_{tt}}$	$w_{tip}/(w_{so}+w_{tip})$	0.30	0.80	NA	NA
$k_{d_{pm}}$	$d_{pm}/d_{pm,max}$	0.25	0.50	0.25	0.50
$k_{w_{pm}}$	$w_{pm}/w_{pm,max}$	0.80	0.93	0.80	0.93
k_{w_q}	$w_q/w_{q,max}$	0.50	0.90	0.50	0.90
h_{pm} (mm)	Fig. 3.1	3.8	9.0	3.8	9.0
α_{pm} (deg.)	Fig. 3.1	20	32	19	26
h_y (mm)	Fig. 3.1	13	25	13	25

addition to the air-gap height. The 12S10P motor under investigation has one less independent design variable due to its open slot configuration, thus eliminating the parameter associated with the tooth tip.

The design variables are confined by upper and lower bounds, also listed in Table 3.1, either to prevent the unintended intersection of various boundary surfaces of components or to address mechanical constraints, e.g. minimum air-gap height. Nevertheless, wide bounds are designated to allow a full exploration of the design space during the optimization process. For both machines, the stator outer and the rotor inner (shaft) diameters are fixed to $260mm$ and $111mm$, respectively.

3.2.2 Time-Stepping FE Models

The 2-D TSFE models of the two machines were developed in ANSYS Maxwell. The core laminations were assumed to be non-oriented silicon steel of $0.36mm$ thickness.

The remenance and coercivity of the NdFeB PMs, and the resistivity of the copper of the stator windings were evaluated corresponding to temperatures of 100 °C, and 150 °C, respectively. This is in order to account for the lowest magnet field and highest winding resistance.

The TSFE analysis with sinusoidal current excitation is utilized to compute the following performance metrics of interest:

1. Active material cost: The normalized active material cost (AMC) is calculated using the same formulation provided in Eq. (2.2.3) in Chapter 2.

2. Power losses: The power losses consist of copper losses in the stator windings with approximations of the end winding copper losses, core losses including hysteresis and eddy current losses in the stator and rotor laminated cores, and the eddy current losses in the rotor PMs for the 12S10P machine with the assumption that these eddy currents are resistance limited. For accurate calculation of the core losses, the frequency domain core loss model introduced in [122] is utilized. The core losses have been obtained on an element by element basis for an excitation current frequency corresponding to a rotor speed of $1800r/min$.

3. Torque ripple: Following the calculation of the average torque per unit length, T_{ave}, using TSFE analysis, the stack-lengths of the designs are adjusted to produce the desired average torque of 300 Nm for a stator current density specifically chosen according to the cooling system of the machine. The torque ripple, T_r, is subsequently determined from the torque profile over a

Table 3.2: Typical current density ranges found in electric machines with different cooling systems.

Cooling	Natural	Fan	Liquid
Current density (A/mm^2)	$1.5-5$	$5-10$	$10-30$

full fundamental ac cycle using Eq. (2.1.4).

4. PM demagnetization: PM demagnetization effects are characterized by the minimum flux density in the rotor PMs over a complete ac cycle. Demagnetization is considered at the magnet piece level. Using NdFeB PMs with reduced heavy earth dysprosium (Dy) content [147] can offer local demagnetization protection, assuming that reasonable measures, such as introducing air pockets around vulnerable areas [148], are adopted at the final stages of the design.

The excitation current densities considered for the TSFE analysis accounts for the type of the cooling system. Typical ranges of current densities are given in Table 3.2, [9]. Here, the fixed current densities of $4A/mm^2$, $8A/mm^2$, and $16A/mm^2$ are assumed for naturally cooled (NC), fan-cooled (FC), and liquid-cooled (LC) machines, respectively.

The phase angle of the current vector is chosen so as to ensure Maximum Torque per Ampere (MTPA) operation. Since the design candidates can be saturated, particularly in FC and LC classes, the torque angle at MTPA for each individual design is numerically calculated by sampling and interpolating the generated torque at multiple phase angles of the stator current phasor [70, 149], in a similar manner

to the procedure described in Chapter 2.

3.3 Parallel Sensitivity Analysis at Different Ampere Loading Levels

The variation of the relationships between the geometric design parameters and the performance metrics can be understood by carrying out a sensitivity analysis at the three levels of stator winding current density. In the following subsections, the sensitivity analysis methodology and the results are presented.

3.3.1 Methodology

For each cooling system, five second order response surfaces were defined corresponding to the cost, copper losses, core losses, torque ripple, and degree of PM demagnetization. The core losses and copper losses were treated separately since the design variables have distinctive effects on these two loss components.

The regression coefficients pertaining to these response surfaces indicate how the variation of the design parameters within their permissible ranges influences the machine performance metrics. The class of Central Composite Designs (CCD) [150] was used for design of experiments (DOE) in order to calculate the regression coefficients associated with each second order response surfaces, y, given in Eq. (3.3.1),

$$y = \beta_o + \sum_{i=1}^{n} \beta_i c_i + \sum_{i=1}^{n} \beta_{ii} c_i^2 + \sum_{i=1}^{n} \sum_{j=i+1}^{n} \beta_{ij} c_i c_j \tag{3.3.1}$$

where β_o, β_i, β_{ii}, and β_{ij} are the regression coefficients for the n design variables, x_i,

$i = 1, \ldots, n$ expressed in the coded form, c_i, according to Eq. (3.3.2).

$$c_i = \frac{x_i - (x_{i,max} + x_{i,min})/2}{(x_{i,max} - x_{i,min})/2}, i = 1, 2, ..., n \tag{3.3.2}$$

In Figs. 3.2 and 3.3, the regression coefficients of the sensitivity analysis are shown for the five examined performance metrics at the three different levels of current densities accounting for the three classes of cooling systems. Since the purpose of the sensitivity analysis is to provide a measure of importance of each design parameter with respect to other design variables, the regression coefficients are normalized to the variable with the maximum influence in each group of metrics. Furthermore, the DOE is conducted so as to ensure no main effect or two-factor interaction is aliased with any other main effect or two-factor interaction of the design variables, i.e. so-called resolution V designs [150]. Therefore, the regression coefficients can be examined independently for each group of metrics.

Each coefficient is associated with a design variable, i.e. input, to indicate how its variation within the permissible range denoted in Table 3.1 would influence the machine's performance, i.e. output. A positive coefficient, (+), indicates that an increase in input will raise the output whereas a negative coefficient, (−), constitutes the opposite trend between the input and output. Accordingly, a close examination of Figs. 3.2 and 3.3 leads to the observation that some trends vary drastically, or even change direction, with respect to the ampere loading for the two 48S8P and 12S10P machines.

3.3.2 Discussion of the Results of the Sensitivity Analysis

The sensitivity analysis for each performance metric is summarized in this section.

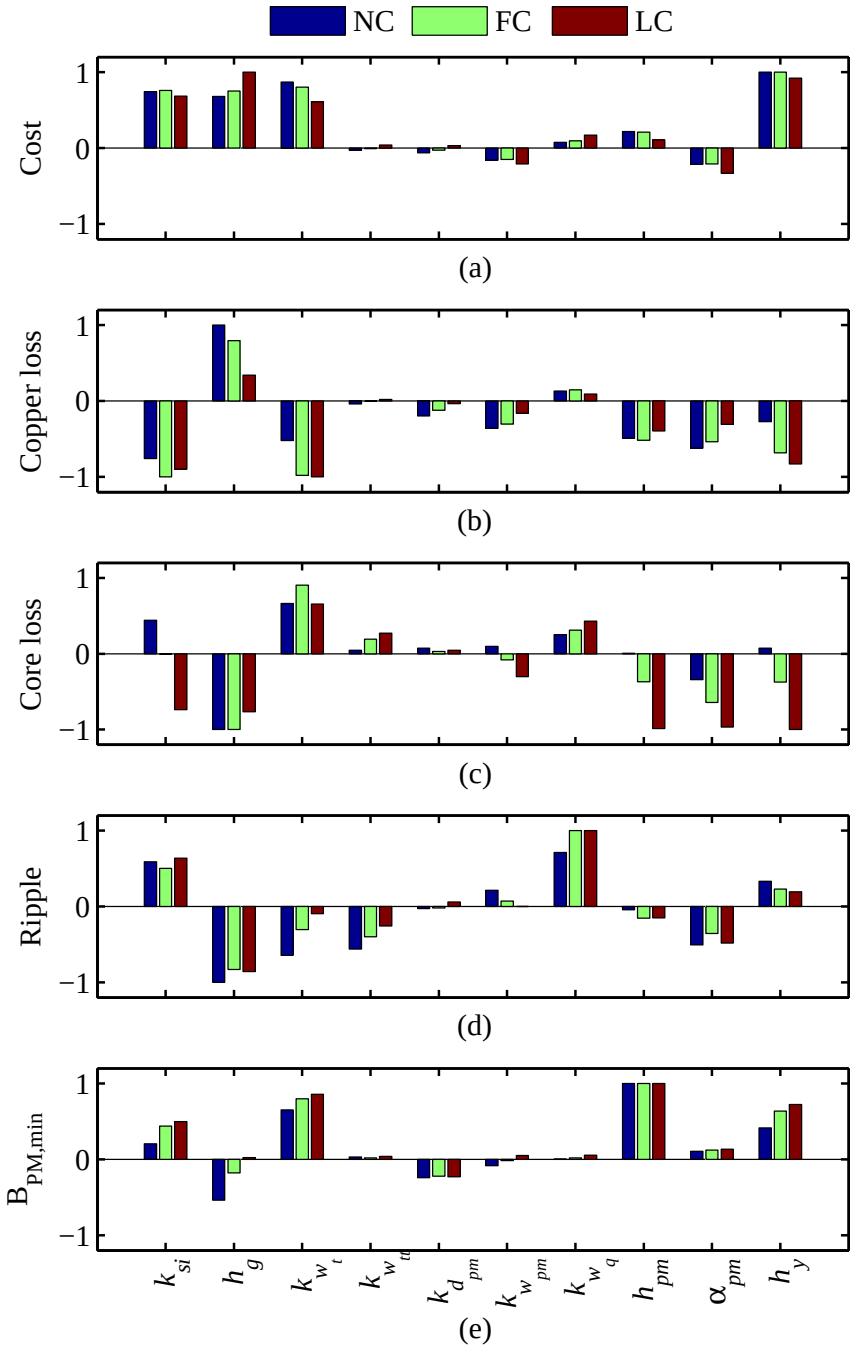

Figure 3.2: Normalized regression coefficients from the sensitivity study indicating the effect of the design variables on, (a) active material cost, (b) copper loss, (c) core loss, (d) minimum PM flux density, and (e) torque ripple for the 48S8P machine.

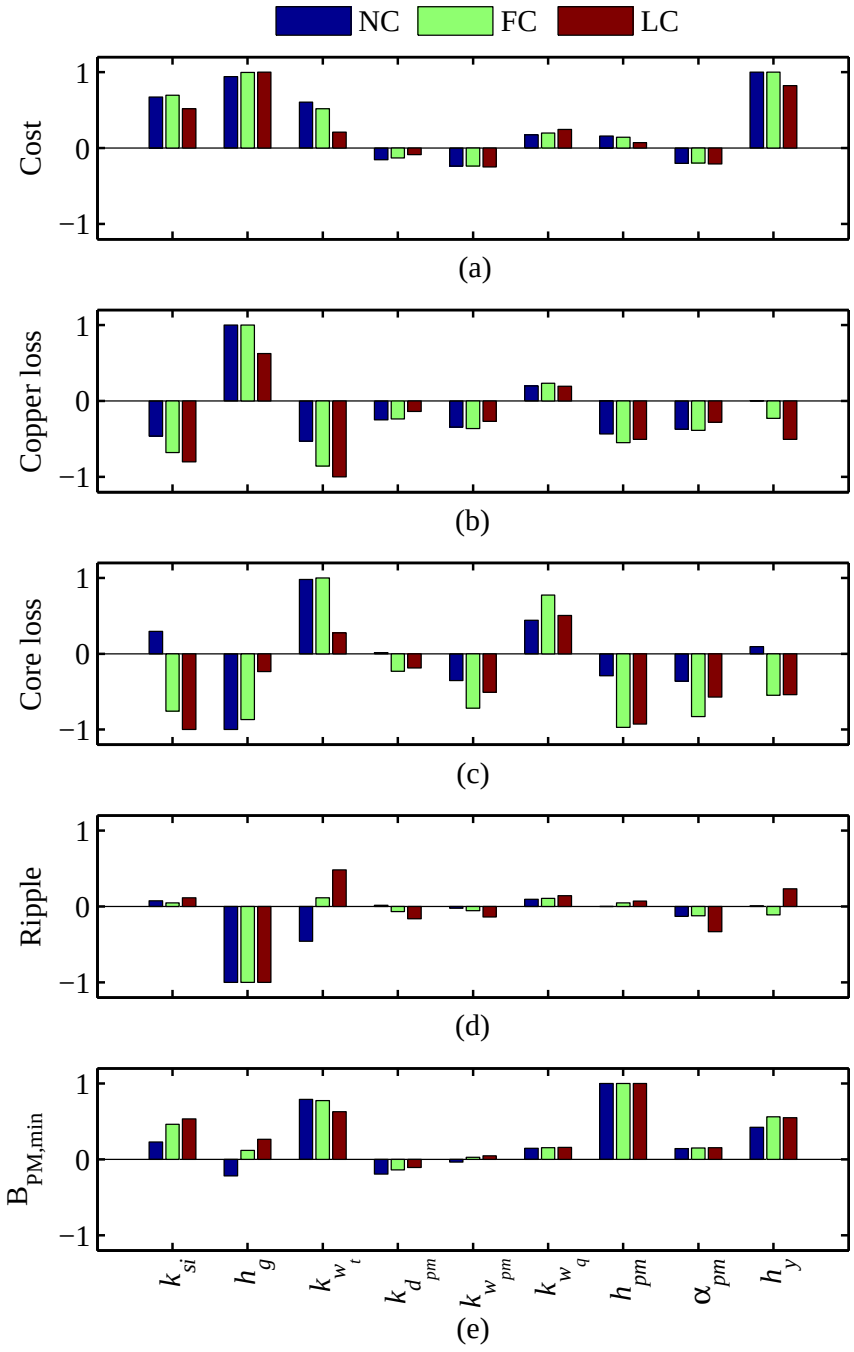

Figure 3.3: Normalized regression coefficients from the sensitivity study indicating the effect of the design variables on, (a) active material cost, (b) copper loss, (c) core loss, (d) minimum PM flux density, and (e) torque ripple for the 12S10P machine.

3.3.2.1 Active Material Cost

According to Figs. 3.2(a) and 3.3(a), for both machine configurations:

- The strongest correlation with AMC in the NC and FC classes is attributed to the yoke height, which is opposite to the slot depth for a given stator bore.
- The yoke height correlation with AMC is superseded by that of the air-gap height in the LC class.
- The positive correlation of the tooth stem width with AMC monotonically decreases as the ampere loading level increases.

3.3.2.2 Copper Losses

According to Figs. 3.2(b) and 3.3 (b):

- The considerable variations of the influences of the design parameters on the copper losses as the ampere loading level increases should be noted for both machine configurations.
- For the 48S8P machine, the air-gap height constitutes the strongest correlation with copper losses in the NC class. In the FC and LC classes, the split ratio, k_{si}, the tooth-stem width, and the yoke height become more influential.
- Similar trends exist for the 12S10P machine, except for the diminished influence of the yoke height.

3.3.2.3 Core Losses

According to Figs. 3.2(c) and 3.3 (c):

- The influences of the design parameters on the core losses are sensitive to the ampere loading to such an extent that some of these relationships, i.e. those associated with the stator inner diameter and yoke height, are reversed as the ampere-loading increases.
- For both machine configurations, in the NC class, the design parameters associated with the stator constitute the strongest correlation with the core losses.
- As the ampere loading increases, the design parameters associated with the rotor become more influential.
- The strong influence of the rotor q-axis bridge on the core losses, especially in the 12S10P motor, should be noted.

3.3.2.4 Torque Ripple

According to Figs. 3.2(d) and 3.3(d):

- Except for the air-gap height which maintains a strong negative correlation with torque ripple under any ampere loading conditions, the two machine configurations have distinctive torque ripple characteristics.
- For the 48S8P machine, the width of the q-axis bridge becomes more influential than the air-gap height as the level of ampere-loading increases. Meanwhile, the

negative correlation of the widths of the tooth stem and tooth tips with torque ripple diminishes as the saturation level of the magnetic core is elevated.

- As opposed to the 48S8P machine, the 12S10P machine is intrinsically less susceptible to torque ripple under any loading conditions.

- It is interesting to note the reversal of the correlation between the torque ripple and the tooth stem width under heavy magnetic core saturation in the 12S10P motor.

3.3.2.5 PM Demagnetization

According to Figs. 3.2(e) and 3.3(e):

- For both machine configurations and under all loading conditions, the PM demagnetization is strongly correlated to the PM height and tooth-stem width.

- The correlation factors of the split ratio, k_{si}, and the yoke height monotonically increase as the level of ampere loading increases.

- Although the air-gap height constitutes a negative correlation with B_{pm} in NC machines, this relationship reverses as the ampere-loading level increases.

3.4 Parallel Statistical Analysis of the Optimized Designs at Different Ampere Loading Levels

The sensitivity analysis merely reveals the independent effects of the design variables on the machine performance. To understand how the interactions between these

variables influence the final optimal design which is subject to a unique set of objectives and constraints, a close examination of the design optimization process and results is in order. Nevertheless, the sensitivity study suggests that the optimal designs for each class should have distinctive features which will be examined in this section.

A large-scale design optimization algorithm has been developed and utilized to optimize the two motor configurations for each level of the current densities. The design optimization is followed by a statistical analysis on the optimized designs to find the range of change, i.e. the statistical distribution of the design variables in the optimized designs residing in the design space for each class of the cooling systems.

3.4.1 Large-Scale Design Optimization

Six runs of a large-scale design optimization, each composed of 6600 candidate designs, were carried out to optimize the machine model at the three aforementioned levels of current densities.

The optimization algorithm relies on the TSFE model developed in Section 3.2. A Combined Multi-objective Optimization with Differential Evolution (CMODE) [110], was implemented as the optimization search algorithm. This CMODE-type optimization is fully described in Chapter 4.

The fitness function of the optimization problem has been defined based on the previously discussed performance metrics. For generic industrial use, it practically consists of the two following objectives:

- Minimization of the AMC given in Eq. (2.2.3)

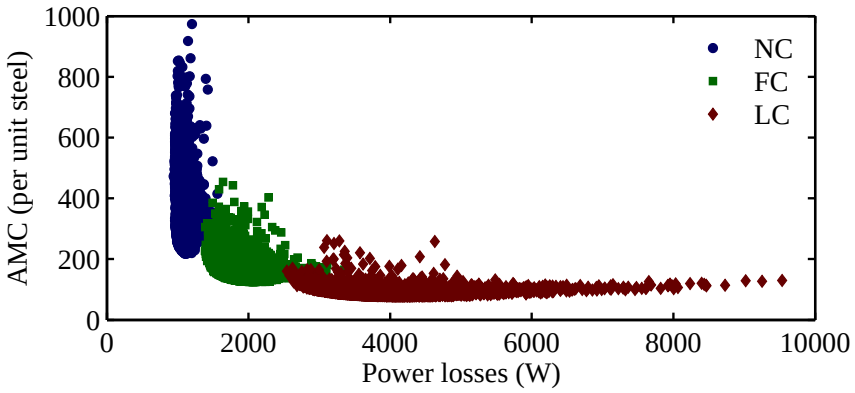

(a) 48S8P design

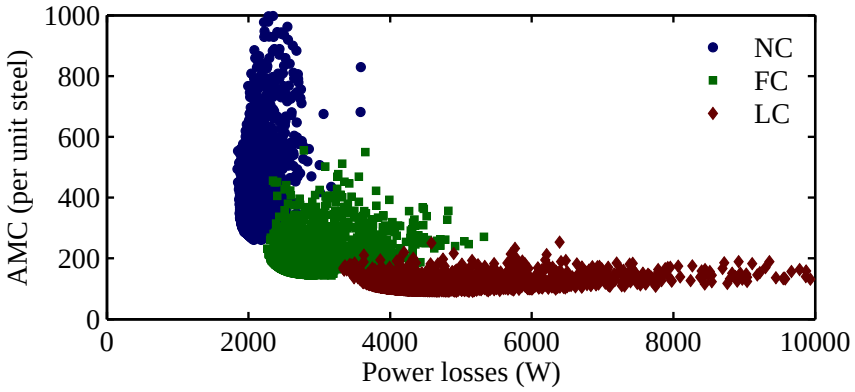

(b) 12S10P design

Figure 3.4: Optimization results for the three case-study cooling systems.

- Minimization of the power losses

Due to the opposite correlations of the design parameters, except the air-gap height, h_g, with AMC and power losses in Figs. 3.2(a), and 3.3(a), the two objectives are conflicting.

Furthermore, the two following constraints are introduced for reliable operation:

- Less than 15% torque ripple

- Less than 70% PM demagnetization

Each run of the optimization was started with an initial generation of 200 members and was carried out over 800 generations of 8 members each [110]. Figures. 3.4(a)-(b) show the optimization results in terms of the conflicting objectives for the 48S8P and 12S10P machines, respectively. The design candidates indicated in Fig. 3.4 are compared in terms of AMC and power losses at the same rated load operating point.

It is evident that increasing the stator winding current density, and thus the ampere loading of the machine, complicates the design of the cooling system by increasing the total dissipated losses. Nevertheless, in many applications, higher torque density can translate into reduced system cost, size, and weight, thus promoting such designs with sophisticated cooling systems [142, 148].

Furthermore, the extremes of the power losses and AMC of the three classes of cooling systems are non-overlapping. That is, the same efficiency characteristics of NC machines cannot be obtained by LC machines. Similarly, the AMC in LC machines can be reduced to values not achievable by NC machines.

It is interesting to notice that due to higher core losses and larger masses of PM in their construction, the Pareto-optimal designs of the 12S10P configuration are located further apart from the origin as compared to the 48S8P configuration, see Tables 3.4 and 3.5.

3.4.2 Scaling Rules of the Optimum Candidate Designs

To differentiate the distinctive optimal design values between the three cooling classes, the statistical distributions of the design variables in the Pareto-optimal designs should be investigated. For this purpose, from each run of optimization, 500 superior

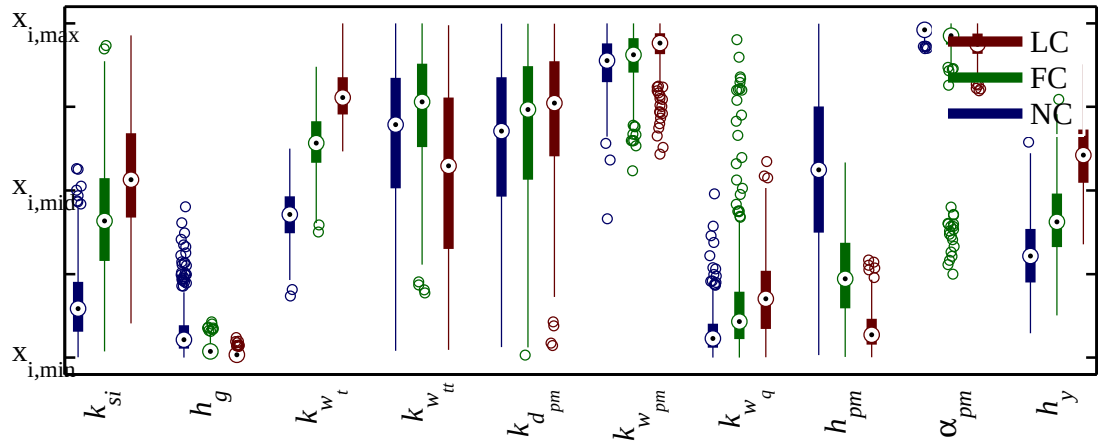

(a) 48S8P design

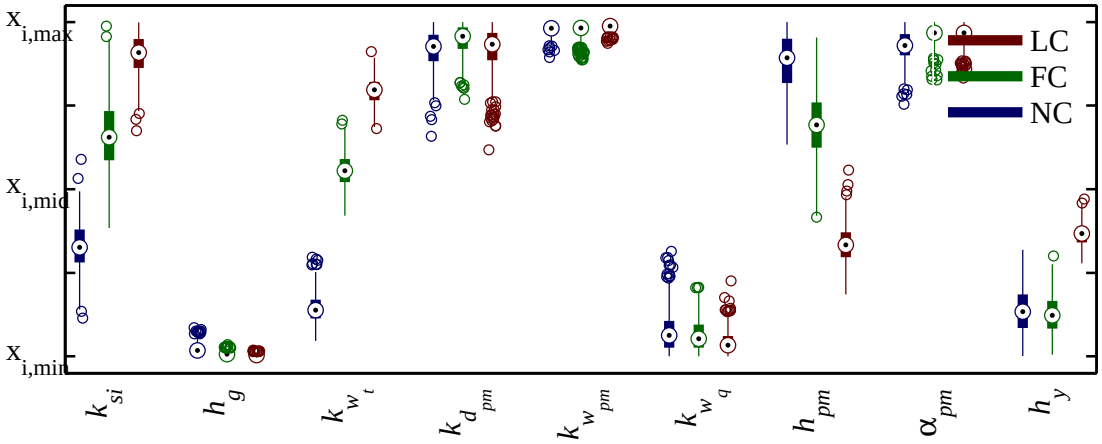

(b) 12S10P design

Figure 3.5: The distribution of the design variables in the optimized designs for the three case study cooling systems.

designs were selected based on a three-step process. First, the designs which do not violate the constraints on the torque ripple and on the PM demagnetization are identified and separated in set P.

Subsequently, a strength value $s(d_i)$ is designated to each of the designs, d_i in P,

according to Eq. (3.4.1).

$$s(d_i) = \#\{d_j \mid d_j \in P \; and \; cost(d_i) < cost(d_j) \; and \; loss(d_i) < loss(d_j)\}, i = 1, 2, ..., k \tag{3.4.1}$$

where "#" is the cardinality of the set [151], and k is the number of the designs in P. The designs in P are thereafter ranked in a descending order based on their strength value, s_{di}, to determine the top 500 superior designs.

The distribution of the design parameters in the selected designs with respect to their bounds can be described by "box plots" shown in Fig. 3.5. The rectangular boxes in Fig. 3.5 represent the first, the second and the third quartiles of the distribution of design values with respect to the upper and lower bounds designated for each design parameter in Table 3.1. The distances between the different parts of these boxes indicate the degree of dispersion and skewness in the value of the optimal designs. The circles in the middle, and the whiskers represent the average, the maximum and the minimum of the optimal design value for each parameter.

The representative cross-sections which were generated based on the means of the design variables in Table 3.3 are provided in Fig. 3.6 which allows one to visualize the distinctive design features of each machine. These features will be subsequently explained with reference to the statistical and sensitivity analyses.

According to Fig. 3.5, the optimal ranges of the design variables are broader in the 48S8P machine. This stems from the imposed criterion on the torque ripple of the selected designs, which leads to the dispersion of the chosen design candidates in the Pareto-front vicinity.

Three different trends can be recognized in the variation of the design parameters

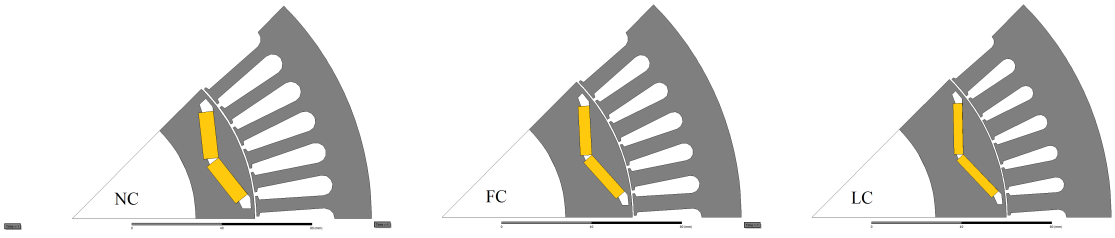

(a) 48S8P design

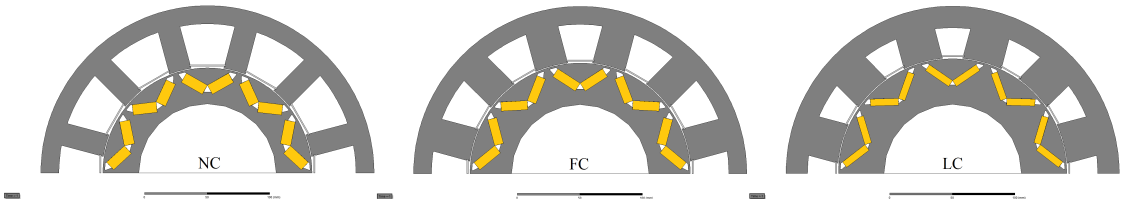

(b) 12S10P design

Figure 3.6: Optimized cross sections derived based on the mean of the design variables in the 500 Pareto-optimal designs listed in Table 3.3, for the three current density levels.

Table 3.3: Average design parameters of the optimized designs at different ampere loading levels.

Parameter(x_i)	48S8P			12S10P		
	NC	FC	LC	NC	FC	LC
k_{si}	0.62	0.64	0.66	0.63	0.67	0.69
h_g (mm)	0.83	0.75	0.72	0.74	0.71	0.71
k_{w_t}	0.52	0.61	0.66	0.41	0.57	0.67
$k_{w_{tt}}$	0.63	0.67	0.57	NA	NA	NA
$k_{d_{pm}}$	0.41	0.42	0.43	0.48	0.49	0.48
$k_{w_{pm}}$	0.91	0.92	0.92	0.47	0.46	0.46
k_{w_q}	0.53	0.56	0.57	0.53	0.53	0.52
h_{pm} (mm)	6.71	5.06	4.22	8.38	7.40	5.55
α_{pm} (deg.)	31.73	31.21	31.21	25.50	25.74	25.73
h_y (mm)	16.52	17.72	20.12	14.63	14.51	17.40

Table 3.4: Mean of the ratio of copper losses to core losses in the Pareto-optimal designs at different ampere loading levels.

Machine	NC	FC	LC
48S8P	2.16	5.57	15.24
12S10P	0.74	1.52	3.47

Table 3.5: Mean of the masses of the optimized designs normalized with respect to the values obtained for NC class.

Mass (m)	48S8P			12S10P		
	NC	FC	LC	NC	FC	LC
m_{PM}%	100	47.47	26.22	100	56.53	32.60
m_{copper}%	100	52.14	30.22	100	45.10	23.31
m_{steel}%	100	59.88	38.34	100	58.14	42.32

which are addressed in the following discussion.

3.4.2.1 Parameters With Increasing Trends in Both Motor Configurations

As can be seen in Fig. 3.5, the split ratio, k_{si}, the ratio k_{w_t}, and the yoke height, h_y, relatively grow with the increase of the ampere loading. This is in line with the sensitivity analysis and the fact that decreasing copper losses, as the major loss component in the case study PM machines according to Table 3.4, takes precedence over decreasing core losses. The $k_{d_{pm}}$ ratio varies widely in the 48S8P machine due to the insignificant correlation of this design variable with the optimization objectives according to the sensitivity analysis in Fig. 3.2. The stronger negative correlation of $k_{d_{pm}}$ ratio with AMC and copper and core losses in 12S10P machine, has resulted in its maximization in the selected 12S10P designs, as shown in Fig. 3.5(b). Similarly, the $k_{w_{pm}}$ ratio and α_{pm} are concentrated towards their higher bounds due to their negative correlations with the two objectives as shown in Figs. 3.2 and 3.3.

3.4.2.2 Parameters With Decreasing Trends in Both Motor Configurations

The PM height, h_{pm}, in Fig. 3.5 monotonically decreases as the ampere loading increases in both 48S8P and 12S10P machines. This can be explained by considering the results of the sensitivity analysis in Figs. 3.2 and 3.3, and the change of the masses of various components in the selected designs for the three cooling systems, as listed in Table 3.5. Accordingly, the PM mass has been reduced in the selected designs proportionately to the masses of other components by reducing the only parameter associated with the PM mass which constitutes a positive correlation with AMC, i.e. h_{pm}. Meanwhile, the excessive PM demagnetization as a result of reducing PM height has been prevented by introducing a constraint on the minimum flux density of the PMs. The air-gap height, h_g, in the optimum designs is minimized due to its positive correlation with AMC and major component of the losses, i.e. copper losses.

3.4.2.3 Parameters With Conflicting Trends in the Two Motor Configurations

For the 48S8P machine, while the k_{w_q} ratio monotonically increases in Fig. 3.5(a) as the torque ripple becomes less of an issue, it decreases constantly in the 12S10P machine, Fig. 3.5(b), in order to reduce the core losses. On the one hand, according to the sensitivity analysis, the core loss has a stronger correlation with this design variable, and on the other hand, the core losses constitute a considerable portion of the overall losses in the 12S10P machine, see Table 3.4.

The tooth-tip width of the 48S8P machine widely varies at higher ampere loading

due to saturation. The tooth-tips are larger at low ampere loading to alleviate the torque ripple, see Fig. 3.2(d). Their variation is ineffective when the machine saturates. Meanwhile, the mean of the tooth-tip width in Fig. 3.5(a) is reduced to mitigate the core losses, although this reduction in width is not significant since the overall ratio of core to copper losses is insignificant, see Table 3.4.

3.5 Summary

A parallel sensitivity analysis was carried out on two case-study IPM machines with concentrated and distributed stator winding configurations and with different cooling systems. It was demonstrated that the correlation between the main design variables and various performance metrics, particularly core losses, copper losses, and torque ripple can be significantly affected by the machine's ampere loading and magnetic core saturation. In some cases, these trends can even be reversed.

The distribution of the optimal design values were investigated for each case-study in a practical optimization problem where the interaction of the performance metrics and design variables occur. Noticeable difference in the optimal design values were observed and the trends were classified for the naturally cooled, fan-cooled, and liquid-cooled machines.

The results of this chapter accentuate the challenges in the design of electric motors with intermittent operating cycles, such as those in traction applications, where an optimal design is to maintain high performance under various loading conditions, as will be dealt with in following chapters.

CHAPTER 4

MULTIOBJECTIVE CMODE-TYPE OPTIMIZATION OF ELECTRIC MACHINES

In the two previous chapters, it was demonstrated that the optimal design rules of PM machines vary with respect to the ampere loading conditions. As a result, for design synthesis of PM machines with a wide range of operation, these ampere loading conditions should be accounted for in the optimization fitness function. As will be discussed in the following chapters, one method to do so is by evaluating the machine performance at multiple load operating points which represent various loading conditions of the machine. This, however, increases the computational complexity of the overall design optimization process, even if computationally efficient modeling approaches such as CE-FEA are used. To further improve the computational efficiency, a new optimization algorithm is developed and presented in this chapter, which can outperform the existing DE optimizer when implemented on multi-core desktop computers. As shown in Chapters 2 and 3, large-scale design optimization of electric machines is oftentimes practiced to achieve a set of objectives under a set of constraints. Accordingly, the design optimization of electric machines can be regarded as a constrained optimization problem (COP). Evolutionary algorithms (EAs) used in the design optimization of electric machines including DE, which has received considerable attention during recent years, are unconstrained optimization methods that need additional mechanisms to handle COPs. In this chapter, a new

optimization algorithm that features combined multi-objective optimization with differential evolution (CMODE) has been developed and implemented in the design optimization of electric machines. A thorough comparison is conducted between the two counterpart optimization algorithms, CMODE and DE, to demonstrate CMODE's superiority in terms of convergence rate, diversity and high definition of the resulting Pareto fronts, and its more effective constraint handling. More importantly, CMODE requires a lesser number of simultaneous processing units which makes its implementation best suited for state-of-the-art desktop computers reducing the need for high performance computing (HPC) systems and associated software licenses.

4.1 Introduction

Large-scale design optimization techniques have become a well-established practice for designing high performance electric machines [73, 84, 85, 96, 119, 129, 152, 153]. In these techniques, the parametrized cross-section of a subject machine is refined to improve certain performance metrics with respect to the application requirements. Cost, power loss, torque density, torque ripple, power factor, and degrees of demagnetization of rotor PMs in PM machines, are common performance metrics which constitute the set of objectives and constraints in any optimization problem.

In principle, a large-scale model-based design optimization process consists of two independent segments: the machine model for computation of performance metrics, and the optimizer for finding the globally optimal design solutions. Regarding the machine model, both analytical [73, 129, 152, 153] and Finite Element (FE)

[84, 85, 96, 119] methods are commonly used in a large-scale design optimization process, with the latter receiving more attention during recent years owing to the ever-increasing processing power of modern computers. Concerning the optimizer, either a deterministic or stochastic search algorithm can be used.

Efficient utilization of computational resources is imperative when the performance evaluation of the design candidates is computationally intensive [78], as in the case of the FE models. Two areas of opportunity exist under each segment of the optimization process that can serve this purpose. On the performance evaluation side, CE-FEA has been recently introduced [79–81, 84] for fast and high fidelity simulation of PM machines. On the optimizer side, the DE algorithm [154] has received extensive attention as a reliable and fast stochastic search algorithm [77, 155]. The DE is thought to have a better performance in comparison with other stochastic optimizers in electric machinery design problems [77, 120]. It has been coupled to the CE-FEA for optimization of several types of PM motors with various sets of objectives and constraints [84–87, 96, 119].

Although DE has proved effective in the design optimization of electric machines [94, 156], similar to other EAs, it has not been developed for handling COPs [151, 157], which is the case in design of electric machines [94, 156, 158]. Popular constraint handling mechanisms include penalty function methods, methods based on preference of feasible solutions, and multi-objective optimization techniques [151, 158]. In the latter, COPs are converted to unconstrained multi-objective optimization problems where minimization of the so-called degree of constraint violation is designated as an additional objective.

In this Chapter, a recently developed CMODE algorithm [110, 151] is adapted for the design optimization of electric machines with application to three IPM motors with distributed and concentrated stator windings. The same design problem is performed using the standard DE to compare the outcomes with those obtained from the CMODE approach. It is demonstrated here that CMODE is superior to DE in terms of convergence rate and constraint handling in all three example motor configurations. Furthermore, CMODE requires a lesser number of simultaneous function evaluations which makes it an attractive solution for implementation of the design optimization on a state-of-the-art desktop computer with a limited number of processors, thus reducing the need for high performance computing (HPC) facilities and associated software licenses. First, the essence of the two optimization algorithms with a focus on their similarities and differences are discussed. Subsequently, following the description of the benchmark studies, the optimization results and the comparison between the two algorithms are provided.

4.2 CMODE Versus DE in the Design Optimization of Electric Machines

The flowcharts of steps of the two counterpart search algorithms, DE and CMODE, applied to the design optimization of electric machines are shown in Fig. 4.1 and Fig. 4.2, respectively. In both cases, an initial design is obtained analytically in reference to the application requirements and specifications [9]. This initial design is subsequently parametrized and the geometric design variables and constants are specified in the

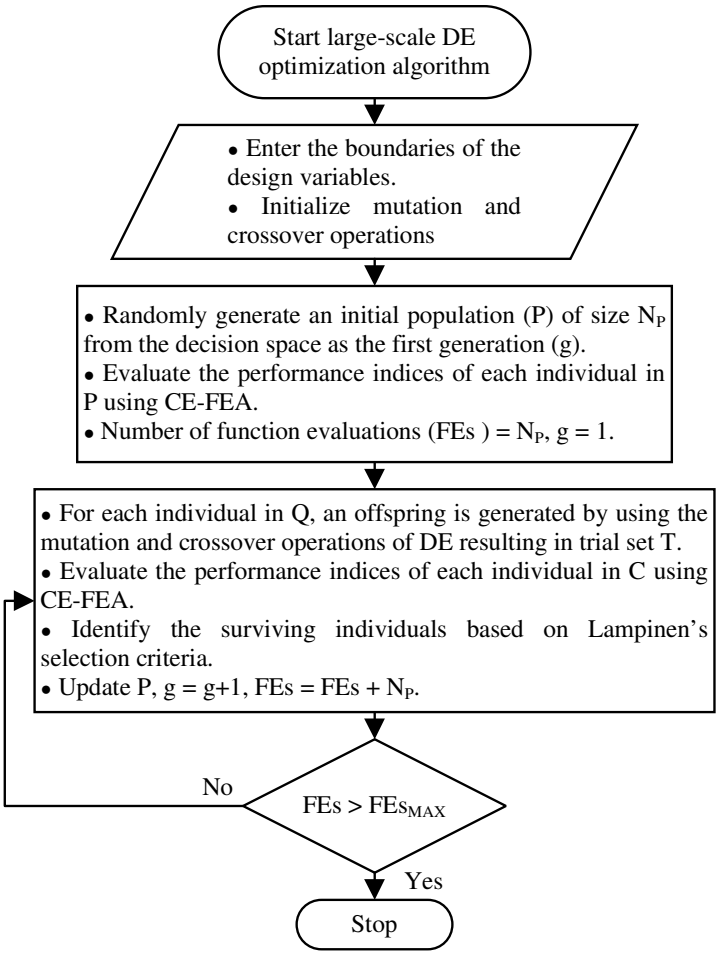

Figure 4.1: Flowchart of the steps of the DE optimization algorithm.

initialization stage. Preparation of a well-defined parameterized model, which on the one hand is flexible for the exploration of the entire design space, and on the other hand is restrained to avoid geometric conflicts between various components of the machine cross-section, is a non-trivial demanding task.

The optimization process involves performance assessment of the resulting design candidates. For this purpose, the CE-FEA approach [80, 84] described in Chapter 2, which accommodates the complex geometry of the machine structure, and incorporates the actual non-linear nature of the magnetic core, is utilized.

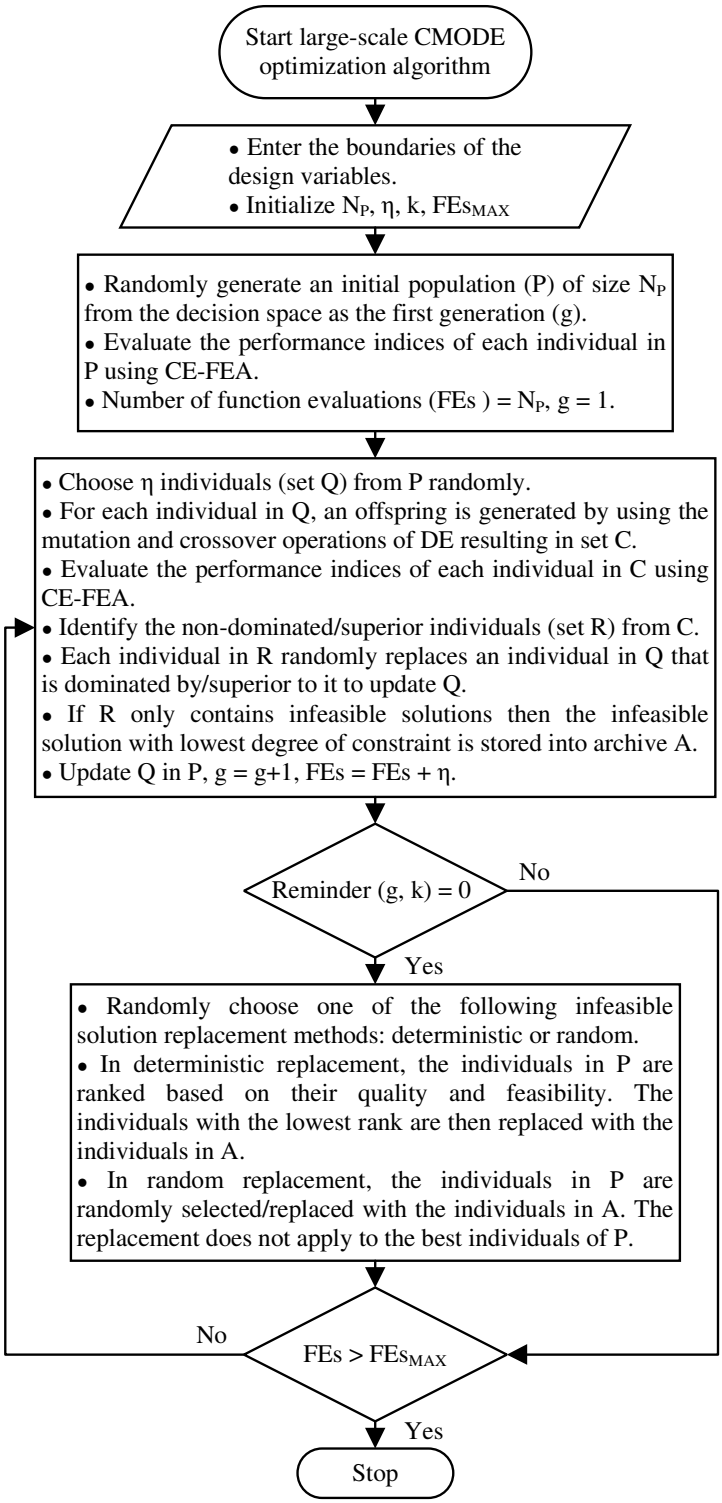

Figure 4.2: Flowchart of the steps of the CMODE optimization algorithm.

Apart from using the same parameterized model and the same technique for performance evaluation of the design candidates, here the CE-FEA method, the optimization procedure differs for the CMODE and the DE algorithms in the following manner:

- Unlike DE in which, as a standard EA, all the population members are used to generate the offspring population, in CMODE, only a portion of the total individuals, denoted by η, are chosen for this purpose. This renders CMODE a steady-state EA where the first randomly generated population has a large number of members, a fraction of which, set Q, are being constantly updated throughout the optimization process. Consequently, CMODE performs a fraction of simultaneous function evaluations (FEs) contrary to what takes place in DE. Here, performing FEs means applying the CE-FEA approach in solving the electromagnetic field in the design candidate machines. Typical numbers recommended for DE are 60 generations each consisting of 80 members [85, 96], in contrast with an initial population of 180 members followed by 400 generations each consisting of 8 members recommended for CMODE [151]. Lesser number of simultaneous FEs, here 8 versus 80, makes CMODE's implementation best suited for state-of-the-art desktop computers.

- The selection procedure for determination of the surviving candidates in CMODE is based on the identification of superior individuals in the trial population, set C, and having them replace the dominated individuals in the parent population, set Q. Therefore, in comparison to DE, there is an additional

round of competition in CMODE. The first round is between all the individuals in the trial population, and the second round is between the winners of the first round, set R, and the individuals in the parent population. Nevertheless, CMODE still benefits from the mutation and crossover operations of DE [151], which produces the trial and ultimately the offspring populations of consecutive generations.

- In CMODE, an additional variable defined as the degree of constraint violation is introduced into the objective function to be minimized with other objectives. Let $\vec{x}$ be the design vector, and $f(\vec{x})$ be the initial objective of the optimization problem subject to a set of q inequality constraints, $g_j(\vec{x})$, and $(m-q)$ equality constraints, $h_j(\vec{x})$. The final objective of the optimization process would be the minimization of $\mathbf{f}(\tilde{\mathbf{x}}) = (f(\vec{x}), G(\vec{x}))$, where $G(\vec{x})$ is the degree of constraint violation given in Eq. (4.2.1) below [151].

$$G(\vec{x}) = \sum_{j=1}^{m} G_j(\vec{x}) \tag{4.2.1}$$

where $G_j(\vec{x}) = \begin{cases} \max\{0, g_j(\vec{x})\}, 1 \leq j \leq q \\ \max\{0, \mid h_j(\vec{x}) \mid -\delta\}, q+1 \leq j \leq m \end{cases}$

- Finally, according to Fig. 4.2, CMODE features an infeasible solution replacement mechanism in which after a certain number of generations, denoted by k, an archive consisting of individuals that violate the constraints, A, replaces the individuals in the main population, P, either through a deterministic or random procedure. This mechanism adds to the diversity of the overall optimization problem to facilitate convergence to the globally optimal solutions.

4.3 Benchmark Study- Application to IPM Motors

4.3.1 Parametrized FE Model

To compare the merits of the two counterpart stochastic search algorithms, three IPM motor configurations with distinctive rotor and stator features, and under different loading conditions have been investigated:

1. A fan-cooled 48-slot, 8-pole motor with single-layer v-shaped magnets and single-layer distributed winding configuration. This design will be referred to as the 48S8P-a design for brevity.

2. A liquid-cooled 48-slot, 8-pole motor with double-layer v-shaped magnets and single-layer distributed winding configuration, which will be referred to as the 48S8P-b design.

3. A naturally cooled 12-slot, 10-pole motor with single-layer v-shaped magnets and a so-called "double-layer", i.e. all teeth wound" concentrated winding configuration, called hereafter the 12S10P design.

The current density of the stator winding can be adjusted to account for the ampere-loading of the machine. Typical current density ranges are provided in Table 3.2 [9]. Here, 22 A/mm^2, 8 A/mm^2, and 4 A/mm^2 are assumed for liquid-, fan-, and naturally cooled machines, respectively. The variety introduced to the selected machine configurations and their electrical loadings provides the basis for a rigorous

comparison between the two search algorithms.

To construct the FE model of the example machines, the parametrized stator and rotor structures, respectively shown in Figs. 4.3 and 4.4 are utilized. The independent design variables defined based on theses parametrized models are listed in Table 4.1. Some of these design variables are rationalized according to Table 4.1 so as to avoid geometric conflicts between the structures of various components of the motor. The parameterized FE model of the 48S8P-a motor is comprised of a total of 10 independent design variables, 5 residing in the rotor, 4 residing in the stator, in addition to the air-gap height. The 48S8P-b motor has 2 additional independent variables introduced to the rotor geometry to accommodate the double-layer PMs. Meanwhile, the open-slot 12S10P motor has one less independent design variable because of its open slot structure. The design variables are confined by upper and lower bounds, also listed in Table 4.1 and depicted in Figs. 4.3 and 4.4 for some of the variables in a typical design, either to prevent the unintended intersection of various boundary surfaces of machine components, or to address mechanical constraints, e.g. minimum air-gap height or the yield stress for the rotor bridges [159]. For all the three machines, the stator outer diameter is fixed to 260mm. The shaft diameter is equal to 111mm, and 74mm for the single-layer and double-layer rotor magnet configurations, respectively. The parameterized geometry together with the introduced bounds allow the model to be flexible in exploring the entire design space to find the globally optimized design candidates.

The CE-FEA method is utilized for fast and high fidelity calculation of the machine performance metrics [80, 84]. This method was explained in Chapter

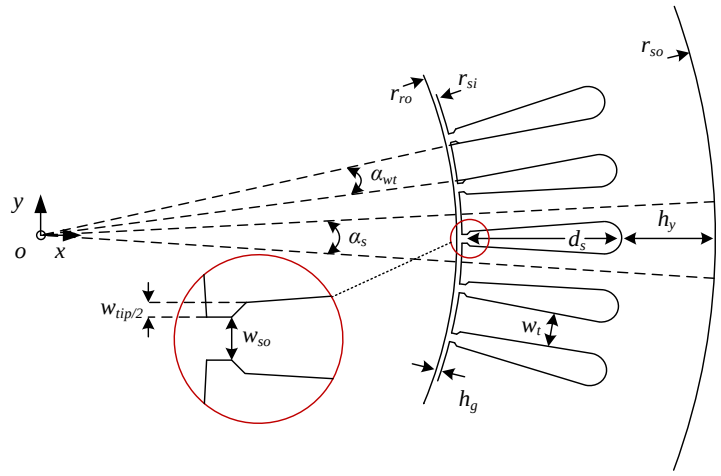

(a) 48-slot stator

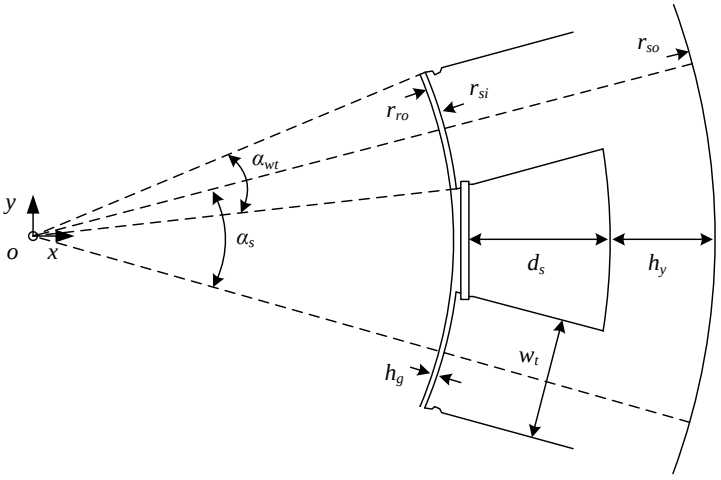

(b) 12-slot stator

Figure 4.3: The parameterized stator structures used for constructing the example IPM motors for comparison between DE and CMODE.

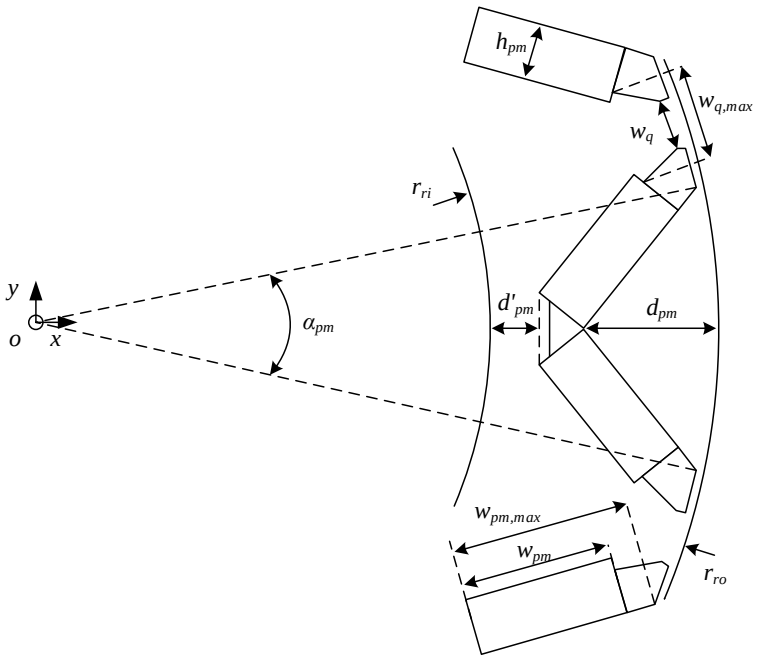

(a) Single-layer rotor PM layout

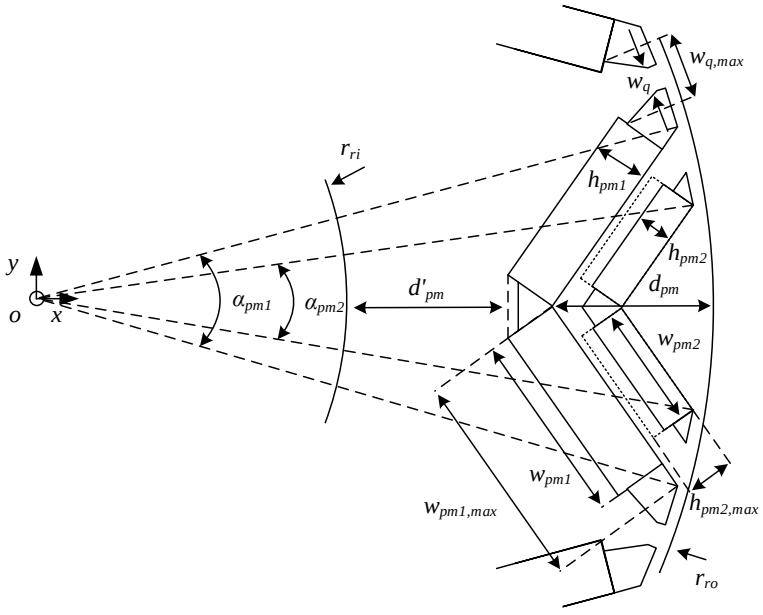

(b) Double-layer rotor PM layout

Figure 4.4: The parameterized rotor structures used for constructing the example IPM motors for comparison between DE and CMODE.

Table 4.1: Independent design variables of the parametric stator and rotor structures shown in Figs. 4.3 and 4.4.

Parameter(x_i)	Description	48S8P-a		48S8P-b		12S10P	
		$x_{i,min}$	$x_{i,max}$	$x_{i,min}$	$x_{i,max}$	$x_{i,min}$	$x_{i,max}$
k_{si}	r_{si}/r_{so}	0.6	0.7	0.6	0.7	0.6	0.7
h_g (mm)	Fig. 4.3	0.7	2.5	0.7	2.5	0.7	2.5
k_{w_t}	α_{w_t}/α_s	0.35	0.75	0.35	0.75	0.35	0.75
k_{wtt}	$w_{tip}/(w_{so}+w_{tip})$	0.3	0.8	0.3	0.8	NA	NA
$k_{d_{pm}}$	$d_{pm}/(d_{pm}+d'_{pm})$	0.25	0.50	0.25	0.50	0.15	0.65
$k_{w_{pm}}$	$w_{pm}/w_{pm,max}$	0.80	0.93	0.80	0.93	0.76	0.94
k_{w_q}	$w_q/w_{q,max}$	0.5	0.9	0.65	0.90	0.3	0.8
h_{pm} (mm)	Fig. 4.4	3.8	9.0	3.8	9.0	2.5	8.0
α_{pm} (deg.)	Fig. 4.4	20	32	20	32	19	26
h_y (mm)	Fig. 4.4	13	25	13	25	13	25
$k_{\alpha_{pm}}$	$\alpha_{pm1}/\alpha_{pm2}$	NA	NA	0.3	0.8	NA	NA
$k_{h_{pm}}$	$h_{pm2}/h_{pm2,max}$	NA	NA	0.4	0.8	NA	NA

2. Using the CE-FEA allows reconstruction of the entire field waveforms through multiple snapshots of magnetostatic FE solutions over a time span corresponding to 60 electrical degrees. The CE-FEA can be up to two orders of magnitude faster compared to the full-fledged time-stepping transient FE solutions [80, 84]. It has been demonstrated to be effective in large-scale design optimizations of PM machines with various rotor layouts and stator winding configurations, including experimental verifications [84, 85, 87, 96, 119].

4.3.2 Optimization Fitness Functions

Since the purpose of the optimization is a comparative study between the search algorithms, the fitness function of the optimization problem can be chosen arbitrarily. In a practical case, the performance metrics of interest can be the machine's active

material cost, power losses, torque ripple, and the degree of demagnetization of the PMs.

1. Active material cost, AMC, is given before by Eq. 2.2.3.

2. The power losses consist of the loss components introduced in 2.1.1, namely copper losses in windings, and the stator core losses including hysteresis and eddy current losses.

3. As mentioned previously, the stator outer diameter and the rotor inner diameter are held constant. Following the calculation of the average torque per unit length, using CE-FEA for the rated current density, the stack-length of the designs are adjusted accordingly to produce the desired average 300 Nm torque at 1500 rev/min. The torque ripple is subsequently determined from the torque profile over a full fundamental ac cycle.

4. The degree of PM demagnetization is characterized by the minimum flux density in the rotor PMs over a complete ac cycle. Demagnetization is considered at the magnet piece level.

The fitness functions of the optimization problem can now be built upon the discussed performance metrics. Two different scenarios of objectives and constraints are pursued for a rigorous comparison between the CMODE and the DE algorithms. In both scenarios, two objectives subjected to two constraints are considered. The first scenario consists of the following two objectives and constraints:

- Objectives: (a) Minimization of AMC, and (b) minimization of power losses

- Constraints: (a) Torque ripple less than 15% , and (b) PM demagnetization less than 70% of the retentivity/remnant B_r

The second scenario is designated as follows:

- Objectives: (a) Minimization of torque ripple, and (b) minimization of power losses

- Constraints: (a) Axial stack length less than 200 mm, 70 mm, and 400 mm for the 48S8P-a, 48S8P-b, and 12S10P machines, respectively, and (b) PM demagnetization less than 70% of B_r

4.4 Comparative Study of the Results

Twelve runs of large-scale design optimizations were carried out on a desktop workstation using 8 simultaneous processing units and 8 ANSYS Maxwell distributed solvers. The machines were optimized for the two aforementioned fitness functions, using either the DE or the CMODE as the stochastic optimizer. The DE consists of 40 generations, each of 80 members. The CMODE starts with an initial generation of 180 members and proceeds with 378 eight-member generations. The number of members in each generation are recommended by references [77, 96] for DE and reference [151] for CMODE. The overall number of design evaluations are approximately equal, 3200 designs in DE versus 3204 designs in CMODE.

In Figs. 4.5 through 4.8, the progress of the optimization process in terms of the conflicting objectives, which are normalized independently for each example machine, is illustrated for the two sets of fitness functions. The number of the function

evaluations, i.e. the sequence of the candidate designs are color coded to provide an indication of the convergence of the design space to the Pareto front vicinity. Furthermore, the designs are differentiated based on their feasibility to provide an indication of the effectiveness of the constraint handling in the two optimization algorithms. It can be seen in these figures that both DE and CMODE successfully converge to the same optimal neighborhood in the design space. However, the concentration of the feasible design candidates in the Pareto front vicinity is larger for CMODE, resulting in a better-defined Pareto front with a lesser number of design evaluations as opposed to DE, also see Figs. 4.9, and 4.10. In addition, the color code in Figs. 4.5 through 4.8 suggests that the convergence to the Pareto front solutions is faster for CMODE.

A comparison between Figs. 4.5 and 4.6, and Figs. 4.7 and 4.8 reveals that the realization of the objectives and constraints is more difficult in the second scenario of the fitness functions. Nonetheless, CMODE is still superior to DE as shown in Figs. 4.7 and 4.8, and in Fig. 4.10.

To further discern the difference between the convergence rates of the two search algorithms, an auxiliary variable is defined as the normalized product of the two objectives in the feasible design candidates. The decay of this quantity over simulation time can serve as an indication of the optimization progress. The mean of this quantity per each generation of optimization is shown in Figs. 4.11, and 4.12. The two previous observations regarding the faster convergence rate of CMODE, and the denser concentration of the feasible design solutions in the vicinity of the Pareto front, are distinctly verified in these figures. As can be seen in Figs. 4.11, and 4.12

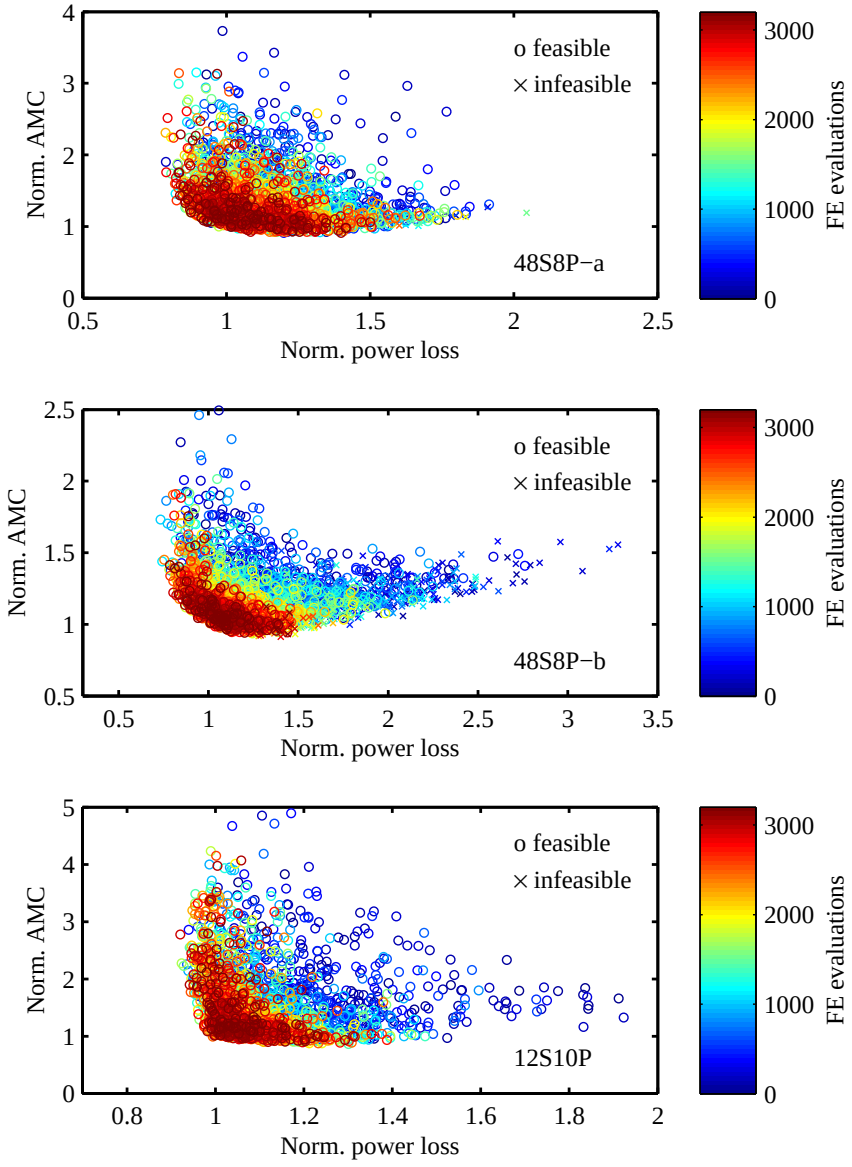

Figure 4.5: The evolution of the optimization process using DE for the three case-study motors under the first scenario.

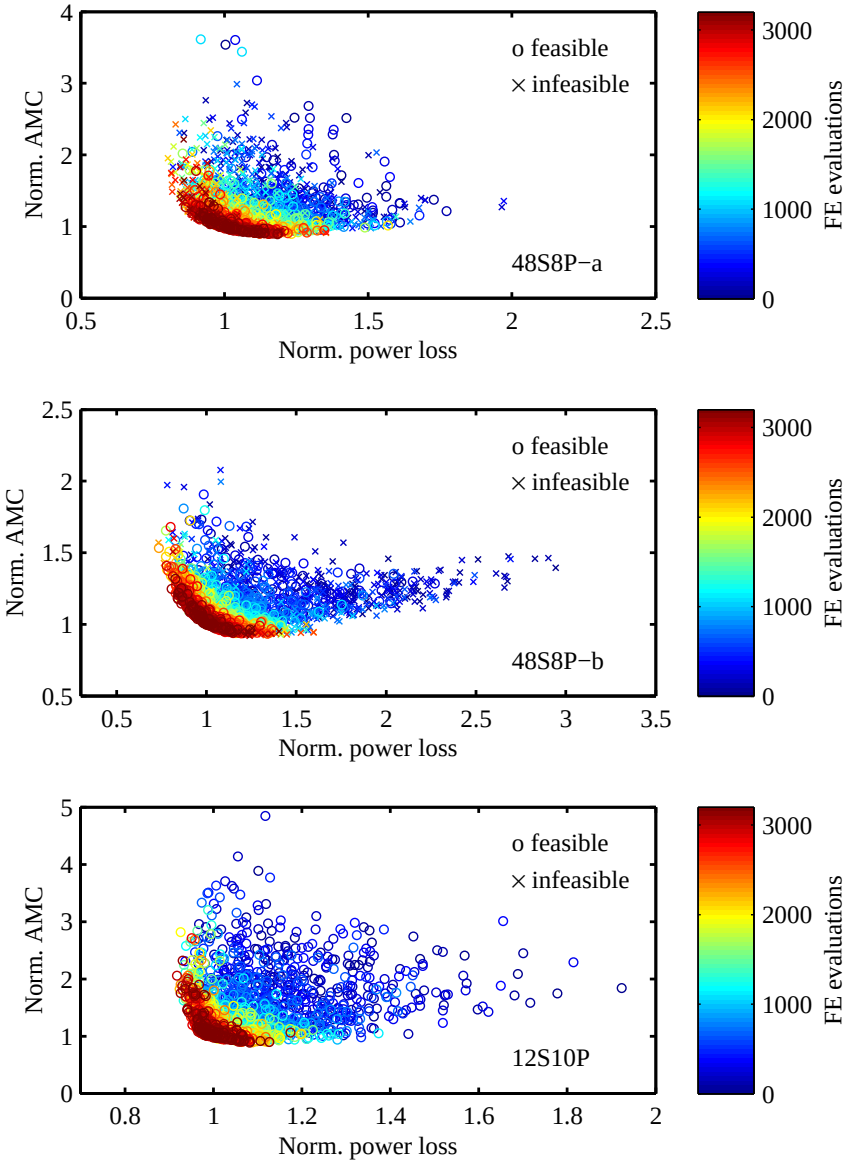

Figure 4.6: The evolution of the optimization process using CMODE for the three case-study motors under the first scenario.

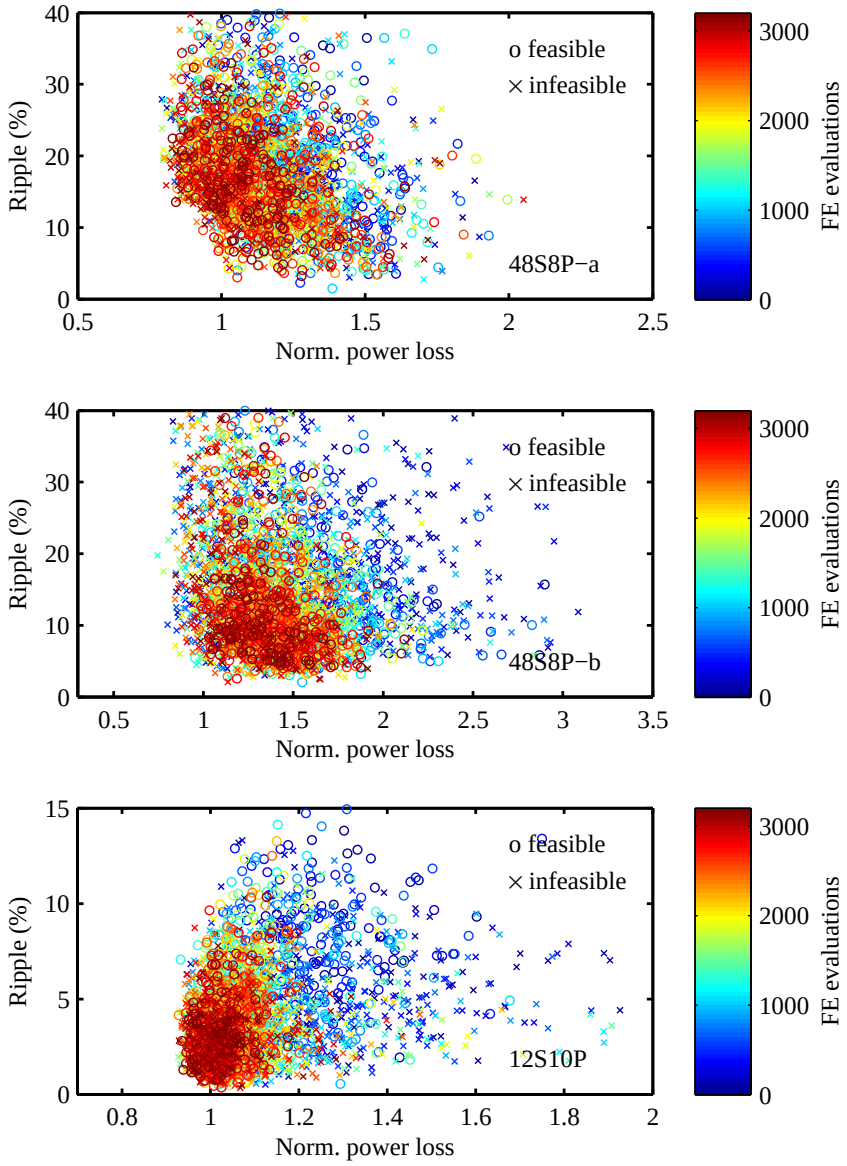

Figure 4.7: The evolution of the optimization process using DE for the three case-study motors under the second scenario.

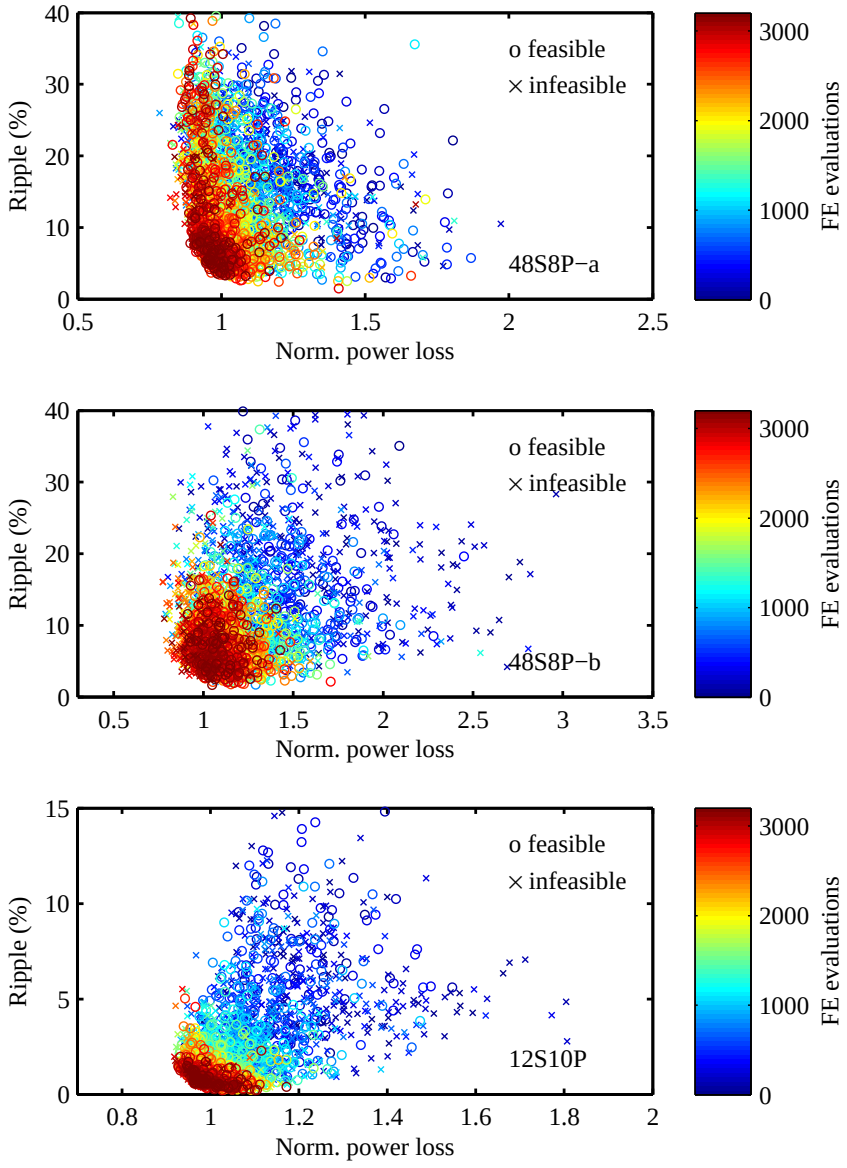

Figure 4.8: The evolution of the optimization process using CMODE for the three case-study motors under the second scenario.

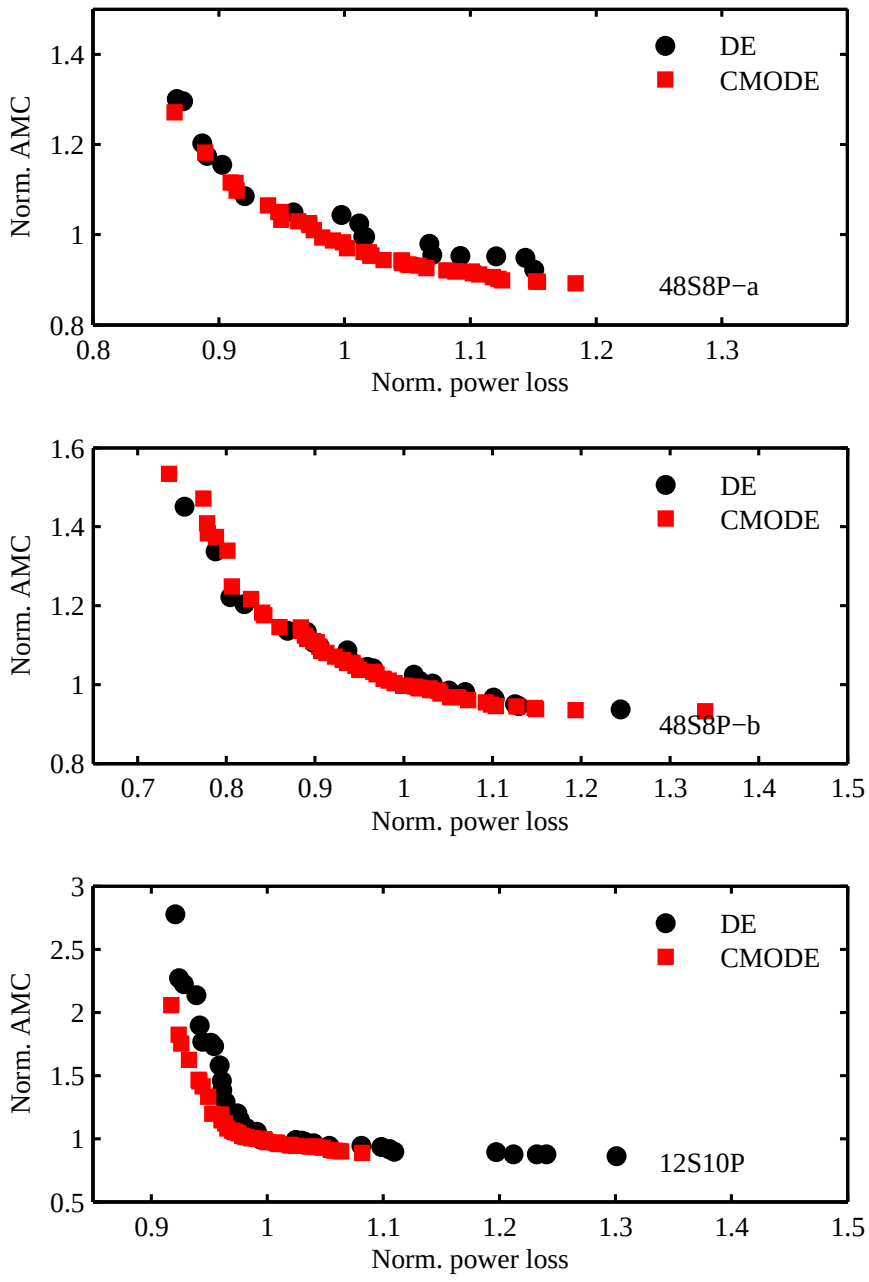

Figure 4.9: Feasible Pareto optimal designs of the two optimization algorithms for scenario 1 of the fitness functions.

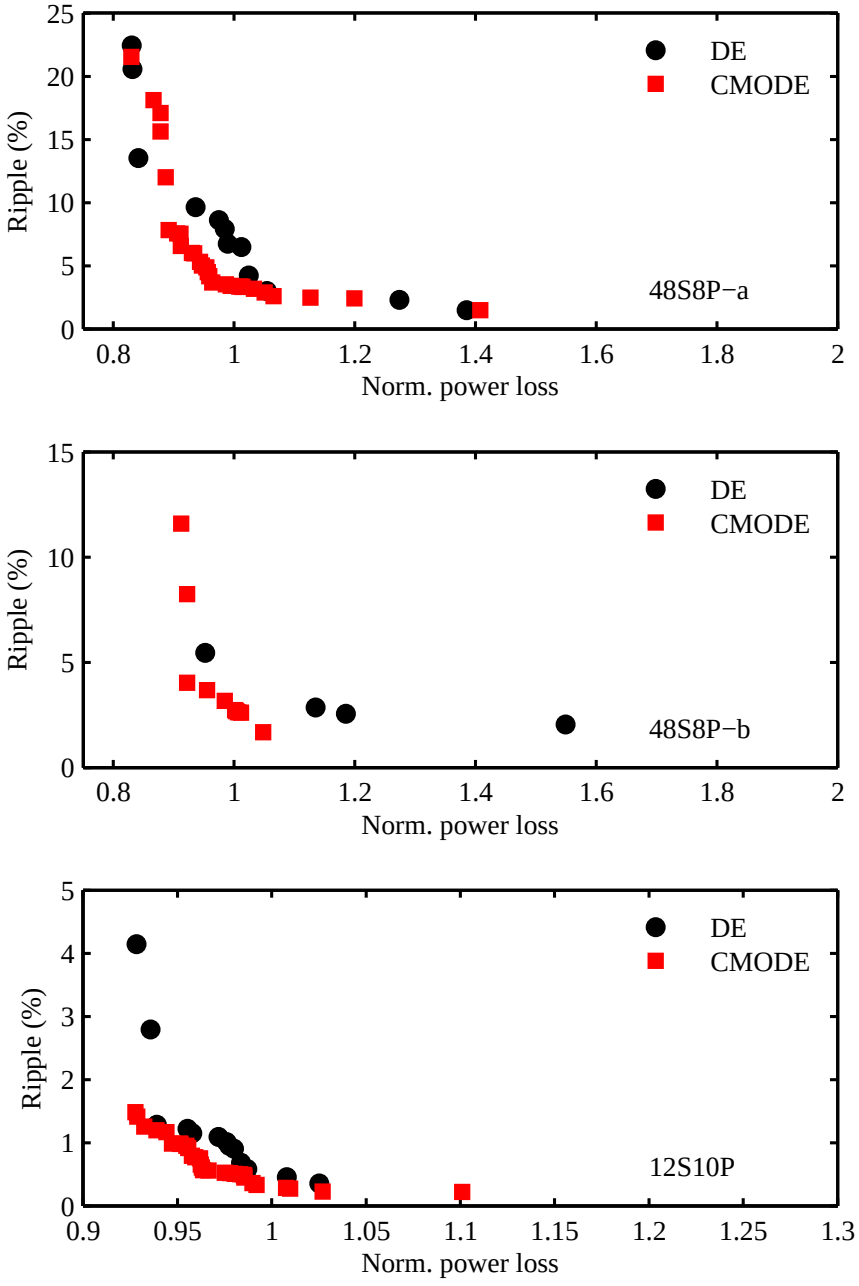

Figure 4.10: Feasible Pareto optimal designs of the two optimization algorithms for scenario 2 of the fitness functions.

the duration and the convergence rate of the two optimization algorithms is very much dependent on the problem definitions. Yet, compared to DE, CMODE reaches steady-state at least twice as fast in all the twelve different case studies.

The optimizations can be continued in steady-state until the Pareto front acquires a well-defined profile. Since the majority of the simulation time is spent to solve the FE-based models, as opposed to the fraction of seconds spent by the optimization search algorithms, the total duration of the optimization procedure is equal for the two algorithms, given that the number of FEs are the same. However, the CMODE algorithm is able to produce a large number of optimal designs in contrast to the DE algorithm, for which the simulation needs to be continued.

As shown in Figs. 4.9 and 4.10, and according to Table 4.2, CMODE also provides a larger number of optimal solutions in the immediate vicinity of the Pareto front, resulting in CMODE's higher definition and better diversity of Pareto front solutions.

To quantitatively compare the Pareto fronts of the two optimization algorithms, the hypervolume indicator [160] is calculated. The hypervolume measures the dominance of the Pareto front solutions with respect to a reference point in the design space [161]. Here, it is calculated with respect to the maximum objective values for each set of Pareto front solutions. The normalized hypervolumes of the two optimization algorithms in Fig. 4.13 clearly indicates the persistent superiority of CMODE in terms of diversity and quality of generated Pareto fronts.

The two search algorithms are also compared in terms of their constraint handling capability in Table 4.3. It can be seen that the overall number of the feasible design candidates, which pass the two constraints imposed either on the torque ripple

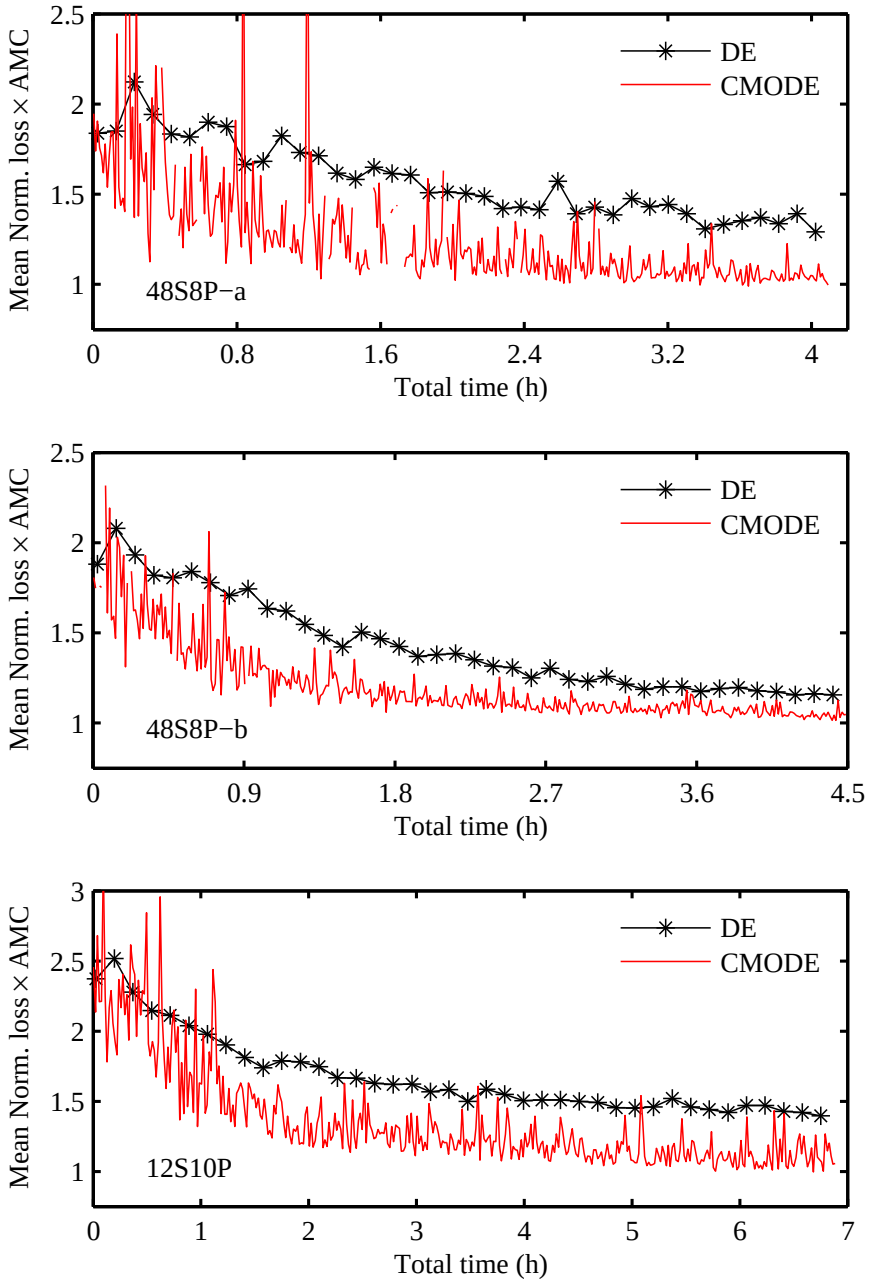

Figure 4.11: Convergence of the feasible design candidates for the three case-study motors in terms of $loss \times AMC$ for scenario 1.

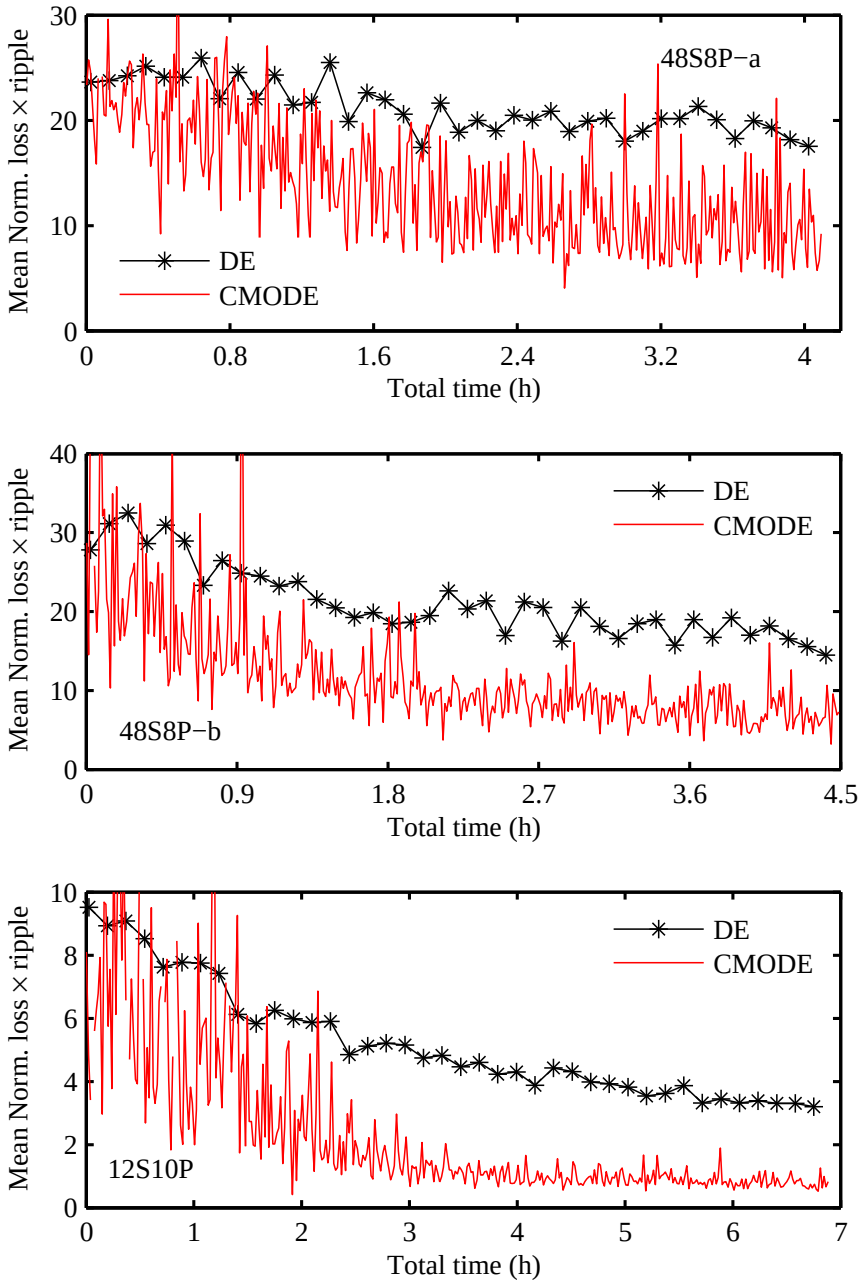

Figure 4.12: Convergence of the feasible design candidates for the three case-study motors in terms of *loss* × *ripple* for scenario 2.

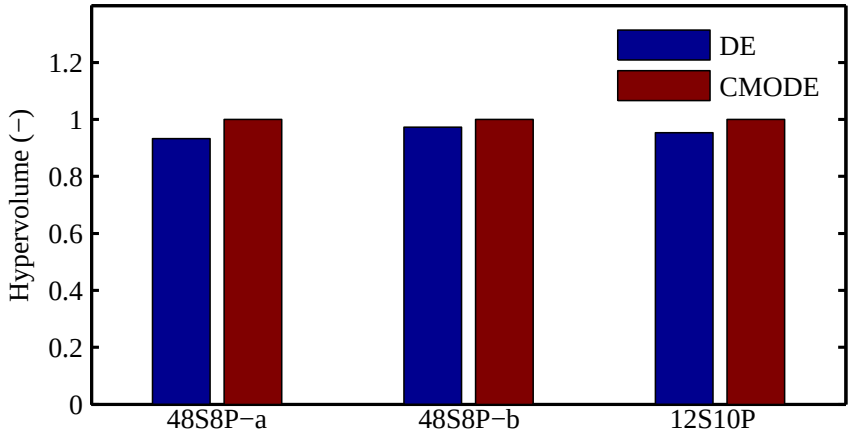

(a) Scenario 1

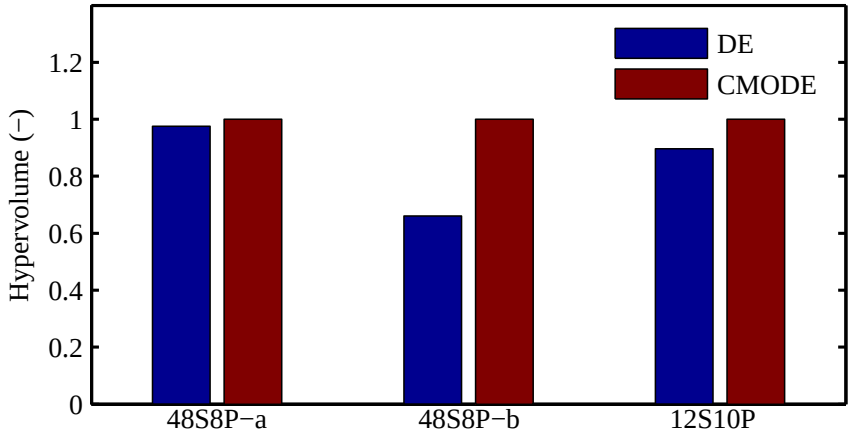

(b) Scenario 2

Figure 4.13: The normalized hypervolumes of the Pareto fronts generated by DE and CMODE for the two scenarios of fitness functions.

and on the PM demagnetization in the first scenario, or on stack length and PM demagnetization in the second scenario are higher in CMODE. The effective constraint handling of the CMODE algorithm, in addition to the denser designs in its Pareto front vicinity, translates into its superior computational efficiency when compared to DE.

Typical cross-sections of the optimal design solutions and their field plots for each scenario are provided in Fig. 4.14.

Table 4.2: Comparison of the number of the feasible Pareto optimal designs between DE and CMODE.

Machine	Scenario 1		Scenario 2	
	DE	CMODE	DE	CMODE
48S8P-a	17	42	12	28
48S8P-b	24	52	4	10
12S10P	34	41	13	30

Table 4.3: Comparison of the number of total feasible design candidates between DE and CMODE.

Machine	Scenario 1		Scenario 2	
	DE	CMODE	DE	CMODE
48S8P-a	1136	1189	1780	2306
48S8P-b	1500	2256	1438	1731
12S10P	3162	3199	1387	1849

Because of the sequential processing of generations in synchronous EAs such as the above implementations of DE and CMODE, the optimum number of distributed solvers is equal to the number of members in each generation. It should be emphasized that in the foregoing comparison between DE and CMODE, eight distributed solvers corresponding to the number of members in each generation of CMODE were utilized. This number of parallel solvers can be readily implemented on a single desktop computer with limited processing power and with a minimum number of software licenses, e.g. eight processing cores/threads and licenses in this investigation. The CMODE algorithm will maintain the discussed superiorities in comparison to DE if a lesser number of distributed solvers were to be used, which is usually the case for smaller motor design companies/groups. However, for implementation on a large number of distributed solvers, such as in HPC systems, the speed of simulations in

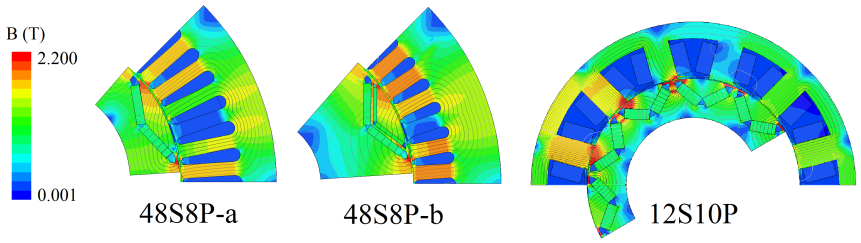

(a) Scenario 1

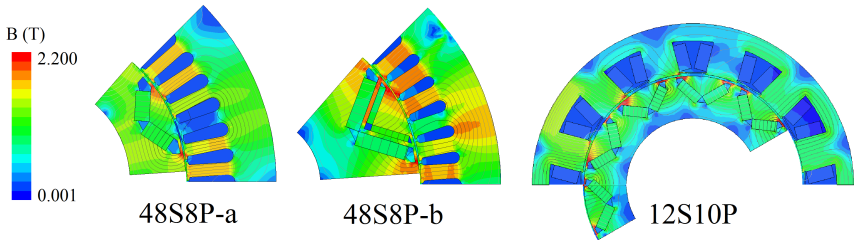

(b) Scenario 2

Figure 4.14: Typical optimized cross-sections and the field plots of the studied motors for the two scenarios of fitness functions.

DE as a standard EA will linearly increase up to the number of members in each generation, whereas the additional computational resources cannot be fully utilized in the CMODE algorithm as a steady state EA, although CMODE still benefits from a faster convergence rate per generation and a more effective constraint handling mechanism. This highlights the importance of choosing the proper optimization algorithm in reference to the available computational resources, a topic that has been the focus of this chapter by introducing CMODE for implementation on desktop computers. Under these premises, the performance of CMODE is expected to surpass other standard population-based multi-objective EAs which have been compared with DE in the literature.

4.5 Summary

A new CMODE-type algorithm was developed for design optimization of electric machines with limited computational resources. In the case-study IPM motors with distinctive stator winding configurations, rotor layouts, and electrical loadings, CMODE consistently demonstrated a faster convergence, at least twice as fast as the convergence rate of DE, a higher definition of Pareto front, and a better constraint handling in comparison with DE. These can be attributed to the distinctive population evolution model of CMODE, and its effective constraint handling method, in which the degree of constraint violation is being minimized simultaneously with other objectives of the optimization problem.

In design problems with more than one constraint, such as the case-study examples in this chapter, it might be required to introduce particular weights in the summation operation given in the definition of the degree of constraint violation. These weights are designated so as to make the violations comparable between all the constraints. This can be accomplished, for example by normalizing such violations with respect to their expected range of variations. The assignment of the weights requires expert knowledge and particular attention in the implementation of CMODE for electric machinery design problems.

CMODE's fast convergence and fewer number of simultaneous function evaluations makes it best suited for implementation in a state-of-the-art multiprocessor desktop computer with a lesser number of software licenses, as opposed to the high-end HPC systems.

CHAPTER 5

DRIVE-CYCLE PERFORMANCE OPTIMIZATION

In Chapters 2 and 3, the need for including the entire range of operation in the optimization algorithm was demonstrated. In this respect, this chapter presents a large-scale FE model-based design optimization algorithm for improving the drive-cycle efficiency of PM synchronous machines with wide operating ranges such as those used in traction propulsion motors. The load operating cycle is efficiently modeled by using a systematic clustering method to identify the operating points representing the high-energy-throughput zones in the torque-speed plane. The machine performance can be evaluated over these cyclic representative points using the previously introduced CE-FEA approach which is upgraded to include both constant torque and extended speed regions in the evaluation of the machine performance metrics. In contrast to the common practice, which aims at enhancing the rated performance, the entire range of operation is considered in the present design optimization method. Practical operational constraints imposed by the voltage and current limits of the motor-drive system, excessive PM demagnetization, and torque ripple are accounted for during the optimization process. The convergence to the optimal design solutions is expedited by utilizing the new stochastic optimizer described in Chapter 4. The developed design algorithm is applicable to any configuration of sine-wave driven PM and synchronous reluctance motors over any

conceivable load profile. The design optimization algorithm is developed in this Chapter, followed by the case-study investigations in the next chapter.

5.1 Introduction

As was elaborated in the previous chapters, depending on the particular application, the CE-FEA based design optimization techniques aim at realizing a set of objectives under certain performance constraints described/embedded in the optimization fitness function [84, 85, 88, 96, 119, 162]. In line with common practice, the CE-FEA based methods evaluate the associated fitness function at the rated load point, i.e. base speed and rated torque without directly incorporating the efficiency requirements of the extended speed range operation into the optimization fitness function.

One of the pioneering FE-based design optimization efforts for improving the field weakening performance was introduced in [92] where an IPM motor was optimized for maximizing electromagnetic torque at base speed and normalized characteristic current. Similarly, the idea of equality of characteristic current, I_{CH}, with rated current, I_R, was introduced as an additional objective for optimization of IPM motors for enhanced field weakening performance [95, 96]. In [99], the following objectives were concurrently pursued: maximization of the torque at base and at maximum speeds, and minimization of the weight. Although the equality of I_{CH} and I_R was not directly introduced in the fitness function, excluding efficiency from the objectives resulted in an optimized design in which the two currents were equal [99].

The equality of I_{CH} and I_R improves the torque production capability. However,

when the non-linear and lossy nature of the machine is considered, from the efficiency standpoint, congruity of I_{CH} and I_R cannot be the ideal criterion for constant power operation [97, 98]. This will be described in more detail later in this chapter. In [100], maximizing the torque and efficiency at the base and maximum speeds were pursued to simultaneously improve the efficiency and operation range of a concentrated flux IPM motor.

In more recent studies, researchers have attempted to optimize the machine performance for a specific drive cycle [105, 106, 163, 164]. In [105, 106], a method known as the cyclic representative points was implemented to efficiently model a target driving cycle by a finite number of torque versus speed points. These points were derived based on the energy distribution function specifically calculated for a given vehicle model and driving cycle. Those investigators subsequently performed the optimization over these cyclic representative points. However, the selection criterion of these points requires a more systematic procedure for identification of the high-energy-throughput zones of the load energy distribution function, especially when more demanding operating cycles are desired. Furthermore, since a large-scale optimization was not pursued, the design space was not fully explored.

Most recently, in [107] a propulsion PM assisted synchronous reluctance (SyR) motor was optimized using the relatively subjective drive cycle modeling method introduced in [105, 106]. Nonetheless, because of the computationally demanding nature of the adopted approach, a limited number of design variables were treated, i.e. tooth width and slot height. Furthermore, the torque ripple was not included in the optimization process.

In this Chapter, the large-scale design optimization of PM machines for a specific load profile is investigated. The CE-FEA approach is upgraded to enable fast and high fidelity performance evaluation of the design candidates at any load operating point residing either in the constant torque or extended speed regions. To further increase the computational efficiency of the design optimization, the new stochastic CMODE-type search algorithm presented in Chapter 4 is adopted.

The presented design optimization method is applicable to interior and surface-mounted PM motors with various slot-pole combinations and rotor magnet layouts, SyR motors, and in essence any PM motor which, through proper drive controls, is energized by sinusoidal terminal currents. Moreover, the design optimization can be performed over any conceivable motor operating cycle, while taking into account the practical operational constraints imposed by the supply voltage and/or the motor current limits [165].

Accordingly, in this chapter, the efficient modeling of the motor load profile is explained first. The control algorithm for derivation of the forcing function for FE analysis at any load point is described next, followed by the optimization algorithm, and a discussion on defining appropriate objectives and constraints. Using the optimization methodologies in this chapter, the optimization of two example traction motors will be presented in Chapter 6.

5.2 Efficient Modeling of the Motor Load Profile

In this section, a systematic method, as an alternative to the method suggested in [105, 106], is presented for efficient modeling of a given operating cycle using a limited number of load points.

5.2.1 Energy Distribution Over the Torque-Speed Plane

The first step of the optimization process is the identification of the motor torque and speed profiles for the specific application, which by itself is a demanding task and might require extensive data collections, field studies, and system modeling. In the case of traction motors, which is adopted in this dissertation as a challenging design example, numerous factors such as the drivetrain technology, transmission system, energy management unit, driving habits, terrain, and the vehicle operating mode determine the motor propulsion requirements.

To address the above mentioned complexities in obtaining the motor torque and speed profiles, here, the Advanced Vehicle Simulator (ADVISOR) developed by the National Renewable Energy Laboratory (NREL) is used. Two hybrid vehicles, which were previously discussed in Chapter 2 with regards to the distribution of the load operating points in their torque-speed plane, are modeled using ADVISOR, namely, the Toyota Prius Gen. 2, and the Honda Insight Gen.1.

Furthermore, the distinctive propulsion requirements of different driving cycles are illustrated by modeling these vehicles over two US driving cycles, namely, the Urban Dynamometer Driving Schedule (UDDS), and the Highway Fuel Economy

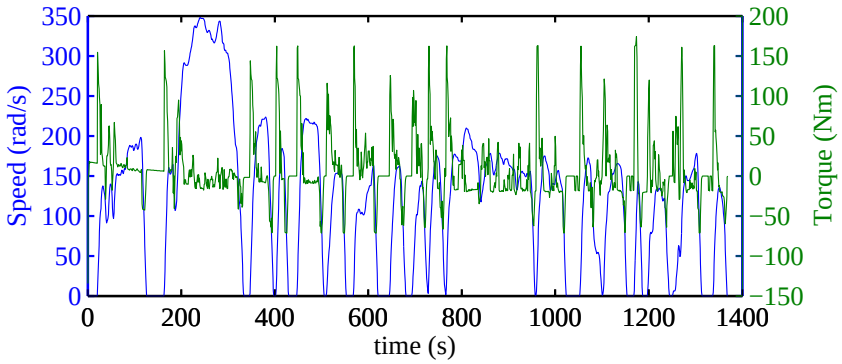

(a) UDDS

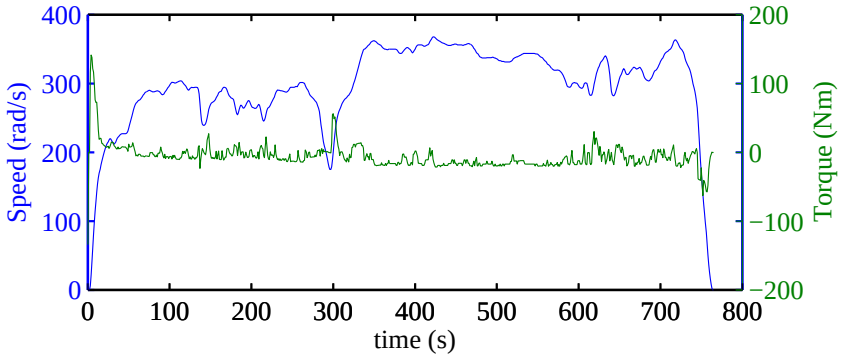

(b) HWFET

Figure 5.1: The Toyota Prius Gen 2. motor load profiles.

Test Driving Schedule (HWFET). The resulting load profiles of the example traction motors under the aforementioned two studied driving cycles are shown in Figs. 5.1 and 5.2.

For each vehicle, the wide variations of the motor torque and speed profiles based on the driving cycles shown in Figs. 5.1 and 5.2 reveal the challenges involved in designing a motor for efficient and reliable operation at all torque and speed levels. Furthermore, by comparing the motor load profiles between the two vehicles in these figures, it becomes obvious that even for this specific traction propulsion motor application, the preferred motor design and specifications, such as slot-pole

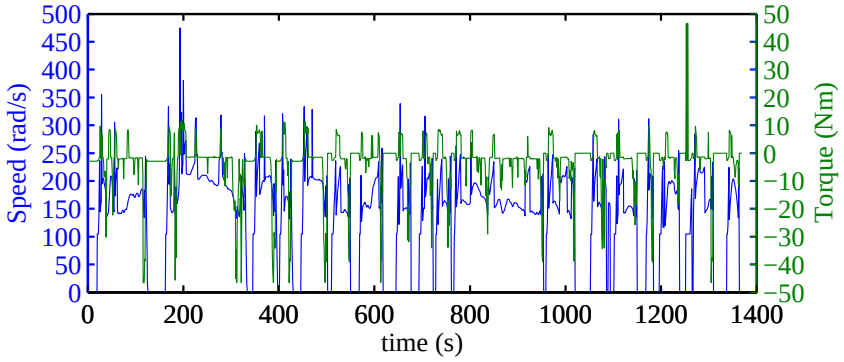

(a) UDDS

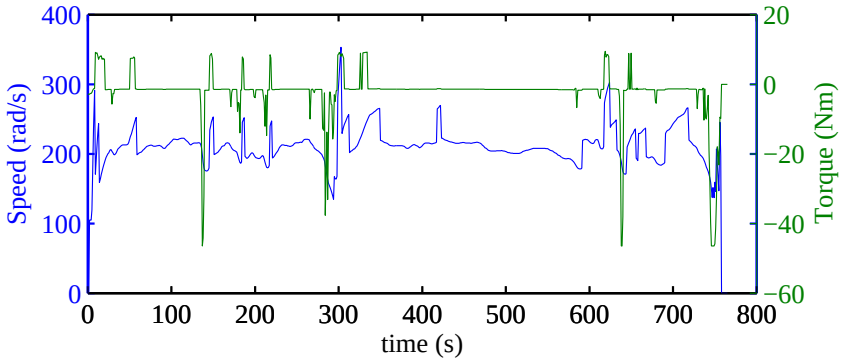

(b) HWFET

Figure 5.2: The Honda Insight Gen. 1 motor load profile.

combination, rotor and stator layouts, rated operating conditions, etc. are vehicle-dependent and one panacea design solution does not exist.

This observation further underscores the need for a systematic design optimization methodology such as the one developed in this dissertation which can accommodate the aforementioned factors, and can also provide a simulation platform for evidence-based comparison of the alternative design solutions.

The motor continuous torque and base speed should be characterized with reference to the load profiles. The continuous torque from the thermal limit

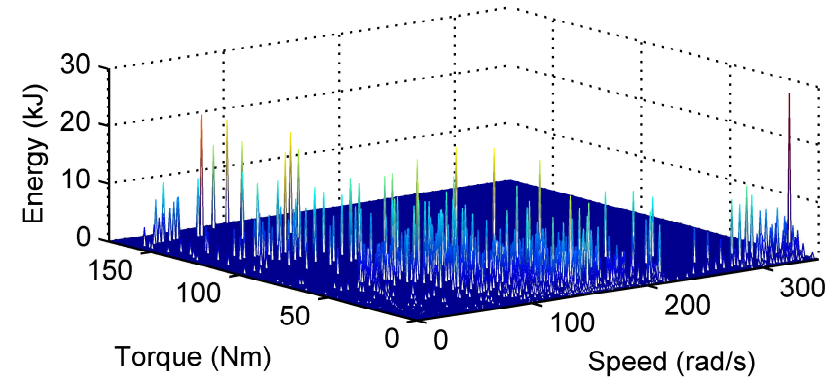

(a) UDDS

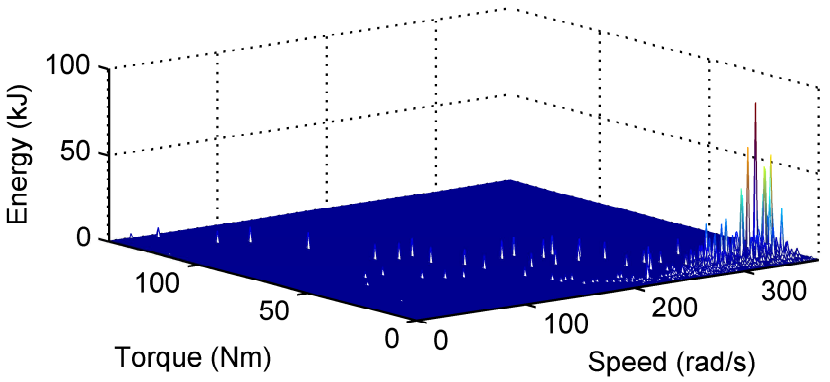

(b) HWFET

Figure 5.3: Toyota Prius Gen. 2 motor output energy over torque-speed plane.

standpoint can be determined based on the root mean square of the torque profiles:

$$T_{rms} = \sqrt{\frac{1}{(t_2 - t_1)} \int_{t_1}^{t_2} T(t)^2 dt} \tag{5.2.1}$$

The determination of the base speed, ω_{base}, and optimum speed ratio, which is the ratio of maximum speed, ω_{max}, to ω_{base}, depends on many figures of merit including the system power specifications, total weight, losses, etc. Previous studies have indicated that this optimum speed ratio falls within a range of 3 to 4 for PM synchronous motors used in propulsion applications [166, 167].

Using the motor output torque and speed profiles, the absolute value of the

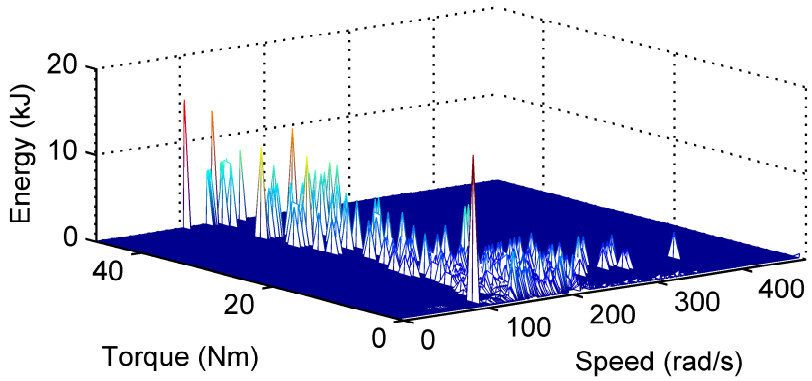

(a) UDDS

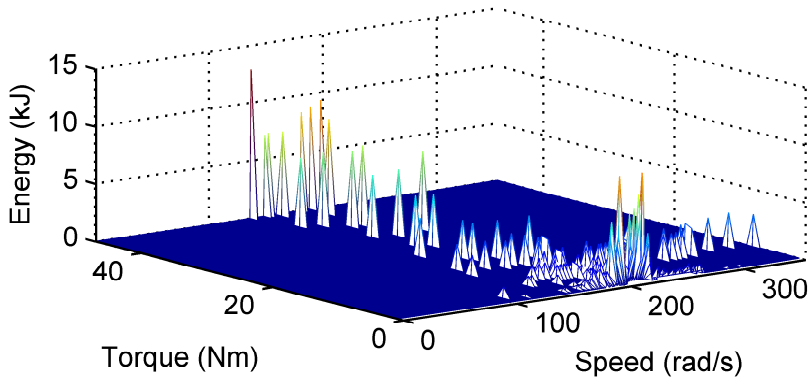

(b) HWFET

Figure 5.4: Honda Insight Gen. 1 motor output energy over torque-speed plane.

energy distribution over the torque-speed plane, obtained from the torque times speed product and the corresponding time spent at this condition, can be calculated as shown in Figs. 5.3 and 5.4.

The motor operating regions, constant torque and constant power, can be recognized in the distribution of the load points in Figs. 5.3 and 5.4. Once again, the considerable variations of the load energy distribution functions based on the driving cycles and the vehicles should be pointed out to the reader.

5.2.2 Cyclic Representative Points

Ideally, the motor performance over each individual load point shown in Figs. 5.3 and 5.4 needs to be considered in its drive-cycle performance evaluation. However, for obvious computational reasons, the swarm of the operating points in the load energy distribution needs to be modeled by a limited number of so-called cyclic representative load points which should convey the main features of the driving cycle in a computationally efficient manner. Specifically, these representative points should indicate (a) the speed and torque at the high-energy-throughput operating zones of the torque-speed plane, and (b) the energy weights associated with these zones which is the measure of significance of these zones in the evaluation of the motor drive-cycle efficiency.

In [105, 106], the idea of computationally efficient modeling of the energy distribution by a small number of representative load points was implemented on an example pure electric vehicle operated over New European (NEDC) and Artemis driving cycles. In their approach, for characterization of these representative points, the investigators first partitioned the torque-speed plane according to the locations of the high-energy-throughput regions. Subsequently, the so-called "centers of gravity" in these regions were calculated according to Eq. (5.2.3) through Eq. (5.2.4):

$$E_i = \sum_{j=1}^{N_i} E_{ij} \tag{5.2.2}$$

$$\omega_i = \frac{1}{E_i} \sum_{j=1}^{N_i} E_{ij}\omega_{ij} \tag{5.2.3}$$

$$T_i = \frac{1}{E_i} \sum_{j=1}^{N_i} E_{ij}T_{ij} \tag{5.2.4}$$

where E_{ij}, ω_{ij}, and T_{ij} are respectively the energy, angular speed, and torque associated with each load point in region i, N_i is the number of load points in region i, and ω_i and T_i indicate the center of gravity of the region, which are identified as the cyclic representative points. The main disadvantage of this approach for identification of the representative load points is the subjective/observation-based selection of the regions, as opposed to a mathematical energy minimization-based approach, which questions the optimality of the discretization process, and also poses an impediment to its application for more sophisticated energy distribution functions.

Here, a systematic method of quantization that is popular for cluster analysis in data mining known as the k-means clustering algorithm [168] is introduced for modeling the load operating cycle. Using this method, all the n observations in the energy function $(x_1, \ldots, x_n)$ can be partitioned into $k \leq n$ clusters $(s_1, \ldots, s_k)$ in which each observation belongs to the cluster with the nearest mean $(m_1, \ldots, m_k)$, serving as the prototype of the cluster. The standard algorithm used here has two iterative steps, the assignment step and the update step.

In the first step, each observation, x_p, is assigned to the cluster, s_i, with the nearest mean, m_i, according to Eq. (5.2.5):

$$s_i^{(t)} = \{x_p \mid\mid x_p - m_i^{(t)} \mid\mid^2 \leq \mid\mid x_p - m_j^{(t)} \mid\mid^2 \forall j, \quad 1 \leq j \leq k\} \tag{5.2.5}$$

where t is the iteration count number. The means for the initial iteration, m_i^0, can be chosen randomly.

In the update step, the centroids of the observations in the new clusters, m_i^{t+1}, given in Eq. (5.2.6) are designated as the new means. These assignment and update

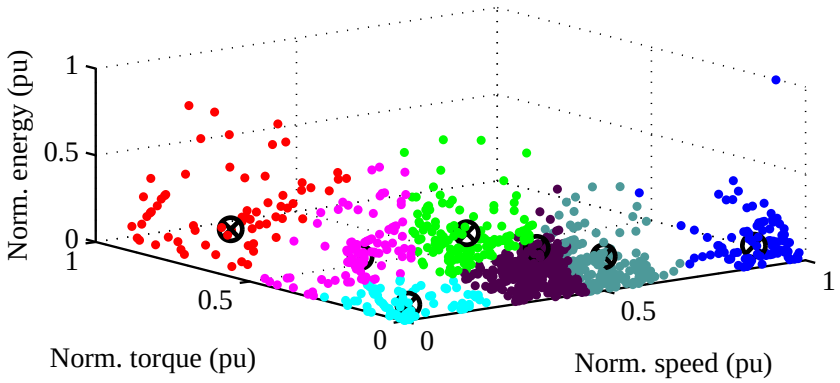

(a) UDDS

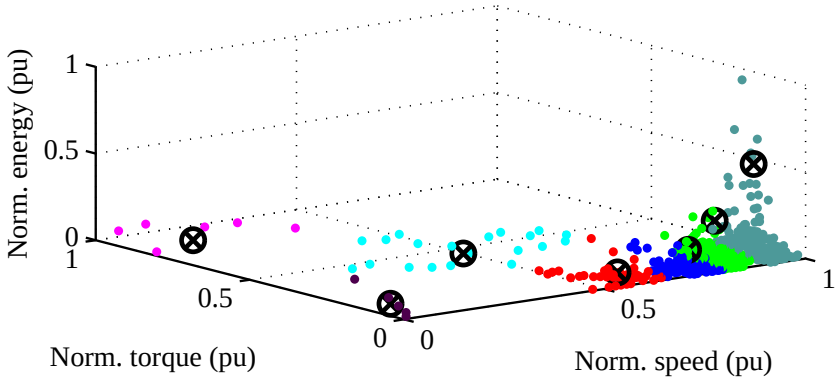

(b) HWFET

Figure 5.5: Cyclic representative points of Toyota Prius Gen. 2 motor output energy over torque-speed plane.

steps are iteratively repeated until convergence is reached, i.e. until the assignments of m_i^t in Eq. (5.2.5) do not change.

$$m_i^{t+1} = \frac{1}{\mid S_i^{(t)} \mid} \sum_{x_j \in S_i^t} x_j \tag{5.2.6}$$

Using the k-means algorithm, first the normalized energy distribution function is partitioned into a limited number of clusters, the means of which yield the representative torque-speed point of that cluster. Thereafter, the energy weights of each representative point are computed based on the ratio of the average energy

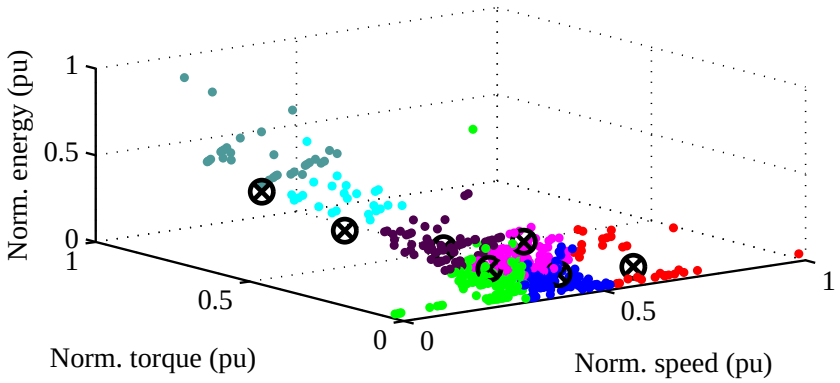

(a) UDDS

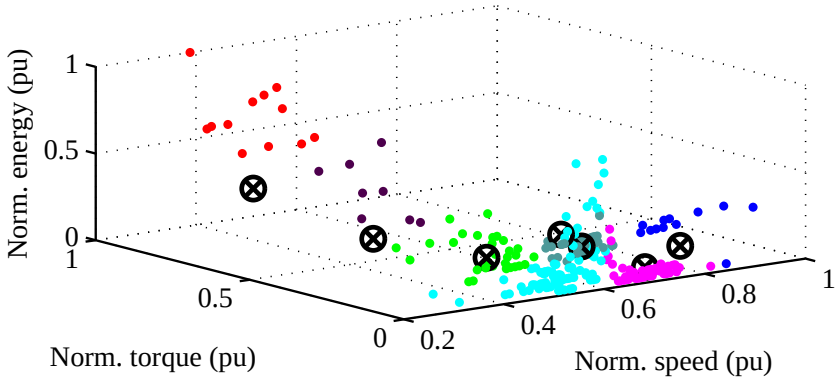

(b) HWFET

Figure 5.6: Cyclic representative points of Honda Insight Gen. 1 motor output energy over torque-speed plane.

consumed in the corresponding cluster to the total energy associated with the drive-cycle.

The cyclic representative points and their associated energy weights for the previously discussed motors and operating cycles are shown in Figs. 5.5 and 5.6. It can be seen in these figures that the distribution of the representative load points and their energy weights vastly vary with respect to the vehicle model and motor operating cycle, suggesting once again that an optimal design which suits one case

might be suboptimal for the other cases.

Although the k-means clustering algorithm is a "computationally difficult" problem, which requires use of iterative optimization algorithms for obtaining a solution, it is only run once at the initialization stage of the drive-cycle optimization to yield the representative load points. The number of clusters can be determined based on the sum of the distances of the load points to their corresponding cluster means, as defined in Eq. (5.2.7).

$$Sum of distances = \sum_{i=1}^{k} \sum_{x_j \in S_i^t} ||x_j - m_i||^2 \tag{5.2.7}$$

This quantity is calculated for the previously discussed vehicles and driving cycles over a wide range of cluster numbers as shown in Fig. 5.7. For these example distributions of load points, it appears to this investigator that a "happy balance" between accuracy and computational speed points to a choice of seven representative load points corresponding to the seven clusters shown in Figs. 5.5 and 5.6. A larger number of clusters would provide a marginally more accurate approximation of the energy distribution function at the cost of diminished computational efficiency, since the performance evaluation is carried out over every individual cyclic point.

5.3 Performance Evaluation at Representative Points

After the determination of the cyclic representative points, the motor performance should be evaluated over them since most of the power is consumed or generated at these points. Characterization of the motor performance at the cyclic representative

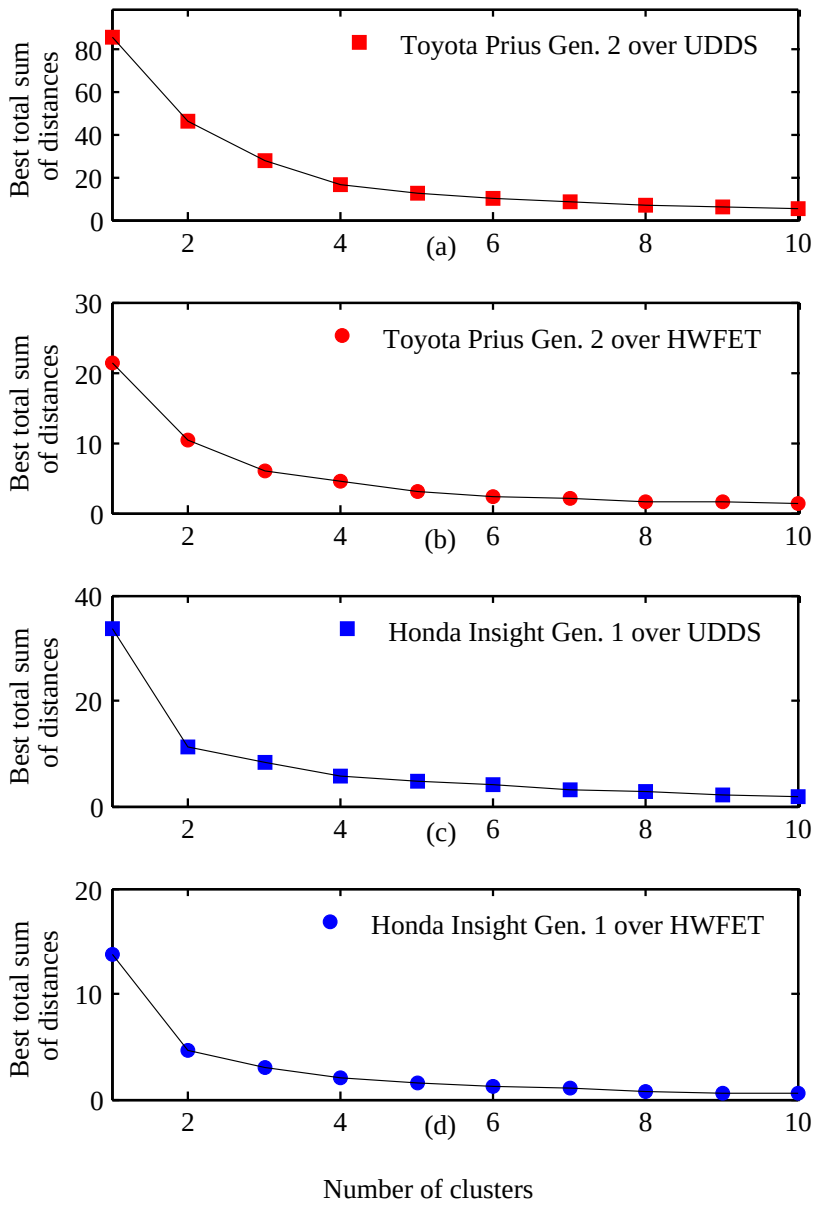

Figure 5.7: The best sum of the distances of the load points to their corresponding cluster means versus the number of clusters.

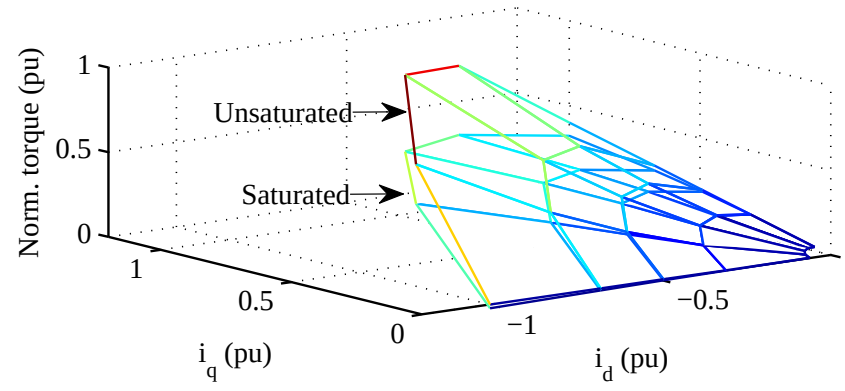

(a) Torque

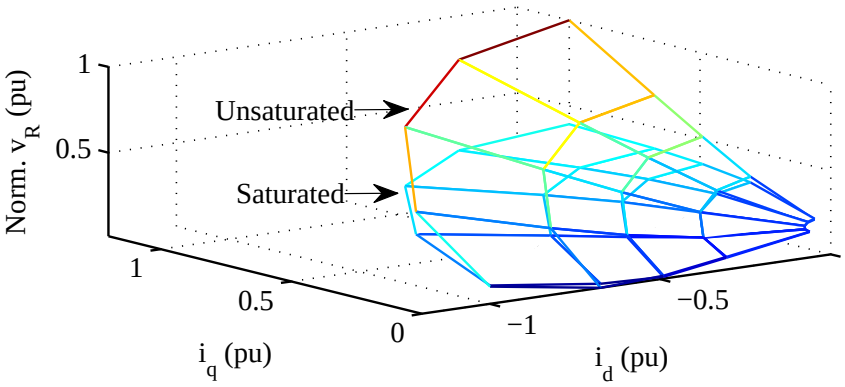

(b) Induced voltage

Figure 5.8: Effects of saturation and cross-saturation in prediction of torque, and induced voltages over the full range of excitation current.

points, which can be located anywhere in the torque-speed plane, requires careful control of the machine excitation current for production of maximum torque per ampere (MTPA) under performance constraints imposed either by the motor rated current in the constant torque region, or by the maximum output voltage of the supply, rated current, and PM demagnetization in the constant power region.

To characterize the motor performance using high fidelity magnetostatic FEA simulations, the magnitude and phase angle of the stator winding excitation current

needs to be determined for each individual design candidate at each representative load point. Accurate estimation of the optimum current density and its angle of advance from the q-axis is imperative in order to ensure a reliable performance comparison between the design candidates. Here, it should be pointed out that the linear inductance-based models for IPM machines fail to accurately predict the machine behavior when saturation and cross-saturation phenomena are prevalent [163, 169]. This issue is addressed next.

To demonstrate the inaccuracy of the linear-parameter models in predicting the performance of the high-power-dense PM motors, in Fig. 5.8, the produced average steady state torque, T_{avg}, and the fundamental value of the total induced phase voltage in the stator windings at steady state and under a constant speed, v_R, of the Toyota Prius IPM motor are computed and compared, over the full range of excitation current for motoring operation, between the linear parameter model given in Eq. (5.3.1) and Eq. (5.3.2), and the actual values obtained from FEA using Eq. (5.3.3) and Eq. (5.3.4).

The contributions of the stator winding resistance to the terminal voltage, and the reduction of torque due to core losses are similar in both cases and are not reflected in these equations and figures.

$$T_{avg} = \frac{3}{2}\frac{P}{2}((L_d i_d + \lambda_{PM}) i_q - L_q i_q i_d) \tag{5.3.1}$$

$$v_R = \omega_e \sqrt{((L_d i_d + \lambda_{PM})^2 + (L_q i_q)^2)} \tag{5.3.2}$$

$$T_{avg} = \frac{3}{2}\frac{P}{2}(\lambda_d i_q - \lambda_q i_d) \tag{5.3.3}$$

$$v_R = \omega_e \sqrt{(\lambda_d^2 + \lambda_q^2)} \tag{5.3.4}$$

where P is the number of poles, ω_e is the motor speed in electrical $rad/s.$, and L_d and L_q are respectively the d-axis and q-axis inductance values derived based on three FEA simulations with different current vectors. That is, the PM flux-linkage, λ_{PM} is obtained at zero current, followed by the calculation of $L_d = (\lambda_d - \lambda_{PM})/i_d$ and $L_q = \lambda_q/i_q$ for small values of excitation current.

It can be seen in Fig. 5.8, that the torque and induced voltage estimation errors steadily creep up as the current density increases. These errors are more evident along the q-axis due to higher permeance of the q-path, and due to the demagnetizing effect of the d-axis component of the armature current. Hence, a new numerical method with built-in control to conform to the motor-drive system voltage and current ratings is developed here, see Fig. 5.9.

For each design candidate, CE-FEA with reduced a number of solutions is performed for various stator excitation currents covering the entire range of motoring operation. The resulting d- and q-axes flux-linkages, λ_d and λ_q, are sampled as the current vector sweeps through the second quadrant of the d-q plane, and are stored in corresponding look-up tables. Subsequently, the average value of the steady-state torque, and the fundamental components of the induced voltage in the stator winding can be calculated using Eq. (5.3.3) and Eq. (5.3.4), respectively. At this point, the machine stack length, and the torque and induced voltage look-up tables are scaled proportionally for production of the required torque at the base speed corresponding to a current density of J_{max}, which is assumed to be the same for all the design candidates and is determined with reference to the cooling system specifications. The maximum torque per unit stack length corresponding to the maximum current density

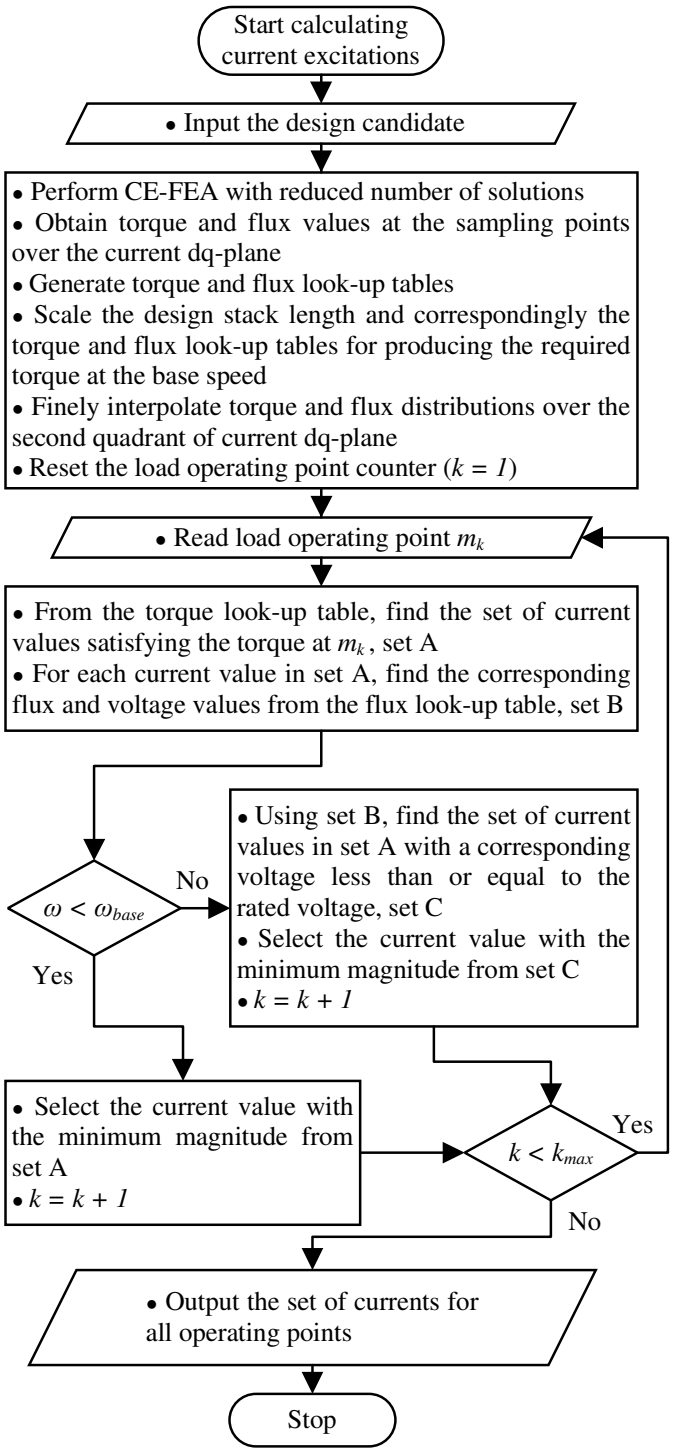

Figure 5.9: Developed method for derivation of the stator winding currents at every load point for time-stepping magneto-static FEA. Optimal control is ensured for constant torque and flux weakening operation.

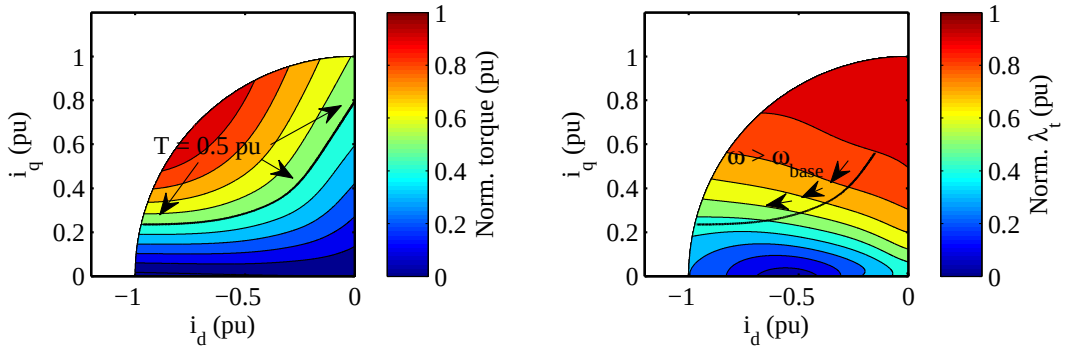

(a) Set of currents which meet the torque requirements

(b) Set of currents which meet the voltage requirements

Figure 5.10: Process of derivation of the excitation current for a typical load point.

in the stator winding, J_{max}, indicates the torque production capability of the design candidate.

After generating the look-up tables and scaling them to produce the required torque at the base speed, the process of determination of the excitation current can be started. Instead of fitting a polynomial equation on the torque and induced voltage samples and using Bisection and Newton-Raphson methods to determine the d- and q-axes currents for MTPA or field weakening operation as was proposed in [89], the optimal excitation current for each load operating point is selected through the simple algorithm shown in Fig. 5.9. Accordingly, for each load point, first the set of current vectors, i_d and i_q, producing the required torque are identified, set A. The flux values associated with these current vectors are also stored in set B. If the rotation speed of the load point is less than the base speed, the vector with the smallest magnitude from set A is chosen as the optimal current vector for MTPA operation. Otherwise, if the rotation speed is greater than the base speed, the set of current vectors that do

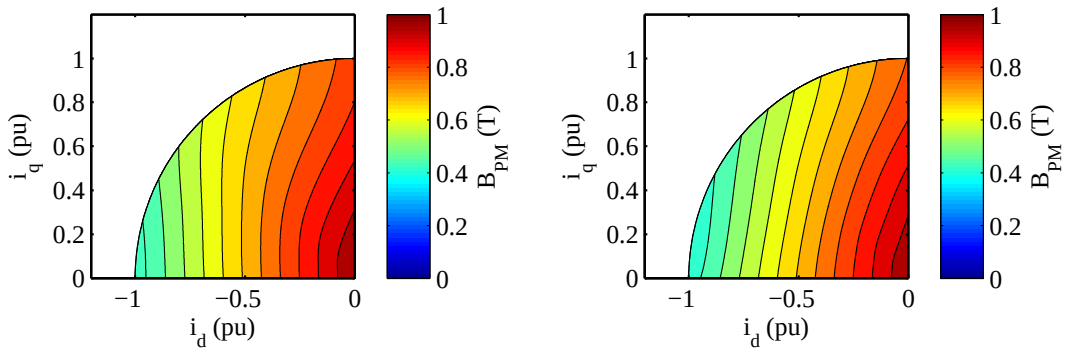

(a) Leading end PM

(b) Trailing end PM

Figure 5.11: PM demagnetization maps of a typical motor for PMs located with respect to the rotor motion for motoring operation.

not violate the constraint on the maximum drive voltage are identified using set B and equation Eq. (5.3.4). Once again, for efficient operation, the current vector with minimum magnitude will be selected. This process is illustrated in Fig. 5.10. Using this method, both MTPA and field weakening operations are successfully incorporated to ascertain the optimal operation and to maintain current controllability throughout the extended speed range under limited supply voltage.

Along with sampling the d- and q-axes flux-linkages for calculation of the torque and induced voltage values, for each individual design candidate, the rotor PM flux density levels are also obtained by placing "virtual search coils" across the PMs in the FEA model. The PM flux density levels are used to create the PM demagnetization maps, such as those shown in Fig. 5.11 for a typical design, in order to characterize the degree of PM demagnetization throughout the entire possible range of operation. The minimum PM flux density in the PM demagnetization map should be checked during the optimization process to prevent excessive/irrevocable demagnetization.

5.4 Extended Speed Operation of PM Machines

In the design optimization of high-speed IPM machines, a fundamental step is the characterization of the machine torque-speed envelope, and investigation of the design factors which influence the extended speed operation of such machines. Traditionally, PM motors are categorized into finite and infinite maximum speed classes according to the ratio of their characteristic current, I_{CH}, with respect to their rated current, I_R [93, 170–172]. A salient pole PM motor that is ideally designed for extended speed operation is assumed to have I_{CH} equal to I_R [93, 96, 170–173]. In [92, 94–96], this criterion has been introduced as an additional objective for large-scale design optimization of IPM motors for constant power operation. Yet, such characterization of an ideal machine for constant power operation falls short to note two factors regarding realistic operation of such machines. First, in any practical design, the rotational speed is limited to an upper bound so as to avoid rotor destruction at excessively high speeds [159]. Second, as will be illustrated here, the equality of I_{CH} and I_R adversely affects the machine's efficiency throughout the extended speed range. This is despite the fact that in many applications such as electric vehicles, efficiency is one of the main concerns.

Another fundamental factor influencing the field-weakening characteristic of a constant parameter PM motor drive is saliency. As suggested in the literature [93], increasing saliency can enhance the power capability under the rated voltage and rated current operating constraints. Nevertheless, increased saliency does not always translate into reduced cost in IPM motors [96] contrary to a commonly held notion

[93]. This can be attributed to the fact that the primary component that contributes to the saliency of the studied machine configurations in [96] are the permanent magnets with a recoil permeability close to that of air. Consequently, the saliency in a particular rotor layout has a direct correlation with the area along the d-axis that is covered by the expensive magnets. In addition to influencing the cost, saliency can be conducive to higher efficiencies by contributing to the generation of reluctance torque from the demagnetizing component of the stator current [93, 170, 171, 174], particularly in the flux weakening operation. Therefore, it is imperative to assess the efficiency of the salient pole machines over their entire operating ranges.

Aside from the equality of characteristic and rated currents, ($I_{CH} = I_R$), which has been previously suggested for reliable operation [93], and enhanced power capability throughout the extended speed region, two other possible scenarios for I_{CH} are: ($I_{CH} > I_R$) or ($I_{CH} < I_R$). Provided that ($I_{CH} > I_R$) as a result of low d-axis inductance or strong magnets, the extended speed operation will be limited due to excessive increase of the internal voltage at high speeds. This, in turn, leads to rapid loss of the control of the stator current, and accordingly a sharp drop of the generated torque and power. In case ($I_{CH} < I_R$) due to weaker magnets or higher d-axis inductance, the infinite speed operation can be achieved at the expense of diminished output power. The latter case as well as the case in which these currents are equal ($I_{CH} = I_R$) are further investigated for the Prius IPM motor configuration.

In Fig. 5.12 the sampled contours of the magnitude of the fundamental component of the flux-linkage of a typical phase are shown over the entire range of the excitation current for three IPM motors with equal torque and current density ratings. The

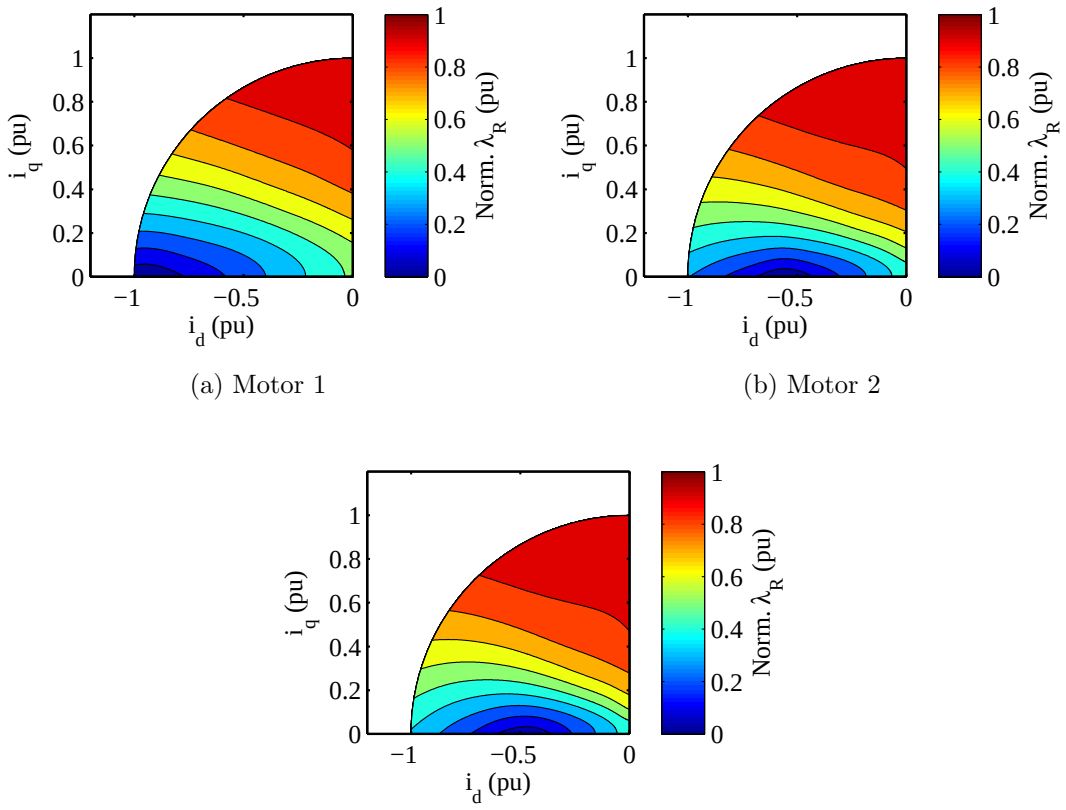

(a) Motor 1

(b) Motor 2

(c) Motor 3

Figure 5.12: Sampled flux contours of the three example motors with equal rated torque and rated current density.

motors are sorted in descending order of their I_{CH}, which can be identified in these figures as the point on the negative side of the d-axis where the flux-linkage reaches zero. To understand how the value of the characteristic current influence the behavior of the three designs for various torque and speed values, their performance maps are computed using the FEA-based method described in Fig. 5.9.

The first series of maps in Fig. 5.13 reveals that Motor 1, which has an I_{CH} closer to its I_R, is superior in terms of power capability in the extended speed range as it can generate more torque with a limited supply voltage. Nevertheless, according to the

same figure, the efficiency drops faster for this motor with the increase of the operating speed. Meanwhile, the designs with lower I_{CH} indicate diminished power capability in the extended speed region. Yet, the high efficiency contours are further expanded to cover more areas of the entire operating range in these designs. Accordingly, by observing Figs. 5.12 and 5.13, one can notice the direct relationship between I_{CH} and the field weakening power generation capability and the inverse relationship between I_{CH} and the extended speed operation energy efficiency.

To discern the cause of the differences between the efficiency maps shown in Fig. 5.13, the loss ratio maps over the entire operating range are provided in Fig. 5.14. The loss ratio is defined here as the ratio of copper loss to the sum of the stator core loss and the friction and windage loss. The latter is provided by the research team at Oak Ridge National Laboratories (ORNL) for the 2004 Toyota Prius motor and is assumed to be equal in all the designs. According to the loss ratio maps, the ratio of copper loss to core loss is greater in motor 1 in the extended speed range.

The larger high-speed copper losses in motor 1 can be ascribed to the increased current densities in the extended speed range as shown in Fig. 5.15. Specifically, as opposed to the comparatively smaller q-axis component of the stator winding current, Fig. 5.16, a larger negative d-axis component of current, Fig. 5.17, is required to weaken the magnet flux at high speeds. Accordingly, as I_{CH} increases, canceling the PM flux-linkage in the stator windings requires larger demagnetizing currents to either demagnetize the stronger magnets, or to compensate for the lower d-axis inductance, since by definition $I_{CH} = \lambda_{PM}/L_d$.

Ultimately, it should be pointed out that although motor 3 has better energy

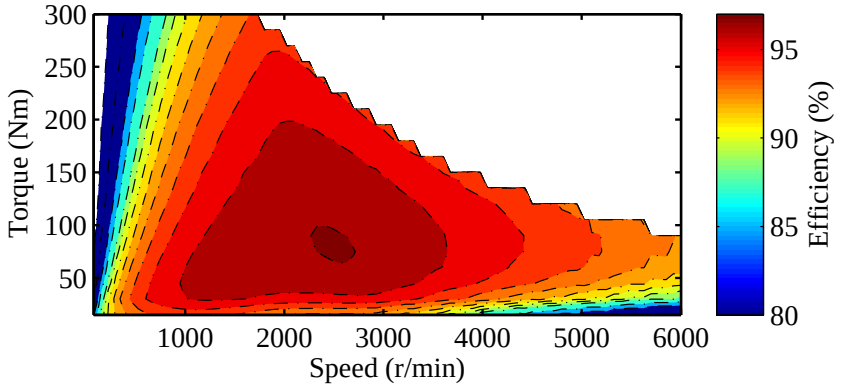

(a) Motor 1

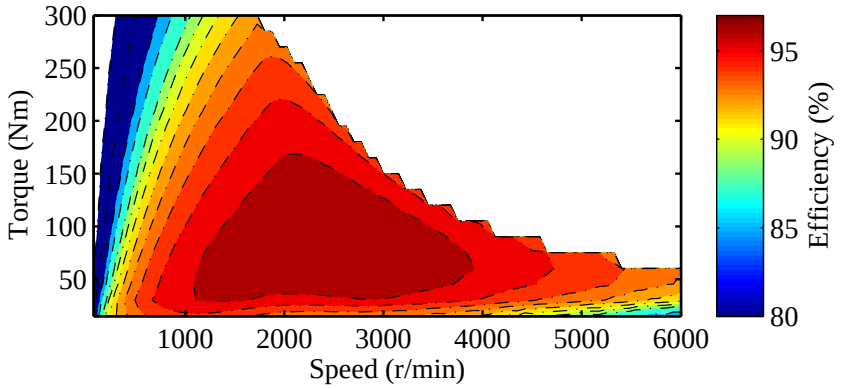

(b) Motor 2

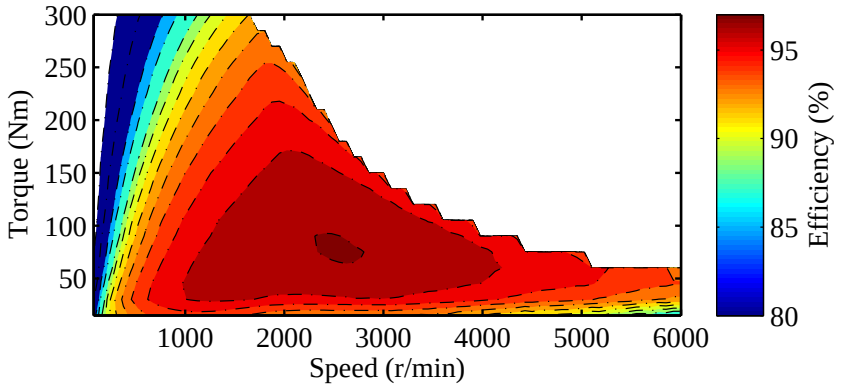

(c) Motor 3

Figure 5.13: Efficiency maps of the three example IPMs with infinite maximum speeds.

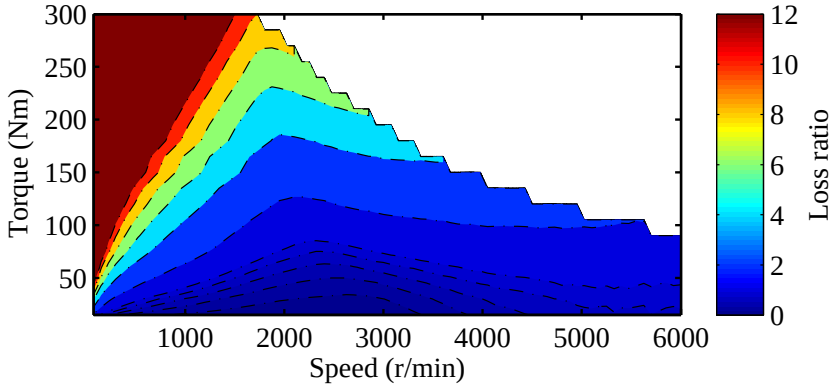

(a) Motor 1

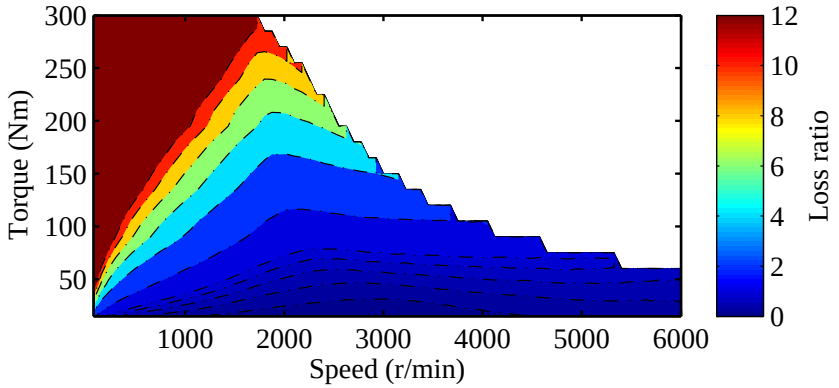

(b) Motor 2

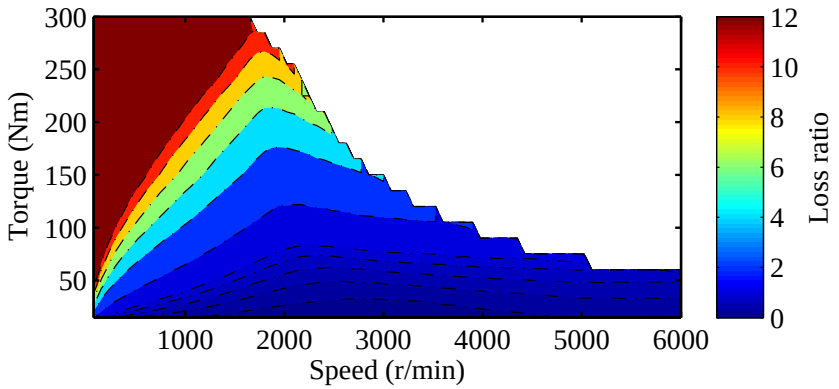

(c) Motor 3

Figure 5.14: Loss ratio maps of the three example IPMs with infinite maximum speeds.

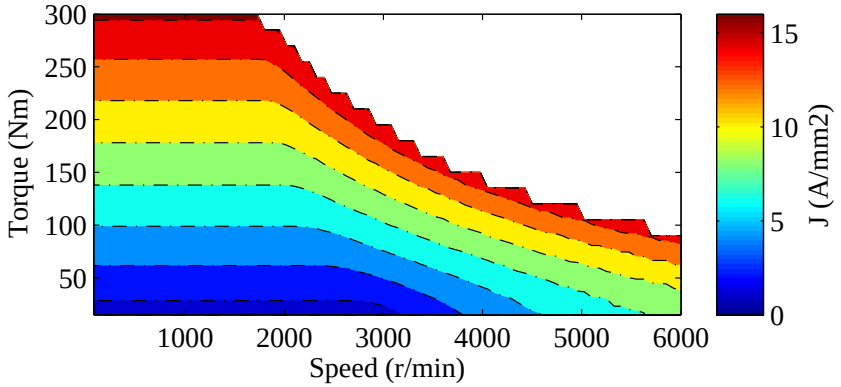

(a) Motor 1

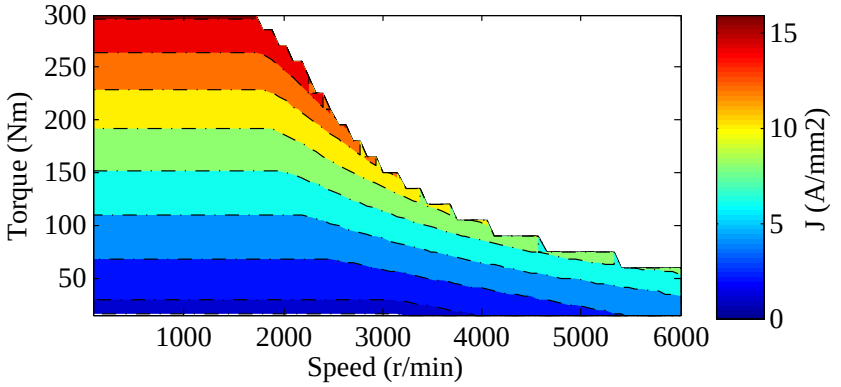

(b) Motor 2

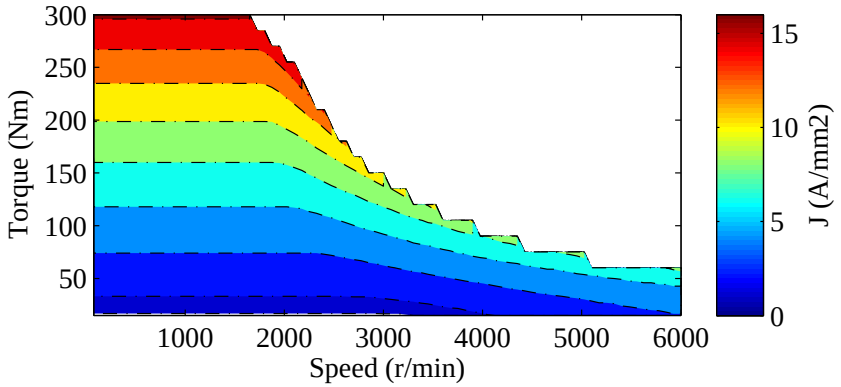

(c) Motor 3

Figure 5.15: Current density maps of the three example IPMs with infinite maximum speeds.

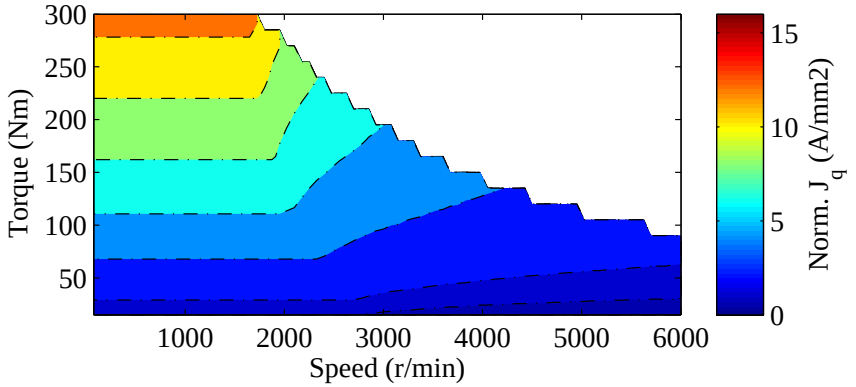

(a) Motor 1

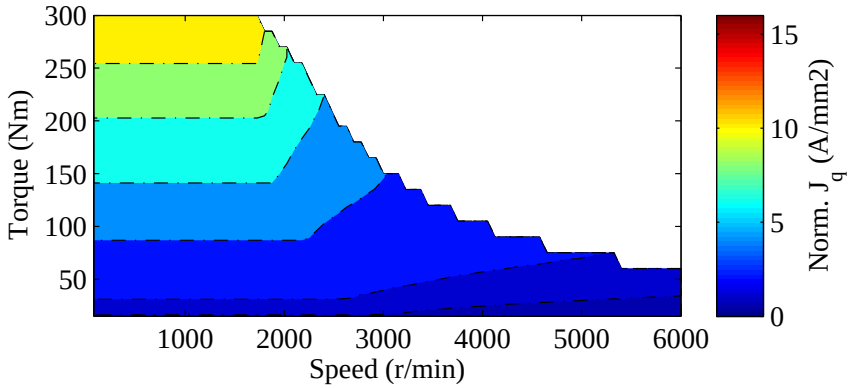

(b) Motor 2

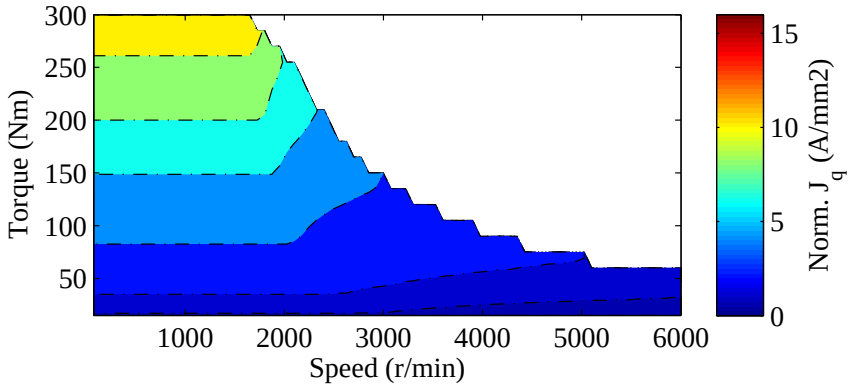

(c) Motor 3

Figure 5.16: Q-axis current density maps of the three example IPMs with infinite maximum speeds.

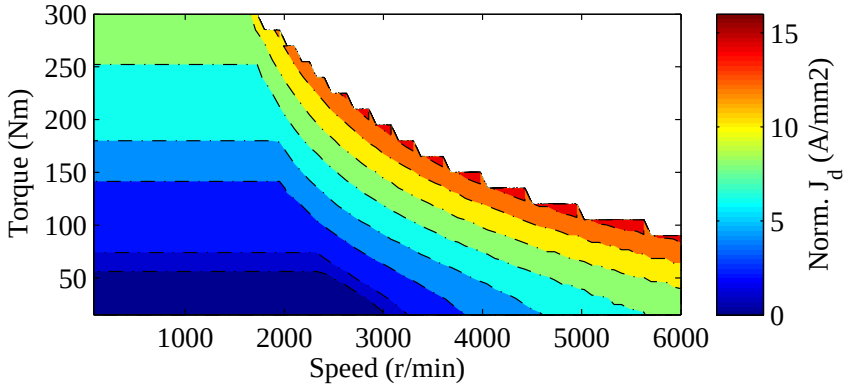

(a) Motor 1

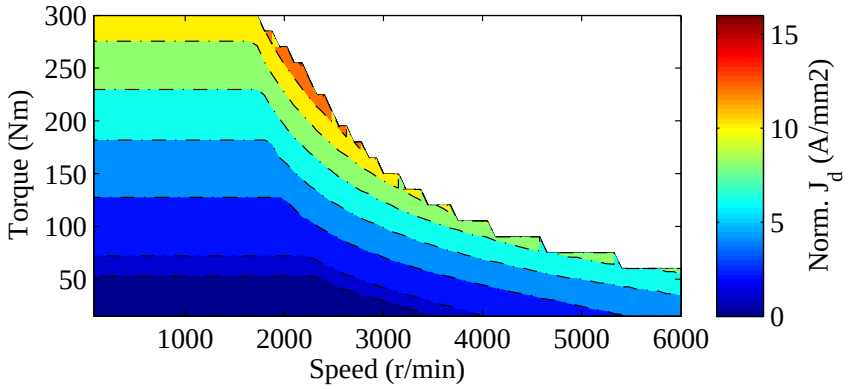

(b) Motor 2

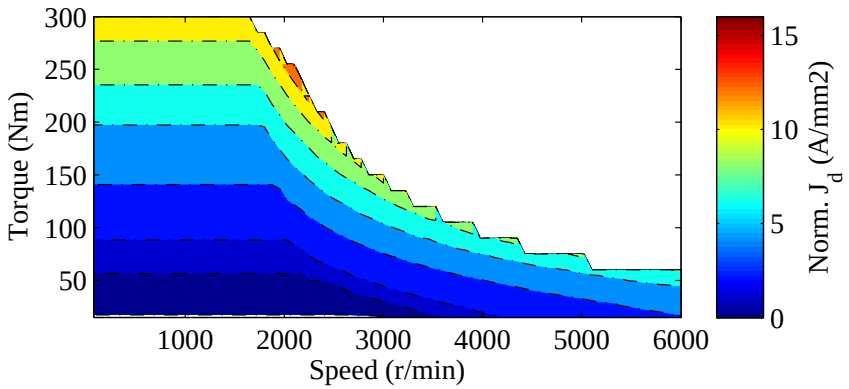

(c) Motor 3

Figure 5.17: Negative d-axis current density maps of the three example IPMs with infinite maximum speeds.

efficiency in the extended speed region, the magnets are excessively demagnetized for this design, as shown in Fig. 5.18. This reveals the existing trade-offs between the I_{CH}, efficiency, power capability, and the degree of PM demagnetization which should be considered in the design of PM machines for the extended speed operation.

In view of all the above mentioned points, Motor 2 is shown to be an acceptable compromise among the three motors in terms of power capability, efficiency, and degree of PM demagnetization. As a matter of fact, this design belongs to the 2004 Toyota Prius IPM motor simulated from the data provided by the team at ORNL. The following section puts forth a method for designing motors as optimized as the 2004 Toyota Prius IPM motor which takes the aforementioned factors into consideration.

5.5 Drive-Cycle Optimization

5.5.1 Algorithm

After developing the required tools for drive-cycle design optimization, and discussing the design factors influencing the extended speed performance of PM machines, the methodology for design optimization of PM machines over a target operating cycle can be presented through the high-level flowchart of the steps in Fig. 5.19.

The design optimization process has three main stages, namely preprocessing, loop iterations, and post-processing. In the first stage, the machine model is parametrized similar to the approach presented in Section 2.2.1, the representative operating points are identified using the clustering algorithm developed in Section 5.2, the objectives and constraints of the fitness function are designated considering the discussion in

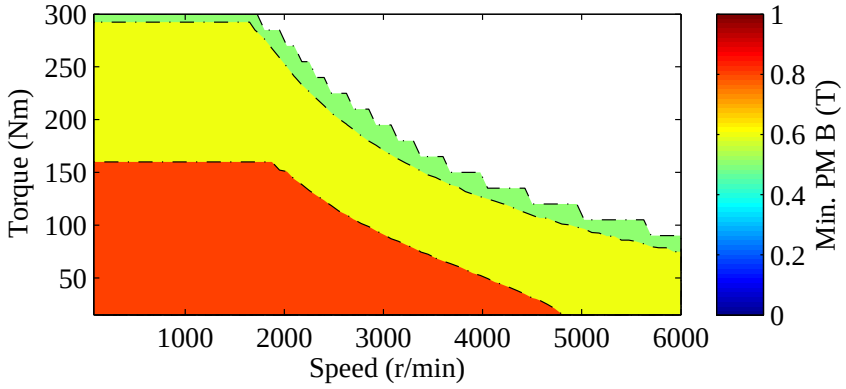

(a) Motor 1

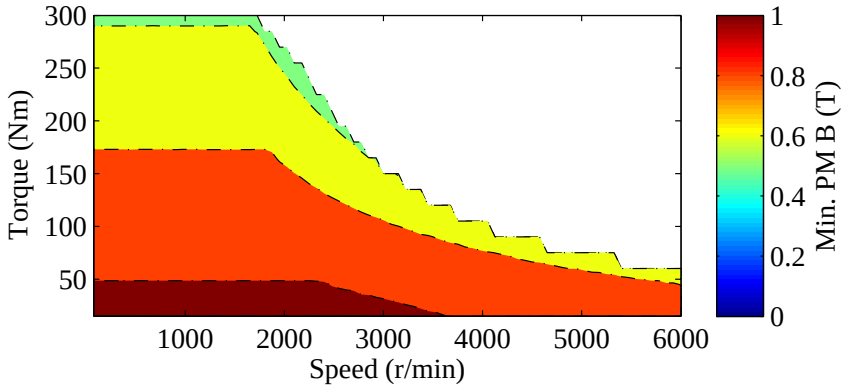

(b) Motor 2

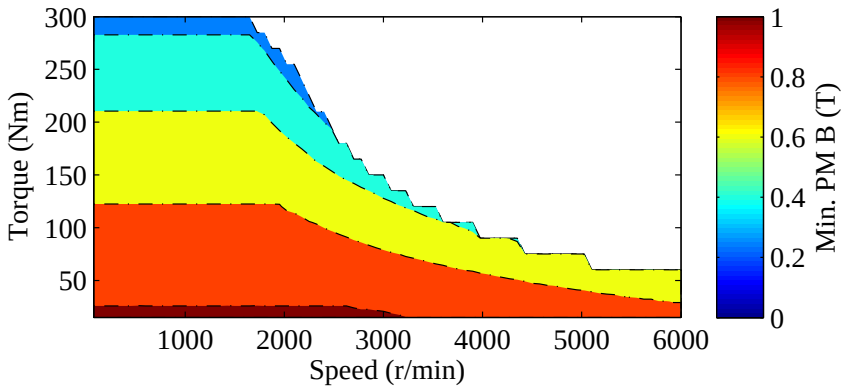

(c) Motor 3

Figure 5.18: Current density maps of the three example IPMs with infinite maximum speeds.

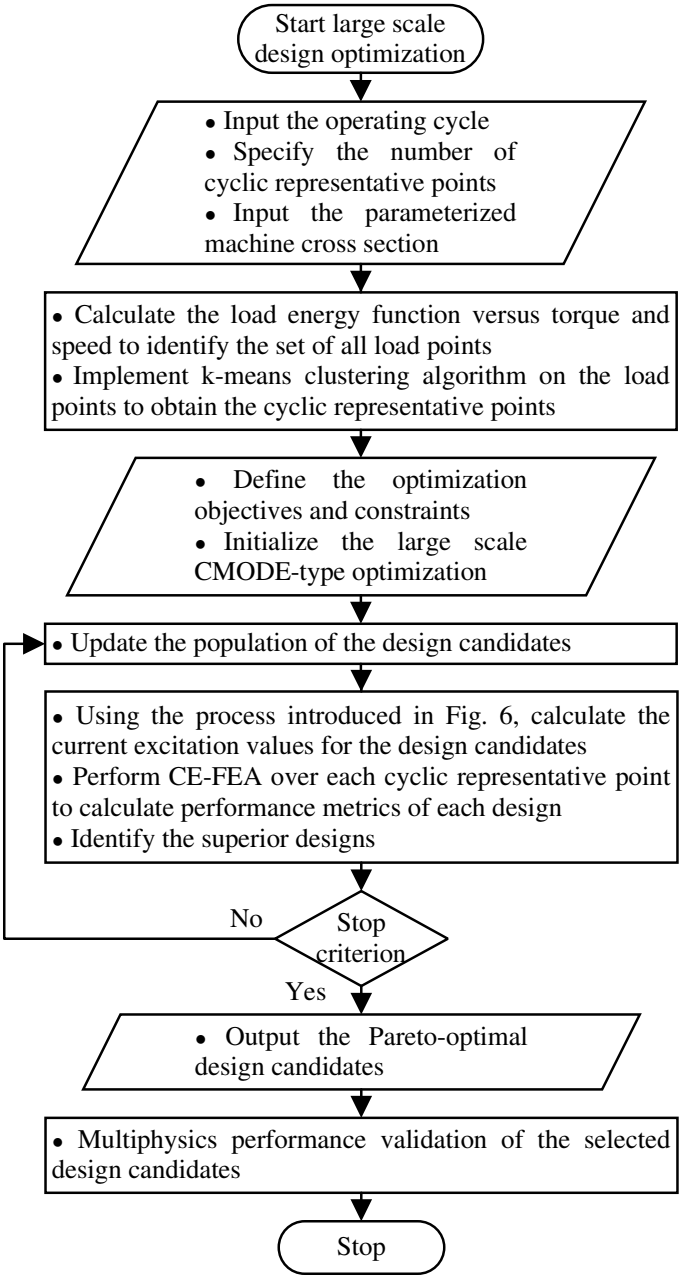

Figure 5.19: The flowchart of steps of the overall optimization algorithm.

Section 5.4, and the large-scale search algorithm is initialized as explained in Chapter 4. Subsequently, in the loop iteration stage, for each design candidate, the excitation currents at the cyclic representative points are calculated using the numerical method developed in Section 5.3. A detailed FE analysis is carried out afterwards over each individual load point using the fast and high fidelity CE-FEA simulations described in Section 2.1.1, or full-fledged FE models if desired. Accordingly, the saturation and cross-saturation are considered both in determining the excitation current and in calculating the machine performance over each representative load point.

The first iteration of the design candidates is generated randomly with respect to the designated bounds of the design parameters. The subsequent iterations are followed by the CMODE-type search algorithm (CMODE). The details of the CMODE-type optimization and its advantages over the conventional Differential Evolution have been previously discussed in Chapter 4 for design optimization of PM motors at the rated operating point. Here, this search algorithm is applied to optimization of PM machines at multiple operating points.

In each iteration of the CMODE-type optimization process, similar to other Evolutionary Algorithms (EA), an offspring population competes with the parent population according a fitness function, i.e. a set of objectives and a set of constraints. The fitness function is determined based on the design requirements. However, as illustrated in the previous section, when the non-linear and lossy nature of the machine is considered, the congruity of I_{CH}, and I_R, cannot be the ideal criterion for constant power operation from the efficiency standpoint. Instead of introducing such criterion into the optimization fitness function, it is recommended to check the

torque production capability of every design candidate at critical load points such as ω_{max}, and penalize the designs failing to produce the desired torque under the rated current and voltage constraints, e.g. by multiplying their associated fitness function by a large positive number in a minimization problem.

5.5.2 Computational Complexity of the Optimization Algorithm

As discussed in the previous section, the overall optimization process consists of the preprocessing, loop iteration, and post-processing stages. The computational burden of the loop iteration stage overshadows that of the other two and is divided between three subroutines: (a) generation of the torque and flux look-up tables for calculation of the excitation current, (b) performance evaluation over representative load points, and (c) determination of the superior design candidates. The first two subroutines involve FEA, and thus are more computationally demanding. For generating relatively accurate torque and flux look-up tables, 25 sample current vectors are recommended, which can be distributed evenly, or can be skewed toward the negative d-axis to better capture the smaller flux-linkage quantities in this vicinity. Using CE-FEA, as few as one FE solution can be used for each sample point to extract the fundamental values of torque and fluxes. Depending on the pole-slot combination, a larger number of FE solutions are required for calculation of torque ripple and core losses over each representative load point. Nonetheless, CE-FEA can still be utilized to significantly expedite the simulation time up to two orders of magnitude when compared to time-stepping transient FEA [80, 119]. The simulations can be continued

until a well defined Pareto front is acquired. Using CMODE-type optimization, this can be achieved within a smaller number of design evaluations.

5.6 Summary

A novel automated design methodology for optimization of PM synchronous machines for an application-specific operating cycle was introduced. The developed method provides a systematic approach for fast and high fidelity design optimization of PM machines with wide ranges of operation. The constraints imposed either by the ampere-loading or by the limited drive voltage were fully integrated into the performance evaluation process, thus enabling the design optimization throughout the constant-torque and constant-power operating regions. Furthermore, the effects of magnetic saturation and cross-saturation were thoroughly taken into account both in determining the current excitation of the stator winding at any load operating point, and in the calculation of the performance metrics.

Utilizing the k-means clustering algorithm, a systematic method was devised for efficient modeling of the motor operating cycle. The resultant cyclic representative points embody the operation zones of the torque-speed plane through which the majority of the electric energy is consumed. Accordingly, the weighted losses are derived and incorporated in assessing the drive-cycle efficiency of the design candidates in the introduced optimization algorithm.

CHAPTER 6

CASE STUDY DRIVE-CYCLE OPTIMIZATION OF TRACTION MOTORS

In this chapter, the optimization algorithm developed in Chapter 5 is utilized for optimizing two case study PM machines. Each case includes multiple steps, namely, the modeling of the motor operating cycle, development of the parametrized FE model, definition of the fitness function, initialization of the search algorithm, performance evaluation over representative load points, and identification of the superior designs. A rigorous post-optimization modeling is also pursued to accurately characterize the performance of the final selected designs.

6.1 Introduction

Two traction propulsion motors are optimized using the techniques presented in the previous chapters:

- The first motor studied in this chapter is the well-established Toyota Prius Gen. 2 IPM motor configuration which was previously investigated in a design optimization for improving its nominal (peak) performance in Chapter 2. This specific motor configuration is chosen here for a twofold purpose: (a) the particular features of the V-type IPM motors with distributed windings including saliency and mechanical robustness, which makes them attractive for high-speed operation; and (b) for performing a detailed comparison between the

optimization results and the experimental verifications documented in several reports published by the Oak Ridge National Laboratory (ORNL) research team during the past years [130, 131, 175].

- The second case study presented in this chapter is the design optimization of a spoke-type IPM with a fractional slot concentrated winding configuration for a formula E racing car propulsion application. The original motor, which has been successfully tested by other investigators in [142], features a very high torque per weight ratio. Here, this motor is optimized to further increase the power density and, at the same time, the drive-cycle efficiency in order to demonstrate the effectiveness of the developed methodologies in a challenging design problem. The results of this case study optimization are also utilized to quantify the performance trade-offs for increasing the power density in spoke-type PM motors. These trade-offs include the impacts on other performance metrics such as power losses, PM demagnetization, and torque ripple.

6.2 Optimization of the Prius IPM Motor Over a Compound Operating Cycle

6.2.1 Initialization

In this section, the 48-slot 8-pole IPM motor of the Toyota Prius Gen. 2 is optimized over a sequence of driving cycles composed of the US Environmental Protection Agency's (EPA) Urban Dynamometer Driving Schedule (UDDS), Supplemental Federal Test Procedure Driving Schedule (US06), Highway Fuel Economy Test Driving Schedule (HWFET), Unified Dynamometer Driving Schedule (LA92), and

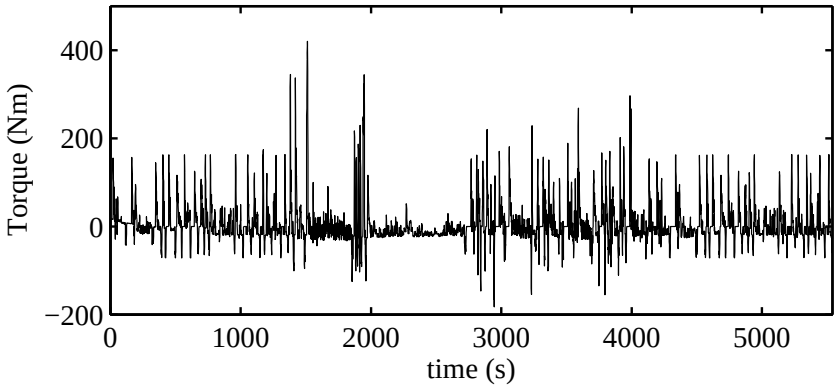

(a) Output torque

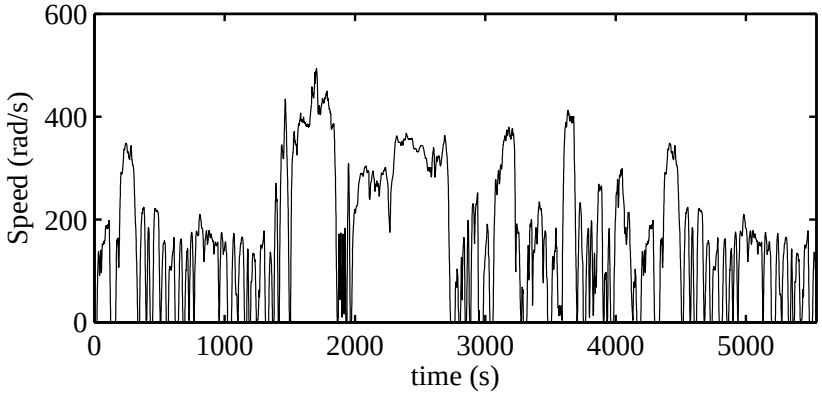

(b) Speed

Figure 6.1: Load profile of the Toyota Prius Gen. 2 IPM over a combined driving cycle.

UDDS. The motor torque and speed profiles which are obtained using ADVISOR are shown in Fig. 6.1. This sequence of driving cycles are chosen so as to improve the motors' performance over a wider variety of operating conditions.

From the load profile provided in Fig. 6.1, the energy distribution versus the torque and speed can be calculated as shown in Fig. 6.2.

Using the k-means clustering algorithm introduced in Chapter 5, the energy distribution function is modeled by seven clusters as can be seen in Fig. 6.3. These

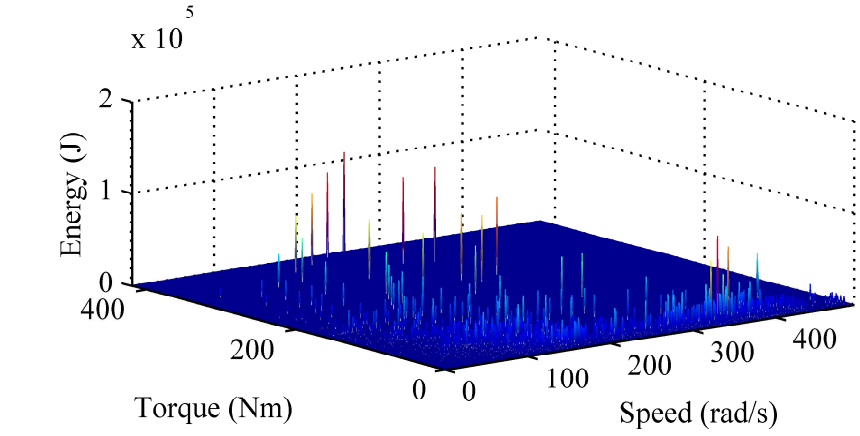

(a) Isometric view

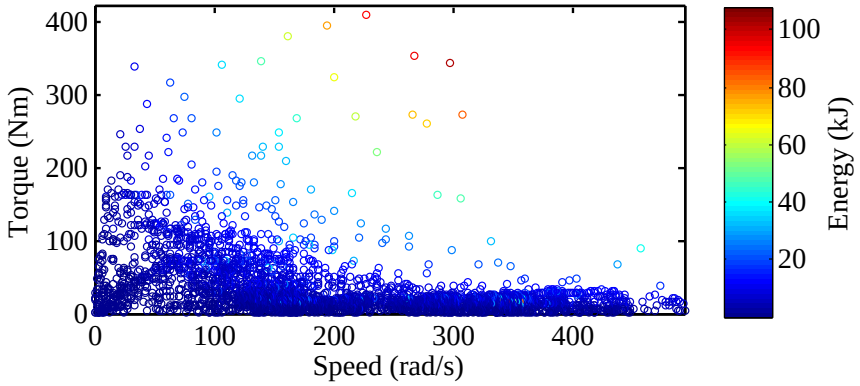

(b) Bird's-eye view

Figure 6.2: Toyota Prius Gen. 2 motor output energy versus torque and speed for the combined US driving cycles.

load points which will be used in the evaluation of the motor performance during the optimization process, along with two critical load points imposed by the design requirements, i.e. required torque at base and maximum speeds are listed in Table 6.1. The numbers next to the means of the clusters in Fig. 6.3 indicate their ranks according to their energy weights in Table 6.1.

The next step in the drive-cycle design optimization is the definition of the parametric FE-model, which for this case study has been previously presented in

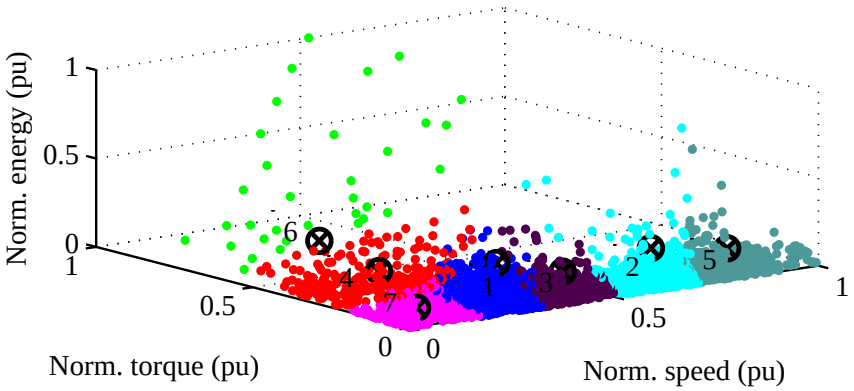

(a) Isometric view

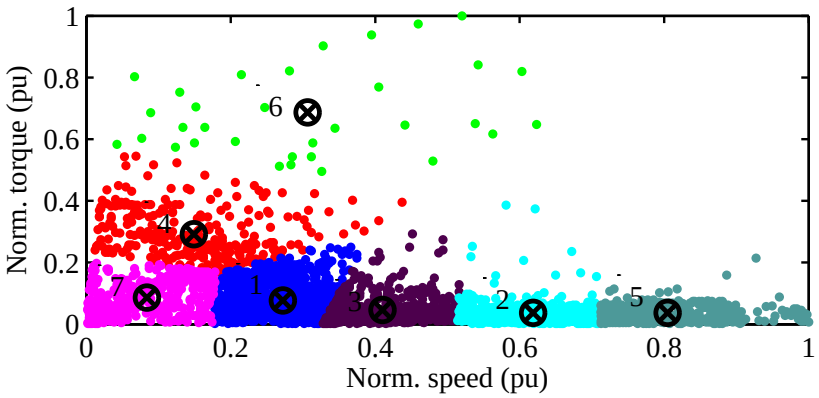

(b) Bird's-eye view

Figure 6.3: Cyclic representative points with seven clusters for the combined US driving cycle.

section 2.2. This model with the same design parameters and boundaries are used here. Similar to the original Toyota Prius motor design, rated stator winding current density is considered to be $16A/mm^2$ for producing a torque of 300 Nm.

In line with the discussion about proper definition of the optimization fitness function, which was presented in Section 5.4, the optimization objectives are designated as follows:

- Minimization of the active material cost given in Eq. (2.2.3);

Table 6.1: Cyclic representative points for the combined US driving cycle shown in Fig. 6.1.

m_i	$\omega(rad/sec)$	$T(Nm)$	$energyweight$
ω_{base}	157	300	
ω_{max}	628	50	
1	140	21	0.2570
2	311	15	0.2273
3	212	19	0.1366
4	74	123	0.1338
5	403	15	0.1265
6	151	288	0.0687
7	44	36	0.0501

- Minimization of the aggregate weighted loss per output power, P_w, defined in Eq. (6.2.1);

$$P_w = \sum_i (P_{dc,i} + P_{Fe,i}) \cdot w_i/(T_i\omega_i) \tag{6.2.1}$$

where w_i is the energy weight of the i^{th} representative load point in Table 6.1, and ω_i is the rotor speed in $mech.rad./sec.$

Furthermore, the following constraints are imposed to ensure reliable performance throughout the entire range of operation:

- Less than 25% torque ripple at the rated operating point;
- Less than 70% PM demagnetization at any point on the PM demagnetization maps.

The thermal aspect of the design is indirectly addressed in the optimization process by confining the highest current density in the stator winding to that reported for the Toyota Prius IPM motor. In general, the optimized designs are expected to be more efficient than the original design, ensuring that the cooling system can properly

conduct the power losses to the ambient surroundings. Still, here in this work, the thermal performance of the most promising design candidates are investigated over a rigorous driving cycle in a post-optimization stage.

From the mechanical design standpoint, the thickness of the rotor bridges is adjusted as required to withstand the maximum tangential stress acting on these bridges. This adjustment is done using approximate calculations of the centrifugal forces based on the material properties and the shape on the rotor pole-pieces. The method for analytical estimation of the centrifugal forces is presented in Chapter 7. Minimum thickness is desired for efficient utilization of the magnet flux linkage and optimal electromagnetic performance, whereas a higher thickness provides better structural robustness for high-speed operation. A post-optimization mechanical FE analysis is conducted on the selected optimized designs to make sure they pass this criterion.

6.2.2 Optimization Results

The drive-cycle design optimization of the 48-slot 8-pole IPM machine with the aforementioned fitness function was carried out over 10,000 designs using 8 simultaneous processing units on a desktop workstation. The global minimum of the design space, and accordingly, optimal design solutions were identified within the first few hundred design evaluations, in this case in less than 24 hours. However, the optimization iterations were continued to capture a very detailed Pareto front. The performance of the design solutions which pass the constraints on the PM demagnetization and torque ripple are shown in Fig. 6.4(a) and (b).

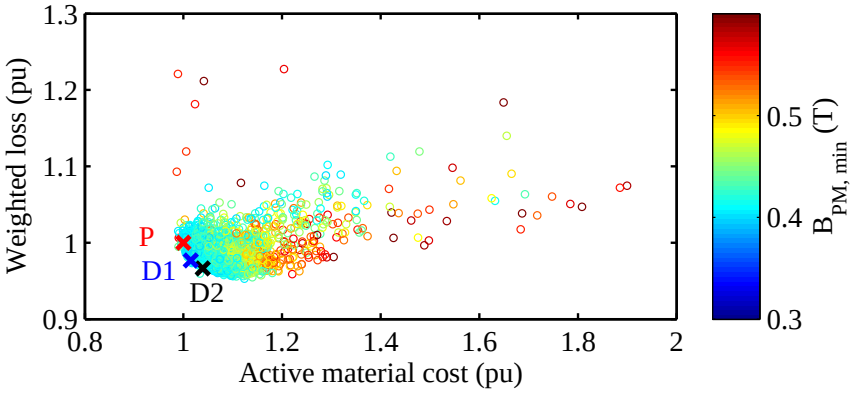

(a) Color-coded for minimum flux density of the rotor PMs

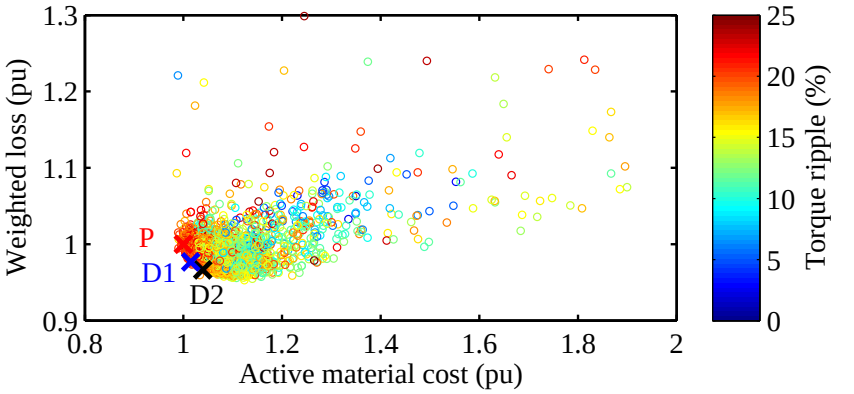

(b) Color-coded for torque ripple

Figure 6.4: Optimization results of Toyota Prius Gen .2 IPM motor over the combined US driving cycles.

Using the same simulation methodology, the Toyota Prius IPM motor drive-cycle performance, denoted by P, is also evaluated and marked along with other results in Fig. 6.4. It can be seen that the Prius design is adjacent to the Pareto-optimal designs at the high-loss, low-cost vicinity.

The ability of the developed design optimization package in providing design solutions comparable to the Prius design should be noted. Furthermore, there are other alternative designs that, at a slightly higher cost, demonstrate better

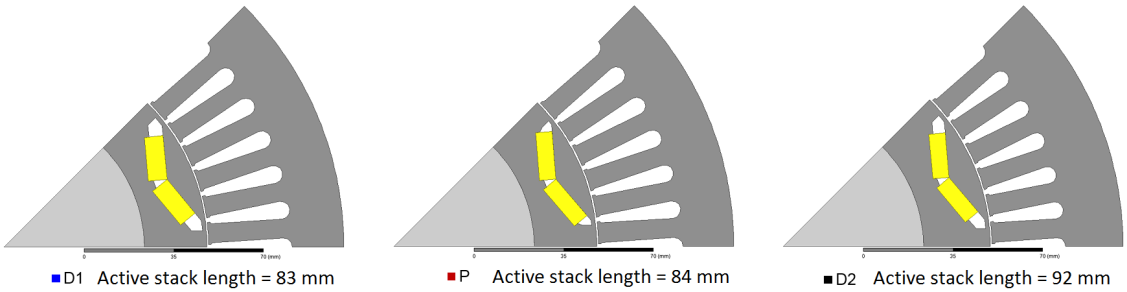

(a) Cross-sections

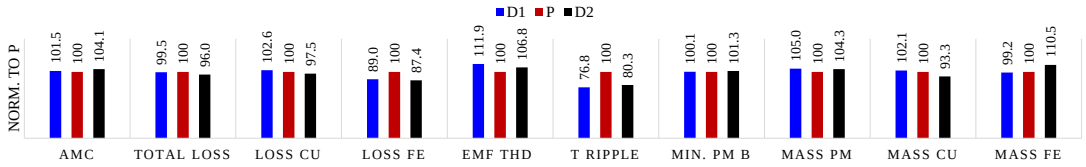

(b) Electromagnetic performance metrics normalized to Prius

Figure 6.5: Comparison of the selected designs obtained from drive-cycle optimization.

performance in terms of aggregate power losses. Two of these design candidates specified by D1 and D2 in Fig. 6.4 are selected for further multi-physics investigation.

6.2.2.1 Electromagnetic Performance

The cross-sections of the three design candidates, D1, P, and D2, and their performance metrics, normalized with respect to the Prius motor design, are shown in Figs. 6.5. In Fig. 6.5 (b), the three loss components, are the sum of the respective losses over the representative load points weighted by their associated energy weights. Furthermore, the Total Harmonic Distortion (THD) of the induced Electromotive Force (EMF), and the torque ripple are considered at the rated load point.

The efficiency maps of the three designs is computed by FE analysis of 1 600 sample load points equidistantly distributed throughout the torque-speed plane, see Fig. 6.6. The excitation current at each sample point is considered under optimal voltage and

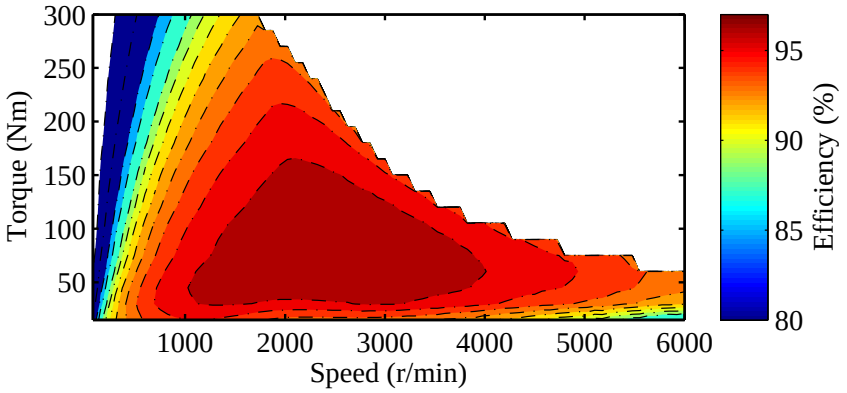

(a) D1

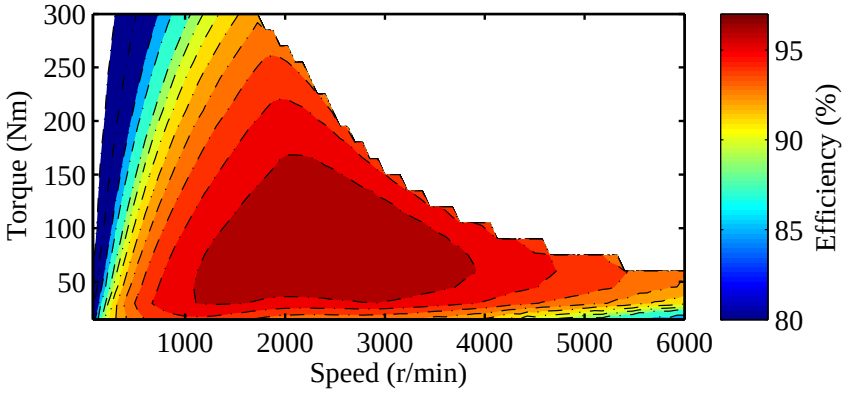

(b) P

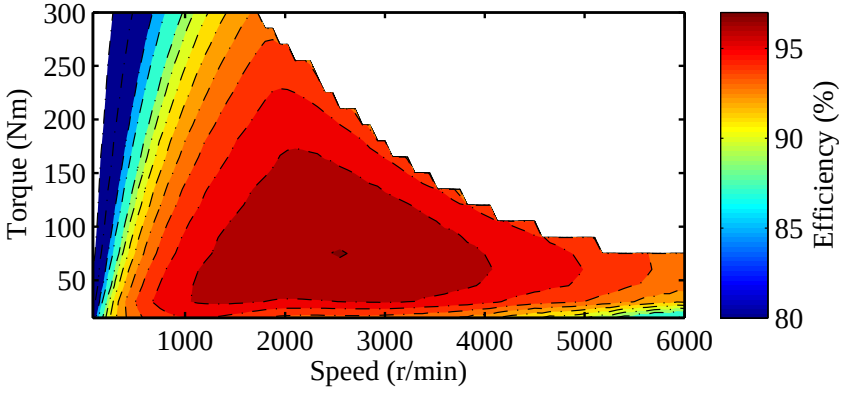

(c) D2

Figure 6.6: Efficiency maps of the selected designs obtained from drive-cycle optimization.

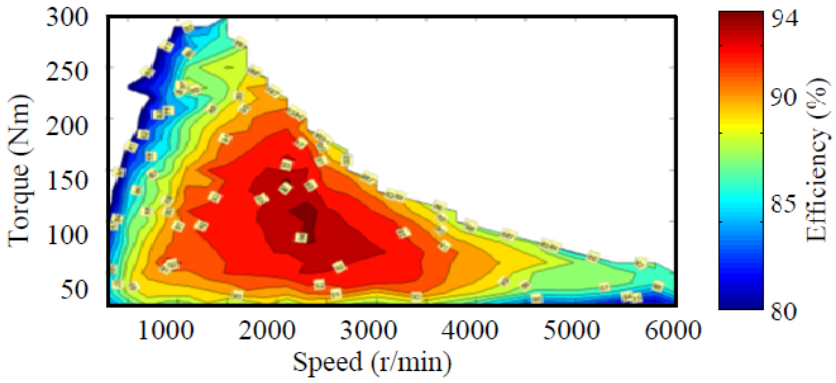

Figure 6.7: Tested efficiency map of the Toyota Prius Gen. 2 IPM motor reported by the research team at ORNL.

current control using the method developed in Section 5.3(B). The efficiency maps should be examined in two specific aspects: first, the highest achievable efficiency, and second, the extended range of high efficiency contours. The latter is of significant importance for motor designs in traction applications, and, in general, for applications in which the motor is to be operated at various load operating points.

To verify the validity of the simulations, the experimentally obtained efficiency map of the Prius motor reported by the ORNL research team is presented in Fig. 6.7. The slight discrepancy between the efficiency maps in Figs. 6.7 and Fig. 6.6(b) can be attributed to the loss components that were not addressed in our 2-D FE calculations including rotor core losses, eddy current losses in the magnets, unaccounted temperature variations, and AC conductor losses. Moreover, the excitation current was assumed to be sinusoidal over the entire operating region ignoring the time harmonics introduced by the inverter pulse width modulation specifically in the field weakening region. Nonetheless, the simulation results show very close correlation to the experimental results. The correlation of the three designs

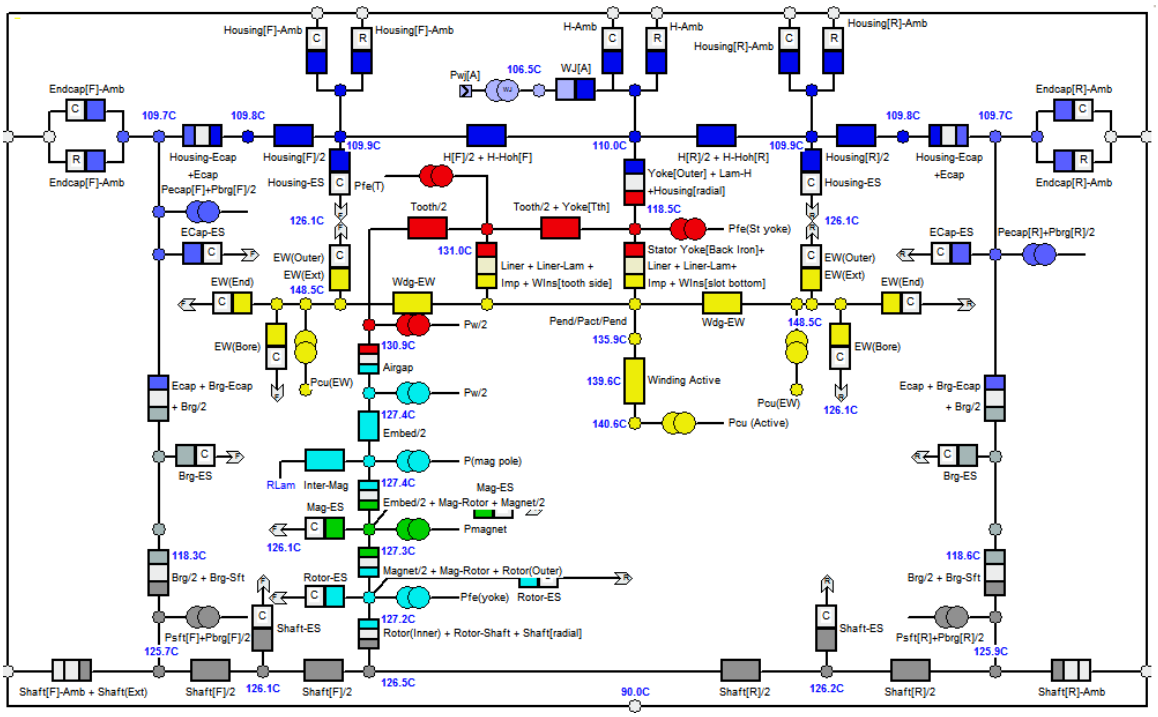

Figure 6.8: Lumped thermal network model of the motor cooling system developed in Motor-CAD.

not only indicates the merits of the original Prius motor design but also confirms the effectiveness of the developed design optimization algorithm.

6.2.2.2 Thermal Performance

To compare the thermal performance of the counterpart design solutions relative to each other, a typical liquid-based cooling system with oil-forced convection through the housing water-jacket was developed in Motor-CAD. The analysis is based on a lumped thermal network model as shown in Fig. 6.8 . The coolant fluid is ethylene glycol compound with 0.375 $W/m.C$ thermal conductivity, 1045 kg/m^3 density, and 0.0008987 $kg/m/s$ dynamic viscosity. A constant volume flow rate of 9 l/min at an inlet temperature of 105 $^{\circ}C$ was considered for the fluid.

The temperatures of various motor components were obtained by performing a

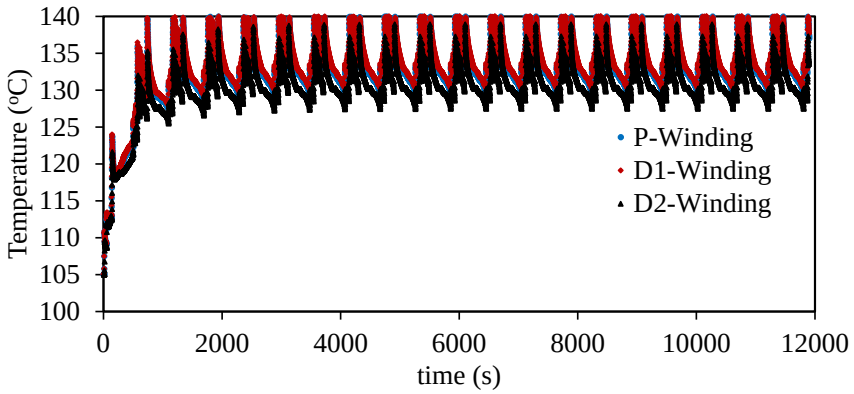

(a) Temperature of stator windings

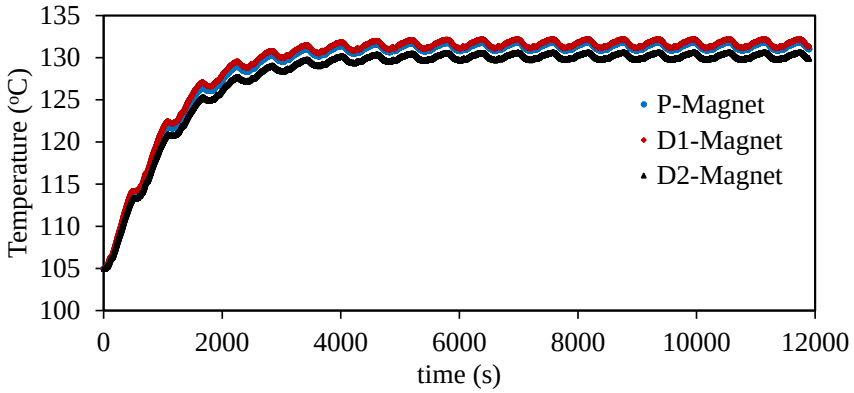

(b) Temperature of rotor PMs

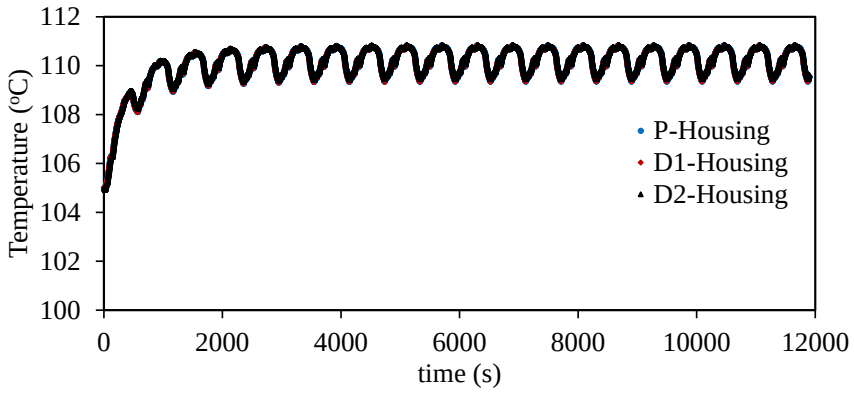

(c) Temperature of active housings

Figure 6.9: The peak temperatures of the counterpart designs evaluated over US06 driving cycle.

transient thermal analysis over the rigorous US06 driving cycle which is characterized by frequent acceleration and deceleration at various torque and speed levels. It can be seen in Fig. 6.9 that with identical cooling systems, the temperatures of the stator windings, rotor PMs, housings, and bearings in the P and D1 counterpart designs closely correspond. These temperatures are slightly lower in the D2 design due to the higher efficiency of this design over a broader range of operating conditions as illustrated in Fig. 6.6(c). The lower operating temperatures can extend the life-time of motor D2, and thus justify the increased material cost of this design.

6.2.2.3 Stress Analysis of the Rotor Bridges

The mechanical stresses on the rotor bridges are mainly due to the centrifugal forces resulting from cavities housing the PMs in the rotor structure [159]. A detailed static structural FE analysis is carried out in ANSYS under steady state maximum speed of $6\,000 r/min$. It is assumed that forces of electromagnetic, vibration, and rotor dynamic origins are negligible. Furthermore, it is assumed that the rotor PMs are not bonded to the cavities since the bonding strength is not permanently constant and diminishes over time. In the analysis, the mass densities of the rotor laminations and NdFeB magnets are 7850 kg/m^3, and 7500 kg/m^3, respectively. As can be seen in Fig. 6.10, the results of the structural analysis demonstrate that the von-Mises [176] stress throughout the rotor structures of the selected optimized D1 and D2 designs are comparable to that of the original P design, and are less than the yield strength of laminations, which is 350 MPa.

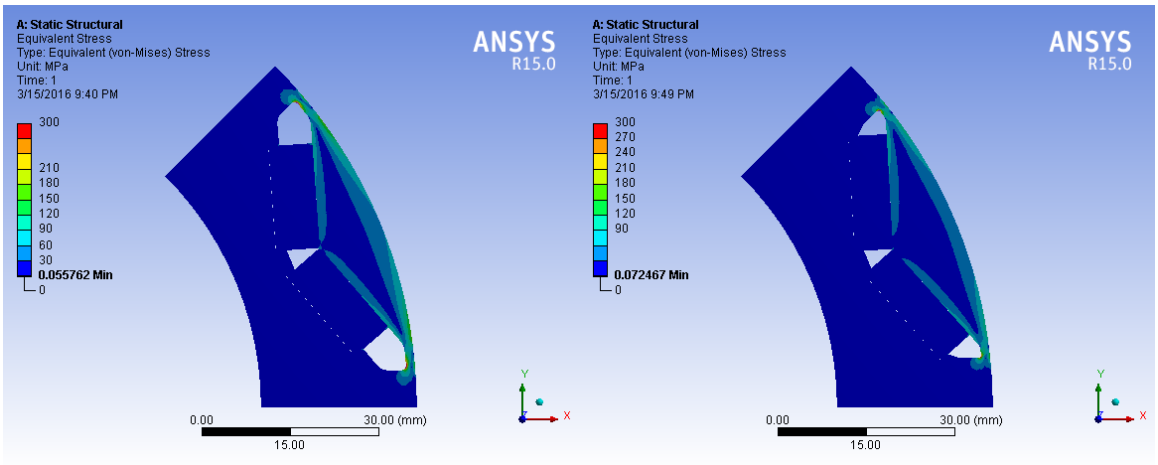

(a) D1 (b) P

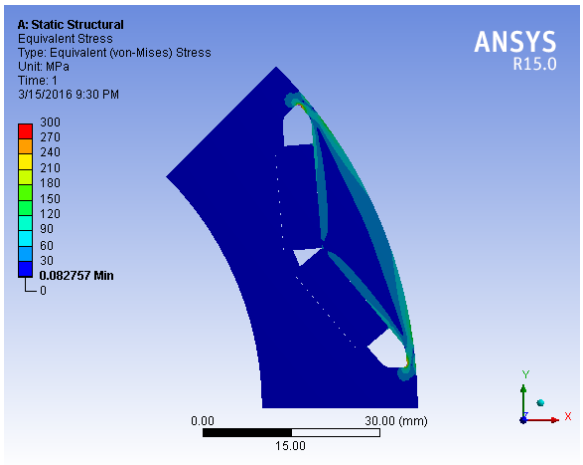

(c) D2

Figure 6.10: Von-Mises stress throughout the rotor structure of the counterpart designs.

6.3 Optimization of a Formula E Racing Car IPM Motor Over the Le Mans Operating Cycle

In this section, the design optimization of an IPM motor with very high power density is investigated. Specifically, the optimization of a concentrated flux spoke-type permanent magnet (PM) motor is in order. These motors can be designed for increased power density using high-cost high-energy PM materials [177, 178], or can be designed for reduced dependency on rare-earth materials using alternative low-cost magnets [179–181]. This is due to the higher air-gap flux density, B_g, of spoke-type PM motors as given in Eq. (6.3.1) which by itself is in part because of the lower reluctance of the rotor flux path [177, 178].

$$\frac{B_g}{B_r} = \left(\frac{\pi}{4k_\sigma} \frac{2d_r}{Ph_{pm}} + 2\mu_{mr} \frac{h'_g}{w_{pm}} \right)^{-1} \tag{6.3.1}$$

where B_r is the PM remnant flux density (retentivity), d_r is the rotor outer diameter, P is the number of poles, h_{pm} is the PM height along the radius of the motor, k_σ is the rotor leakage coefficient, μ_{mr} is the PM relative permeability, h'_g is the air-gap height adjusted to account for saturation and slotting effects, and w_{pm} is the PM width along the magnetization direction.

There are two aspects in the study of high power density motors which require special treatment, namely, the nonlinearity of the ferrous core, and the thermal behavior of the machine. Equation (6.3.1) has been used for assessment and rough approximation of high power density spoke-type machines in many studies such as in [179, 180]. However, as reported in [179], the effects of saturation and slotting cannot be accurately modeled in such machines using Eq. (6.3.1), due to the excessive

saturation levels of the ferrous core. This fact leaves numerical methods as the only means for accurate investigation of the design traits in such high power density machines. Meanwhile, the power density cannot be the sole objective of any realistic design practice without simultaneously considering the generated power losses, which directly impact the thermal performance of the machine as the ultimate limiting factor in increasing the power density. Therefore, a multi-objective approach should be pursued for the design of such high power density motors.

In this section, an 18-slot, 16-pole spoke-type PM motor configuration is adopted in order to achieve high drive-cycle energy efficiency, and high torque density for a direct drive racing car application. Several initial design measures are assumed in order to realize these objectives, including: (a) the use of special materials for lamination steels and PMs, i.e. non-oriented thin-gage laminated steel, and thermally robust SmCo magnets, (b) the adoption of special construction methods for minimizing PM and winding eddy current losses, i.e. PM segmentation and twisted wires, and (c) the utilization of a highly efficient cooling system with forced oil convection through the slot and forced air convection in the air-gap.

Through the FE-based multi-objective large scale design optimization process developed in the previous chapters, increase of torque ratio per weight (TRW), and at the same time decrease of power losses over the entire motor load profile are pursued. The optimization results lay the ground for an FE-based study of high power density spoke-type motor design in a practical approach, as has been the goal of many previous investigations using semi-quantitative analytical/closed-form methods [179, 180]. The existing performance trade-offs in terms of losses, PM demagnetization, and torque

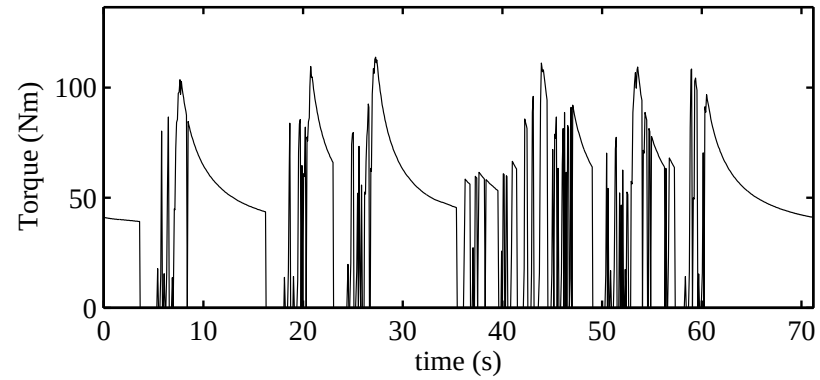

(a) Output torque

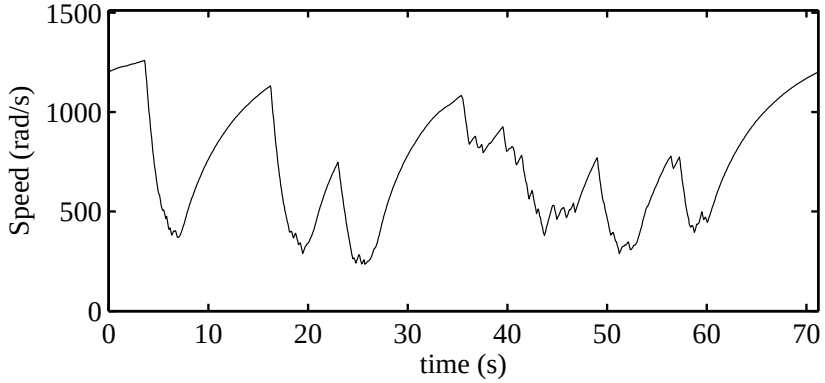

(b) Speed

Figure 6.11: Formula E motor load profile for the Le Mans driving cycle.

ripple for achieving high power density are quantified, and the relationships between optimal design parameters for high drive cycle efficiency and maximum torque density are examined. Furthermore, an optimized design which establishes a higher torque density than the original Formula E racing car motor is achieved.

6.3.1 Initialization

The motor load profiles over the Le Mans driving cycle are shown in Fig. 6.11. The frequent and oftentimes large fluctuations of the torque profile in Fig. 6.11(a), and the high speed of operation in Fig. 6.11(b) are characteristics of an electric propulsion

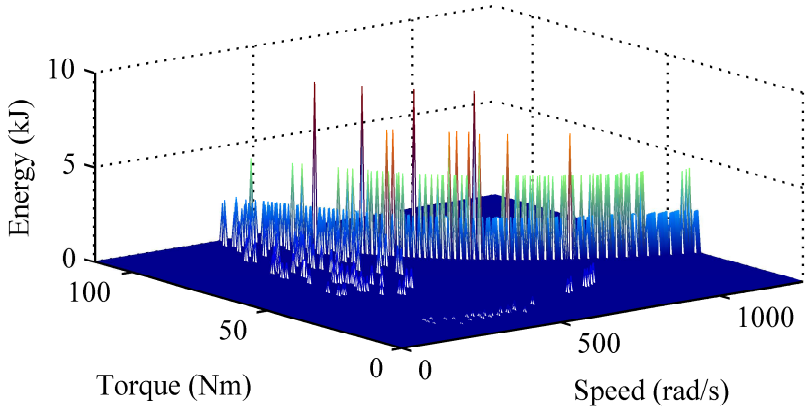

(a) Isometric view

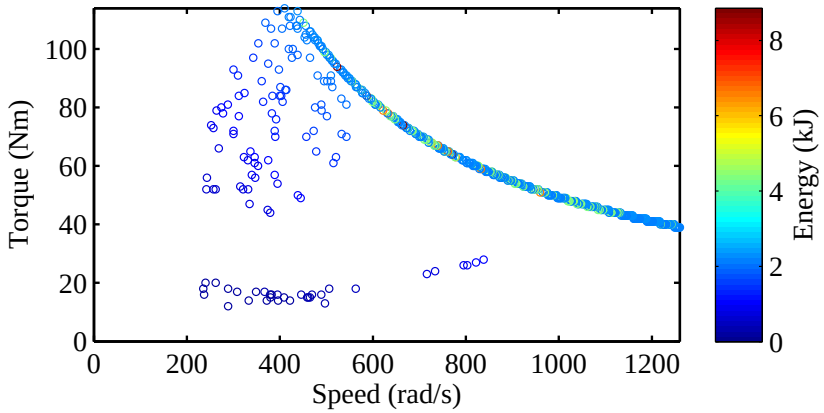

(b) Bird's-eye view

Figure 6.12: Formula E motor energy consumption in the torque-speed plane.

motor in such a racing car application, which underscore the challenges involved in the design of such a motor-drive system and its cooling apparatus.

Using the motor load profile, the distribution of the motor output energy consumed over the entire driving cycle can be obtained from the torque times speed product and the corresponding time spent at this condition, as shown in Fig. 6.12. In Fig. 6.12(b), the concentration of the load operating points along the maximum torque line reveals the importance of efficient and reliable field weakening operation of this motor.

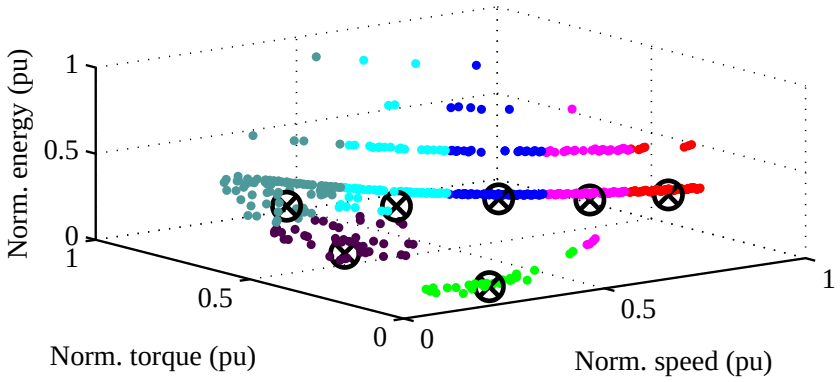

(a) Isometric view

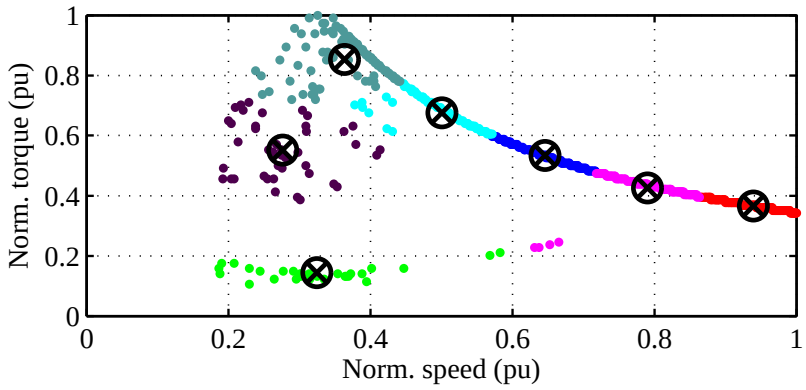

(b) Bird's-eye view

Figure 6.13: Le Mans driving cycle representative points obtained from k-means algorithm with seven clusters.

The high energy-throughput-zones in the torque-speed plane are identified through the k-means clustering algorithm with seven clusters. The number of the clusters is chosen in order to, on the one hand, provide a reasonable estimation of the energy distribution function, and on the other hand, efficiently model the multitude of the load operating points with a small number of cyclic representative points.

The centroids of these clusters are listed in Table 6.2 and are marked in Fig. 6.13. The centroids of the top five clusters, over which most of the energy is consumed, are

Table 6.2: Cyclic representative points of Le Mans driving cycle shown in Fig. 6.13.

i	$\omega\,(rad/sec)$	$T\,(Nm)$	energy weight w
ω_{base}	628	105	NA
ω_{max}	1257	40	NA
1	814	61	0.2245
2	1184	42	0.2213
3	995	49	0.2161
4	631	77	0.1675
5	458	97	0.1343
6	348	63	0.0298
7	409	16	0.0065

used for drive-cycle performance evaluation of the design members throughout the optimization process.

It is interesting to notice that, similar to the distribution of the load operating points, the majority of the cyclic representative points are located on the envelope of the torque-speed plane in the extended speed range in this racing drive cycle.

A parametric 2-D FE model of the all-tooth-wound machine is developed in Ansys Maxwell for the 18-slot, 16-pole spoke-type IPM motor. The parametrization of the stator open slot structure and the rotor spoke-type layout is described in Appendix I. As can be seen in Fig. 6.14, the SmCo PMs are segmented radially as well as axially to minimize eddy current losses in the magnets. The designated design variables and their bounds are listed in Table 6.3. They are so defined to allow full exploration of the design space without causing any interference between surfaces of various components.

The main geometric design constraints are the stator outer diameter and the rotor inner/shaft diameter which are equal to $80mm$, and $30mm$, respectively. Accordingly, the stack length of each design candidate is adjusted to produce a torque of 110 Nm at 6,000 r/min. Furthermore, for all the design members throughout the optimization

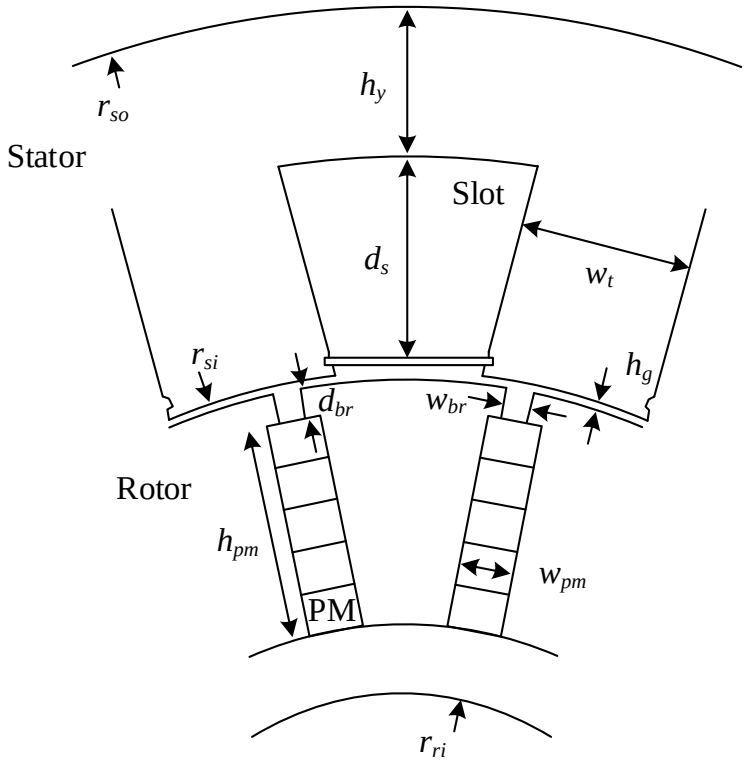

Figure 6.14: The parameterized FE model of the spoke-type PM motor, see Table 6.3.

Table 6.3: Independent design variables and their upper and lower bounds of the 18-slot 16-pole spoke-type machine.

Parameter(x_i)	Description	$x_{i,min}$	$x_{i,max}$
k_{si}	r_{si}/r_{so}	0.60	0.75
h_g	Fig. 6.14	0.7 mm	2.5 mm
k_{w_t}	w_t/α_s	0.45	0.75
$k_{h_{pm}}$	$h_{pm}/h_{pm,max}$	0.55	0.95
$k_{w_{pm}}$	$w_{pm}/w_{pm,max}$	0.2	0.6
$k_{w_{br}}$	w_{br}/w_{pm}	0.35	0.65
d_{br}	Fig. 6.14	1.5 mm	3.0 mm
h_y	Fig. 6.14	7 mm	15 mm

process, the slot fill factor is assumed to be 0.4, and the temperatures of the stator windings and PMs are assumed to be 160 $^{\circ}C$, and 120 $^{\circ}C$, respectively.

Due to heavy saturation and cross-saturation of the high power density motor, linear parameter models cannot be used to characterize the performance of the design candidates. Instead, the two-stage approach presented in Section 5.3 is adopted for this purpose. In the first place, FE simulations with a minimum number of magnetostatic solutions are used to generate look-up tables of samples of the stator winding d-axis and q-axis flux linkages over the second quadrant of the current dq-plane for motoring operation. Using the flux linkage look-up tables, the developed torque and the induced voltages are computed, and are subsequently incorporated for determination of the current excitation required for producing the torque and speed at each representative operating point. The current excitation is determined taking into account the current and voltage limits of the motor-drive system in the constant torque, and field weakening regions.

Upon derivation of the current excitation, a detailed FE solution is carried out at each representative load point to calculate: (a) power losses including the core losses, copper losses, and the PM eddy current losses, (b) torque ripple, and (c) minimum flux density in the PMs. As for the latter, the PM demagnetization is also evaluated under short circuit conditions when the rated current is fully imposed on the negative d-axis direction. These performance metrics, in addition to the machine total mass, are subsequently used to compare the merits of the different design solutions in the optimization algorithm.

After obtaining the machine performance metrics over each operating point, the

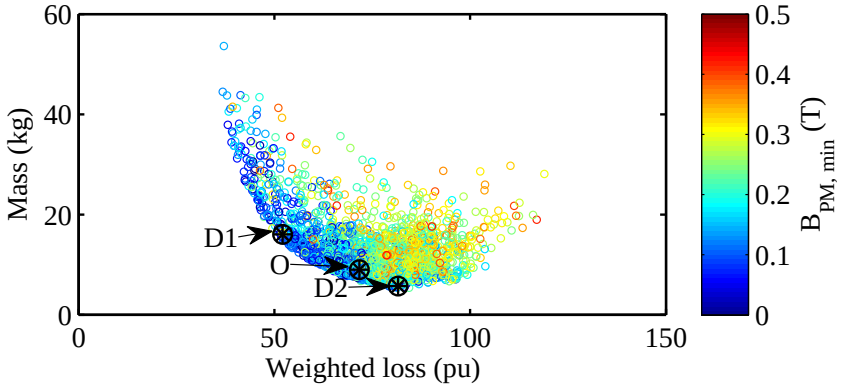

(a) Color-coded for PM minimum flux density

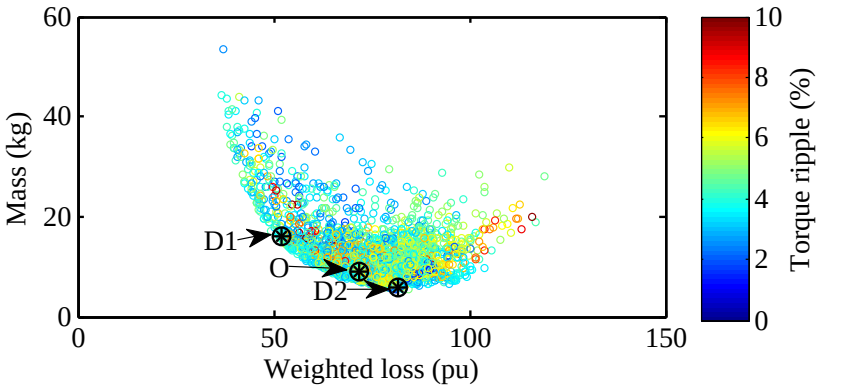

(b) Color-coded for torque ripple

Figure 6.15: The results of optimization of the spoke-type IPM over 3,400 design solutions.

CMODE-type search algorithm is utilized for converging toward the optimal design solutions. In this multi-objective design optimization, the two following objectives are considered:

1. Minimization of the machine weight for the given peak torque of 105 Nm at $6\,000 r/min$.

2. Minimization of losses over the high-energy-throughput zones according to Eq. (6.2.1).

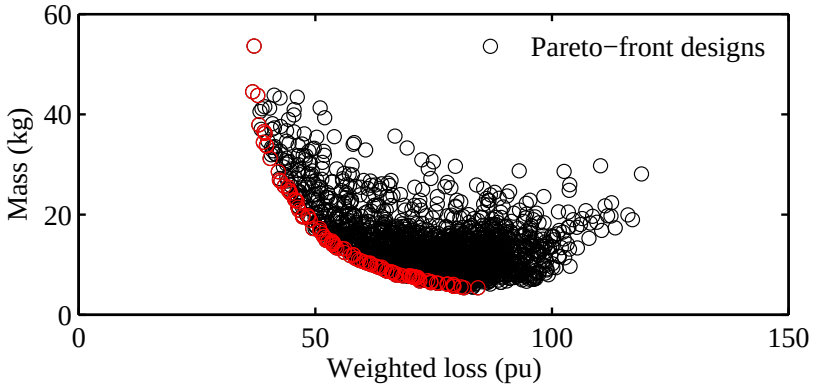

(a) Selected Pareto-optimal designs

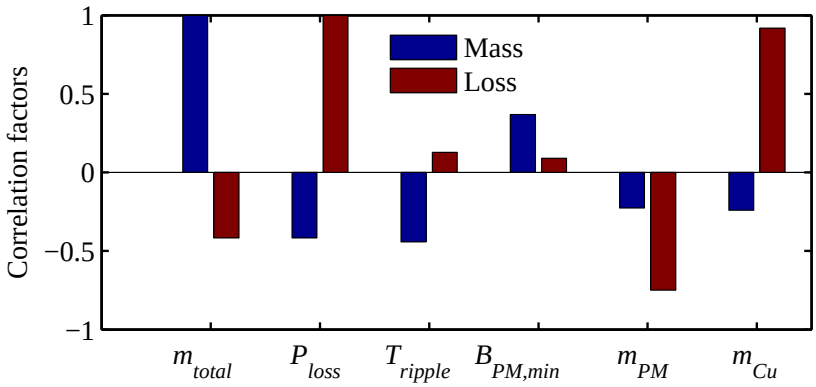

(b) Correlation factors

Figure 6.16: Correlation of performance metrics with mass and power losses in the designs optimized for efficiency and high power density.

In addition, two performance constraints are defined in order to:

1. Restrain the maximum toque ripple below 5% at all operating points.

2. Prevent the excessive demagnetization of the rotor PMs over the entire range of current excitation, i.e. to maintain the degree of PM demagnetization above 20% of the retentivity.

6.3.2 Optimization Results

The drive-cycle design optimization of the spoke-type IPM motor over the Le Mans cycle under the aforementioned objectives and constraints was carried out for 3 400 design candidates. The results of this large-scale design optimization shown in Fig. 6.15 suggest that motor mass is strongly related to other design characteristics which is described in the following section.

6.3.2.1 Performance Trade-Offs for Achieving High Power Density

To investigate these relationships, Pearson correlation coefficients given in Eq. (6.3.2) were calculated for the 100 Pareto-optimal designs marked in red in Fig. 6.16(a).

$$\rho_{X,Y} = \frac{\mathrm{Cov}(X,Y)}{\sigma_X \sigma_Y} \tag{6.3.2}$$

where X and Y are the statistic population of the respective design characteristics in the 100 Pareto optimal members, Cov is the covariance, and σ is the standard deviation.

Accordingly, as can be seen in Fig. 6.16(b), the total masses of the selected designs are inversely proportional to power losses, torque ripple, and mass of PM and copper. In other words, to increase the power density, larger amounts of PM and copper are to be used. Meanwhile, increased power density translates to higher power losses, larger torque ripple, and greater demagnetization of the PMs.

It is interesting to note that as opposed to the torque density, the power losses constitute a strong positive correlation with the copper mass, suggesting the conflicting influence of copper mass on the two objectives in a multi-objective design approach. Furthermore, the negative correlation of power losses with PM mass

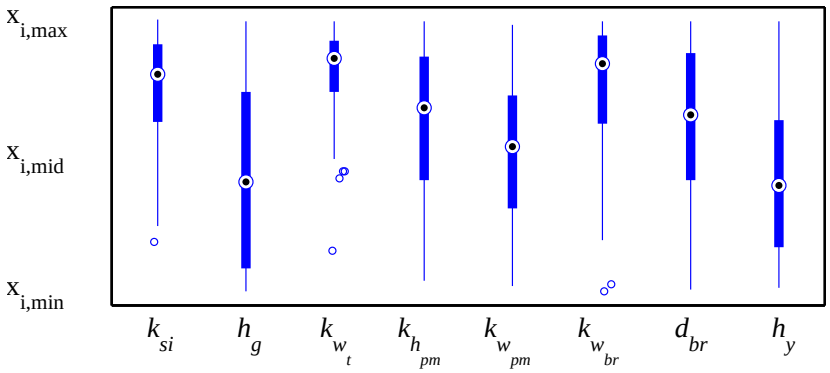

(a) Box plots of the design paramteres

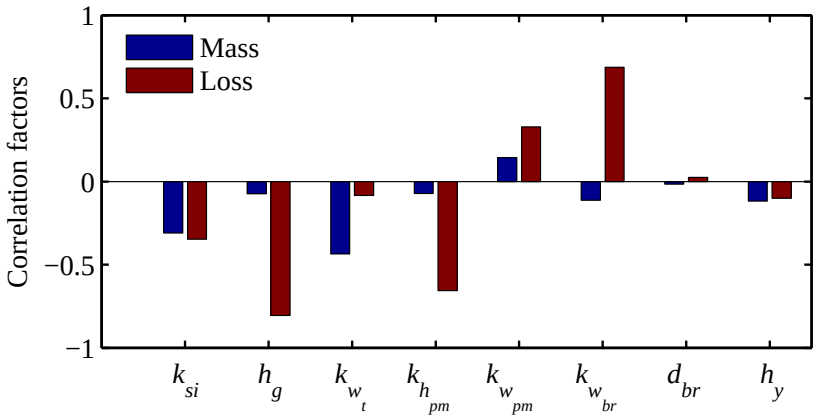

(b) Correlation factors

Figure 6.17: Distribution of the design parameters in the Pareto-optimal designs, and their correlation with total mass and power losses.

indicates that the designs with greater power losses are expected to utilize less PM material.

To unscramble the relationships between the design parameters listed in Table 6.3 and the power density and power losses, the distribution of the design parameters within their predefined bounds in the Pareto-optimal designs, Fig. 6.17(a), and their correlations with the two objectives, i.e. power density and drive-cycle efficiency, Fig. 6.17(b), should be examined.

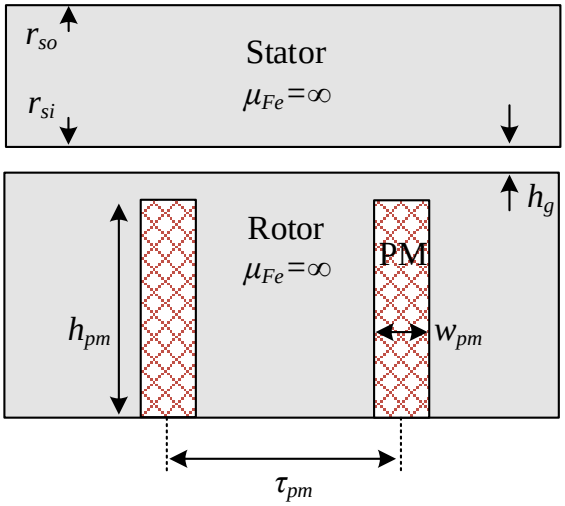

Figure 6.18: Equivalent machine model used for analytical investigation of the optimal design of spoke-type FSCWs.

Accordingly, the design parameters which constitute negative correlations with both mass and losses, and thus are relatively confined within narrower upper bands are the split ratio, k_{si}, and the tooth-stem width ratio, k_{w_t}. In essence, to simultaneously achieve high power density and high efficiency, these two parameters are expected to assume higher values.

Base on an analytical investigation of the optimal design of spoke-type FSCWs, with assumptions of infinite core permeability and slot-less stator as illustrated in Fig. 6.18, it was reported in [179] that the optimal values for the two critical design parameters, namely, the split ratio, $k_{si} = r_{si}/r_{so}$, and PM thickness ratio, $k_{w_{pm}} = w_{pm}/\tau_p$, are respectively in the range of 0.5-0.55, and 0.4-0.5, respectively, for a high power density 18-slot 16-pole machine, similar to the configuration studied in this paper. However, according to the results of the large-scale design optimization,

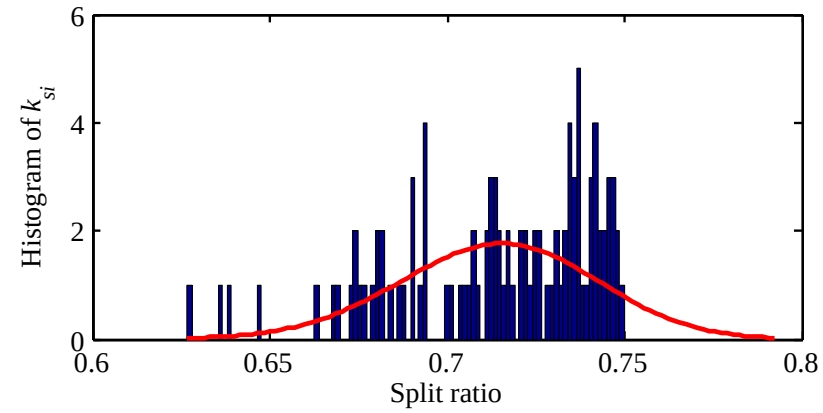

(a)

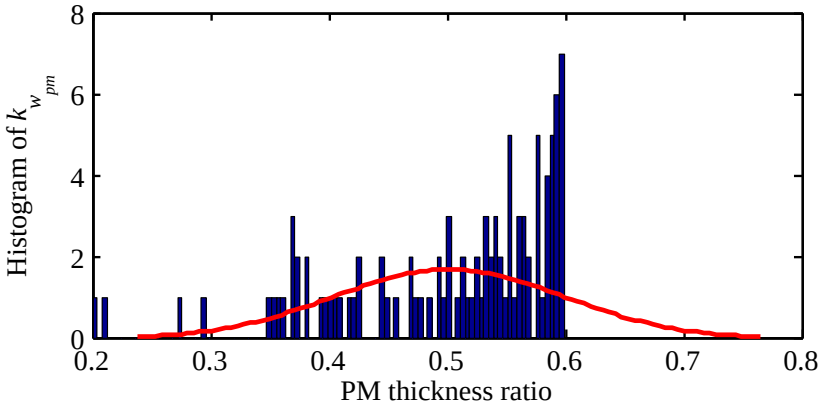

(b)

Figure 6.19: Histogram of the distributions of (a) k_{si}, and (b) $k_{w_{pm}}$ in the 100 Pareto-optimal designs.

in a practical case, when non-linearity of the ferrous core, various loss components, and complex geometry of the machine is fully taken into account, optimal ranges other than those derived by analytical models are obtained, see Fig. 6.19 for the histogram of the k_{si}, and $k_{w_{pm}}$ parameters in the Pareto-optimal designs. These results underscore the importance of using high-fidelity models for derivation of optimal design rules in such high power density and highly saturated machines.

Table 6.4: The design characteristics of the counterpart spoke-type motors.

	$m_{total}(kg)$	$P_{loss}(pu)$	$T_{ripple,rated}(\%)$	$B_{PM,min}(T)$	$m_{PM}(kg)$	$m_{Cu}(kg)$
D1	16.1	52.0	3	0.31	2.14	0.7
O	9.1	71.7	4.5	0.29	1.00	0.7
D2	5.9	81.6	4	0.36	0.98	0.8

6.3.2.2 Increasing Efficiency or Power Density

From the Pareto-optimal design solutions, two feasible design candidates, which do not violate the performance constraints imposed on the torque ripple and degree of PM demagnetization, denoted by "D1", and "D2" in Fig. 6.15, are selected. The designs "D1", and "D2" feature minimum gross power losses, and maximum power density, respectively . A comparative analysis between these designs with respect to a design denoted by "O" in Fig. 6.15, which establishes a compromise performance, is carried out in this section.

The cross-sections and the flux line distributions under rated load conditions of these three machines are shown in Fig. 6.20. Their main design features are compared in Table 6.4. As can be seen in Fig. 6.20, the saturation becomes more prevalent throughout the ferrous core as the power density increases.

The efficiency maps of the three counterpart designs are provided in Figs. 6.21(a) through (c). The high efficiency contours of the optimized design "D1" are expanded towards the representative load points with the highest energy weights, see Table 6.2, which are distributed along the high torque, and high speed vicinity. The design "D2" has diminished efficiency, mainly due to the elevated copper losses, as opposed to the core losses which are confined by the saturation phenomena and by the lower

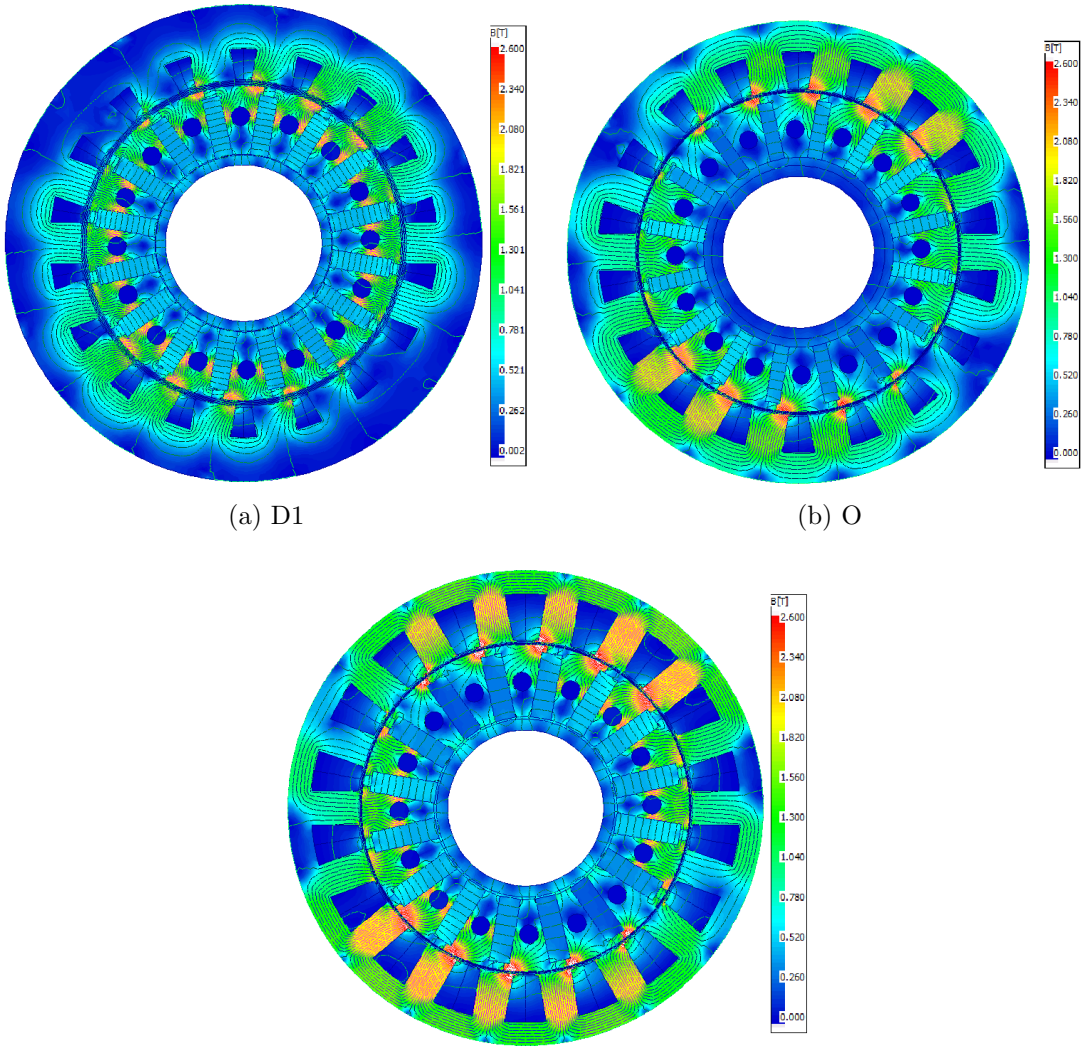

(a) D1

(b) O

(c) D2

Figure 6.20: Flux lines distributions of the optimized designs at 6 000 r/min under rated load.

Table 6.5: The design characteristics of the optimized high power density "D3" motor.

	$m_{total}(kg)$	$P_{loss}(pu)$	$T_{ripple}(\%)$	$B_{PM,min}(T)$	$m_{PM}(kg)$	$m_{Cu}(kg)$
Original Formula E (AIM)	9.1	71.7	4.5	0.29	1.0	0.7
Optimized Design	7.7	70.6	3.3	0.34	1.0	0.7

volume of the magnetic core in this design. This can be seen in the copper loss and core loss maps provided in Figs. 6.22 and 6.23, respectively.

6.3.2.3 Increasing Efficiency and Power Density

The results of the optimization suggest that although the original design is a very well conceived one, its mass and gross losses can be further decreased simultaneously. From the Pareto-optimal design solutions, a design candidate denoted by "D3" in Fig. 6.24, which features a higher power density and lower weighted drive-cycle power losses, is selected for a comparative analysis with respect to the original design.

The cross-sections and the flux line distributions under open circuit, and rated load conditions of the two machines are shown in Fig. 6.25. Their main design features are compared in Table 6.5, according to which the optimized design has also a lower torque ripple and lower degree of PM demagnetization. As can be seen in Fig. 6.25, the saturation is more prevalent throughout the ferrous core of the optimized design due to the stronger rotor field.

The efficiency map of the optimized design "D3" is provided in Fig. 6.26. The efficiency map of the original design is also repeated in Fig. 6.26 for comparison. It can be seen in Fig. 6.26 that the high efficiency contours of the optimized design are directed towards the representative load points with the highest energy weights, see Table 6.2, which are scattered along the high torque, and high speed vicinity.

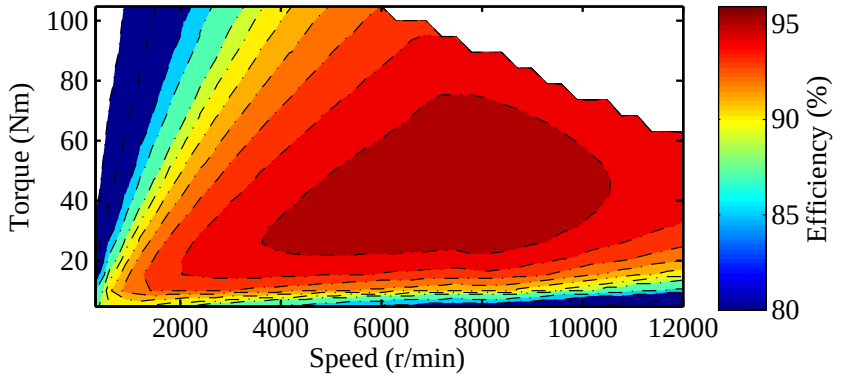

(a) D1

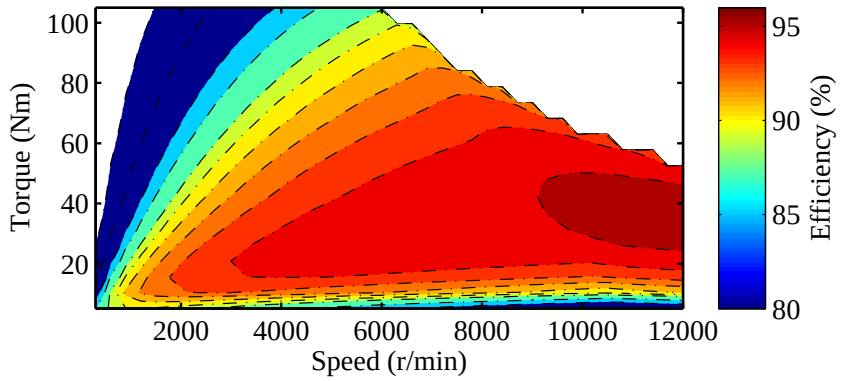

(b) O

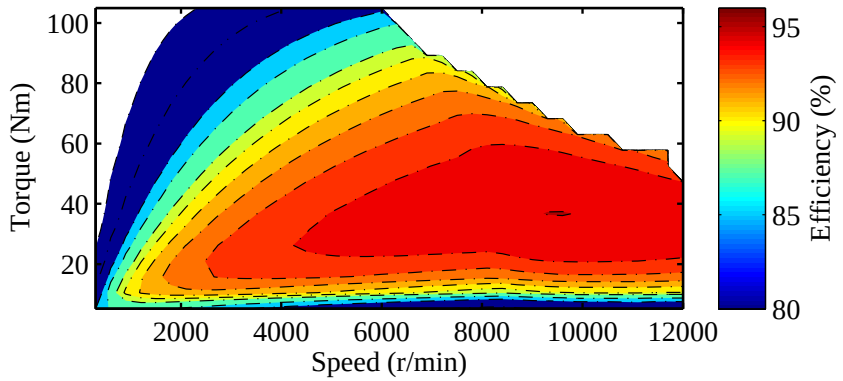

(c) D2

Figure 6.21: Efficiency maps of the optimized spoke-type designs.

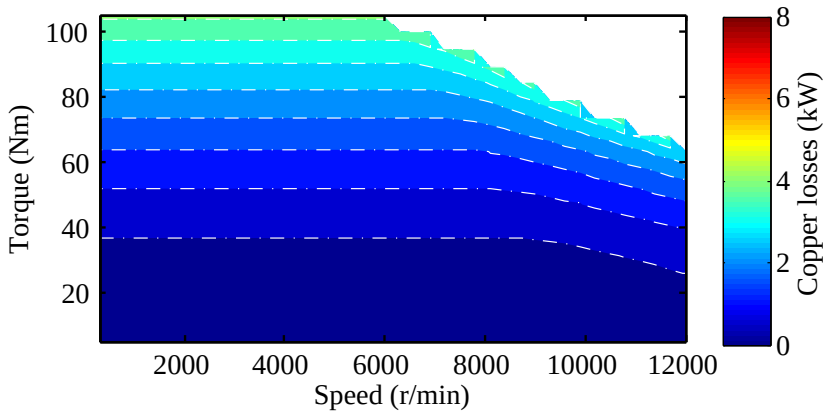

(a) D1

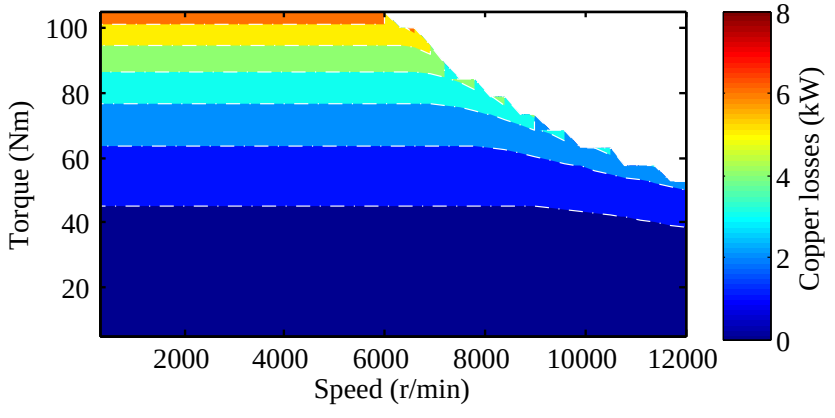

(b) O

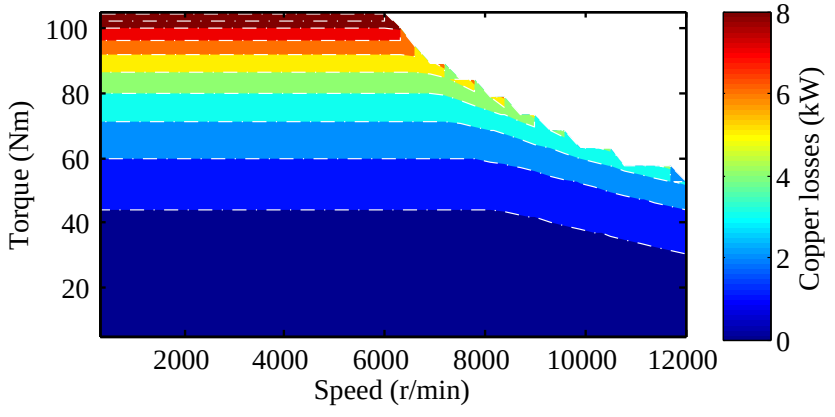

(c) D2

Figure 6.22: Copper loss maps of the optimized spoke-type designs.

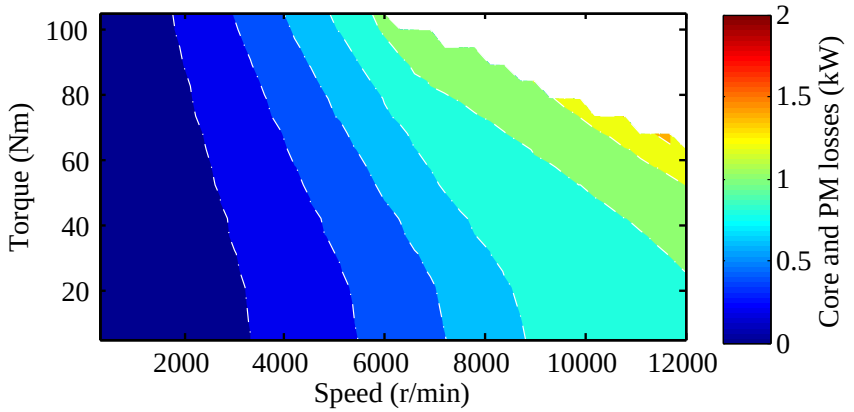

(a) D1

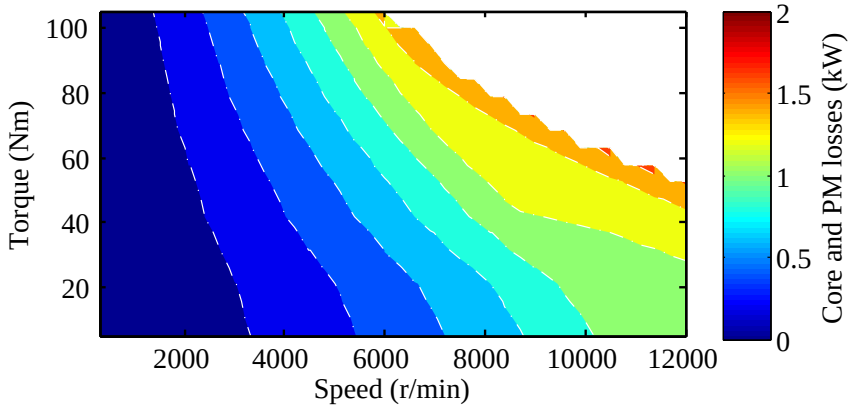

(b) O

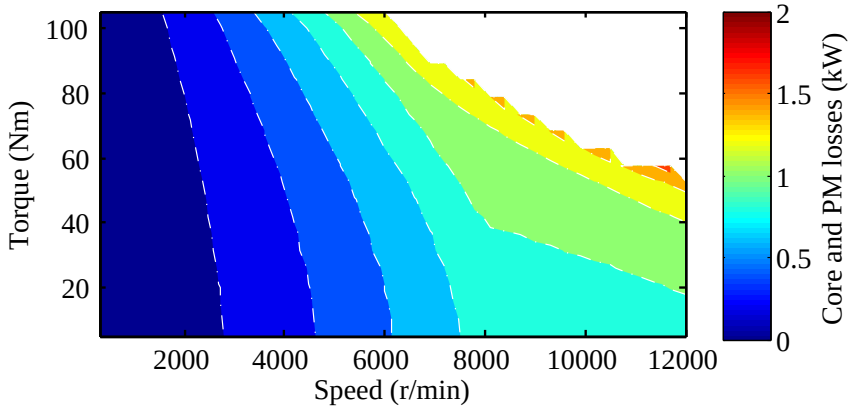

(c) D2

Figure 6.23: Core loss maps of the optimized spoke-type designs.

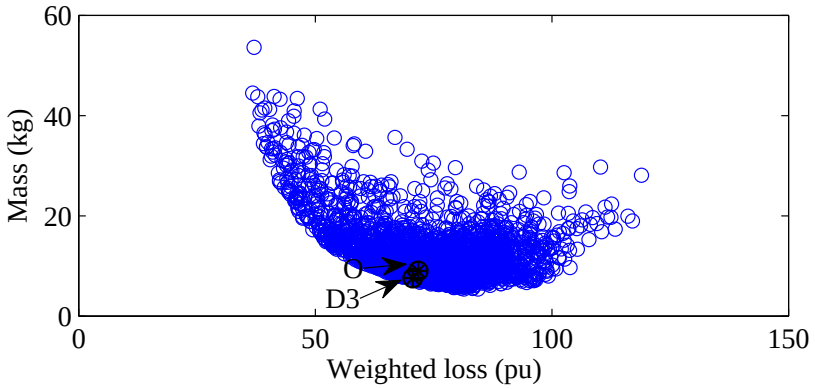

Figure 6.24: Identifying a design with higher power density and drive-cycle efficiency than the original design.

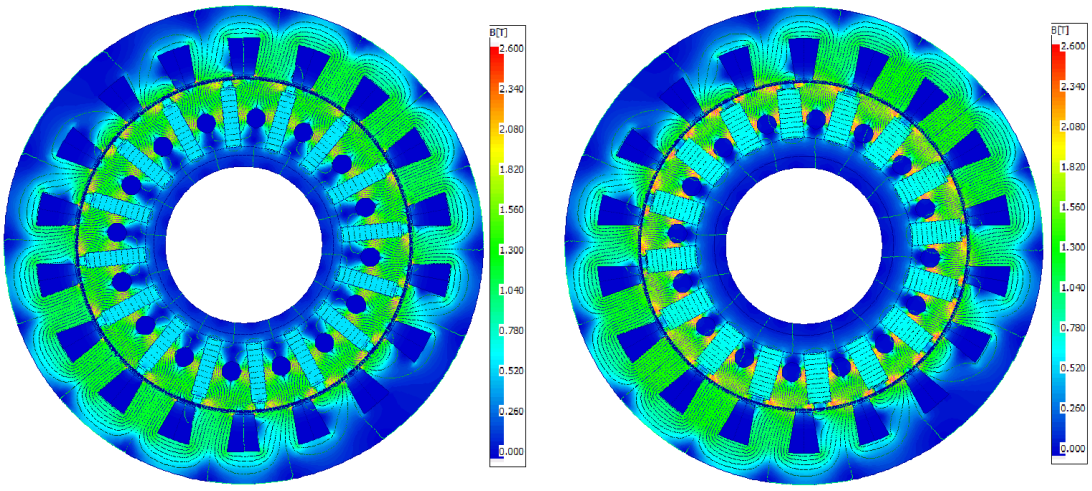

(a) Original, open circuit

(b) "D3", open circuit

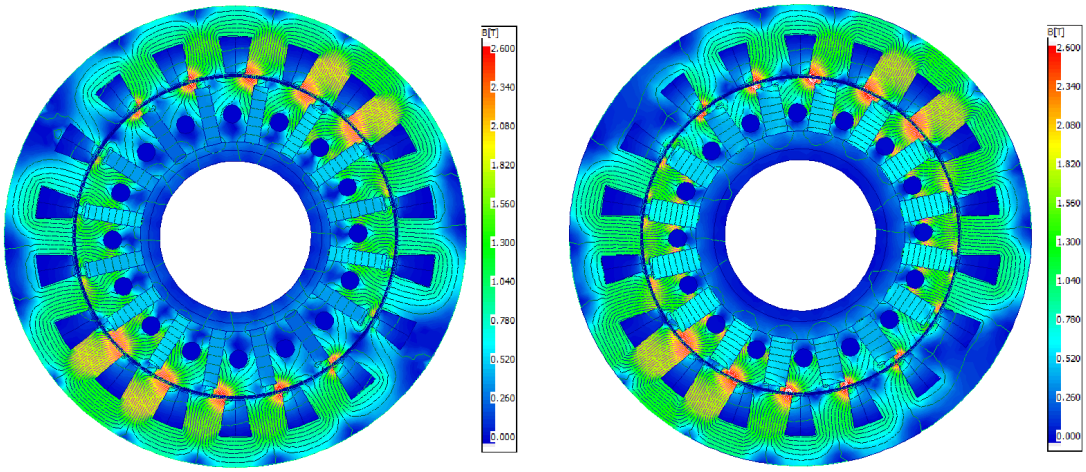

(c) Original, rated load

(d) "D3", rated load

Figure 6.25: Flux lines distributions at 6000 r/min.

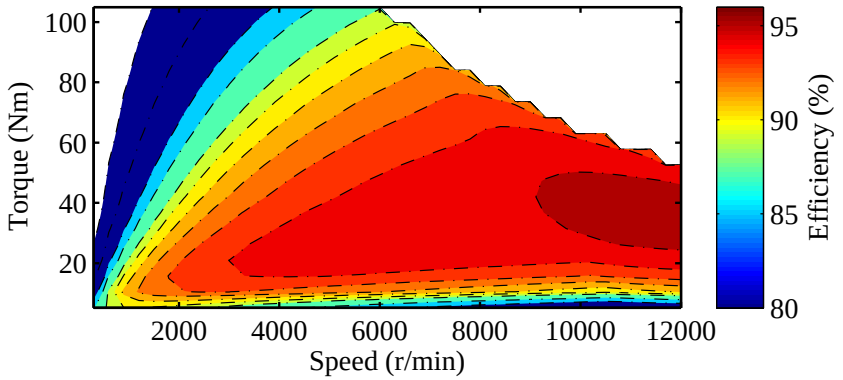

(a) O

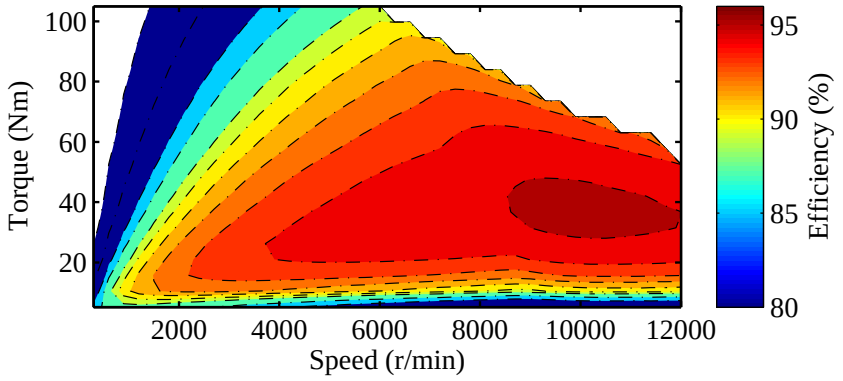

(b) D3

Figure 6.26: Efficiency maps of the high power density spoke-type designs.

Furthermore, the optimized design has better torque production capability in the extended speed range.

6.4 Summary

In the first case study, the large-scale CMODE-type design optimization approach was successfully performed on the Toyota Prius Gen. 2 IPM traction motor, and the results were verified through multi-physics performance analysis of the optimized designs.

The optimization results confirmed the cost-effectiveness of the original motor design. However, the large-scale multi-objective optimization was able to provide alternative designs with higher drive-cycle efficiency, and with minimum additional cost compared to the original design.

The second case study was performed on a high power density spoke-type PM motor to further increase the power density of the original design. The performance trade-offs associated with achieving high power density in such motors were investigated. It was demonstrated that, in general, high power density is directly correlated with higher losses, higher torque ripple, and larger PM demagnetization. Furthermore, larger amounts of copper and PM are to be used in high power density motors. The developed design optimization method was able to increase the power density of the original design by 15%, and at the same time decrease the drive-cycle power losses by 1%.

CHAPTER 7

ADDITIONAL IMPLICATIONS OF PM MACHINES' DESIGN OPTIMIZATION

In this chapter, three different aspects of design optimization of PM machines are investigated.

In the first section, a numerical technique is developed for sensitivity analysis of active material cost (AMC) in PM motors with distributed and fractional slot concentrated windings. A comprehensive analysis is carried out to identify how the optimal design rules and proportions of IPM motors with sintered NdFeB magnets vary with respect to the changes in the commodity prices of permanent magnet material, copper, and steel. The sensitivities of the correlations between the design parameters and the AMC with respect to the commodity price ranges are investigated based on response surface methodology (RSM) and large-scale design optimization practice using differential evolution (DE) optimizer. An innovative application of artificial neural network (ANN)-based design optimization is introduced. Multi-objective minimization of cost and losses is pursued for an overall of 200,000 design candidates in 30 different optimization instances subjected to different cost scenarios according to a systematic design of experiments (DOE) procedure. An interesting finding is that, despite common expectations, the average mass of steel in the optimized designs is more sensitive to changes in the commodity prices than the masses of copper and rotor PMs.

In the second section, a fast FE-based method for calculation of eddy current losses in the stator windings of randomly wound electric machines will be presented. The method is particularly suitable for implementation in large-scale design optimization algorithms where a qualitative characterization of such losses at higher speeds is most beneficial for identification of the design solutions which exhibit lowest overall losses including the ac losses in the stator windings. Unlike the common practice of assuming a constant slot fill (SF) factor for all the design variations, the maximum SF in the developed method is determined based on the individual slot structure/dimensions and strand wire specifications. Furthermore, in lieu of detailed modeling of the conductor strands in the initial FE model, which significantly adds to the complexity of the problem, an alternative rectangular coil modeling subject to a subsequent flux mapping technique for determination of the impinging flux on each individual strand is pursued. The research focus of the chapter is placed on the development of a computationally efficient technique for the ac winding loss derivation applicable to design optimization, where both the electromagnetic and thermal machine behaviors are accounted for. The analysis is supplemented with an investigation of the influence of the electrical loading on ac winding loss effects for a particular machine design, a subject which has received less attention in the literature.

The last section of this chapter is dedicated to a revealing investigation of the mechanical design of the rotor bridges in a typical single-layer V-type rotor PM layout, similar to the one used throughout this dissertation. Particularly, the approximate calculation of the centrifugal forces on the rotor bridges at high rotational speed which is required to be estimated for adjustment of the width of the rotor bridges to,

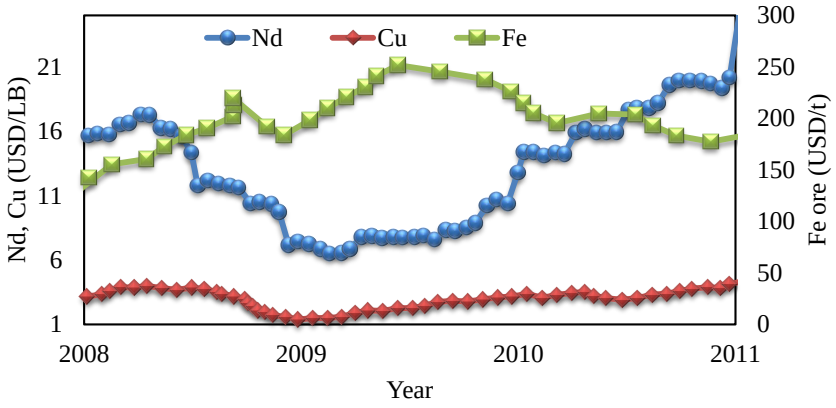

Figure 7.1: Variation of the price of constructive commodities of Nd-based PM motors for three consecutive years leading the surge of the Nd price in 2011 [4, 5].

on the one hand, withstand the maximum mechanical stress and, on the other hand, minimize the leakage PM flux, which is magnetically shorted through these bridges, will be discussed here. An analytical method to approximate the structural stress due to centrifugal forces is implemented and its accuracy is compared to high fidelity structural analysis using FEM.

7.1 RSM-DE-ANN Sensitivity Analysis of Material Cost in PM Motors with Distributed and Concentrated Windings

The price of active material from which PM motors are constructed, especially the NdFeB- magnets, has experienced steep variations in the last few years. Figure 7.1 shows such variations over three consecutive years prior to the surge of the Nd price in 2011 [4, 5, 182].

The minimization of such PM motor cost by eliminating the dependency on the

rare-earth PMs as in [183, 184], or by maximizing the effective utilization of costly PM materials using optimization procedures as in [88, 185], has been the subject of numerous studies. As for the latter case, a popular practice is to minimize the cost associated to the active materials which are utilized in the machine construction. Accordingly, a cost function is commonly defined as in (7.1.1) by aggregating the masses of the active materials which are weighted by price coefficients corresponding to their market values:

$$AMC = [p_{pm}, p_{cu}, p_{fe}] \cdot [m_{pm}, m_{cu}, m_{fe}]^T \tag{7.1.1}$$

where $[p_{pm}, p_{cu}, p_{fe}]$ and $[m_{pm}, m_{cu}, m_{fe}]$ are the commodity price coefficient vector and the commodity mass vector, respectively.

One of the early investigations which incorporated this cost model is the work of Lovelace et al. [74, 186], according to which the cost factors of 5 USD per unit weight (USD/w), 1 USD/w, and 11 USD/w were respectively considered for copper, steel, and bonded Ferrite for IPM machines. Other investigators have adopted this method of machine cost modeling with different price coefficients depending on the market values and material specifications in their design optimization endeavors. In their series of works, Zhang et al. assumed price coefficients of 8, 1, and 140 [85], or 8, 1, and 65 [88] for copper, lamination steel, and sintered NdFeB PMs, whereas Duan and Ionel assumed price coefficients of 10, 1, and 100 [87], and Fatemi et al. assumed price coefficients of 3, 1, and 24 [108–110] for the corresponding materials. Also in [187], price coefficients of 6, and 140 were assumed for copper and PMs, respectively.

As stated above, based on the material specifications and market values, different

price coefficients have been incorporated in the definition of the cost model in Eq. 7.1.1. However, a systematic investigation of dependency of active material cost of PM motors on the changes in the prices of such motors' construction commodities, to the best of these investigators' knowledge, is not available in the literature. Furthermore, although in all of aforementioned investigations various PM machine topologies were optimized for cost minimization, the question still remains as to whether and how the optimal design of such machines varies with respect to the assumed commodity price coefficients.

In this regard, two sets of sensitivity analyses on two generic industrial IPM motor topologies with distributed and concentrated winding configurations are conducted in this chapter. In the first set, the change of the design parameters' impacts on the motor active material cost (AMC) due to variations in the price coefficients in a typical cost function, similar to that expressed in Eq. (7.1.1), will be investigated. In the second set, the sensitivities of the distribution of the design parameters in the optimized candidate designs, which were obtained from large-scale optimization processes, to the changes in the commodity price coefficients are presented.

7.1.1 FE-Based Machine Models

Two IPM machine configurations that were previously introduced in Section 3.2 are chosen for this analysis. The vectors of the design parameters defined over the cross sections of the two machines are given in Eq. (7.1.2), and Eq. (7.1.3) for the 48-slot 8-pole, 48S8P, and the 12-slot 10-pole, 12S10P, machines, respectively. These design parameters and their bounds are identical to those previously described in Section

3.2.

$$\bar{X}_{48S8P} = (k_{si}, h_g, k_{wt}, k_{wtt}, k_{dPM}, k_{wPM}, k_{wq}, h_{PM}, \alpha_{PM}, h_y)^T \tag{7.1.2}$$

$$\bar{X}_{12S10P} = (k_{si}, h_g, k_{wt}, k_{dPM}, k_{wPM}, k_{wq}, h_{PM}, \alpha_{PM}, h_y)^T \tag{7.1.3}$$

The two following performance metrics are evaluated using the FE models:

- Active material cost (AMC) according to Eq. (7.1.1).
- Power losses including dc copper losses, PM eddy current losses and core losses at 100 °C.

7.1.2 Effects of the Commodity Price on the Design Correlations

The correlation between the AMC defined in Eq. (7.1.1) and the design vectors given in Eq. (7.1.2) and Eq. (7.1.3) is bilateral; that is, on the one hand, for a given set of commodity price coefficients, the design parameters determine the AMC. On the other hand, the influences of the design parameters on the AMC are by themselves a function of the commodity price coefficients. In this section, these bilateral effects of design parameters and commodity price coefficients on the AMC will be discussed. For this purpose, the information about the range of the changes of the design parameters and the commodity price coefficients are required. The range of the design parameters are designated in Table 3.1 whereby wide ranges are assumed to fully explore the design space. As for the vector of the commodity price coefficients, a range of [50, 4, 1] to [100, 8, 2] is assumed based on realistic variations

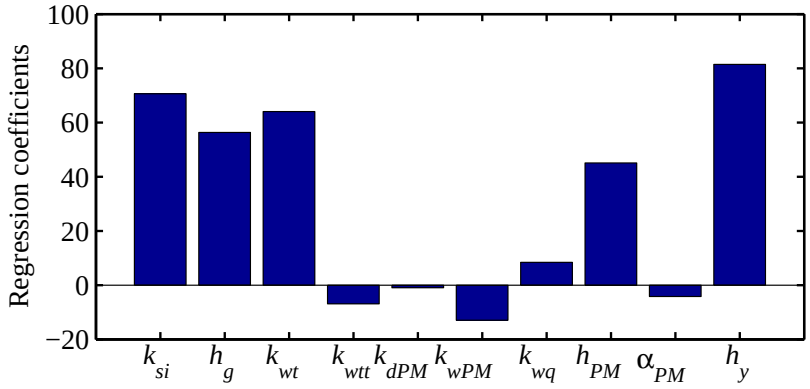

(a) 48S8P motor configuration

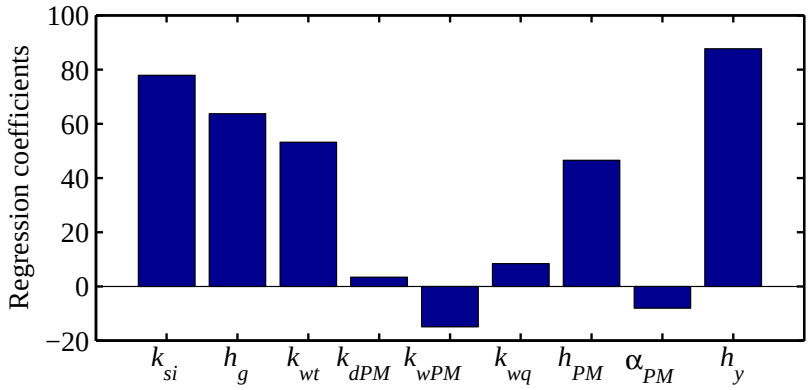

(b) 12S10P motor configuration

Figure 7.2: Influence of the design parameters on AMC in the two case-study motors.

of the utilized materials, i.e. sintered NdFeB magnets, electrical steel, and copper, within the next few years.

In the first place, a sensitivity analysis is carried out to understand how the changes in the design parameters influence the AMC for the mid-range of the commodity price coefficients, i.e $p_{PM} = 75, p_{Cu} = 6, p_{Fe} = 1.5$. The regression coefficients of the second order response surface associated with AMC which are given in Eq. (3.3.1) are calculated for the two 48S8P, and 12S10P configurations, and are illustrated in Fig. 7.2(a) and (b), respectively.

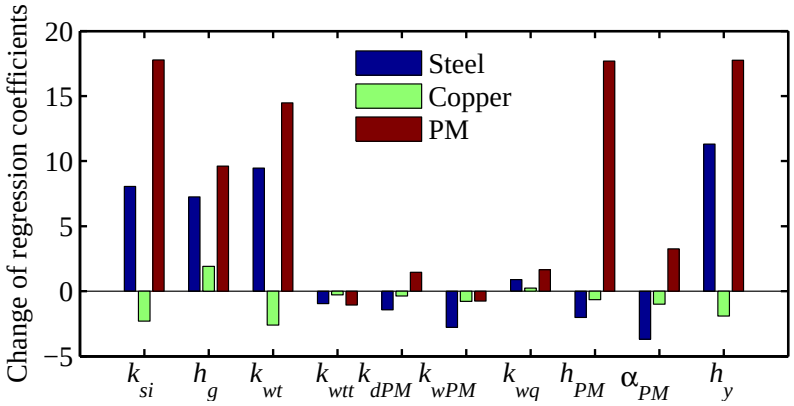

(a) 48S8P motor configuration

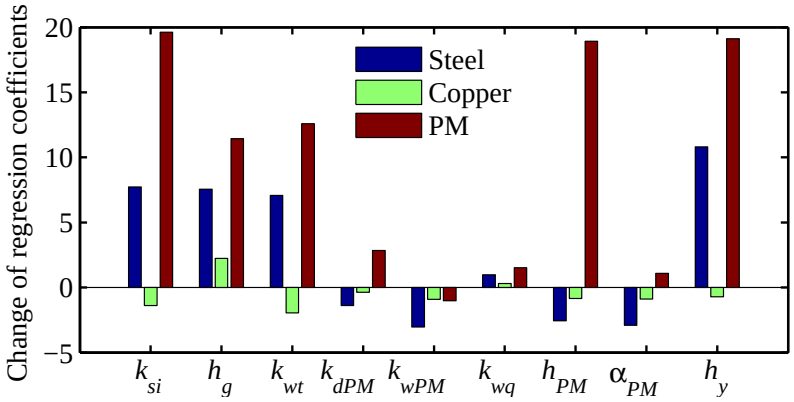

(b) 12S10P motor configuration

Figure 7.3: Change of the influences of the design parameters on AMC based on the value of the commodity price coefficients.

For both motor configurations, the split ratio, k_{si}, air-gap height, h_g, tooth-stem width, k_{wt}, PM height, h_{PM}, and yoke height, h_y, show the strongest positive correlation with AMC, indicating that an increase in these parameters would add to AMC. It is interesting to note that despite the fact that the PM has the greatest price coefficients, the design parameters directly associated with the mass of PM, i.e. k_{wPM}, h_{PM}, and α_{PM} constitute marginal contributors to AMC.

As mentioned previously, the results of the sensitivity analysis shown in Fig. 7.2

are derived for the mid-range of the commodity price coefficients. It is not understood yet whether and how these correlations between the design parameters and AMC would change depending on the variations of the commodity price coefficients. To discern the influence of the commodity price variations on the correlations between the design parameters and AMC, a second set of sensitivity analysis is in order. In this case, the sensitivities of the correlations between the design parameters and AMC due to the changes of the commodity price coefficients are investigated. For this purpose, depending on the motor configuration, ten or nine second order response surfaces are defined according to Eq. (3.3.1) for the correlations of each design parameter of the 48S8P and 12S10P motors, respectively. The regression coefficients for the correlation of each design parameter are solved by a DOE study based on CCD method, which is conceived this time for the coded commodity price coefficients. The results of this analysis are illustrated in Fig. 7.3(a) and (b), for the 48S8P and 12S10P machines, respectively.

Accordingly, it can be seen in Fig. 7.3 that the PM price, due to the greater designated coefficients, followed by the steel price, owing to the larger masses of steel used in the machine construction, show the strongest influences on the correlations of the design parameters on AMC. Particularly, the design parameters which were demonstrated to have the strongest correlations with the AMC for the medium range of commodity price coefficients in Fig. 7.2 are affected most severely. For example, according to Fig. 7.2, increasing the split ratio, k_{si}, translates into higher AMC. Meanwhile, according to Fig. 7.3, the increase of the commodity price coefficients associated with the PM or steel materials further intensifies the already positive

correlation between k_{si} and AMC. Similar trends exist for air-gap height, h_g, tooth-stem width, k_{wt}, PM height, h_{PM}, and yoke height, h_y. That is, on the one hand, increasing these parameters would increase the AMC according to Fig. 7.2, and on the other hand, the increase of PM price, and steel price with the exception of h_{PM}, would make these positive correlations stronger.

Similarly, by comparing the values of the regression coefficients in Fig. 7.3 with those illustrated in Fig. 7.2, it is evident that the strongest changes of the most influencing design parameters due to variations of the commodity prices are in the same direction as the original effects of the design parameters. This fact suggests that the optimal design parameters for AMC minimization should not differ substantially if the price coefficients are changed.

It is also interesting to note that although copper has a higher price coefficient in comparison to ferrous lamination materials, the variation of the copper price does not affect the influence of the design parameters on the AMC in a meaningful way in these case study design examples.

7.1.3 ANN-Based Design Optimization with Different Commodity Price Coefficients

The results of the sensitivity analysis in the previous section demonstrated that the existing correlations between the design parameters and AMC are dependent on the commodity price coefficients, particularly on the price of the PM material and lamination steel. However, it is not clear yet to what extent the optimal ranges of the design parameters for cost-effective design of PM machines change commensurate

with the variations of the active material prices.

To fully explore the degree of this dependency in a practical design problem, where the interactions between various design parameters subject to a set of objectives are involved, an evidence-based study of optimal design of cost-effective PM machines through the large-scale optimization of such machines should be conducted. Subsequently, a sensitivity analysis of the optimal design parameters with respect to the commodity price coefficients, similar to what was performed in the previous section, should be pursued. For this purpose, the optimal design parameters need to be derived for a series of price coefficients which are prescribed by DOE. For the three components of PM, copper, and steel, a second order response surface using CCD method would require 15 distinct runs of large-scale optimization for each motor configuration. To implement a design optimization with such a large extent, surrogate modeling techniques for fast performance characterization of the design candidates are desired. Here, artificial neural networks (ANN) are utilized [188] for this aim.

The ANN-based modeling has been previously investigated in the literature for the design optimization of electromagnetic devices [189–191]. The application of the ANN-based modeling is particularly suitable in the overall procedure for the sensitivity analysis of the optimal design parameters with respect to commodity price variations shown in Fig. 7.4. This is due to the fact that the same machine configuration needs to be modeled in several runs of large-scale design optimizations, here 15 runs for each example machine. The high fidelity FE-based machine models which were developed in the previous section can be used during the first run of the optimization. The resultant design members of this first optimization run can then be

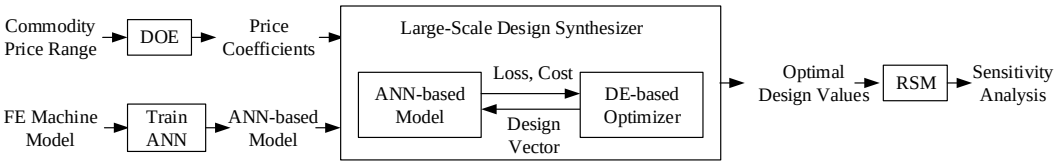

Figure 7.4: Developed procedure for sensitivity analysis of the optimal design values.

utilized to train the artificial neural networks for fast modeling of each corresponding machine configuration in the subsequent optimization runs.

Here, a two-layer feedforward network with one layer of 100 neurons with hyperbolic tangent sigmoid transfer function, followed by an output layer of linear neurons was created in MATLAB. The network was trained using the Levenberg-Marquardt training method using the mean square error performance function [188].

The FE-based models developed in the previous section were used to train the network for computation of the two performance metrics discussed in the previous section. However, instead of calculating the AMC directly, the masses of the constitutive components are obtained to be implemented in the AMC expression in Eq. (7.1.1) with each set of commodity price coefficients, which are determined by DOE, for each run of the optimization. The values of these performance metrics calculated by the developed ANN-based method were compared to the values derived from the FE-based model for a 1000 designs. This is in order to verify that the estimation error of the ANN-based model is less than 1% for the two machine configurations, as can be seen in Fig. 7.5.

The ANN-based models were incorporated into a large-scale design optimization process with two main objectives:

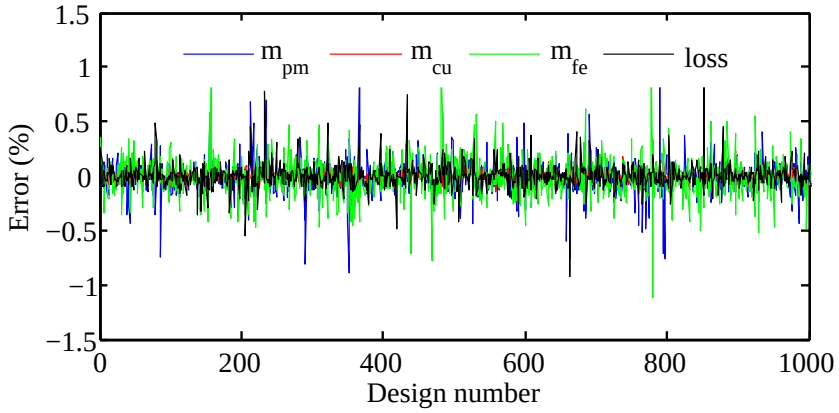

(a) 48S8P motor configuration

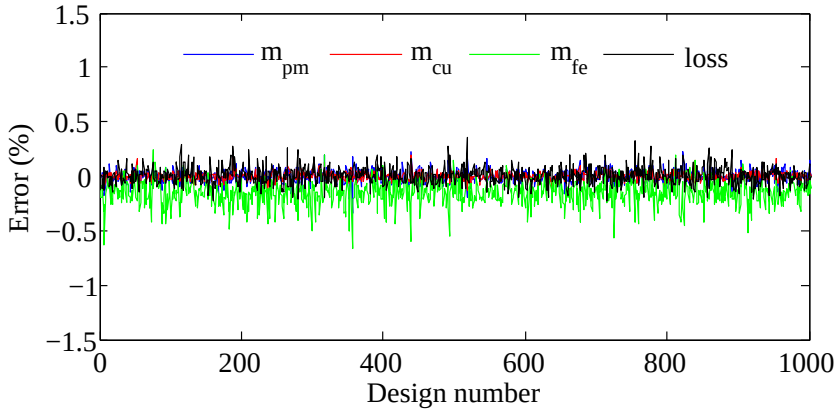

(b) 12S10P motor configuration

Figure 7.5: Estimation error of the ANN-based models when compared to FE-based machine models.

1. Minimization of AMC based on the set of commodity price coefficients generated by DOE.

2. Minimization of power losses including core and copper losses which are estimated using the ANN-based model.

The differential evolution (DE)-based optimizer [110] presented in Chapter 4, was used as the stochastic search engine to identify the Pareto optimal designs. Accordingly, 30 runs of optimization with various sets of price coefficients determined

by DOE were carried out. The optimization results for the mid-range price coefficients expressed in terms of the objectives and color-coded with respect to the cost of the utilized active materials are shown in Figs. 7.6 and 7.7 for the 48S8P and 12S10P machines, respectively.

The correlations between the design objectives and the costs of the individual constitutive active materials in Figs. 7.6 and 7.7 should be pointed out. The cost component associated with the PM material has a strong positive correlation with both high efficiency and AMC. That is, in order increase the efficiency, larger amounts of PM is to be utilized, which in turn translates into higher overall AMC. Similar trends exist between the steel mass and the optimization objectives, although the correlations are not as strong as those attributed to the PM material. Meanwhile, these correlations are reversed between the copper mass and the optimization objectives. That is, as the utilized copper increases, the overall AMC decreases whereas the total losses increase. It is also interesting to note that lesser amounts of copper are required in the construction of the 12S10P machines when compared to the 48S8P machine because of the shorter stack lengths and shorter end windings of the 12S10P machine. However, the 12S10P machine suffers from slightly higher power losses mainly due to the increased rotor core losses.

7.1.4 Sensitivity of Optimal Design Values to Commodity Price Coefficients

In order to understand the dependency of the optimal design of PM machines on the commodity price coefficients, a sensitivity analysis on the averages of the

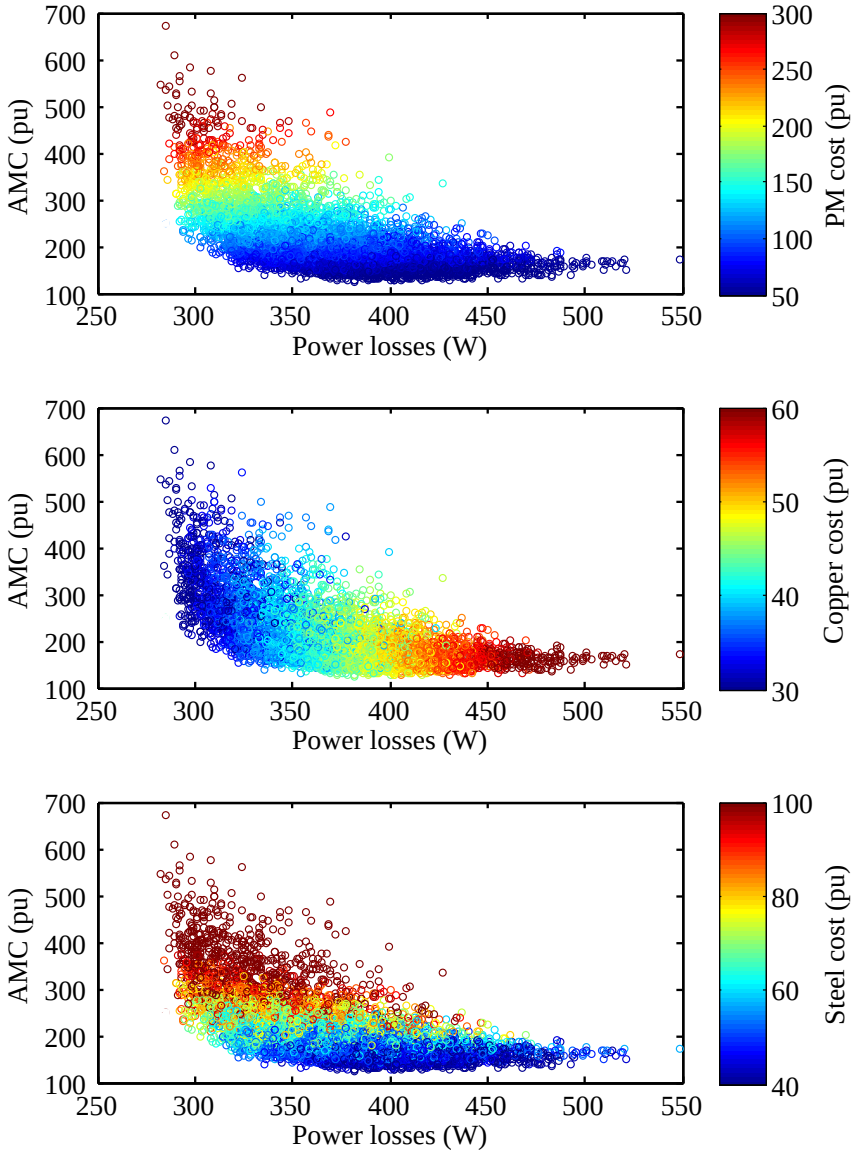

Figure 7.6: Optimization results of the 48S8P motor configuration for a typical set of commodity price coefficients.

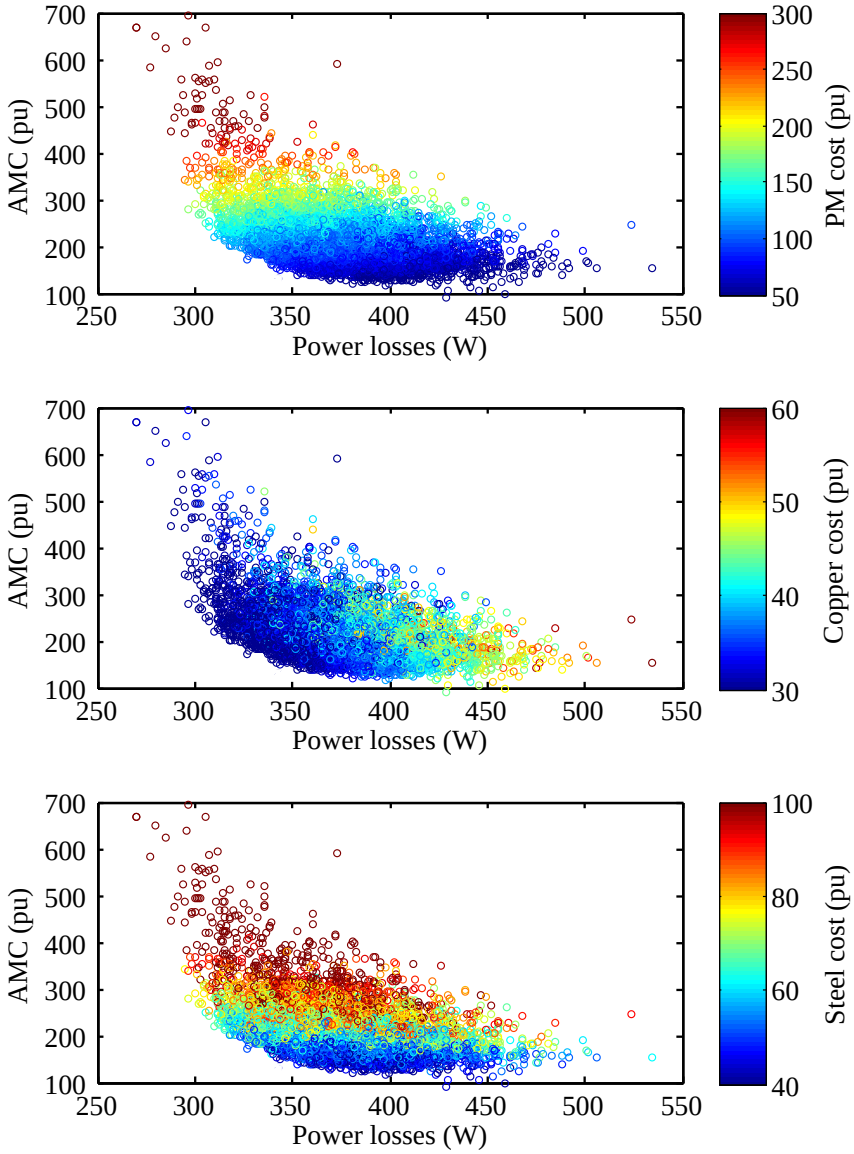

Figure 7.7: Optimization results of the 12S10P motor configuration for a typical set of commodity price coefficients.

design parameters in the optimized designs yielded by each round of optimization is performed in this section. For this purpose, 100 of best design solutions with minimized AMC and losses are identified from each set of optimization results. For each set of the selected designs, the averages of the design parameters are obtained together with the average masses of their active components. Subsequently, a sensitivity analysis similar to what was described in Section 7.1.2 is conducted to reveal how the changes of the commodity price coefficients influence the optimal range of the design parameters. Figures 7.8(a) and (b) show the results of this sensitivity analysis for the the 48S8P, and 12S10P motor configurations, respectively.

According to Fig. 7.8, for both machine configurations, the average values of the optimal design parameters as well as the average masses of the PM material and copper in the optimal designs are not sensitive to changes of the commodity price coefficients. Meanwhile, the average masses of electric steel in the selected optimized designs show the largest correlations with the price coefficients particularly since the mass of the utilized steel in the machine construction is affected by all the design parameters, and thus reflects the aggregate effects of the variations of the commodity price coefficients. As can be seen in Fig. 7.8, an increase in steel price results in lower average steel mass in the optimized designs for both motor configurations. The impacts of changes of copper and magnet prices on the steel mass in the optimal designs differ between the two motor configurations. Most notably, the steel mass is expected to increase if the copper price coefficient in the 48S8P machine, or the PM price coefficient in the 12S10P machine increases. Overall, a comparison between the magnitudes of the regression coefficients in Fig. 7.8 with those provided in Figs. 7.2

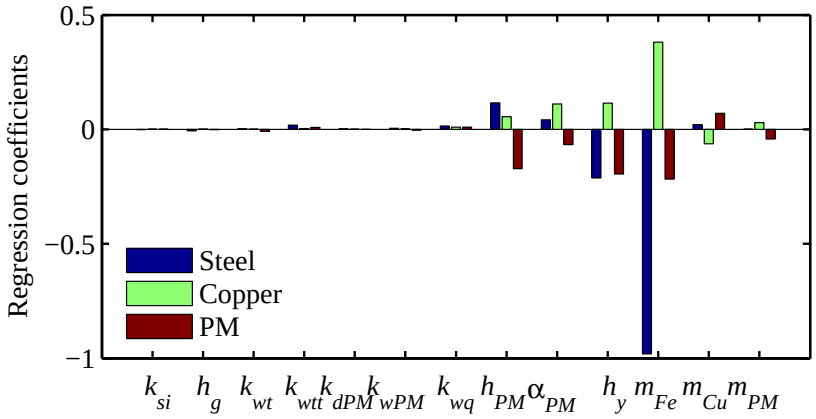

(a) 48S8P motor configuration

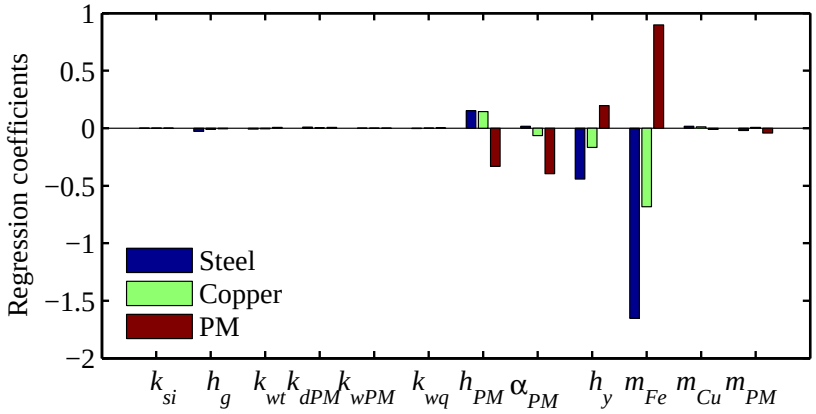

(b) 12S10P motor configuration

Figure 7.8: The sensitivity of the optimal design parameters to variation of the commodity price coefficients.

and 7.3 suggests that the optimal design values are relatively independent from the assumed set of commodity price coefficients.

7.2 A Computationally Efficient Method for Calculation of Strand Eddy Current Losses

The eddy current effects including the skin, strand-level, and bundle-level proximity effects [192] potentially constitute a significant contributor to the overall copper

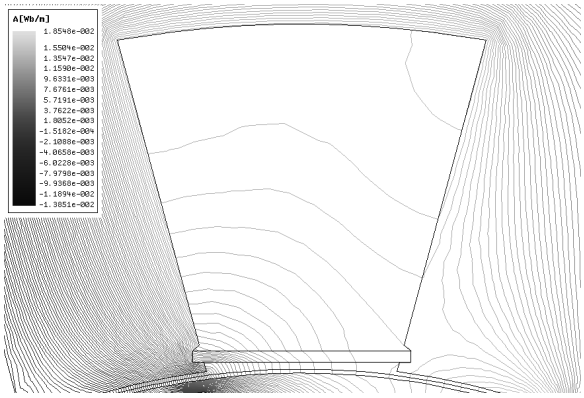

Figure 7.9: Slot leakage and fringing flux in a typical open-slot FSCW PM machine.

losses in the stator windings of high speed permanent magnet (PM) machines. Even if preventive measures such as stranding and transposition are adopted, the ac conductor losses in the stator windings of PM motors can still be significant for high power density-high speed open-slot fractional-slot concentrated winding (FSCW) machines due to the prevalence of slot leakage flux, and slot opening fringing flux, e.g. see Fig. 7.9. Common techniques for the estimation of such losses are especially prohibitive for randomly wound coil configurations and require a significant amount of time to formulate and solve the ac electromagnetic problem at the conductor strand level. The development of an FEA loss characterization method to provide a basis of qualitative ac loss comparison between thousands of design candidates, which is suitable for implementation in large-scale design optimization algorithms, is imperative. In addition to the value of the ac loss, the distribution of the overall copper losses in the stator winding is of interest particularly if coupled-thermal electromagnetic design optimization is pursued [193, 194].

In a broad categorization, the popular methods for analysis of eddy current losses in PM machines rely on analytical models as in [195–203], numerical finite

element/difference analysis as in [16, 204–206], or rely on combined analytical-FE-experimental procedures as in [207–209]. The analytical models lack the desired accuracy under magnetic core saturation and are not applicable to complex geometry without compromising further the accuracy. The numerical models are not suitable for integration into large-scale design optimization processes due to time consuming computations. The combined procedures require extensive a priori experimentations and are best suited for accurate loss analysis between different motor and winding configurations as opposed to application for large-scale design optimization of one particular configuration.

In this section, a finite element (FE)-based modeling technique is presented for estimation of the strand eddy current losses in the stator windings of electric machines, with an emphasis on sinusoidally excited PM synchronous machines. This is in order to include the portion of the ac losses which stems from the presence of slot leakage and fringing fluxes in the performance characterization of such machines. The developed hybrid analytical-numerical loss calculation method is rendered computationally efficient through adopting several measures such as alternative coil modeling which reduces the computation time required for solving the FE model, exploiting the existing electric symmetry in addition to the magnetic periodicity of PM machines with sinusoidal current excitation, and implementing fast analytical techniques for mapping the flux within the slot area, estimating the fill factor and strand locations, and finally characterization of the eddy current losses based on the value of the flux density impinging on each stator winding conductor. The presented loss calculation method provides a reasonable compromise between computational time and accuracy,

which makes it suitable for application in large-scale design optimization of PM machines in the initial stages of the design.

Using the developed method, strand eddy current losses under various loading conditions are computed and the existing trends between the ratio of ac to dc losses, P_{ac}/P_{dc}, with respect to the loading level are studied. Through this analysis, it is demonstrated that the traditional figure of merit for comparison of ac losses in electric machines, which is established by the ratio of ac to dc resistance, R_{ac}/R_{dc}, is by definition incapable of modeling the effects of the loading level on the ratio of P_{ac}/P_{dc}.

7.2.1 Strand Eddy Current Loss Characterization

Analytical models are reported for (a) 1-D single-slot models as in [197], (b) 2-D single-slot models as in [198], or (c) 2-D machine models as in [199]. These methods provide an insight into the nature of eddy current losses but do not accurately account for the non-linearity of the magnetic core, and are difficult to apply to complex machine geometries.

Numerical models require a significantly large number of elements in the stator slots and are therefore time-consuming. In some studies with detailed coil models [16, 205], an even distribution of current is assumed in the conductors so that a time-stepping magnetostatic solution can be performed. Subsequently, a detailed distribution of the radial and tangential components of the flux density, $B_{R,T}$, in each stator slot is obtained by establishing a fine grid over each slot pitch of the stator from one tooth axis to the next. These values are used in a numerical harmonic analysis

expressed by:

$$B_{R,T}(t) = \sum_{k=1}^{\infty} |B_{2k-1,(R,T)}| \sin\left((2k-1)\omega t - \phi_{2k-1,(R,T)}\right) \tag{7.2.1}$$

Accordingly, the eddy current loss, P_e, in watts per strand per depth of axial length, for a rectangular copper strand of width a, and height b subject to a uniform time varying flux density of Eq. (7.2.1) can be obtained using [199]:

$$P_e = ab \sum_{k=1}^{\infty} \frac{(2k-1)^2\omega^2}{24\rho} \left(|B_{2k-1,R}|^2 a^2 + |B_{2k-1,T}|^2 b^2\right) \eta_{2k-1} \tag{7.2.2}$$

where the skin effect coefficient η_{2k-1} is given by [210]:

$$\eta_{2k-1} = \frac{3}{4\alpha_{2k-1}^2} \frac{\sinh(2\alpha_{2k-1}) - \sin(2\alpha_{2k-1})}{\cosh(2\alpha_{2k-1}) - \cos(2\alpha_{2k-1})}, \alpha_{2k-1} = \frac{a}{6320}\sqrt{\frac{\mu_r(2k-1)f}{\rho}} \tag{7.2.3}$$

In the case of round conductors of diameter d, and resistivity ρ, Eq. (7.2.1) can be used for calculating the magnitude of the impinging flux $|B_{2k-1}| = \sqrt{|B_{2k-1,R}|^2 + |B_{2k-1,T}|^2}$, with the eddy current loss per depth of axial length given by [192]:

$$P_e = \pi d^4 \sum_{k=1}^{\infty} \frac{(2k-1)\omega^2 |B_{2k-1}|^2}{128\rho} \tag{7.2.4}$$

The ratio of ac to dc resistance, $k_{r_{ac}}$, of round conductors can be modified according to Eq. (7.2.5) in order to also include the skin effect [192]:

$$k_{r_{ac}} = \frac{d}{8\delta} Re\left((1+j)\frac{I_0(\frac{d}{2\delta}(1+j))}{I_1(\frac{d}{2\delta}(1+j))}\right), \delta = \sqrt{\frac{2\rho}{\omega\mu}} \tag{7.2.5}$$

where I_0 and I_1 are Bessel functions of zero and first orders, respectively, and δ is the skin depth. The solution of r_{ac} for round conductors is documented through charts and graphs in [192], and can be readily found for a given conductor diameter and excitation frequency.

7.2.2 FE-Based Eddy Current Loss Estimation for Randomly Wound Stator Windings

For a given machine configuration, the distribution of the leakage/fringing flux within any slot is dependent on:

- various dimensions of the cross section,
- the loading level,
- the location of the conductors within the stator slots,
- the temperatures of various components, and
- the frequency of operation.

Only a thermally coupled-time-harmonic finite element (FE) model with detailed knowledge of conductor locations can account for all the aforementioned parameters. The formulation and solution of such an electromagnetic (EM) problem is an extensively and computationally demanding process, not suitable for early design stage optimization purposes.

In this section, an alternative method will be presented. The steps of this computationally efficient loss calculation method which can be integrated into a large-scale design optimization process are described in the following section.

7.2.2.1 Modeling of the Coils

Detailed modeling of the coils in the slots, such as the one shown in Fig. 7.10(a), adds to the complexity of the FE model, and thus increases the computation time to reach

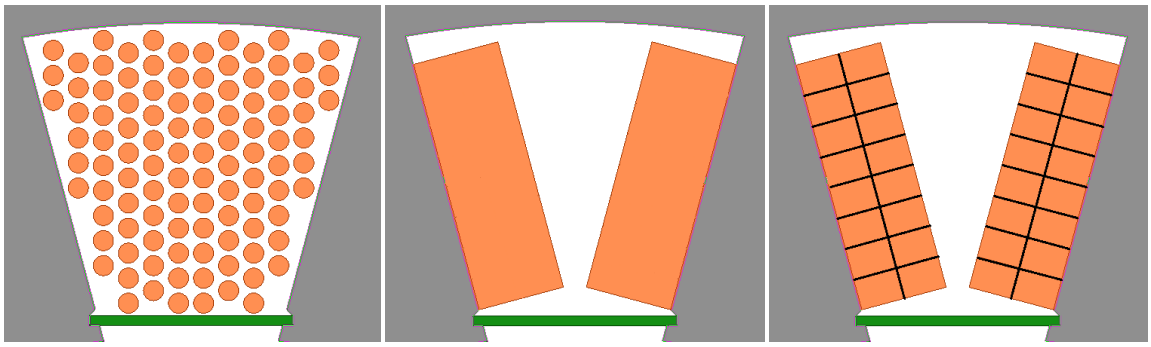

(a) Detailed model (b) Commonly used model (c) Alternative model

Figure 7.10: Alternative coil models for strand eddy current loss analysis.

a solution. As opposed to the crude coil model commonly used for EM-FE analysis, shown in Fig. 7.10(b), here an alternative representation is developed. According to Fig. 7.10(c), the winding is divided into a number of rectangular areas over its radial and tangential dimensions.

The heights and the widths of the sections can be all equal or skewed to provide more details at the slot opening. In Fig. 7.10(c), 32 sections with equal heights and equal widths are defined. The number of sections should be selected so that a reasonable distribution of B samples are obtained within the slot. The radial and tangential components of the flux densities at the middle of each rectangular section can then be extracted. The sampled B profiles are subsequently used to map the flux density at any point in the slot.

7.2.2.2 Extraction of B Field Profiles Inside the Slot

The value of B at the middle of each section can be obtained by any time-stepping magnetostatic FE analysis including the computationally efficient FEA (CE-FEA) method introduced in [81, 119], which exploits the electric symmetry in the stator

windings of sinewave operated/energized PM motors. As described in Section 2.1.1, using CE-FEA, the profile of the flux density waveforms over the full electrical cycle can be reconstructed by performing FEA over a window of 60 elec. deg.

Here, the CE-FEA method is used to extract the radial and tangential components of the sampled B profiles for the coil pieces shown in Fig. 7.10(c) for a typical machine under full-load motoring operation with counterclockwise rotation. The profiles for selected sections are shown in Figs. 7.11(a) through (d). It is interesting to note that the major component of the slot leakage flux is tangential. Furthermore, the decreasing trend of this slot leakage flux from top to bottom of the slot, and from left to right for the motoring operation, should be noted.

7.2.2.3 Determination of the Slot Fill Factor and the Associated Conductor Positions

The slot fill factor, s_f, is defined as follows:

$$s_f = \frac{A_{Cu}}{A_{slot}} = \frac{n_C \pi d^2}{4 A_{slot}} \tag{7.2.6}$$

where A_{Cu} is the copper area within the slot area, A_{slot}, and n_C is the number of conductors. In a large-scale design optimization problem, the slot dimensions and area vary between the design candidates. Accordingly, the maximum slot fill factor, $s_{f,\max}$, and the location of the conductors vary between the design candidates and should be calculated for each individual design. Here, the $s_{f,\max}$ is needed for the FEA to accurately account for the available Ampere Turn flowing through the alternate coil model described in the previous section. Furthermore, the conductor positions inside the slot are required for determining the impinging field on each strand in a post-FEA

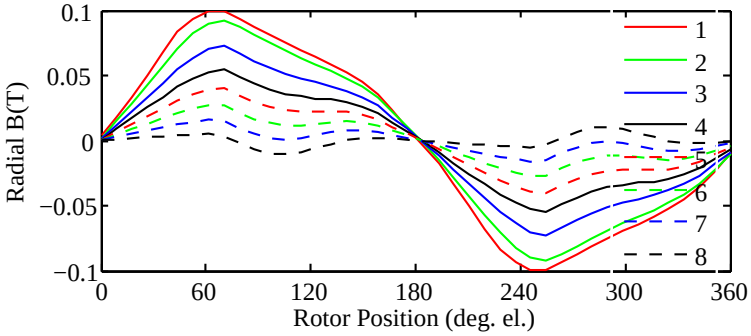

(a) Radial component of B moving into the slot

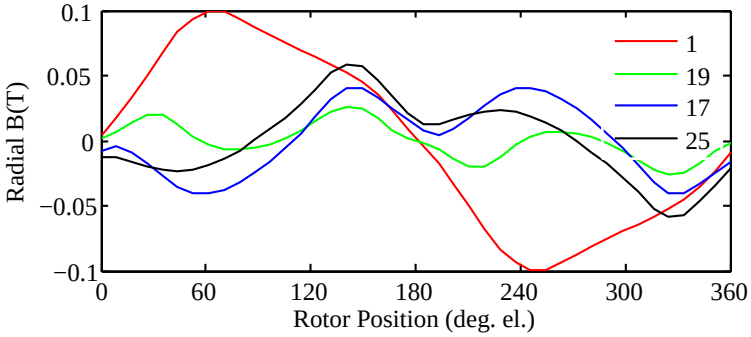

(b) Radial component of B moving along the slot opening

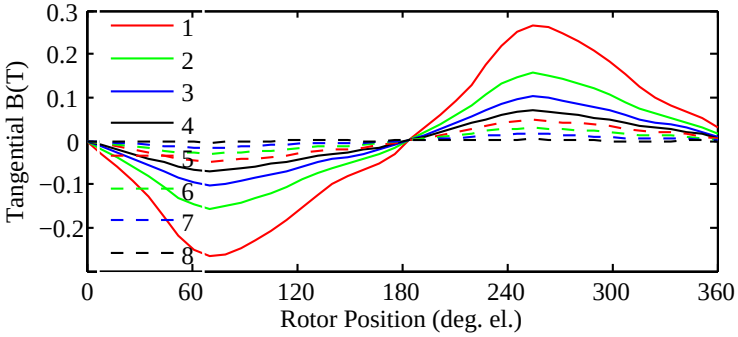

(c) Tangential component of B moving into the slot

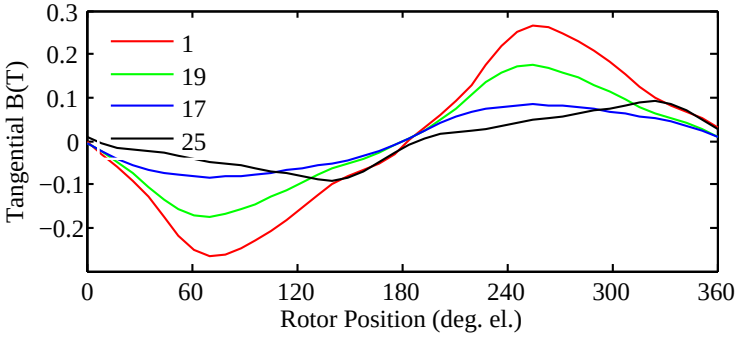

(d) Tangential component of B moving along the slot opening

Figure 7.11: Radial and tangential components of the field sections in Fig. 7.10(c) for a typical motor.

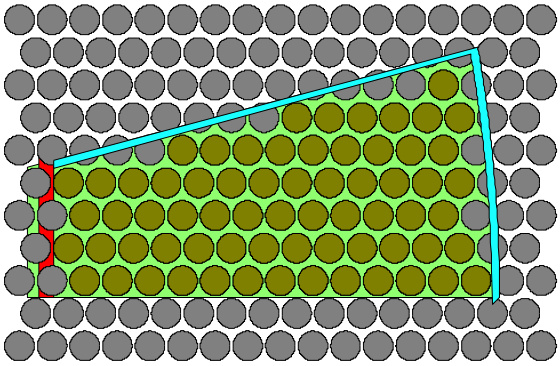

Figure 7.12: Determination of $s_{f,\max}$ and conductor positions by moving the slot geometry over a grid of conductors.

process using the B samples from FEA. This mapping process will be described in a later section.

The method that was implemented here for the calculation of $s_{f,\max}$ and the associated positions of the conductors within the slot, which yields such $s_{f,\max}$, relies on an optimization approach that is based on random perturbation of the slot geometry [117]. As can be seen in Fig. 7.12, a given slot geometry is randomly moved with respect to a grid of tightly packed circular conductors. The fill factor is then compared for various slot perturbations and strand arrangements to determine the $s_{f,\max}$ and the associated locations of the strands.

This method is used for the determination of $s_{f,\max}$ in the example slot geometries shown in Figs. 7.13(a) through (c). As can be seen in this illustration, for a given conductor diameter, the achievable $s_{f,\max}$ diminishes as the slot area decreases, which is successfully predicted by the method implemented here.

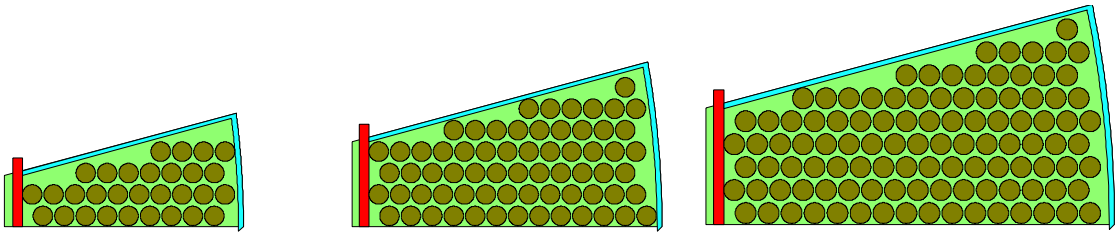

(a) $s_{f,\max} = 0.47$ (b) $s_{f,\max} = 0.51$ (c) $s_{f,\max} = 0.53$

Figure 7.13: Slot fill factor and strand positions for example slot geometries as the net slot area increases.

7.2.2.4 Mapping the Flux on Each Individual Strand

When the B profiles over the full fundamental cycle are obtained for each rectangular coil section, the radial and tangential components are separately used in a time harmonic analysis according to (7.2.1). Subsequently, for each harmonic, a Delaunay triangulation method is implemented in MATLAB for interpolating the samples scattered over the slot at the points where the center of each strand conductor is located. This process is illustrated in Fig. 7.14 for the reconstruction surfaces of the first harmonic of the B field throughout the slot area.

The order of harmonics that should be included is design dependent. When the field values throughout the slot area are determined, using the prior information of the strand positions, the impinging field on each strand can be mapped. In Fig. 7.15, the mapped values of the impinging B over each strand are shown for the fundamental and the third field harmonics. It can be seen once again that the magnitude of the slot leakage flux density monotonically increases for the strands that are closer to the air gap. The same trend exists for strands that are located towards the leading end of the rotor pole under motoring operation for CCW direction of rotation.

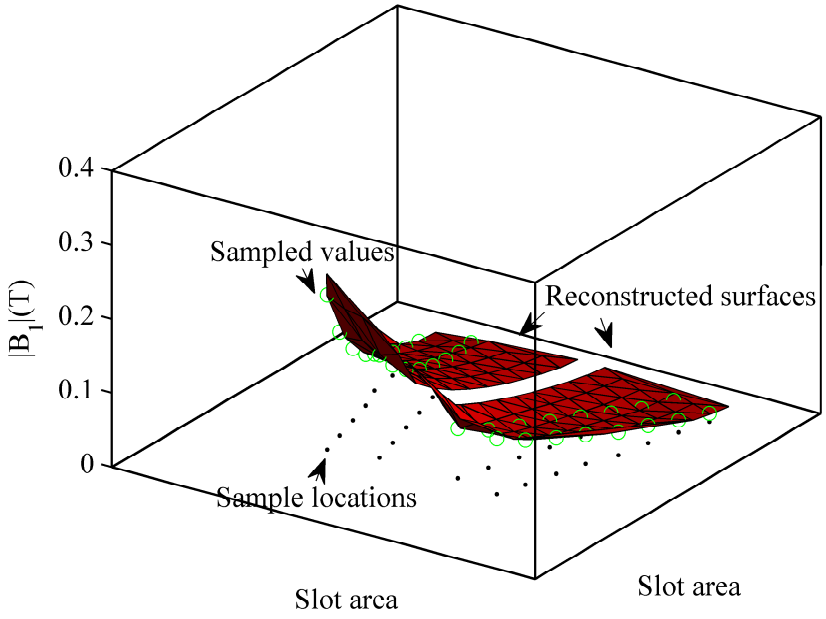

Figure 7.14: Reconstruction of the field harmonics from the sample points using Delaunay triangulation method.

7.2.2.5 Estimation of Value and Distribution of Eddy Current Losses

Upon derivation of the impinging $|B|$ on each strand, depending on the conductor shape, the loss models given in Eq. (7.2.2) through Eq. (7.2.5) can be used for estimation of strand eddy current losses in the conductors at the strand level. The resultant loss values using such an analysis on a typical slot is shown in Figs. 7.16(a) through (f) for a wide range of loading levels.

7.2.3 Case-Study Analysis

The method developed here was used for the calculation of eddy current losses in a 12-slot 10-pole IPM machine with V-type magnet layouts as shown in Fig. 7.17(a). The all-teeth-wound stator winding consists of series coils each composed of 53 turns of AWG 12.5 wires, thus reducing to negligible levels the losses associated with

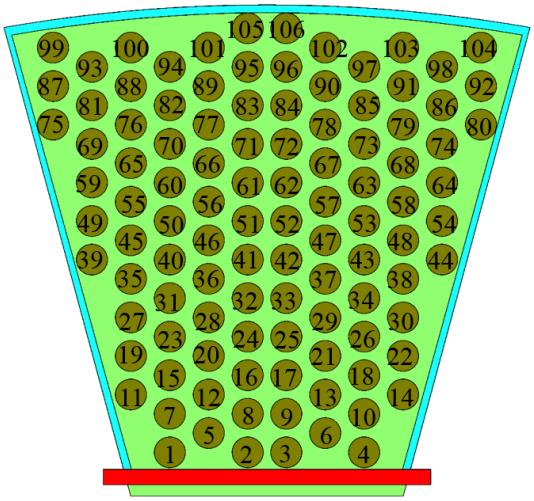

(a) Typical slot and strand numbers

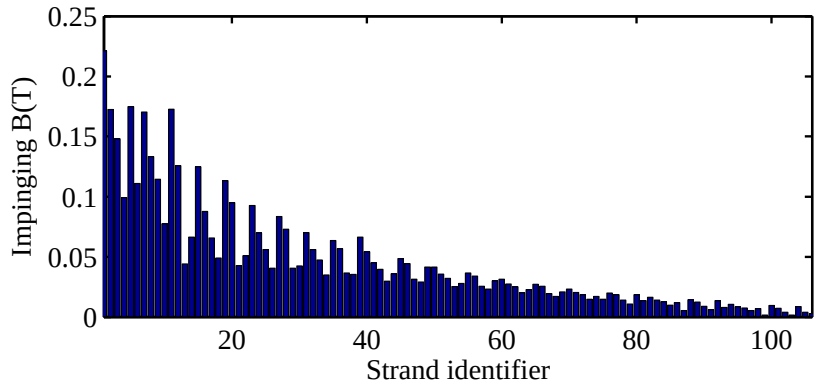

(b) The fundamental component of the impinging B

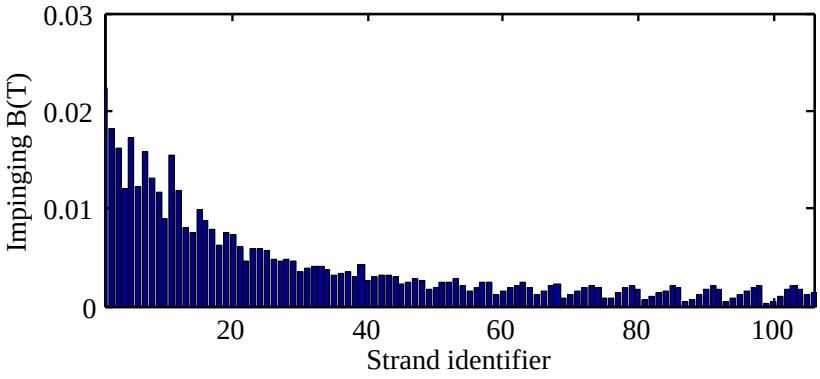

(c) The third harmonic component of the impinging B

Figure 7.15: Mapped flux on each individual strand.

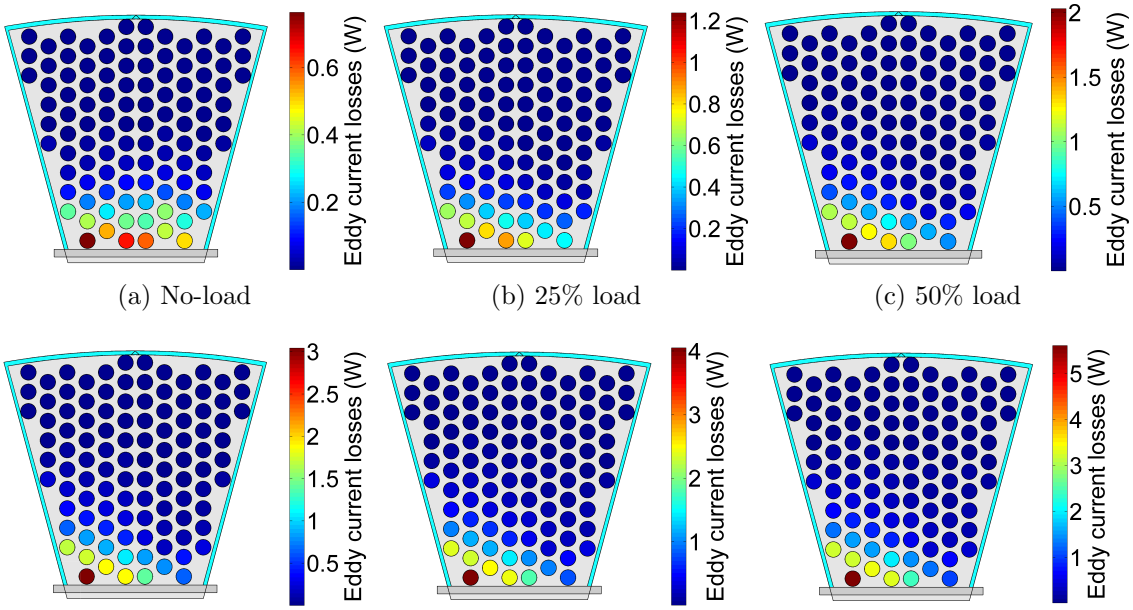

(a) No-load (b) 25% load (c) 50% load

(d) 75% load (e) 100% load (f) 125% load

Figure 7.16: Distribution of strand eddy current losses under various loading levels.

circulating currents, which are essentially of a three-dimensional nature and cannot be accounted for by two-dimensional models.

The stator winding losses including the strand eddy current losses are calculated by the developed method and the results are compared with those obtained from a time-stepping FEA with detailed coil modeling as shown in Fig. 7.17(b).

The strand eddy current losses are calculated over a wide range of motor loading conditions under MTPA control for three different speeds at a winding temperature of 100°C. The results obtained from the developed method and those from the time harmonic FEA with detailed coil modeling are compared in Figs. 7.18(a)-(c). The required computation time is less than 80 seconds using the proposed method as opposed to 3370 seconds using the detailed FEA.

The estimation error of the proposed method when compared to the detailed

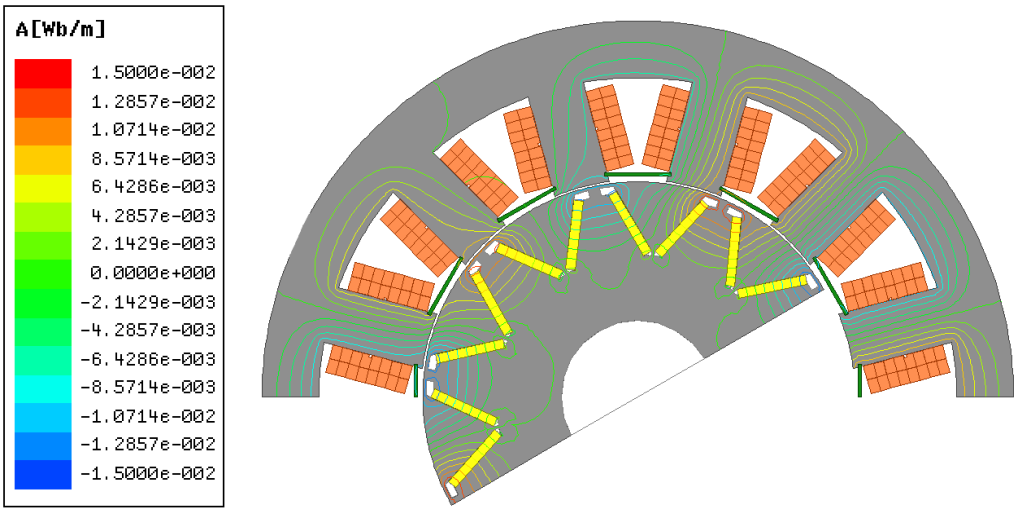

(a) CE-FEA with flux mapping (FM)

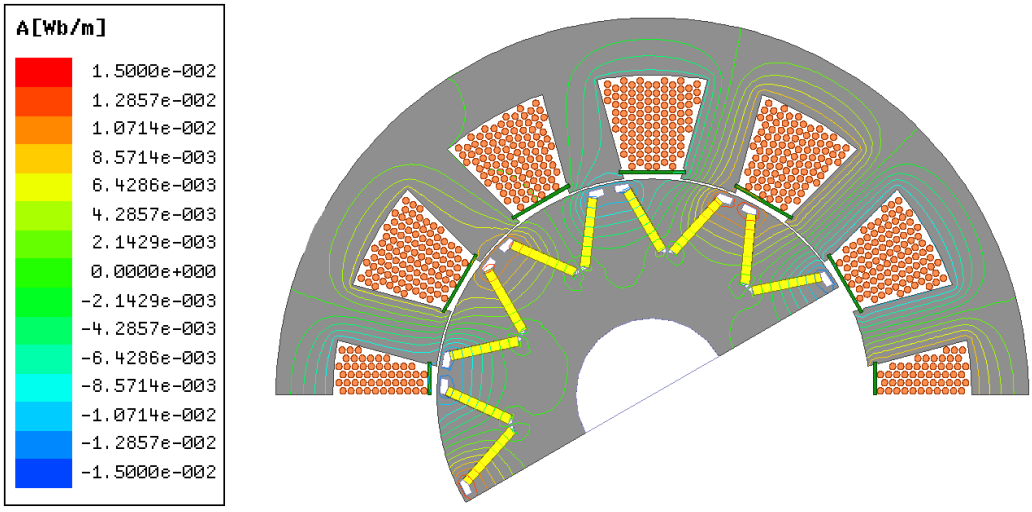

(b) FEA with detailed coil modeling

Figure 7.17: Case-study investigation of strand eddy current losses.

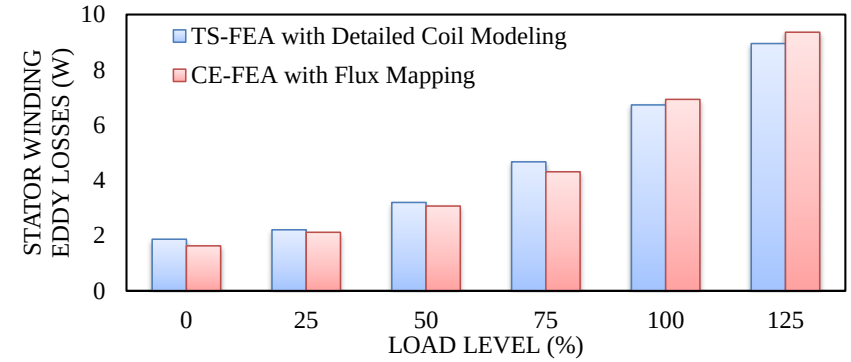

(a) 150 Hz

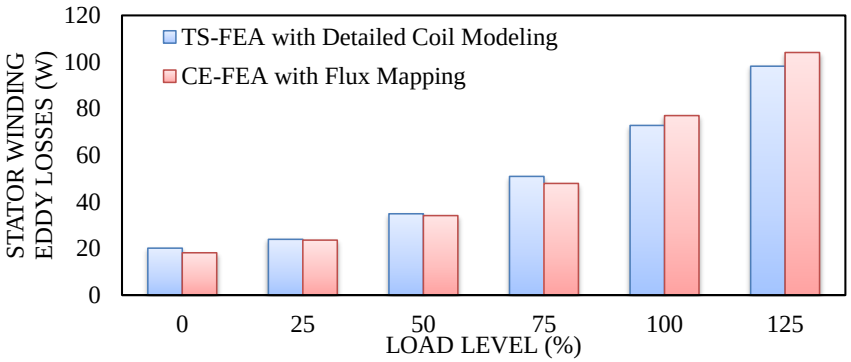

(b) 500 Hz

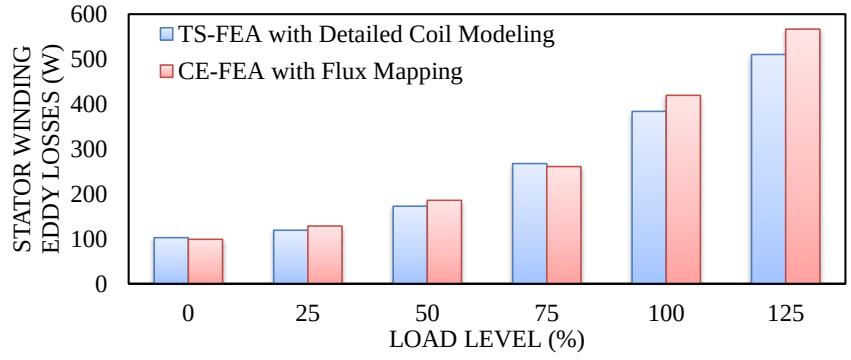

(c) 1200 Hz

Figure 7.18: Comparison of the accuracy of the loss calculation method over a wide range of frequencies and loading conditions.

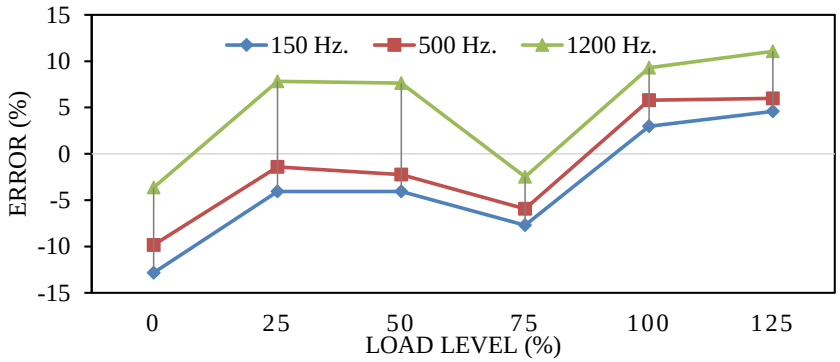

Figure 7.19: Estimation error of the computationally efficient method of calculation of strand eddy current losses compared to the full-fledged time harmonic analysis with detailed coil modeling.

TS-FE model is shown in Fig. 7.19 for several speeds and over a wide range of loading. The error is within a reasonable range given the computational efficiency of the proposed method.

The variation of the ac to dc loss ratio, P_{ac}/P_{dc}, due to the armature reaction under different loading levels is shown in Fig. 7.21. As can be seen in Figs. 7.21(a) through (c), strand eddy current losses constitute a larger contribution to the overall losses, $P_{ac} = P_{dc} + P_e$, under light load levels. The rate of increase of eddy current losses with respect to loading, which is mainly due to the elevated saturation level of the ferrous core and therefore increased leakage and fringing of flux into the slot area, is less than the rate of increase of dc copper losses P_{dc}, which is directly proportional to the current squared. This is especially true at lower frequencies as can be seen in Fig. 7.20. However, the eddy current losses are constantly present even at no-load conditions due to the presence of the time-varying field in the slots.

The ratio of R_{ac}/R_{dc}, which is commonly used in the literature, is by definition not exposed to such large variations, and thus does not reflect them. Therefore, if the

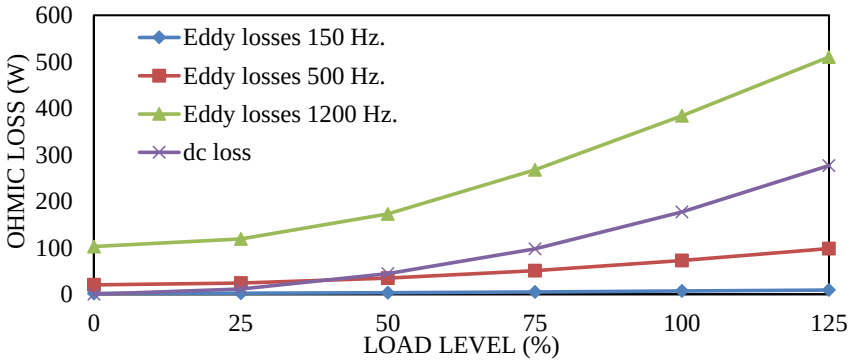

Figure 7.20: Variation of dc ohmic losses and strand eddy current losses with respect to loading level.

ratio of R_{ac}/R_{dc} is to be used as a figure of merit for comparison of ac losses between different design solutions, it should be derived and formulated under various loading conditions.

7.3 Estimation of Tangential Mechanical Stresses on the Rotor Bridges

In this section, the analytical method introduced in [211] is used to develop relevant formulations for the calculation of mechanical stresses in the bridges of a single-layer V-type IPM rotor layout. The results are compared to those obtained from the mechanical finite element analysis of the rotor structure. The comparison is performed through a sensitivity analysis of the stresses on the bridges of the case-study rotor using the two analytical and structural FE techniques for stress estimation. Although the emphasis is placed on the single layer V-type rotor layout which has been used throughout this dissertation, the methodology is applicable to many rotor configurations commonly seen in axially laminated rotary IPM machines. The

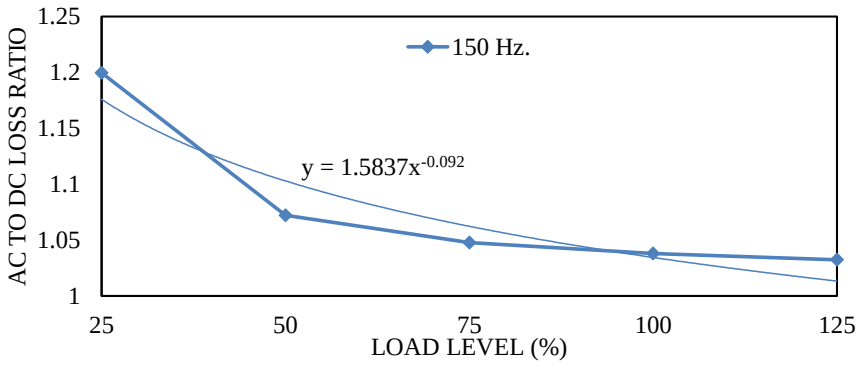

(a) 150 Hz

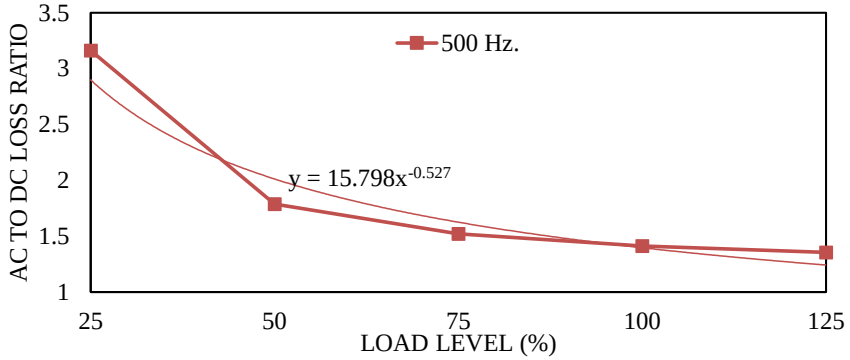

(b) 500 Hz

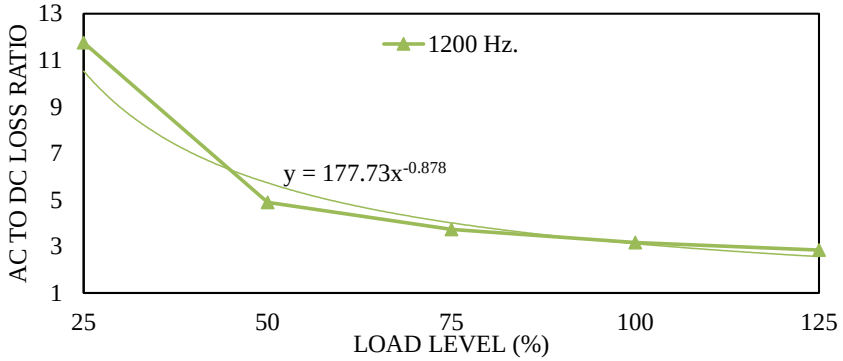

(c) 1200 Hz

Figure 7.21: Ratio of ac to dc losses over a wide range of loading conditions.

purpose of this development is to approximate the required adjustments of the widths of the rotor bridges of various design candidates with different rotor parameters in a large-scale design optimization process, and to account for the influence of the PM leakage flux shorted through the rotor bridges on the electromagnetic performance of the design solutions. The purpose of this analysis is not to omit the post-design optimization investigation of the mechanical stresses followed by adopting necessary measures for reducing the magnitude and/or the concentration of mechanical stresses throughout the rotor geometry.

7.3.1 Adopted Analytical Stress Estimation Method

Numerous investigators have reported analytical procedures for calculation of mechanical stresses in the rotor of the surface mounted permanent magnet machines. These procedures are used to ensure adequate enclosure contact pressure is maintained at high rotational speeds [176] in order to keep the magnets from flying off the rotor surface. These analytical developments are based on stress formulations in rotating concentric cylinders with different boundary equations with respect to the type of the contact surfaces [212, 213]. Such analytical derivations do not exist for complex geometries of IPM machines [159] without further sacrifice on accuracy of calculations of the maximum stress [214]. Furthermore, analytical techniques are unable to yield the distribution of the stress over the machine geometry. Still, a few attempts have been made to estimate the maximum stress values for IPM machines which suit the initial stages of the design process.

According to the method developed in [211], the tangential stress, σ_t, in the rotor

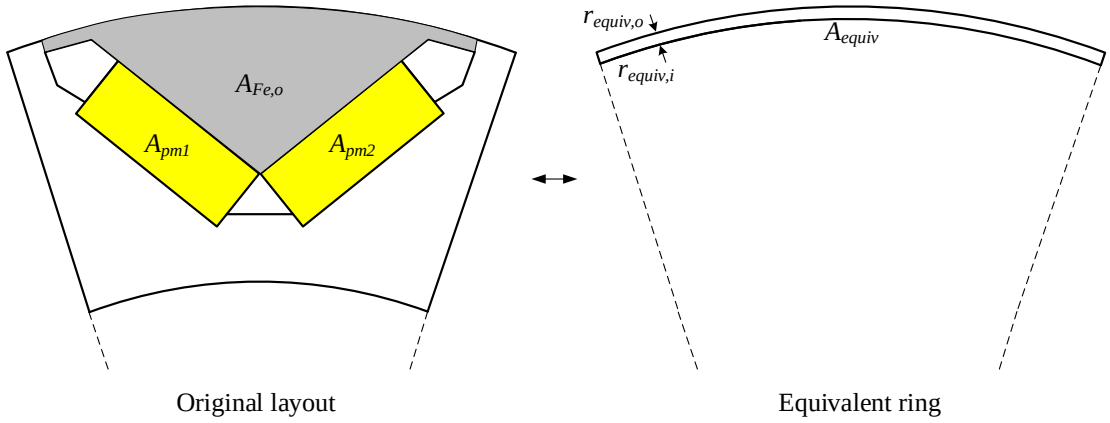

Figure 7.22: Modeling of the original layout on the left with the equivalent ring on the right.

bridges of an IPM machine can be estimated using an equivalent ring arrangement as sown in Fig. 7.22. In this approach, a hypothetical ring with is assumed. The height of this equivalent ring is equal to the narrowest height of the rotor iron bridges. Furthermore, it is characterized by an increased mass density, D_{equiv}, calculated according to Eq. (7.3.1) as follows:

$$D_{equiv} = \frac{D_{Fe} \cdot A_{Fe,o} + D_{pm} \cdot A_{pm}}{A_{equiv}} \tag{7.3.1}$$

where D_{Fe} is the mass density of rotor steel laminations, D_{pm} is the mass density of PMs, $A_{Fe,o}$ is the area of the iron under each pole piece, and A_{pm} is the area of the PMs per pole.

Subsequently, it can be assumed that the tangential stress inside the equivalent rotating ring, $\sigma_{t,equiv}$, expressed in Eq. (7.3.2), is an indication of the tangential stress present in the original layout. Eq. (7.3.2) is obtained based on formulations of the

hoop stress in rotating cylinders which are well-developed in the literature [176, 213].

$$\sigma_{t,equiv} = \frac{r_{equiv,o} + r_{equiv,i}}{2}^2 \cdot \omega_{\max}^2 \cdot D_{equiv} \tag{7.3.2}$$

where $r_{equiv,o}$ and $r_{equiv,i}$ are the outer and inner radii of the equivalent ring, respectively.

To account for the stress concentrations due to the irregular magnet slot shape, the calculated stress can be multiplied by a form factor, e.g. a factor of 2 as reported in [211] provided that the sharp corners are rounded. The thickness of the rotor bridges can be increased to reduce the stress on the rotor bridges to values less than the yield strength of the laminations [214].

7.3.2 Evaluation of the Accuracy of the Analytical Stress Estimation Method

In a large-scale design optimization, the methods utilized for modeling various performance aspects of the design candidates should be capable of accurately relating the design parameters to the desired performance metrics over the entire design space. As mentioned in the previous discussion, the analytical methods for calculation of the mechanical stresses in the rotor of IPM machines, do not reveal the concentration and the distribution of the stresses throughout the rotor geometry. Furthermore, many approximations are involved in derivation of such formulations. Therefore, it is imperative to systematically compare these methods with high fidelity FE models before employing them in the design practice.

Here, to understand the effectiveness of the method described in the previous section in identifying the existing correlations between various design parameters and

maximum stress in the rotor bridges of a V-type PM machine, two rounds of sensitivity analysis are performed. One uses the high fidelity structural FE model, and the other one uses the aforementioned analytical method as means for stress calculations.

In preparing the FE model, the sharp edges in the rotor geometry are slightly rounded, as shown in Fig. 7.23 for the two extremes of the rotor design parameters, to avoid large stress concentration values in the ribs. The radius of filleting is deliberately chosen to be small to minimize the effects on the machine electromagnetic performance.

The sensitivity analysis methodology described in Section 7.1.2 is used with the same range of design parameters associated with the rotor geometry indicated in Table 2.1, i.e. $k_{d_{pm}}$, $k_{w_{pm}}$, k_{w_q}, h_{pm}, α_{pm}, in addition to r_{ro} which is defined by k_{si} and h_g parameters. A total of 45 distinct designs identified by the Design of Experiments procedure using Central Composite Design methodology were analyzed using both analytical and structural FEA. The stress magnitudes and distributions of these designs obtained from structural FEA are provided in Appendix II. The stress found from the analytical method, and the maximum stress from the structural FEA are used for formulating two second order response surfaces expressed in Eq. (3.3.1). The normalized regression coefficients obtained from the two methods of stress calculation are shown in Fig. 7.24.

A comparison between the regression coefficients in Fig. 7.24 reveals that the analytical method is successful in modeling the effects of the design parameters on the bridge mechanical stresses except for two cases, namely, the PM depth ratio, $k_{d_{pm}}$, and the web width ratio, k_{w_q}. According to the analytical formulations, increasing

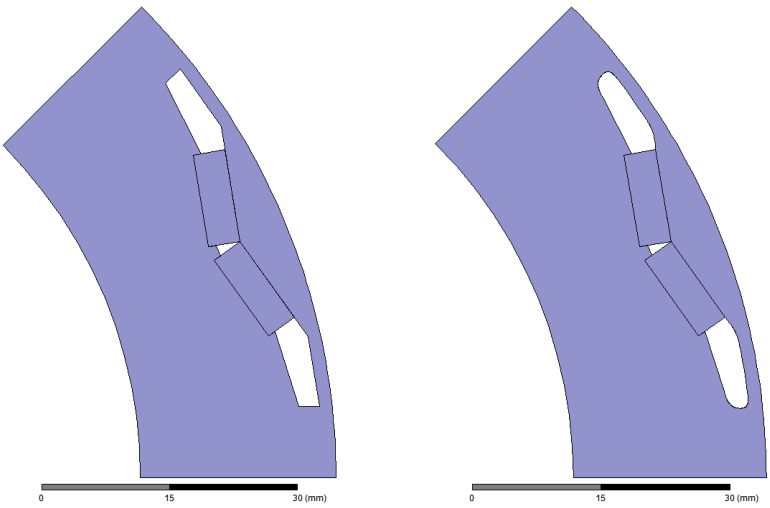

(a) Minimum values of the design parameters

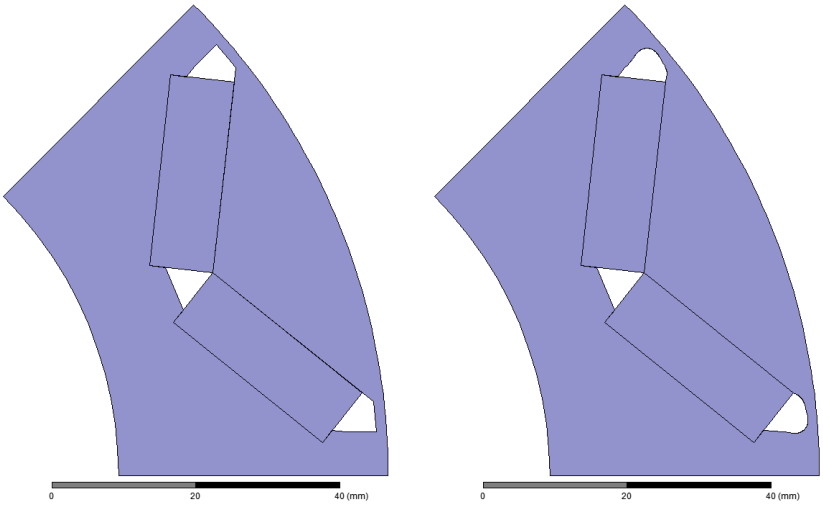

(b) Maximum values of the design parameters

Figure 7.23: Preparing the rotor geometry for structural FE analysis.

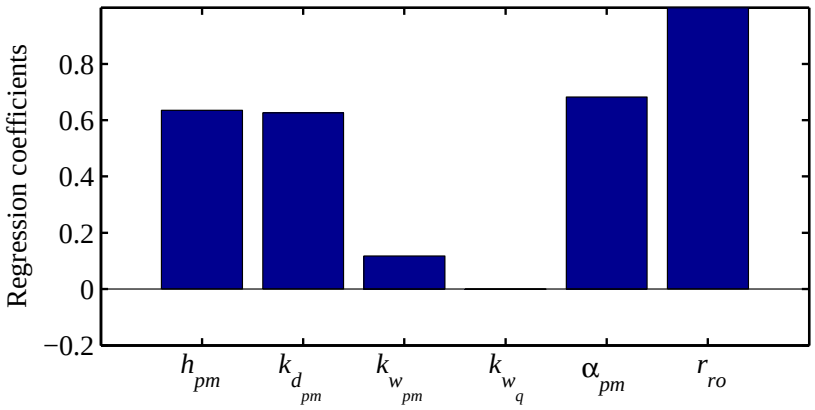

(a) Minimum values of the design parameters

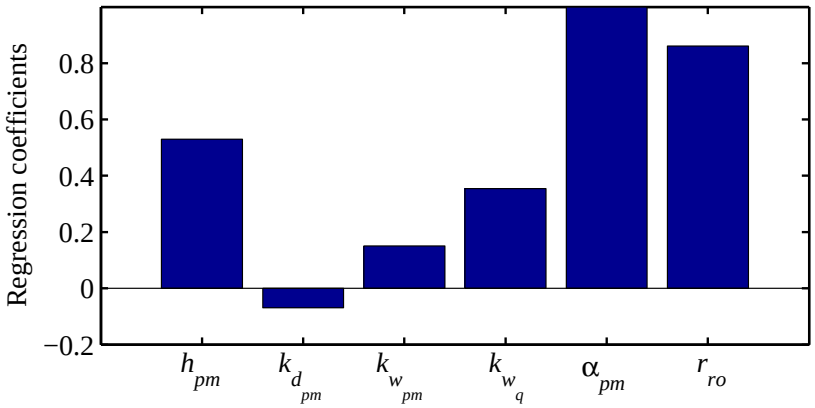

(b) Maximum values of the design parameters

Figure 7.24: Comparison of the accuracy of the analytical stress estimation method through a sensitivity analysis.

the PM depth ratio when other design parameters are constant will increase the mass under the pole piece, and thus elevates the stresses on the rotor bridges. This would have held true had it not been for the existing features in the rotor geometry which are not accounted for in the analytical model. Particularly, as the magnet burial depth increases, the magnets are better retained from the centrifugal forces because of the tilted inner edges at the two ends of the rotor slots marked in Fig. 7.25.

The analytical approach is also unable to effectively model the influence of k_{w_q} on

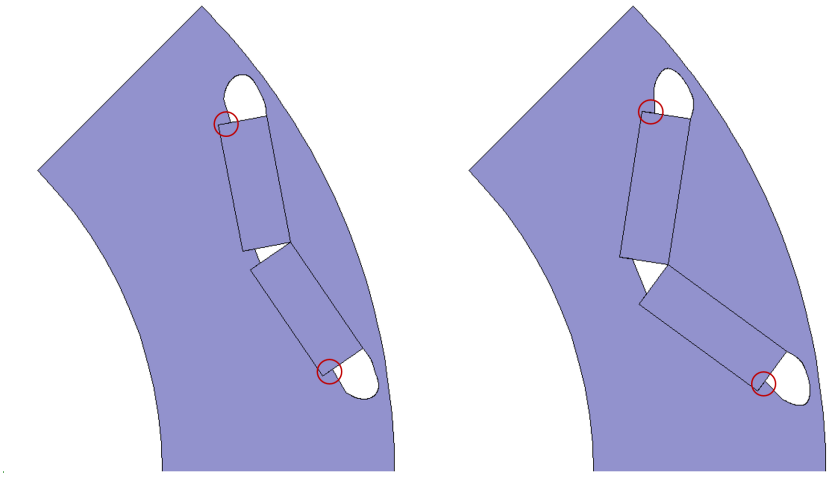

Figure 7.25: Change of $k_{d_{pm}}$ ratio from lower to upper bound.

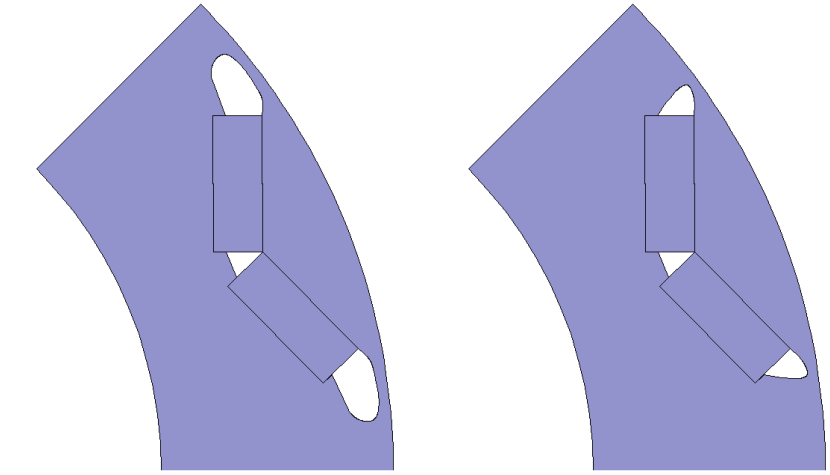

Figure 7.26: Change of k_{w_q} ratio from lower to upper bound.

the bridge stresses according to Fig. 7.24. This is due to the fact that the changes in the mass of the pole piece due to variations of k_{w_q} are marginal as shown in Fig. 7.26. Overall, the analytical approach provides an acceptable indication of stress which suits the large-scale design optimization.

7.4 Summary

In this chapter, three additional aspects of design optimization of PM machines were discussed:

In the first part, the sensitivity of the optimal design rules of IPM machines with sintered NdFeB magnets to the variations of the commodity price coefficients within a practical range of change was investigated in this section. Two sets of rigorous sensitivity analysis were performed for this purpose. First, a comprehensive sensitivity analysis was conducted on the impact of the commodity price variations on the relationships between design parameters and the AMC. The results of this sensitivity analysis demonstrated that the strongest changes of the most influential design parameters due to variations of the commodity prices were in the same direction as the original effects of these parameters.

In a second round of analysis, a comprehensive procedure based on a combined RSM-DE-ANN technique was developed for large-scale multi-objective ANN-based design optimization of over 200,000 design candidates to investigate the change in the optimal design values due to the commodity price variations. The results indicated that the average optimal design parameters are not prone to significant changes due to the variations of the commodity price coefficients within the assumed ranges. Similar conclusions would be expected for PM machines with Ferrite or bonded NdFeB magnets, since the use of less expensive magnet materials translates into a lower price coefficient, and thus reduces the influence of the PM price variations on the overall active material cost.

In the second part of this chapter, a method was developed for the calculation of strand eddy current losses in the stator windings of electric machines that (a) is finite-element based to take into account the complex geometry of the machine and the effects of saturation, (b) is computationally efficient and suitable for integration into large-scale design optimization algorithms, (c) is applicable to any variety of machines with different combinations of stator slots and rotor pole structures, (d) estimates the maximum SF factor for each design candidate based on winding specs and slot geometry, (e) estimates the value of eddy current losses due to slot leakage and fringing flux effects under any loading conditions, i.e. various torque and speed operating points, and (f) estimates the distribution of copper losses including the eddy current losses in the slots for rigorous thermal analysis of the stator windings.

The developed loss calculation method was implemented on a FSCW 12-slot 10-pole IPM machine with relatively large slot openings. The results over a wide range of loading conditions and operating frequencies were in good agreement with those obtained from a time harmonic FEA with detailed coil modeling. Meanwhile the required computation time was significantly reduced using the presented method. The distribution of the losses in this case study machine can be used for a subsequent thermal performance analysis due to the importance of including strand eddy losses as a major loss component in high speed machines, even if the stator winding conductors are stranded and transposed.

Using the developed loss calculation method, it was also shown that the variations of P_{ac}/P_{dc} loss ratio with reference to the machine loading levels are not reflected in the common figure of merit represented by R_{ac}/R_{dc} resistance ratio. Thus if the

R_{ac}/R_{dc} ratio is to be used, additional treatment will be required to include the loading effects.

In the third and last part of this chapter, an analytical method was implemented for the estimation of mechanical stresses in the rotor bridges of V-type IPM machines. Through conducting rigorous sensitivity analyses using analytical and numerical modeling tools, the capability of the utilized methodology in accurately describing the relationships between the design parameters and the centrifugal stresses on the rotor bridges were quantified. In the case study analysis, as expected, the analytical modeling approach which was derived based on stress formulations in rotating cylinders was not able to account for the effects of two of the design parameters, namely the burial depth of PMs and the width of the q-axis webs, on the stress concentrations in the rotor structure. However, the effects of the remaining four parameters were predicted with reasonable accuracy using the analytical method, thus rendering this approach one of the best available options for implementation in large-scale design optimization procedures.

CHAPTER 8
CONCLUSIONS

8.1 Summary and Conclusion

In this dissertation, the following aspects of large-scale design optimization of permanent magnet synchronous machines were presented:

In Chapter 1, the significance of research on high performance motor drive systems and the challenges and opportunities for efficiency improvement in such systems were discussed. In addition, the existing literature on numerical analysis and model-based optimization of permanent magnet synchronous machines was reviewed. It was pointed out that there is need for a more comprehensive design optimization approach which is inclusive of the entire range of possible operating conditions. The organization of this dissertation vis-a-vis the various investigated topics was also outlined in this chapter.

In Chapter 2, a recently introduced model-based methodology for design synthesis of synchronous PM machines was presented in detail. This approach, which features computationally efficient-finite element analysis for the characterization of performance of the design candidates, and utilization of the differential evolution search algorithm for finding the globally optimal designs, was carried out for large-scale design optimization of the Toyota Prius Gen 2 48-slot 8-pole V-type IPM machine at its peak (nominal) operating condition. The optimization was performed

over 4 800 design candidates for realizing two objectives of minimization of active material cost and power losses, in addition to satisfying two performance constraints on maximum torque ripple and maximum permissible degree of PM demagnetization. It was shown that more efficient and cost effective designs with superior rated performance indices at the nominal (peak) operating point could be found from the Pareto front of the optimization results. However, when the efficiency throughout the entire range of operation is considered, the original Prius design outperformed the selected Pareto optimal designs.

Demonstrating the necessity of including the entire range of operation in the optimization process is one key contribution of this research which was described in Chapter 3. Through a rigorous sensitivity analysis, it was shown that the correlation indices between the design parameters and the performance metrics vary with respect to the machine loading levels. In some instances, e.g. for the core and copper losses, torque ripple, and degree of PM demagnetization, these correlation indices undergo significant variations, or even change direction. These results put into perspective the considerable amount of research in the literature, which based on performance characterization at one operating point, prescribe various sizing/scaling ratios for achieving or alleviating desired or undesired performance metrics. In a second set of analyses in this chapter, six parallel design optimization runs consisting of an overall of 40 000 design candidates were carried out at three different levels of current densities, which are typically found in naturally cooled, fan-cooled, and liquid-cooled machines. In addition, the analysis was conducted on two different winding configurations, namely distributed and fractional slot concentrated windings.

The statistical distributions of the design parameters in the 500 optimal designs of each optimization run were subsequently investigated. The results indicated that the optimal design of PM machines vary with respect to the ampere loading level. This highlight the challenges in the design of electric motors with wide operating ranges, such as those used in traction applications, where an optimal design is to maintain high performance under various complex patterns of loading conditions.

Taking into account the entire range of complex operation patterns in the optimization fitness function contributes to the computational complexity of the modeling process, especially when FE-based models are utilized. Accordingly, a second key contribution of this dissertation is to mitigate the computational complexity of the design optimization process. For this purpose, in Chapter 4, a fast search algorithm was developed in this work for design optimization of electric machines. Namely, this new combined multiobjective optimization with differential evolution (CMODE-type) algorithm is best suited for implementation on multi-core workstation computers owing to its distinctive steady-state evolution model, which requires a lesser number of simultaneous function evaluations when compared to the standard DE or GA. This CMODE-type algorithm was implemented here and was thoroughly examined, and its superiorities over the standard DE algorithm in terms of convergence rate, constraint handling, and quality of the final generated Pareto fronts in a multiobjective design problem were confirmed and quantified. For this purpose, 12 independent runs of optimization, each consisting of 3 200 function evaluations, were conducted on different machine topologies with various loading levels and fitness functions, using either CMODE or DE as the search algorithm. Both counterpart

algorithms were able to identify the same global optima for all the optimization cases. However, in all of the examined cases, CMODE's convergence to the Pareto optimal vicinity was faster, at least twice as fast as DE. Furthermore, CMODE's constraint handling was more effective in the sense that a larger number of design candidates passed the designated performance constraints when compared to results from the design space produced by DE. Thus, a salient finding in this dissertation is that these characteristics of the CMODE algorithm render it the preferred search algorithm for implementation on desktop workstation computers when a limited number of processing cores and software licenses are available.

Another main contribution of this dissertation is the algorithm for large-scale design optimization of PM machines over a target operating cycle which was presented in Chapter 5. The resulting optimization process consists of the identification of the motor torque and speed profiles, computationally efficient modeling of the load energy distribution function, FEA-based performance evaluation at the cyclic representative load points residing in the constant torque or extended speed regions, and finding the optimal design solutions using the CMODE-type stochastic search algorithm. The original CE-FEA algorithm was upgraded to include any load operating point residing anywhere in the constant torque or extended speed regions of the torque-speed plane. Furthermore, a new k-means clustering algorithm was implemented for efficient modeling of the motor energy distribution function. Proper designation of the objectives and constraints of the optimization fitness function was also conceived in this chapter. It was demonstrated that the equality of the characteristic and rated currents should not be considered as an objective of the design

optimization. Alternatively, a number of performance criteria should be pursued, including improving upon the energy efficiency, while simultaneously checking the torque production capability at the required load points.

The optimization algorithm which was developed in Chapter 5 is applicable to the large family of sine-wave driven radial flux synchronous PM and synchronous reluctance machines over any conceivable operating cycle. Another contribution is that in Chapter 6, this approach was successfully applied to two case study traction propulsion motors. In the first case study, the Toyota Prius Gen 2 motor was optimized for reduced active material cost and increased drive-cycle efficiency over a combination of common US driving schedules. By investigating roughly 10 000 design candidates over seven representative load points, the cost effectiveness of the original design was confirmed and alternative designs with better energy efficiency characteristics were identified. The viability of the final counterpart designs were examined in a multiphysis performance analysis, including transient thermal modeling over the rigorous US06 driving cycle, and mechanical FEA of the rotor structure at the maximum rotational speed. The second case study presented in Chapter 6 pertains to the design optimization of a spoke-type IPM machine characterized with very high power density for propulsion application in a formula E racing car. Two objectives of increasing the power density, and minimizing the aggregate losses over the Le Mans driving cycle were pursued. The optimization results were used for establishing the performance trade-offs, and identification of the optimal design rules of high-power-dense spoke-type IPM machines.

As an additional set of contributions, the last chapter of this dissertation was

dedicated to the investigation of three different aspects of the design optimization of electric machines. First, it was demonstrated that when the minimization of the active material cost is considered, the optimal design rules of PM machines barely change due to the variation of the commodity price coefficients. In this case, a cost function based on the weighted masses of the main active components, and a realistic commodity price variation by a factor of two was considered. In the continuation of this chapter, a computationally efficient FE-based method for calculation of strand eddy current power losses in the stator windings of PM machines, and including this loss component in the design evaluation process was introduced. This method was implemented on an example 12-slot 10-pole machine configuration to characterize the strand eddy current losses under various speeds and loading conditions. The comparison of the results with a time harmonic transient FE model confirmed the accuracy and computational efficiency of the developed method. Finally, in this chapter, an analytical method for calculation of the centrifugal forces on the rotor bridges of V-type IPM machines was described, and its ability in capturing the influence of the design parameters on such forces was investigated. Although the presented method cannot take into account the stress concentrations due to the structural details introduced by some of the design parameters, such as the PM burial depth or width of the q-axis web, it can provide a first approximation of the magnitude of stress, which is suitable for implementation in a large-scale design optimization process.

8.2 Recommendation for Future Work

There are numerous research studies in the literature which perform a comparison between various motor topologies and configurations with an aim to identify the proper design decision for a given application. It is not uncommon to find such comparisons being performed between alternative design configurations which are not necessarily optimized a priori for the specific application, thus leaving much to be desired for a systematic, objective, and evidence-based comparison. The techniques and the optimization package developed in this dissertation provide a high-fidelity simulation platform for realizing such a comparison between different PM motor configurations for various applications. The studies carried out on PM machines with 48-slot 8-pole and 12-slot 10-pole configurations in Chapters 3 and 7 can be mentioned as an example of such analysis.

To bypass the need for a coupled thermal-electromagnetic optimization, and at the same time meet the thermal performance requirements, the three following measures were adopted in the developed design optimization package. First, the starting point of the process was based on an already existing design which meets the thermal performance requirements. Second, the current density was fixed for all the design candidates in a given optimization problem with reference to the original design. And third, the minimization of power losses has been always designated as an objective of the design optimization. Correspondingly, not only are the designs with power losses lower than the original design expected to meet the thermal performance requirements, but the ampere loading of such designs can be further increased, with

reference to a post-design optimization thermal performance analysis and as long as other performance constraints are not violated. This can translate into further improvement of the optimized designs. Nevertheless, if the computational complexity of the design optimization is not of concern, the coupled thermal-electromagnetic approach can be pursued by inspecting the peak and continuous power operation of the design candidates corresponding to the specifications of the cooling system.

There are other areas of opportunity for improving the developed design optimization package. To name a few, the implemented cost model can be improved to also account for the manufacturing cost associated with the power electronics drives. The loss model can be upgraded to include the additional losses introduced by the time harmonics of the PWM drives which might be significant during the extended speed operation. Furthermore, in case the CE-FEA modeling approach is to be improved, possible methods for taking into account the rotor core and the magnet losses can be studied and incorporated into the CE-FEA model.

BIBLOGRAPHY

[1] M. Lowe, R. Golini, and G. Gereffi, "U.S. Adoption of High-Efficiency Motors and Drives: Lessons Learned," Center on Globalization Governance and Competitiveness, Durham, NC 27705, Tech. Rep., February 2010. [Online]. Available: http://www.cggc.duke.edu

[2] G. A. McCoy and J. G. Douglass, *Premium Efficiency Motor Selection and Application Guide*. U.S. Department of Energy's Office of Energy Efficiency and Renewable Energy, 2014.

[3] "EV Everywhere Grand Challenge Blueprint," U.S. Department of Energy, Washington, DC 20585-0121, Tech. Rep., January 2013. [Online]. Available: http://www.energy.gov

[4] S. Zhang, J. Xu, J. Junak, D. Fiederling, G. Sawczuk, M. Koch, A. Schalja, M. Podack, and J. Baumgartner, "Permanent magnet technology for electric motors in automotive applications," in *Electric Drives Production Conference (EDPC), 2012 2nd International*, 2012, pp. 1–11.

[5] T. Vaimann, A. Kallaste, A. Kilk, and A. Belahcen, "Magnetic properties of reduced Dy NdFeB permanent magnets and their usage in electrical machines," in *AFRICON, 2013*, 2013, pp. 1–5.

[6] "United State Industrial Electric Motor Systems Market Opportunities Assessment," U.S. Department of Energy's Office of Energy Efficiency and Renewable Energy, Washington, DC 20585-0121, Tech. Rep., December 2002. [Online]. Available: http://www.energy.gov

[7] A. EL-Refaie and F. Johnson, "Scalable, Low-Cost, High Performance IPM Motor for Hybrid Vehicle," GE Global Research, Niskayuna, NY, Tech. Rep. DE-FC26-07NT43122, May 2011. [Online]. Available: http://www.energy.gov

[8] W. Larsen, O. Howlett, K. Forsman, and M. Zeller, "Exploring the Customer Benefits of Permanent Magnet Motors: Test Results and Opportunities for Next Generation Motor Programs ," American Council for an Energy-Efficient Economy, Washington, DC, Tech. Rep., August 2015. [Online]. Available: http://www.aceee.org

[9] T. M. J.R. Hendershot, *Design of brushless permanent-magnet machines*. Motor Design Books LLC; Second Edition, 2010.

[10] C. W. Trowbridge and J. K. Sykulski, "Some key developments in computational electromagnetics and their attribution," *IEEE Transactions on Magnetics*, vol. 42, no. 4, pp. 503–508, 2006.

[11] F. C. Trutt, *Analysis of homopolar inductor alternators*. University of Delware, 1962.

[12] S. V. Ahamed and E. A. Erdelyi, "Non-Linear Vector Potential Equations for Highly Saturated Heteropolar Electrical Machines," *IEEE Transactions on Aerospace*, vol. 2, no. 2, pp. 896–903, 1964.

[13] E. A. Erdelyi, S. V. Ahamed, and R. E. Hopkins, "Nonlinear Theory of Synchronous Machines On-Load," *IEEE Transactions on Power Apparatus and Systems*, vol. PAS-85, no. 7, pp. 792–801, 1966.

[14] S. V. Ahamed and E. A. Erdelyi, "Flux Distribution in DC Machines On-Load and Overloads," *IEEE Transactions on Power Apparatus and Systems*, vol. PAS-85, no. 9, pp. 960–967, 1966.

[15] E. A. Erdelyi and E. F. Fuchs, "Nonlinear Magnetic Field Analysis of DC Machines, Part I: Theoretical Fundamentals," *IEEE Transactions on Power Apparatus and Systems*, vol. PAS-89, no. 7, pp. 1546–1554, 1970.

[16] N. A. Demerdash and H. Hamilton, "Effect of Rotor Asymmetry on Field Forms and Eddy Current Losses in Stator Conductors Due to Radial Flux," *Power Apparatus and Systems, IEEE Transactions on*, vol. PAS-91, no. 5, pp. 1999–2010, 1972.

[17] N. A. Demerdash, H. B. Hamilton, and G. W. Brown, "Simulation for Design Purposes of Magnetic Fields in Turbogenerators with Symmetrical and Asymmetrical Rotors Part I-Model Development and Solution Technique," *IEEE Transactions on Power Apparatus and Systems*, vol. PAS-91, no. 5, pp. 1985–1992, 1972.

[18] N. A. Demerdash and H. B. Hamilton, "Simulation for Design Purposes of Magnetic Fields in Turbogenerators with Asymmetrical and Symmetrical Rotors Part II - Model Calibration and Applications," *IEEE Transactions on Power Apparatus and Systems*, vol. PAS-91, no. 5, pp. 1992–1999, 1972.

[19] N. Demerdash and H. Hamilton, "Use of computerized magnetic field solutions in design optimization of turbogenerators," *IEEE Transactions on Magnetics*, vol. 11, no. 5, pp. 1532–1534, 1975.

[20] N. Demerdash and T. Nehl, "Flexibility and economics of implementation of the finite element and difference techniques in nonlinear magnetic fields of power

devices," *IEEE Transactions on Magnetics*, vol. 12, no. 6, pp. 1036–1038, 1976.

[21] ——, "An Evaluation of the Methods of Finite Elements and Finite Differences in the Solution of Nonlinear Electromagnetic Fields in Electrical Machines," *IEEE Transactions on Power Apparatus and Systems*, vol. PAS-98, no. 1, pp. 74–87, 1979.

[22] P. Silvester and M. V. K. Chari, "Finite Element Solution of Saturable Magnetic Field Problems," *IEEE Transactions on Power Apparatus and Systems*, vol. PAS-89, no. 7, pp. 1642–1651, 1970.

[23] M. V. K. Chari and P. Silvester, "Finite-Element Analysis of Magnetically Saturated D-C Machines," *IEEE Transactions on Power Apparatus and Systems*, vol. PAS-90, no. 5, pp. 2362–2372, 1971.

[24] ——, "Analysis of Turboalternator Magnetic Fields by Finite Elements," *IEEE Transactions on Power Apparatus and Systems*, vol. PAS-90, no. 2, pp. 454–464, 1971.

[25] P. Silvester, H. S. Cabayan, and B. T. Browne, "Efficient Techniques for Finite Element Analysis of Electric Machines," *IEEE Transactions on Power Apparatus and Systems*, vol. PAS-92, no. 4, pp. 1274–1281, 1973.

[26] M. Chari, "Nonlinear finite element solution of electrical machines under no-load and full-load conditions," *IEEE Transactions on Magnetics*, vol. 10, no. 3, pp. 686–689, 1974.

[27] J. R. Brauer, "Saturated Magnetic Energy Functional for Finite Element Analysis of Electric Machines," in *IEEE-PES Winter Meeting*, 1975.

[28] O. W. Andersen, "Transformer Leakage Flux Program Based on the Finite Element Method," *IEEE Transactions on Power Apparatus and Systems*, vol. PAS-92, no. 2, pp. 682–689, 1973.

[29] N. Demerdash, T. Nehl, and F. Fouad, "Finite element formulation and analysis of three dimensional magnetic field problems," *IEEE Transactions on Magnetics*, vol. 16, no. 5, pp. 1092–1094, 1980.

[30] T. Nehl and N. Demerdash, "Application of finite element eddy current analysis to nondestructive detection of flaws in metallic structures," *IEEE Transactions on Magnetics*, vol. 16, no. 5, pp. 1080–1082, 1980.

[31] N. A. Demerdash and T. W. Nehl, "Dynamic Modeling of Brushless dc Motors for Aerospace Actuation," *IEEE Transactions on Aerospace and Electronic Systems*, vol. AES-16, no. 6, pp. 811–821, 1980.

[32] S. Salon and B. Istfan, "Inverse non-linear finite element problems," *IEEE Transactions on Magnetics*, vol. 22, no. 5, pp. 817–818, 1986.

[33] B. Istfan and S. J. Salon, "Inverse nonlinear finite element problems with local and global constraints," *IEEE Transactions on Magnetics*, vol. 24, no. 6, pp. 2568–2572, 1988.

[34] T. Nakata and N. Takahashi, "Direct finite element analysis of flux and current distributions under specified conditions," *IEEE Transactions on Magnetics*, vol. 18, no. 2, pp. 325–330, 1982.

[35] ——, "Application of the finite element method to the design of permanent magnets," *IEEE Transactions on Magnetics*, vol. 18, no. 6, pp. 1049–1051, 1982.

[36] ——, "New design method of permanent magnets by using the finite element method," *IEEE Transactions on Magnetics*, vol. 19, no. 6, pp. 2494–2497, 1983.

[37] N. Takahashi, T. Nakata, and N. Uchiyama, "Optimal design method of 3-D nonlinear magnetic circuit by using magnetization integral equation method," *IEEE Transactions on Magnetics*, vol. 25, no. 5, pp. 4144–4146, 1989.

[38] O. Pironneau, *Optimal Shape Design for Elliptic Systems*, ser. Springer series in computational physics. Springer-Verlag, 1984. [Online]. Available: https://books.google.com/books?id=6JqyAAAAIAAJ

[39] K. Preis and A. Ziegler, "Optimal design of electromagnetic devices with evolution strategies," *COMPEL*, vol. 9, no. A, pp. 119–122, 1990.

[40] S. Subramaniam, S. Kanaganathan, and S. R. H. Hoole, "Two requisite tools in the optimal design of electromagnetic devices," *IEEE Transactions on Magnetics*, vol. 27, no. 5, pp. 4105–4109, 1991.

[41] M. Guamieri, A. Stella, and F. Trevisan, "A methodological analysis of different formulations for solving inverse electromagnetic problems," *IEEE Transactions on Magnetics*, vol. 26, no. 2, pp. 622–625, 1990.

[42] A. G. Armstrong, M. Fan, J. Simkin, and C. Trowbridge, "Automated optimization of magnet design using the boundary integral method," *IEEE Transactions on Magnetics*, vol. 18, no. 2, pp. 620–623, 1982.

[43] S. Gitosusastro, J. L. Coulomb, and J. C. Sabonnadiere, "Performance derivative calculations and optimization process," *IEEE Transactions on Magnetics*, vol. 25, no. 4, pp. 2834–2839, 1989.

[44] C. S. Koh, H. S. Yoon, K. W. Nam, and H. S. Choi, "Magnetic pole shape optimization of permanent magnet motor for reduction of cogging torque," *IEEE Transactions on Magnetics*, vol. 33, no. 2, pp. 1822–1827, 1997.

[45] I.-H. Park, B.-T. Lee, and S.-Y. Hahn, "Design sensitivity analysis for nonlinear magnetostatic problems using finite element method," *IEEE Transactions on Magnetics*, vol. 28, no. 2, pp. 1533–1536, 1992.

[46] S. R. H. Hoole, S. Subramaniam, R. Saldanha, J. L. Coulomb, and J. C. Sabonnadiere, "Inverse problem methodology and finite elements in the identification of cracks, sources, materials, and their geometry in inaccessible locations," *IEEE Transactions on Magnetics*, vol. 27, no. 3, pp. 3433–3443, 1991.

[47] P. G. Alotto, C. Eranda, B. Brandstatter, G. Furntratt, C. Magele, G. Molinari, M. Nervi, K. Preis, M. Repetto, and K. R. Richter, "Stochastic algorithms in electromagnetic optimization," *IEEE Transactions on Magnetics*, vol. 34, no. 5, pp. 3674–3684, 1998.

[48] R. R. Saldanha, J. L. Coulomb, A. Foggia, and J. C. Sabonnadiere, "A dual method for constrained optimization design in magnetostatic problems," *IEEE Transactions on Magnetics*, vol. 27, no. 5, pp. 4136–4141, 1991.

[49] R. R. Saldanha, J. L. Coulomb, and J. C. Sabonnadiere, "An ellipsoid algorithm for the optimum design of magnetostatic problems," *IEEE Transactions on Magnetics*, vol. 28, no. 2, pp. 1573–1576, 1992.

[50] K. Weeber and S. R. H. Hoole, "Structural design optimization as a technology source for developments in the electromagnetics domain," *IEEE Transactions on Magnetics*, vol. 29, no. 2, pp. 1807–1811, 1993.

[51] A. Gottvald, "Comparative analysis of optimization methods for magnetostatics," *IEEE Transactions on Magnetics*, vol. 24, no. 1, pp. 411–414, 1988.

[52] ——, "Optimal magnet design for NMR," *IEEE Transactions on Magnetics*, vol. 26, no. 2, pp. 399–402, 1990.

[53] K. Preis, O. Biro, M. Friedrich, A. Gottvald, and C. Magele, "Comparison of different optimization strategies in the design of electromagnetic devices," *IEEE Transactions on Magnetics*, vol. 27, no. 5, pp. 4154–4157, 1991.

[54] A. Gottvald, K. Preis, C. Magele, O. Biro, and A. Savini, "Global optimization methods for computational electromagnetics," *IEEE Transactions on Magnetics*, vol. 28, no. 2, pp. 1537–1540, 1992.

[55] C. A. Magele, K. Preis, W. Renhart, R. Dyczij-Edlinger, and K. R. Richter, "Higher order evolution strategies for the global optimization of electromagnetic devices," *IEEE Transactions on Magnetics*, vol. 29, no. 2, pp. 1775–1778, 1993.

[56] G. Drago, A. Manella, M. Nervi, M. Repetto, and G. Secondo, "A combined strategy for optimization in nonlinear magnetic problems using simulated annealing and search techniques," *IEEE Transactions on Magnetics*, vol. 28, no. 2, pp. 1541–1544, 1992.

[57] J. Simkin and C. W. Trowbridge, "Optimizing electromagnetic devices combining direct search methods with simulated annealing," *IEEE Transactions on Magnetics*, vol. 28, no. 2, pp. 1545–1548, 1992.

[58] S. Russenschuck, "Mathematical optimization techniques for the design of permanent magnet synchronous machines based on numerical field calculation," *IEEE Transactions on Magnetics*, vol. 26, no. 2, pp. 638–641, 1990.

[59] S. Ratnajeevan, H. Hoole, K. Weeber, and S. Subramaniam, "Fictitious minima of object functions, finite element meshes, and edge elements in electromagnetic device synthesis," *IEEE Transactions on Magnetics*, vol. 27, no. 6, pp. 5214–5216, 1991.

[60] K. Weeber and S. R. H. Hoole, "A structural mapping technique for geometric parametriiation in the synthesis of magnetic devices," *Int. J. Num. Meth. Eng.*, vol. 33, pp. 2145–2179, 1992.

[61] ——, "Geometric parametrization and constrained optimization techniques in the design of salient pole synchronous machines," *IEEE Transactions on Magnetics*, vol. 28, no. 4, pp. 1948–1960, 1992.

[62] K. Preis, C. Magele, and O. Biro, "FEM and evolution strategies in the optimal design of electromagnetic devices," *IEEE Transactions on Magnetics*, vol. 26, no. 5, pp. 2181–2183, 1990.

[63] M. Schafer-Jotter and W. Muller, "Optimization of electrotechnical devices using a numerical laboratory," *IEEE Transactions on Magnetics*, vol. 26, no. 2, pp. 815–818, 1990.

[64] J. Simkin and C. W. Trowbridge, "Optimization problems in electromagnetics," *IEEE Transactions on Magnetics*, vol. 27, no. 5, pp. 4016–4019, 1991.

[65] G. F. Uler, O. A. Mohammed, and C.-S. Koh, "Utilizing genetic algorithms for the optimal design of electromagnetic devices," *IEEE Transactions on Magnetics*, vol. 30, no. 6, pp. 4296–4298, 1994.

[66] O. A. Mohammed, "Practical issues in the application of genetic algorithms to optimal design problems in electromagnetics," in *Southeastcon '96. Bringing Together Education, Science and Technology., Proceedings of the IEEE*, 1996, pp. 634–640.

[67] J.-S. Chun, H.-K. Jung, and J.-S. Yoon, "Shape optimization of closed slot type permanent magnet motors for cogging torque reduction using evolution strategy," *IEEE Transactions on Magnetics*, vol. 33, no. 2, pp. 1912–1915, 1997.

[68] T. K. Chung, S. K. Kim, and S.-Y. Hahn, "Optimal pole shape design for the reduction of cogging torque of brushless DC motor using evolution strategy," *IEEE Transactions on Magnetics*, vol. 33, no. 2, pp. 1908–1911, 1997.

[69] N. Bianchi and S. Bolognani, "Design optimisation of electric motors by genetic algorithms," *IEE Proceedings - Electric Power Applications*, vol. 145, no. 5, pp. 475–483, 1998.

[70] N. Bianchi and A. Canova, "FEM analysis and optimisation design of an IPM synchronous motor," in *Power Electronics, Machines and Drives, 2002. International Conference on (Conf. Publ. No. 487)*, 2002, pp. 49–54.

[71] T. Ohnishi and N. Takahashi, "Optimal design of efficient IPM motor using finite element method," *IEEE Transactions on Magnetics*, vol. 36, no. 5, pp. 3537–3539, 2000.

[72] F. A. Fouad, T. W. Nehl, and N. A. Demerdash, "Magnetic Field Modeling of Permanent Magnet Type Electronically Operated Synchronous Machines Using Finite Elements," *IEEE Transactions on Power Apparatus and Systems*, vol. PAS-100, no. 9, pp. 4125–4135, 1981.

[73] B. Cassimere and S. Sudhoff, "Population-Based Design of Surface-Mounted Permanent-Magnet Synchronous Machines," *Energy Conversion, IEEE Transactions on*, vol. 24, no. 2, pp. 338–346, June 2009.

[74] E. C. Lovelace, T. M. Jahns, and J. H. Lang, "Impact of saturation and inverter cost on interior PM synchronous machine drive optimization," *IEEE Transactions on Industry Applications*, vol. 36, no. 3, pp. 723–729, 2000.

[75] A. A. Arkadan and Y. Chen, "Artificial neural network for the inverse electromagnetic problem of system identification," in *Southeastcon '94. Creative Technology Transfer - A Global Affair., Proceedings of the 1994 IEEE*, 1994, pp. 162–164.

[76] G. Y. Sizov, D. M. Ionel, and N. A. O. Demerdash, "A review of efficient FE

modeling techniques with applications to PM AC machines," in *2011 IEEE Power and Energy Society General Meeting*, 2011, pp. 1–6.

[77] Y. Duan and D. M. Ionel, "A Review of Recent Developments in Electrical Machine Design Optimization Methods With a Permanent-Magnet Synchronous Motor Benchmark Study," *IEEE Transactions on Industry Applications*, vol. 49, no. 3, pp. 1268–1275, 2013.

[78] G. Bramerdorfer, A. Zavoianu, S. Silber, E. Lughofer, and W. Amrhein, "Speed Improvements for the Optimization of Electrical Machines - a Survey," in *Electric Machines Drives Conference (IEMDC), 2015 IEEE International*, May 2015.

[79] F. Poltschak and W. Amrhein, "A dynamic nonlinear model for permanent magnet synchronous machines," in *2008 IEEE International Symposium on Industrial Electronics*, 2008, pp. 724–729.

[80] D. M. Ionel and M. Popescu, "Finite-Element Surrogate Model for Electric Machines with Revolving Field-Application to IPM Motors," *IEEE Transactions on Industry Applications*, vol. 46, no. 6, pp. 2424 –2433, Nov.-Dec. 2010.

[81] D. M. Ionel and M. M. Popescu, "Ultrafast Finite-Element Analysis of Brushless PM Machines Based on SpaceTime Transformations," *IEEE Transactions on Industry Applications*, vol. 47, no. 2, pp. 744 –753, March-April 2011.

[82] G. Y. Sizov, D. M. Ionel, and N. A. O. Demerdash, "Modeling and Parametric Design of Permanent-Magnet AC Machines Using Computationally Efficient Finite-Element Analysis," *IEEE Transactions on Industrial Electronics*, vol. 59, no. 6, pp. 2403–2413, 2012.

[83] W. Jiang, T. M. Jahns, T. A. Lipo, W. Taylor, and Y. Suzuki, "Machine design optimization based on finite element analysis in a high-throughput computing environment," in *2012 IEEE Energy Conversion Congress and Exposition (ECCE)*, 2012, pp. 869–876.

[84] G. Sizov, P. Zhang, D. Ionel, N. Demerdash, and M. Rosu, "Automated Multi-Objective Design Optimization of PM AC Machines Using Computationally Efficient- FEA and Differential Evolution," *IEEE Transactions on Industry Applications*, vol. 49, no. 5, pp. 2086–2096, 2013.

[85] P. Zhang, G. Sizov, M. Li, D. Ionel, N. Demerdash, S. Stretz, and A. Yeadon, "Multi-Objective Tradeoffs in the Design Optimization of a Brushless Permanent-Magnet Machine With Fractional-Slot Concentrated Windings," *Industry Applications, IEEE Transactions on*, vol. 50, no. 5, pp.

3285–3294, 2014.

[86] I. P. Brown, M. W. Critchley, J. Yin, S. B. Memory, G. Y. Sizov, S. W. Elbel, C. D. Bowers, M. Petersen, and P. S. Hrnjak, "Design and Evaluation of Interior Permanent-Magnet Compressor Motors for Commercial Transcritical CO2 (R-744) Heat Pump Water Heaters," *IEEE Transactions on Industry Applications*, vol. 51, no. 1, pp. 576–586, 2015.

[87] Y. Duan and D. Ionel, "Nonlinear Scaling Rules for Brushless PM Synchronous Machines Based on Optimal Design Studies for a Wide Range of Power Ratings," *Industry Applications, IEEE Transactions on*, vol. 50, no. 2, pp. 1044–1052, March 2014.

[88] P. Zhang, G. Sizov, D. Ionel, and N. Demerdash, "Establishing the Relative Merits of Interior and Spoke-Type Permanent-Magnet Machines With Ferrite or NdFeB Through Systematic Design Optimization," *Industry Applications, IEEE Transactions on*, vol. 51, no. 4, pp. 2940–2948, 2015.

[89] Y. Wang, D. Ionel, and D. Staton, "Ultrafast Steady-state Multi-physics Model for PM and Synchronous Reluctance Machines," *Industry Applications, IEEE Transactions on*, vol. PP, no. 99, pp. 1–1, 2015.

[90] Y. Wang, D. M. Ionel, M. Jiang, and S. J. Stretz, "Establishing the Relative Merits of Synchronous Reluctance and PM Assisted Technology Through Systematic Design Optimization," *IEEE Transactions on Industry Applications*, vol. PP, no. 99, pp. 1–1, 2016.

[91] S. E. Sibande, M. J. Kamper, R. Wang, and E. T. Rakgati, "Optimal design of a PM-assisted rotor of a 110 kW reluctance synchronous machine," in *AFRICON, 2004. 7th AFRICON Conference in Africa*, vol. 2, 2004, pp. 793–797 Vol.2.

[92] D. Zarko, D. Ban, and T. A. Lipo, "Design optimization of interior permanent magnet (IPM) motors with maximized torque output in the entire speed range," in *Power Electronics and Applications, 2005 European Conference on*, 2005, pp. 10 pp.–P.10.

[93] R. Schiferl and T. Lipo, "Power capability of salient pole permanent magnet synchronous motors in variable speed drive applications," *Industry Applications, IEEE Transactions on*, vol. 26, no. 1, pp. 115–123, Jan 1990.

[94] W. Ouyang, D. Zarko, and T. Lipo, "Permanent Magnet Machine Design Practice and Optimization," in *Industry Applications Conference, 2006. 41st IAS Annual Meeting. Conference Record of the 2006 IEEE*, vol. 4, 2006, pp. 1905–1911.

[95] G. Pellegrino and F. Cupertino, "IPM motor rotor design by means of FEA-based multi-objective optimization," in *Industrial Electronics (ISIE), 2010 IEEE International Symposium on*, 2010, pp. 1340–1346.

[96] P. Zhang, D. Ionel, and N. Demerdash, "Saliency ratio and power factor of IPM motors optimally designed for high efficiency and low cost objectives," in *Energy Conversion Congress and Exposition (ECCE), 2014 IEEE*, Sept 2014, pp. 3541–3547.

[97] S. Morimoto, S. Ooi, Y. Inoue, and M. Sanada, "Experimental Evaluation of a Rare-Earth-Free PMASynRM With Ferrite Magnets for Automotive Applications," *Industrial Electronics, IEEE Transactions on*, vol. 61, no. 10, pp. 5749–5756, 2014.

[98] A. Fatemi, N. Demerdash, and D. Ionel, "Design optimization of IPM machines for efficient operation in extended speed range," in *Transportation Electrification Conference and Expo (ITEC), 2015 IEEE*, 2015, pp. 1–8.

[99] F. Parasiliti, M. Villani, S. Lucidi, and F. Rinaldi, "Finite-Element-Based Multiobjective Design Optimization Procedure of Interior Permanent Magnet Synchronous Motors for Wide Constant-Power Region Operation," *IEEE Transactions on Industrial Electronics*, vol. 59, no. 6, pp. 2503 –2514, June 2012.

[100] J. hee Lee and B.-I. Kwon, "Optimal Rotor Shape Design of a Concentrated Flux IPM-Type Motor for Improving Efficiency and Operation Range," *Magnetics, IEEE Transactions on*, vol. 49, no. 5, pp. 2205–2208, 2013.

[101] K. Yamazaki, M. Kumagai, T. Ikemi, and S. Ohki, "A Novel Rotor Design of Interior Permanent-Magnet Synchronous Motors to Cope with Both Maximum Torque and Iron-Loss Reduction," *Industry Applications, IEEE Transactions on*, vol. 49, no. 6, pp. 2478–2486, 2013.

[102] K. Yamazaki and H. Ishigami, "Rotor-Shape Optimization of Interior-Permanent-Magnet Motors to Reduce Harmonic Iron Losses," *IEEE Transactions on Industrial Electronics*, vol. 57, no. 1, pp. 61–69, 2010.

[103] F. Cupertino, G. Pellegrino, E. Armando, and C. Gerada, "A SyR and IPM machine design methodology assisted by optimization algorithms," in *Energy Conversion Congress and Exposition (ECCE), 2012 IEEE*, 2012, pp. 3686–3691.

[104] M. Barcaro, N. Bianchi, and F. Magnussen, "Permanent-Magnet Optimization in Permanent-Magnet-Assisted Synchronous Reluctance Motor for a Wide Constant-Power Speed Range," *Industrial Electronics, IEEE Transactions on*, vol. 59, no. 6, pp. 2495–2502, 2012.

[105] P. Lazari, J. Wang, and L. Chen, "A Computationally Efficient Design Technique for Electric-Vehicle Traction Machines," *Industry Applications, IEEE Transactions on*, vol. 50, no. 5, pp. 3203–3213, Sept 2014.

[106] J. Wang, X. Yuan, and K. Atallah, "Design Optimization of a Surface-Mounted Permanent-Magnet Motor With Concentrated Windings for Electric Vehicle Applications," *Vehicular Technology, IEEE Transactions on*, vol. 62, no. 3, pp. 1053–1064, March 2013.

[107] E. Carraro, M. Morandin, and N. Bianchi, "Traction PMASR Motor Optimization According to a Given Driving Cycle," *IEEE Transactions on Industry Applications*, vol. 52, no. 1, pp. 209–216, 2016.

[108] A. Fatemi, D. M. Ionel, N. A. O. Demerdash, and T. W. Nehl, "Optimal Design of IPM Motors with Different Cooling Systems and Winding Configurations," *IEEE Transactions on Industry Applications*, vol. PP, no. 99, pp. 1–1, 2016.

[109] A. Fatemi, N. Demerdash, T. Nehl, and D. Ionel, "Large-scale Design Optimization of PM Machines Over a Target Operating Cycle," *IEEE Transactions on Industry Applications*, vol. PP, no. 99, pp. 1–1, 2016.

[110] A. Fatemi, D. M. Ionel, N. A. O. Demerdash, and T. W. Nehl, "Fast Multi-Objective CMODE-Type Optimization of PM Machines Using Multicore Desktop Computers," *IEEE Transactions on Industry Applications*, vol. PP, no. 99, pp. 1–1, 2016.

[111] A. Fatemi, D. M. Ionel, M. Popescu, and N. A. O. Demerdash, "Design optimization of spoke-type pm motors for formula e racing cars," in *2016 IEEE Energy Conversion Congress and Exposition (ECCE)*, 2016, p. in press.

[112] A. Fatemi, D. M. Ionel, N. A. O. Demerdash, S. Stretz, and T. M. Jahns, "RSM-DE-ANN Method for Sensitivity Analysis of Active Material Cost in PM Motors," in *2016 IEEE Energy Conversion Congress and Exposition (ECCE)*, 2016, p. in press.

[113] A. Fatemi, D. M. Ionel, N. A. O. Demerdash, D. Staton, R. Wrobel, and Y. C. Chong, "Computationally Efficient Method for Calculation of Strand Eddy Current Losses in Stator Windings of Electric Machines," in *2016 IEEE Energy Conversion Congress and Exposition (ECCE)*, 2016, pp. 4383–4390.

[114] A. Fatemi, N. A. O. Demerdash, D. M. Ionel, and T. W. Nehl, "Large-scale electromagnetic design optimization of PM machines over a target operating cycle," in *2015 IEEE Energy Conversion Congress and Exposition (ECCE)*, 2015, pp. 4383–4390.

[115] A. Fatemi, D. M. Ionel, N. A. O. Demerdash, and T. W. Nehl, "Fast multi-objective CMODE-type optimization of electric machines for multicore desktop computers," in *2015 IEEE Energy Conversion Congress and Exposition (ECCE)*, 2015, pp. 5593–5600.

[116] A. Fatemi, D. Ionel, and N. Demerdash, "Identification of design rules for interior PM motors with different cooling systems," in *Electric Machines Drives Conference (IEMDC), 2015 IEEE International*, May 2015.

[117] G. Y. Sizov, *Design synthesis and optimization of permanent magnet synchronous machines based on computationally-efficient finite element analysis*. Marquette University, 2013.

[118] P. Zhang, *A novel design optimization of a fault-tolerant ac permanent magnet machine-drive system*. Marquette University, 2013.

[119] G. Y. Sizov, D. M. Ionel, and N. A. O. Demerdash, "Modeling and Parametric Design of Permanent-Magnet AC Machines Using Computationally Efficient-Finite Element Analysis," *IEEE Transactions on Industrial Electronics*, vol. 59, no. 6, pp. 2403 –2413, June 2012.

[120] K. V. Price, R. M. Storn, and J. A. Lampinen, *Differential Evolution-A Practical Approach to Global Optimization*. Springer-Verlag Berlin Heidelberg, 2005.

[121] J. Coulomb and G. Meunier, "Finite element implementation of virtual work principle for magnetic or electric force and torque computation," *IEEE Transactions on Magnetics*, vol. 20, no. 5, pp. 1894–1896, 1984.

[122] D. Ionel, M. Popescu, M. McGilp, T. Miller, S. Dellinger, and R. Heideman, "Computation of Core Losses in Electrical Machines Using Improved Models for Laminated Steel," *IEEE Transactions on Industry Applications*, vol. 43, no. 6, pp. 1554 –1564, nov.-dec. 2007.

[123] A. Boglietti, A. Cavagnino, D. Ionel, M. Popescu, D. Staton, and S. Vaschetto, "A General Model to Predict the Iron Losses in PWM Inverter-Fed Induction Motors," *IEEE Transactions on Industry Applications*, vol. 46, no. 5, pp. 1882–1890, 2010.

[124] D. Ionel, M. Popescu, C. Cossar, M. McGilp, A. Boglietti, and A. Cavagnino, "A General Model of the Laminated Steel Losses in Electric Motors with PWM Voltage Supply," in *IEEE Industry Applications Society Annual Meeting (IAS)*, 2008, pp. 1–7.

[125] M. Popescu, D. Ionel, A. Boglietti, A. Cavagnino, C. Cossar, and M. McGilp, "A General Model for Estimating the Laminated Steel Losses Under PWM

Voltage Supply," *IEEE Transactions on Industry Applications*, vol. 46, no. 4, pp. 1389–1396, 2010.

[126] A. EL-Refaie, "Fractional-Slot Concentrated-Windings Synchronous Permanent Magnet Machines: Opportunities and Challenges," *IEEE Transactions on Industrial Electronics*, vol. 57, no. 1, pp. 107–121, 2010.

[127] K. Zielinski, P. Weitkemper, R. Laur, and R. L. K.-D. Kammeyer, K. Zielinski, "Examination of Stopping Criteria for Differential Evolution based on a Power Allocation Problem," in *10th International Conference on Optimization of Electrical and Electronic Equipment*, Brasov, Romania, May 2006.

[128] K. Zielinski and R. Laur, "Stopping Criteria for a Constrained Single-Objective Particle Swarm Optimization Algorithm," *Informatica (03505596)*, vol. 31, pp. 51–59, March 2007.

[129] N. Bianchi and S. Bolognani, "Brushless DC motor design: an optimisation procedure based on genetic algorithms," in *Electrical Machines and Drives, 1997 Eighth International Conference on (Conf. Publ. No. 444)*, Sep 1997, pp. 16–20.

[130] M. Olszewski, "Evaluation of 2004 Toyota Prius Hybrid Electric Drive System," in *Oak Ridge National Laboratory, U.S. Department of Energy*, Sept 2004.

[131] ——, "Evaluation of the 2007 Toyota Camry Hybrid Synergy Drive System," in *Oak Ridge National Laboratory, U.S. Department of Energy*, Apr 2008.

[132] D. Dorrell, M. Hsieh, M. Popescu, L. Evans, D. Staton, and V. Grout, "A Review of the Design Issues and Techniques for Radial-Flux Brushless Surface and Internal Rare-Earth Permanent-Magnet Motors," *Industrial Electronics, IEEE Transactions on*, vol. 58, no. 9, pp. 3741–3757, 2011.

[133] E. Armando, P. Guglielmi, G. Pellegrino, M. Pastorelli, and A. Vagati, "Accurate Modeling and Performance Analysis of IPM-PMASR Motors," *Industry Applications, IEEE Transactions on*, vol. 45, no. 1, pp. 123–130, 2009.

[134] W. Jiang and T. Jahns, "Coupled electromagnetic/thermal machine design optimization based on finite element analysis with application of artificial neural network," in *Energy Conversion Congress and Exposition (ECCE), 2014 IEEE*, Sept 2014, pp. 5160–5167.

[135] S. Semidey, Y. Duan, J. Mayor, R. Harley, and T. Habetler, "Optimal Electromagnetic-Thermo-Mechanical Integrated Design Candidate Search and Selection for Surface-Mount Permanent-Magnet Machines Considering Load

Profiles," *Industry Applications, IEEE Transactions on*, vol. 47, no. 6, pp. 2460–2468, 2011.

[136] J. Wang and D. Howe, "Design optimization of radially magnetized, iron-cored, tubular permanent-magnet machines and drive systems," *Magnetics, IEEE Transactions on*, vol. 40, no. 5, pp. 3262–3277, 2004.

[137] G. Sizov, D. Ionel, and N. Demerdash, "Multi-Objective Optimization of PM AC Machines Using Computationally Efficient-FEA and Differential Evolution," in *IEEE International Electric Machines Drives Conference 2011 (IEMDC '11)*, may 2011, pp. 1528 –1533.

[138] G. Lei, C. Liu, J. Zhu, and Y. Guo, "Techniques for Multilevel Design Optimization of Permanent Magnet Motors," *Energy Conversion, IEEE Transactions on*, vol. PP, no. 99, pp. 1–11, 2015.

[139] C. Xia, L. Guo, Z. Zhang, T. Shi, and H. Wang, "Optimal Designing of Permanent Magnet Cavity to Reduce Iron Loss of Interior Permanent Magnet Machine," *Magnetics, IEEE Transactions on*, vol. 51, no. 12, pp. 1–9, 2015.

[140] F. Parasiliti, M. Villani, S. Lucidi, and F. Rinaldi, "A new optimization approach for the design of IPM synchronous motor with wide constant-power region," in *Electrical Machines (ICEM), 2010 XIX International Conference on*, 2010, pp. 1–7.

[141] F. Dubas, C. Espanet, and A. Miraoui, "Design of a high-speed permanent magnet motor for the drive of a fuel cell air-compressor," in *Vehicle Power and Propulsion, 2005 IEEE Conference*, 2005, pp. 8 pp.–.

[142] M. Popescu, I. Foley, D. A. Staton, and J. E. Goss, "Multi-physics analysis of a high torque density motor for electric racing cars," in *Energy Conversion Congress and Exposition, 2015. ECCE 2015. IEEE*, Sept 2015.

[143] A. Boglietti, A. Cavagnino, D. Staton, M. Shanel, M. Mueller, and C. Mejuto, "Evolution and Modern Approaches for Thermal Analysis of Electrical Machines," *Industrial Electronics, IEEE Transactions on*, vol. 56, no. 3, pp. 871–882, March 2009.

[144] Z. Azar, Z. Zhu, and G. Ombach, "Influence of Electric Loading and Magnetic Saturation on Cogging Torque, Back-EMF and Torque Ripple of PM Machines," *Magnetics, IEEE Transactions on*, vol. 48, no. 10, pp. 2650–2658, 2012.

[145] J. Cros and P. Viarouge, "Synthesis of high performance PM motors with concentrated windings," *Energy Conversion, IEEE Transactions on*, vol. 17, no. 2, pp. 248–253, 2002.

[146] M. Nakano and H. Kometani, "A study on eddy-current losses in rotors of surface permanent magnet synchronous machines," in *Industry Applications Conference, 2004. 39th IAS Annual Meeting. Conference Record of the 2004 IEEE*, vol. 3, 2004, pp. 1696–1702 vol.3.

[147] K. Hirota, H. Nakamura, T. Minowa, and M. Honshima, "Coercivity Enhancement by the Grain Boundary Diffusion Process to Nd amp;8211;Fe amp;8211;B Sintered Magnets," *Magnetics, IEEE Transactions on*, vol. 42, no. 10, pp. 2909–2911, 2006.

[148] S. Jurkovic, K. Rahman, N. Patel, and P. Savagian, "Next Generation Voltec Electric Machines; Design and Optimization for Performance and Rare-Earth Mitigation," *SAE Intnational Journal of Alternative Powertrains*, vol. 4, no. 2, pp. 336–342, Apr 2015.

[149] G. Pellegrino and F. Cupertino, "FEA-based Multi-Objective Optimization of IPM Motor Design Including Rotor Losses," in *IEEE Energy Conversion Congress and Exposition (ECCE)*, Sept. 2010, pp. 3659–3666.

[150] R. H. Myers and D. C. Montgomery, *Response Surface Methodology: Process and Product Optimization Using Designed Experiments* . John Wiley & Sons, 2002.

[151] Y. Wang and Z. Cai, "Combining Multiobjective Optimization With Differential Evolution to Solve Constrained Optimization Problems," *Evolutionary Computation, IEEE Transactions on*, vol. 16, no. 1, pp. 117–134, Feb 2012.

[152] R. Ramarathnam, B. Desai, and V. Rao, "A Comparative Study of Minimization Techniques for Optimization of Induction Motor Design," *Power Apparatus and Systems, IEEE Transactions on*, vol. PAS-92, no. 5, pp. 1448–1454, Sept 1973.

[153] D.-J. Sim, D.-H. Cho, J.-S. Chun, H.-K. Jung, and T.-K. Chung, "Efficiency optimization of interior permanent magnet synchronous motor using genetic algorithms," *Magnetics, IEEE Transactions on*, vol. 33, no. 2, pp. 1880–1883, Mar 1997.

[154] R. O. Kuehl, *Design of Experiments: Statistical Principle of Research Design and Anlysis, Second edition.* Duxbury/Thomson Learning, 2000.

[155] D. Zarko and S. Stipetic, "Criteria for optimal design of interior permanent magnet motor series," in *Electrical Machines (ICEM), 2012 XXth International Conference on*, Sept 2012, pp. 1242–1249.

[156] D. Zarko, D. Ban, and D. Goricki, "Improvement of a Servo Motor Design

Including Optimization and Cost Analysis," in *12th International Power Electronics and Motion Control Conference (EPE-PEMC)*, 2006, pp. 302–307.

[157] E. Mezura Montes and C. A. Coello Coello, "A simple multimembered evolution strategy to solve constrained optimization problems," *Evolutionary Computation, IEEE Transactions on*, vol. 9, no. 1, pp. 1–17, Feb 2005.

[158] K. Weeber and S. Hoole, "Geometric parametrization and constrained optimization techniques in the design of salient pole synchronous machines," *Magnetics, IEEE Transactions on*, vol. 28, no. 4, pp. 1948–1960, Jul 1992.

[159] E. Lovelace, T. Jahns, T. Keim, and J. H. Lang, "Mechanical design considerations for conventionally laminated, high-speed, interior PM synchronous machine rotors," *Industry Applications, IEEE Transactions on*, vol. 40, no. 3, pp. 806–812, May 2004.

[160] E. Zitzler and L. Thiele, "Multiobjective evolutionary algorithms: a comparative case study and the strength Pareto approach," *Evolutionary Computation, IEEE Transactions on*, vol. 3, no. 4, pp. 257–271, 1999.

[161] C. M. Fonseca, P. J. Fleming, E. Zitzler, L. Thiele, and K. Deb, "The measure of Pareto optima: Applications in multiobjective metaheuristics," in *Evolutionary Multi-Criterion Optimization: Second International Conference, EMO 2003*, 2003, pp. 519–533.

[162] P. Zhang, G. Sizov, J. He, D. Ionel, and N. Demerdash, "Calculation of Magnet Losses in Concentrated-Winding Permanent-Magnet Synchronous Machines Using a Computationally Efficient Finite-Element Method," *Industry Applications, IEEE Transactions on*, vol. 49, no. 6, pp. 2524–2532, 2013.

[163] J. Goss, P. Mellor, R. Wrobel, D. Staton, and M. Popescu, "The design of AC permanent magnet motors for electric vehicles: A computationally efficient model of the operational envelope," in *Power Electronics, Machines and Drives (PEMD 2012), 6th IET International Conference on*, 2012, pp. 1–6.

[164] J. Goss, R. Wrobel, P. Mellor, and D. Staton, "The design of AC permanent magnet motors for electric vehicles: A design methodology," in *Electric Machines Drives Conference (IEMDC), 2013 IEEE International*, 2013, pp. 871–878.

[165] T. Jahns, "Flux-Weakening Regime Operation of an Interior Permanent-Magnet Synchronous Motor Drive," *Industry Applications, IEEE Transactions on*, vol. IA-23, no. 4, pp. 681–689, July 1987.

[166] E. H. M and J. C. Balda, "Permanent magnet synchronous motor drive for HEV

propulsion: optimum speed ratio and parameter determination," in *Vehicular Technology Conference, 2002. Proceedings. VTC 2002-Fall. 2002 IEEE 56th*, vol. 3, 2002, pp. 1500–1504 vol.3.

[167] Z. Rahman, K. Butler, and M. Ehsani, "Effect of Extended-speed, Constant-power Operation of Electric Drives on the Design and Performance of EV Propulsion System," in *SAE Future Car Congress, Paper No. 2001-01-0699*, 2000.

[168] S. Z. Selim and M. A. Ismail, "K-Means-Type Algorithms: A Generalized Convergence Theorem and Characterization of Local Optimality," *Pattern Analysis and Machine Intelligence, IEEE Transactions on*, vol. PAMI-6, no. 1, pp. 81–87, Jan 1984.

[169] B. Stumberger, G. Stumberger, D. Dolinar, A. Hamler, and M. Trlep, "Evaluation of saturation and cross-magnetization effects in interior permanent-magnet synchronous motor," *Industry Applications, IEEE Transactions on*, vol. 39, no. 5, pp. 1264–1271, 2003.

[170] D. Ionel, J. Eastham, T. Miller, and E. Demeter, "Design considerations for permanent magnet synchronous motors for flux weakening applications," *Electric Power Applications, IEE Proceedings* -, vol. 145, no. 5, pp. 435–440, Sep 1998.

[171] A. Adnanes, "Torque analysis of permanent magnet synchronous motors," in *Power Electronics Specialists Conference, 1991. PESC '91 Record., 22nd Annual IEEE*, Jun 1991, pp. 695–701.

[172] S. Morimoto, Y. Takeda, T. Hirasa, and K. Taniguchi, "Expansion of operating limits for permanent magnet motor by current vector control considering inverter capacity," *Industry Applications, IEEE Transactions on*, vol. 26, no. 5, pp. 866–871, Sep 1990.

[173] V. Zivotic-Kukolj, W. Soong, and N. Ertugrul, "Iron Loss Reduction in an Interior PM Automotive Alternator," *Industry Applications, IEEE Transactions on*, vol. 42, no. 6, pp. 1478–1486, 2006.

[174] B. Chalmers, L. Musaba, and D. Gosden, "Variable-frequency synchronous motor drives for electric vehicles," *Industry Applications, IEEE Transactions on*, vol. 32, no. 4, pp. 896–903, Jul 1996.

[175] J. Miller, "Oak Ridge National Laboratory Annual Progress Report for the Power Electronics and Electric Motors Program," in *Oak Ridge National Laboratory, U.S. Department of Energy*, Nov 2013.

[176] A. Borisavljevic, H. Polinder, and J. A. Ferreira, "On the Speed Limits of Permanent-Magnet Machines," *IEEE Transactions on Industrial Electronics*, vol. 57, no. 1, pp. 220–227, 2010.

[177] G.-H. Kang, J. Hur, H.-G. Sung, and J.-P. Hong, "Optimal design of spoke type BLDC motor considering irreversible demagnetization of permanent magnet," in *Electrical Machines and Systems, 2003. ICEMS 2003. Sixth International Conference on*, vol. 1, 2003, pp. 234–237 vol.1.

[178] B. kuk Lee, G.-H. Kang, J. Hur, and D.-W. You, "Design of spoke type BLDC motors with high power density for traction applications," in *Industry Applications Conference, 2004. 39th IAS Annual Meeting. Conference Record of the 2004 IEEE*, vol. 2, 2004, pp. 1068–1074 vol.2.

[179] E. Carraro, N. Bianchi, S. Zhang, and M. Koch, "Permanent magnet volume minimization of spoke type fractional slot synchronous motors," in *Energy Conversion Congress and Exposition (ECCE), 2014 IEEE*, 2014, pp. 4180–4187.

[180] H.-W. Kim, K.-T. Kim, Y.-S. Jo, and J. Hur, "Optimization Methods of Torque Density for Developing the Neodymium Free SPOKE-Type BLDC Motor," *Magnetics, IEEE Transactions on*, vol. 49, no. 5, pp. 2173–2176, 2013.

[181] D. Ionel, D. Jackson, G. Starr, and A. Turner, "Permanent magnet brushless motors for industrial variable speed drives," in *Power Electronics, Machines and Drives, 2002. International Conference on (Conf. Publ. No. 487)*, 2002, pp. 650–654.

[182] "Critical Materials Strategy," U.S. Department of Energy's Office of Energy Efficiency and Renewable Energy, Washington, DC 20585-0121, Tech. Rep., December 2011. [Online]. Available: http://www.energy.gov

[183] M. Barcaro and N. Bianchi, "Interior PM Machines Using Ferrite to Replace Rare-Earth Surface PM Machines," *Industry Applications, IEEE Transactions on*, vol. 50, no. 2, pp. 979–985, 2014.

[184] I. Petrov and J. Pyrhonen, "Performance of Low-Cost Permanent Magnet Material in PM Synchronous Machines," *Industrial Electronics, IEEE Transactions on*, vol. 60, no. 6, pp. 2131–2138, 2013.

[185] M. Barcaro, N. Bianchi, and F. Magnussen, "Permanent-Magnet Optimization in Permanent-Magnet-Assisted Synchronous Reluctance Motor for a Wide Constant-Power Speed Range," *IEEE Transaction on Industrial Electronics*, vol. 59, no. 6, pp. 2495–2502, June 2012.

[186] E. C. Lovelace, T. M. Jahns, J. L. Kirtley, and J. H. Lang, "An interior PM

starter/alternator for automotive applications," in *Proc. ICEM*, vol. 3, 1998, pp. 1802–1808.

[187] G. Lei, C. Liu, Y. Guo, and J. Zhu, "Robust Multidisciplinary Design Optimization of PM Machines With Soft Magnetic Composite Cores for Batch Production," *IEEE Transactions on Magnetics*, vol. 52, no. 3, pp. 1–4, 2016.

[188] M. Hagan, H. Demuth, M. Beale, and O. de Jesús, *Neural Network Design (2nd Edition)*. Martin Hagan, 2014.

[189] O. A. Mohammed, D. C. Park, F. G. Uler, and C. Ziqiang, "Design optimization of electromagnetic devices using artificial neural networks," *IEEE Transactions on Magnetics*, vol. 28, no. 5, pp. 2805–2807, 1992.

[190] S. R. H. Hoole, "Artificial neural networks in the solution of inverse electromagnetic field problems," *IEEE Transactions on Magnetics*, vol. 29, no. 2, 1993.

[191] G. Tsekouras, S. Kiartzis, A. G. Kladas, and J. A. Tegopoulos, "Neural network approach compared to sensitivity analysis based on finite element technique for optimization of permanent magnet generators," *IEEE Transactions on Magnetics*, vol. 37, no. 5, pp. 3618–3621, 2001.

[192] E. Snelling, *Soft ferrites: properties and applications*. Butterworths, 1988.

[193] Y. Wang, D. Ionel, and D. Staton, "Ultrafast Steady-State Multiphysics Model for PM and Synchronous Reluctance Machines," *Industry Applications, IEEE Transactions on*, vol. 51, no. 5, pp. 3639–3646, 2015.

[194] W. Jiang and T. Jahns, "Coupled electromagnetic-thermal analysis of electric machines including transient operation based on finite element techniques," in *Energy Conversion Congress and Exposition (ECCE), 2013 IEEE*, 2013, pp. 4356–4363.

[195] M. Popescu and D. Dorrell, "Proximity Losses in the Windings of High Speed Brushless Permanent Magnet AC Motors With Single Tooth Windings and Parallel Paths," *Magnetics, IEEE Transactions on*, vol. 49, no. 7, pp. 3913–3916, 2013.

[196] L. Wu, Z. Zhu, D. Staton, M. Popescu, and D. Hawkins, "Analytical Model of Eddy Current Loss in Windings of Permanent-Magnet Machines Accounting for Load," *Magnetics, IEEE Transactions on*, vol. 48, no. 7, pp. 2138–2151, 2012.

[197] A. Thomas, Z. Zhu, and G. Jewell, "Proximity Loss Study In High Speed Flux-Switching Permanent Magnet Machine," *Magnetics, IEEE Transactions on*,

vol. 45, no. 10, pp. 4748–4751, 2009.

[198] P. Reddy, Z. Zhu, S.-H. Han, and T. Jahns, "Strand-level proximity losses in PM machines designed for high-speed operation," in *Electrical Machines, 2008. ICEM 2008. 18th International Conference on*, 2008, pp. 1–6.

[199] Y. Amara, P. Reghem, and G. Barakat, "Analytical Prediction of Eddy-Current Loss in Armature Windings of Permanent Magnet Brushless AC Machines," *Magnetics, IEEE Transactions on*, vol. 46, no. 8, pp. 3481–3484, 2010.

[200] L. Wu and Z. Zhu, "Analytical investigation of open-circuit eddy current loss in windings of PM machines," in *Electrical Machines (ICEM), 2012 XXth International Conference on*, 2012, pp. 2759–2765.

[201] P. Reddy, T. Jahns, and T. Bohn, "Modeling and analysis of proximity losses in high-speed surface permanent magnet machines with concentrated windings," in *Energy Conversion Congress and Exposition (ECCE), 2010 IEEE*, 2010, pp. 996–1003.

[202] W. Zhang and T. Jahns, "Analytical 2-D slot model for predicting AC losses in bar-wound machine windings due to armature reaction," in *Transportation Electrification Conference and Expo (ITEC), 2014 IEEE*, 2014, pp. 1–6.

[203] A. Bellara, H. Bali, R. Belfkira, Y. Amara, and G. Barakat, "Analytical Prediction of Open-Circuit Eddy-Current Loss in Series Double Excitation Synchronous Machines," *Magnetics, IEEE Transactions on*, vol. 47, no. 9, pp. 2261–2268, 2011.

[204] S. Iwasaki, R. Deodhar, Y. Liu, A. Pride, Z. Zhu, and J. Bremner, "Influence of PWM on the Proximity Loss in Permanent-Magnet Brushless AC Machines," *Industry Applications, IEEE Transactions on*, vol. 45, no. 4, pp. 1359–1367, 2009.

[205] A. Arkadan, R. Vyas, J. Vaidya, and M. Shah, "Effect of toothless stator design and core and stator conductors eddy current losses in permanent magnet generators," *Energy Conversion, IEEE Transactions on*, vol. 7, no. 1, pp. 231–237, 1992.

[206] R.-J. Wang and M. Kamper, "Calculation of eddy current loss in axial field permanent-magnet machine with coreless stator," *Energy Conversion, IEEE Transactions on*, vol. 19, no. 3, pp. 532–538, 2004.

[207] R. Wrobel, J. Goss, A. Mlot, and P. Mellor, "Design Considerations of a Brushless Open-Slot Radial-Flux PM Hub Motor," *Industry Applications, IEEE Transactions on*, vol. 50, no. 3, pp. 1757–1767, 2014.

[208] R. Wrobel, D. Salt, A. Griffo, N. Simpson, and P. Mellor, "Derivation and Scaling of AC Copper Loss in Thermal Modeling of Electrical Machines," *Industrial Electronics, IEEE Transactions on*, vol. 61, no. 8, pp. 4412–4420, 2014.

[209] P. Mellor, R. Wrobel, D. Salt, and A. Griffo, "Experimental and analytical determination of proximity losses in a high-speed PM machine," in *Energy Conversion Congress and Exposition (ECCE), 2013 IEEE*, 2013, pp. 3504–3511.

[210] G. Carter, *The electromagnetic field in its engineering aspects*, ser. Electrical engineering series. American Elsevier Pub. Co., 1967.

[211] A. Binder, T. Schneider, and M. Klohr, "Fixation of buried and surface-mounted magnets in high-speed permanent-magnet synchronous machines," *IEEE Transactions on Industry Applications*, vol. 42, no. 4, pp. 1031–1037, 2006.

[212] W. Fei, P. C. K. Luk, and T. S. El-Hasan, "Rotor Integrity Design for a High-Speed Modular Air-Cored Axial-Flux Permanent-Magnet Generator," *IEEE Transactions on Industrial Electronics*, vol. 58, no. 9, pp. 3848–3858, 2011.

[213] R. Larsonneur, *Design and control of active magnetic bearing systems for high speed rotation*. Swiss Federal Institute of Technology, 1990.

[214] M. Barcaro, G. Meneghetti, and N. Bianchi, "Structural Analysis of the Interior PM Rotor Considering Both Static and Fatigue Loading," *IEEE Transactions on Industry Applications*, vol. 50, no. 1, pp. 253–260, 2014.

APPENDIX I

Parametric Open-Slot Stator Structure

The parametrization of the open-slot stator configuration used in Chapter 3 is illustrated below.

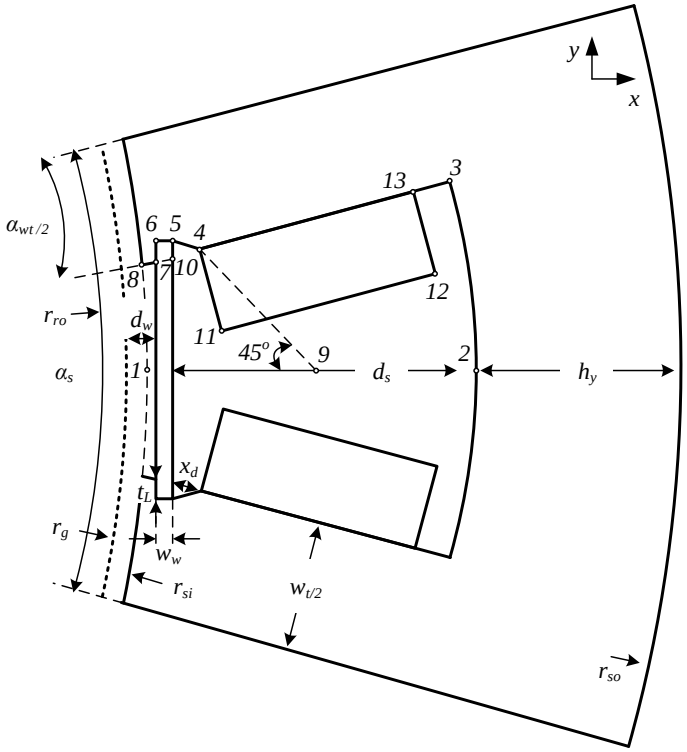

The structure can be characterized by defining the following points:

$$\begin{cases} x_{p1} = r_{si} \\ y_{p1} = 0 \end{cases}$$

$$\begin{cases} x_{p2} = r_{so} - h_y \\ y_{p2} = 0 \end{cases}$$

$$\begin{cases} x_{p3} = r_{slot}\cos(Ang_{P3}),\ \text{where } Ang_{P3} = \alpha_s/2 - \arcsin(w_t/2/r_{slot}) \\ y_{p3} = r_{slot}\sin(Ang_{P3}),\ \text{where} r_{slot} = r_{so} - h_y \end{cases}$$

$$\begin{cases} x_{p4} = x_{p5} + x_d,\ \text{where } x_d = \frac{y_{p5}(x_{p5}-OO_S)-y_{p10}(x_{p5}-OO_S)}{y_{p10}+x_{p5}-OO_S} \\ y_{p4} = y_{p5} - x_d,\ \text{where} OO_s = w_t/2/\sin(\alpha_s/2) \end{cases}$$

$$\begin{cases} x_{p5} = x_{p6} + w_w \\ y_{p5} = y_{p6} \end{cases}$$

$$\begin{cases} x_{p6} = d_w + r_{si} - h_g/2 \\ y_{p6} = (x_{p6} - OO_S)\tan(\alpha_s/2) + t_L \end{cases}$$

$$\begin{cases} x_{p7} = x_{p6} \\ y_{p7} = (x_{p6} - OO_S)\tan(\alpha_s/2) \end{cases}$$

$$\begin{cases} x_{p8} = r_{si}\cos(\alpha_s/2 - \arcsin(w_t/2/r_{si})) \\ y_{p8} = R_{si}\sin(\alpha_s/2 - \arcsin(w_t/2/r_{si})) \end{cases}$$

$$\begin{cases} x_{p15} = x_{p5} + y_{p5} \\ y_{p15} = 0 \end{cases}$$

$$\begin{cases} x_{p10} = x_{p5} \\ y_{p10} = (x_{p5} - OO_S)\tan(\alpha_s/2) \end{cases}$$

$$\begin{cases} x_{p11} = x_{p4} + y_{p8}\sin(\alpha_s/2) \\ y_{p11} = y_{p4} - y_{p8}\cos(\alpha_s/2) \end{cases}$$

$$\begin{cases} x_{p12} = x_{p13} + y_{p8}\sin(\alpha_s/2) \\ y_{p12} = y_{p13} - y_{p8}\cos(\alpha_s/2) \end{cases}$$

$$\begin{cases} x_{p13} = x_{p2} - (x_{p2} - OO_S)\sin(\alpha_s/2)\sin(\alpha_s/2) \\ y_{p13} = (x_{p2} - OO_S)\sin(\alpha_s/2)\cos(\alpha_s/2) \end{cases}$$

Parametric Spoke-Type PM Layout

The parametrization of the spoke-type PM layout used in Chapter 6 is illustrated below.

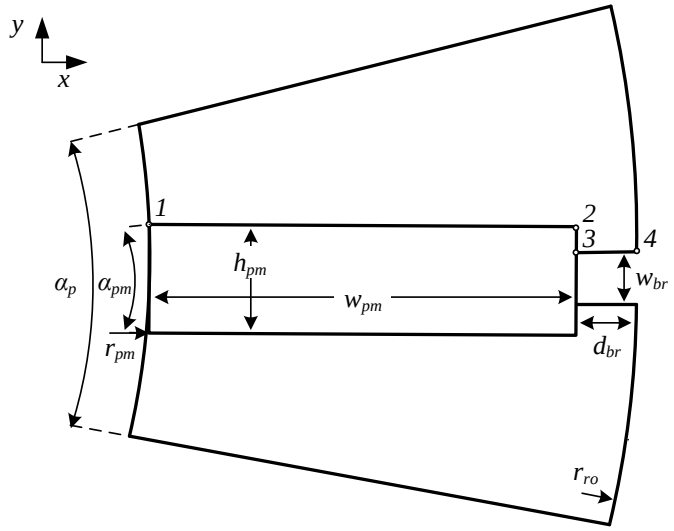

The structure can be characterized by defining the following points:

$$\begin{cases} x_{q1} = x_{q4} - d_{br} - w_{pm} \\ y_{q1} = h_{pm}/2 \end{cases}$$

$$\begin{cases} x_{q2} = x_{q4} - d_{br} \\ y_{q2} = h_{pm}/2 \end{cases}$$

$$\begin{cases} x_{q3} = x_{q4} - d_{br} \\ y_{q3} = w_{br}/2 \end{cases}$$

$$\begin{cases} x_{q4} = \sqrt{R_{ro}^2 - (w_{br}/2)^2} \\ y_{q4} = w_{br}/2 \end{cases}$$

APPENDIX II

Structural FEA for Sensitivity Analysis

The following static structural FEA on the V-type rotor layout was carried out in Section 7.3 for sensitivity analysis of the stress to the variations of the design parameters. Values of $k_{d_{pm}}$, $k_{w_{pm}}$, k_{w_q}, h_{pm}, α_{pm}, and r_{ro} are listed in coded form in the table below for each design.

Design No.	h_{pm}	$k_{d_{pm}}$	$k_{w_{pm}}$	k_{w_q}	α_{pm}	r_{ro}
1	-1	-1	-1	-1	-1	-1
2	-1	-1	-1	-1	1	1
3	-1	-1	-1	1	-1	1
4	-1	-1	-1	1	1	-1
5	-1	-1	1	-1	-1	1
6	-1	-1	1	-1	1	-1
7	-1	-1	1	1	-1	-1
8	-1	-1	1	1	1	1
9	-1	1	-1	-1	-1	1
10	-1	1	-1	-1	1	-1
11	-1	1	-1	1	-1	-1
12	-1	1	-1	1	1	1
13	-1	1	1	-1	-1	-1
14	-1	1	1	-1	1	1
15	-1	1	1	1	-1	1

Design No.	h_{pm}	$k_{d_{pm}}$	$k_{w_{pm}}$	k_{w_q}	α_{pm}	r_{ro}
16	-1	1	1	1	1	-1
17	1	-1	-1	-1	-1	1
18	1	-1	-1	-1	1	-1
19	1	-1	-1	1	-1	-1
20	1	-1	-1	1	1	1
21	1	-1	1	-1	-1	-1
22	1	-1	1	-1	1	1
23	1	-1	1	1	-1	1
24	1	-1	1	1	1	-1
25	1	1	-1	-1	-1	-1
26	1	1	-1	-1	1	1
27	1	1	-1	1	-1	1
28	1	1	-1	1	1	-1
29	1	1	1	-1	-1	1
30	1	1	1	-1	1	-1
31	1	1	1	1	-1	-1
32	1	1	1	1	1	1
33	-1	0	0	0	0	0
34	1	0	0	0	0	0
35	0	-1	0	0	0	0
36	0	1	0	0	0	0
37	0	0	-1	0	0	0
38	0	0	1	0	0	0
39	0	0	0	-1	0	0
40	0	0	0	1	0	0
41	0	0	0	0	-1	0
42	0	0	0	0	1	0
43	0	0	0	0	0	-1
44	0	0	0	0	0	1
45	0	0	0	0	0	0

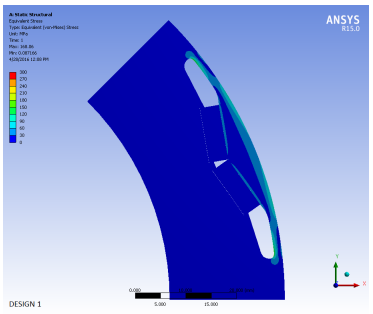
ANSYS
R15.0
DESIGN 1

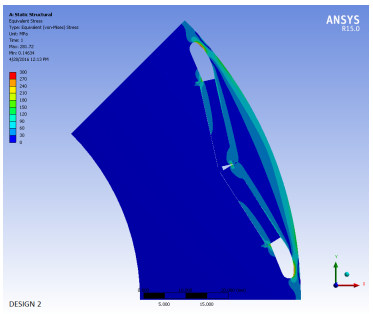
ANSYS
R15.0
DESIGN 2

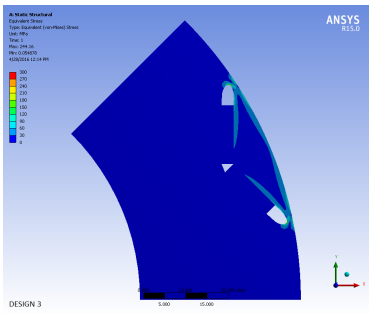
ANSYS
R15.0
DESIGN 3

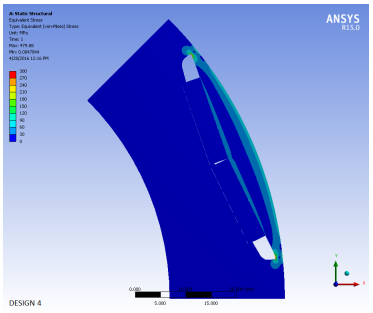
ANSYS
R15.0
DESIGN 4

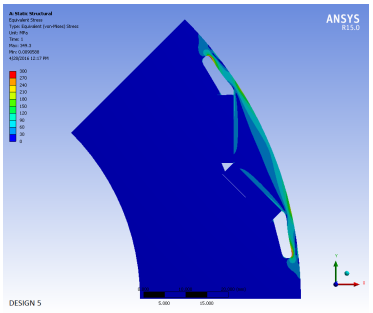
ANSYS
R15.0
DESIGN 5

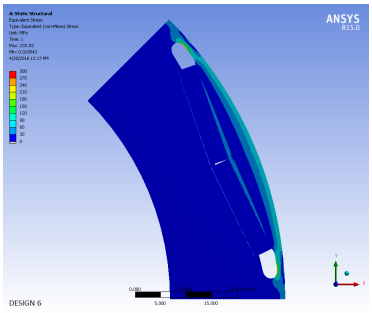
ANSYS
R15.0
DESIGN 6

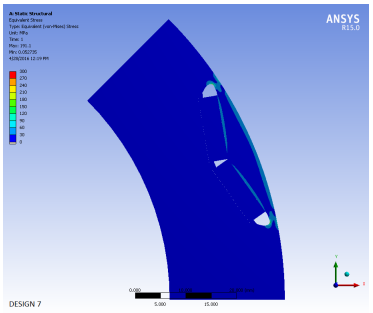
ANSYS
R15.0
DESIGN 7

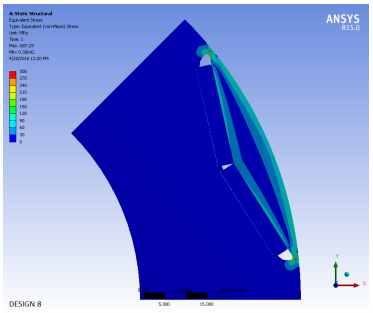
ANSYS
R15.0
DESIGN 8

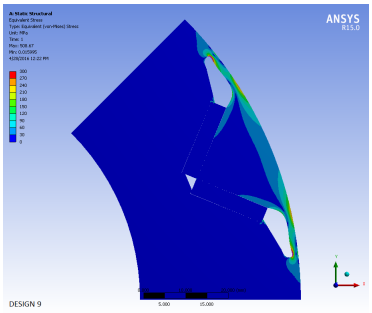
ANSYS
R15.0
DESIGN 9

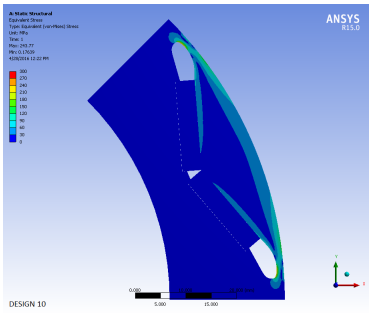
ANSYS
R15.0
DESIGN 10

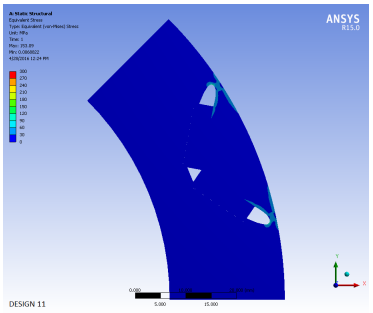
ANSYS
R15.0
DESIGN 11

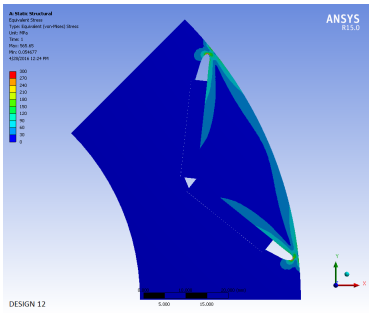
ANSYS
R15.0
DESIGN 12

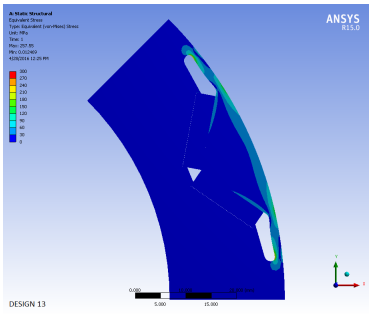
ANSYS
R15.0
DESIGN 13

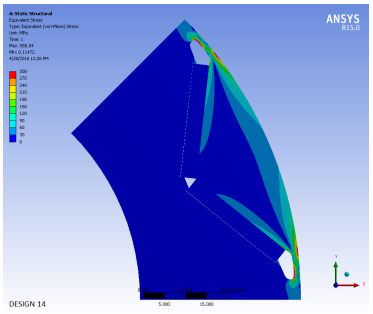
ANSYS
R15.0
DESIGN 14

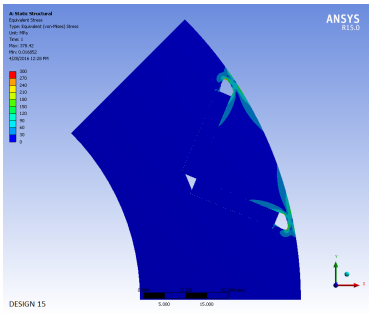
ANSYS
R15.0
DESIGN 15

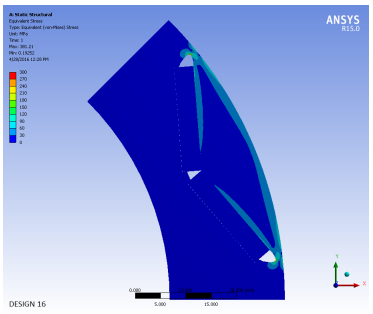
ANSYS
R15.0
DESIGN 16

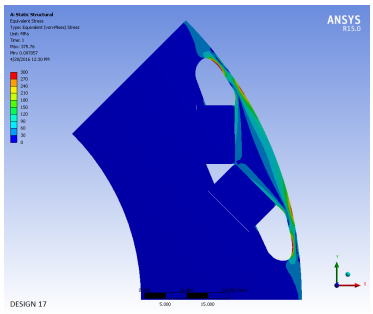
ANSYS
R15.0
DESIGN 17

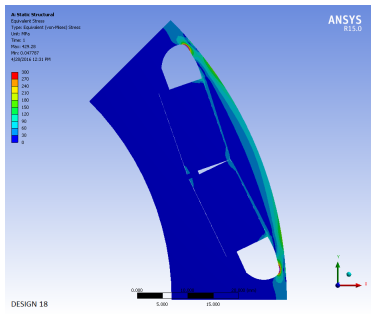
ANSYS
R15.0
DESIGN 18

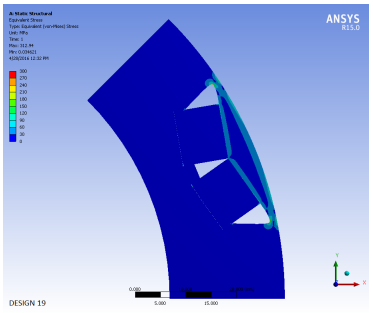
ANSYS
R15.0
DESIGN 19

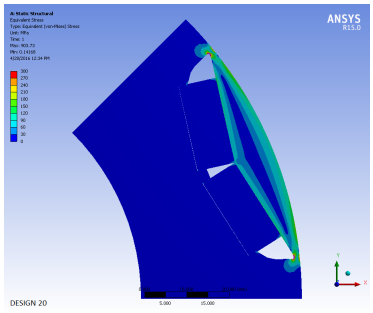
ANSYS
R15.0
DESIGN 20

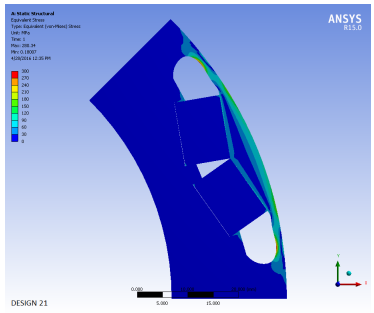
ANSYS
R15.0
DESIGN 21

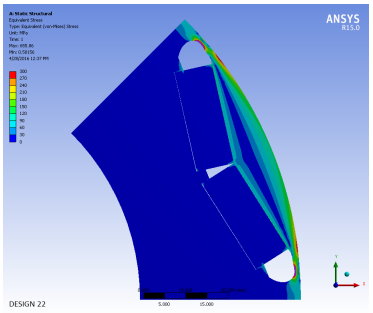
ANSYS
R15.0
DESIGN 22

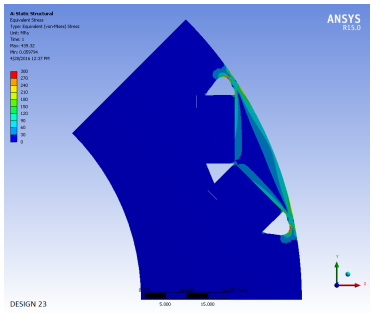
ANSYS
R15.0
DESIGN 23

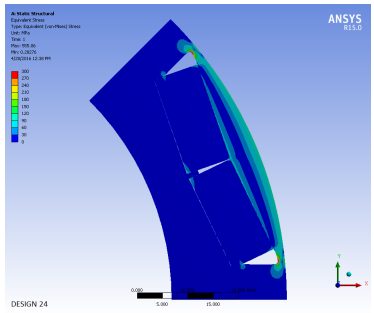
ANSYS
R15.0
DESIGN 24

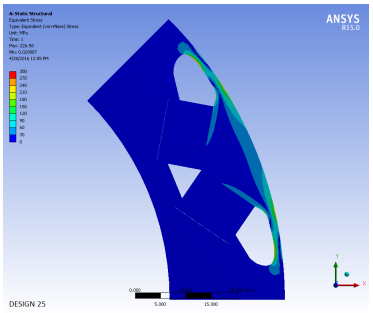
ANSYS
R15.0
DESIGN 25

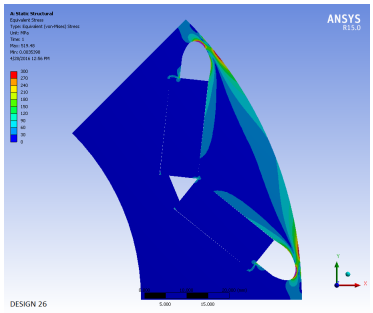
ANSYS
R15.0
DESIGN 26

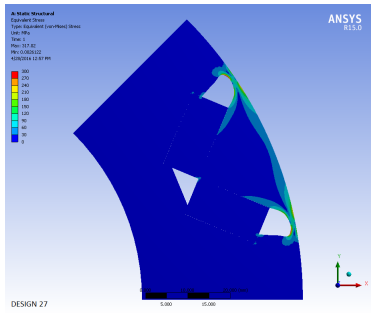
ANSYS
R15.0
DESIGN 27

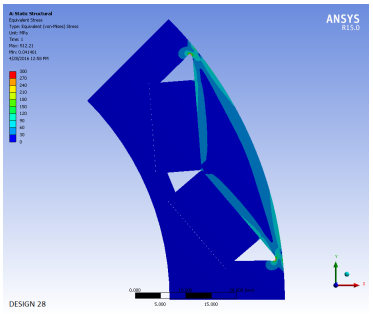
ANSYS
R15.0
DESIGN 28

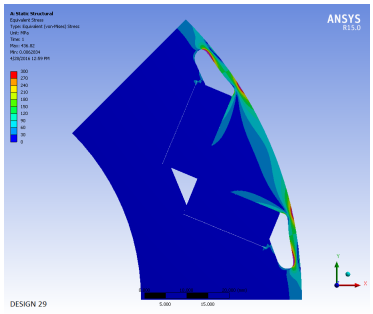
ANSYS
R15.0
DESIGN 29

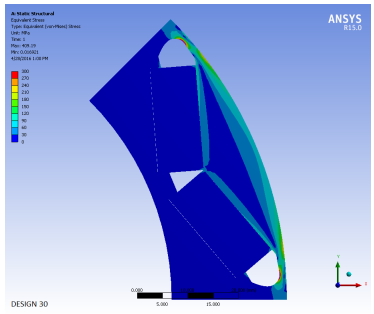
ANSYS
R15.0
DESIGN 30

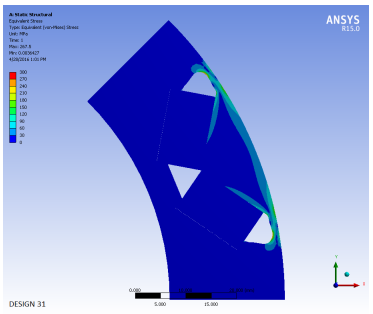
ANSYS
R15.0
DESIGN 31

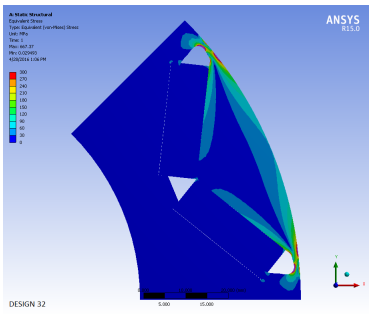
ANSYS
R15.0
DESIGN 32

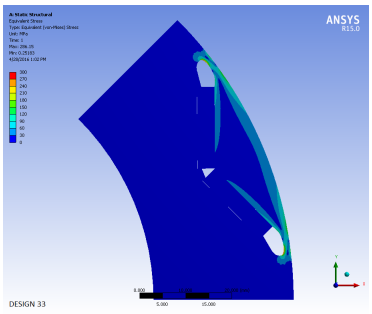
ANSYS
R15.0
DESIGN 33

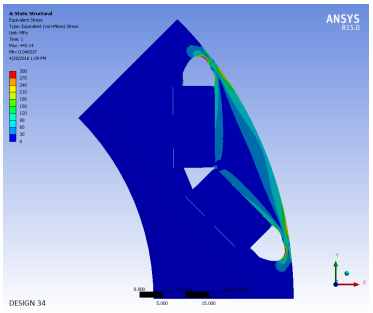
ANSYS
R15.0
DESIGN 34

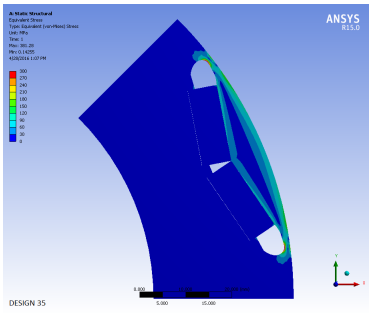
ANSYS
R15.0
DESIGN 35

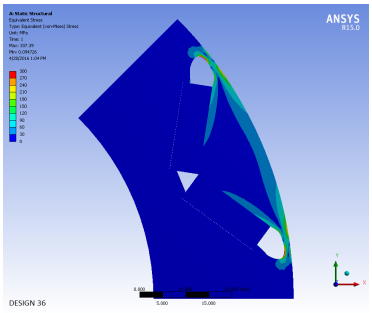
ANSYS
R15.0
DESIGN 36

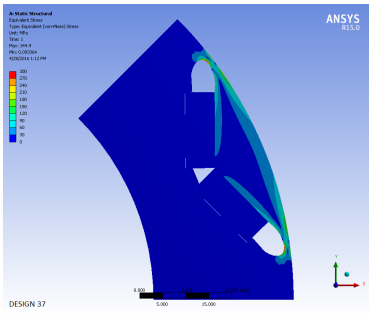
ANSYS
R15.0
DESIGN 37

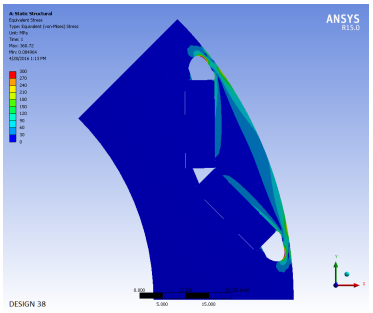
ANSYS
R15.0
DESIGN 38

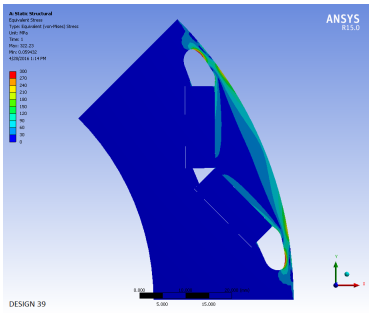
ANSYS
R15.0
DESIGN 39

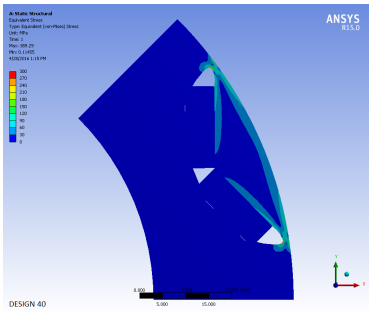
ANSYS
R15.0
DESIGN 40

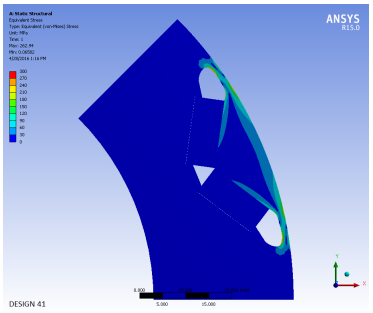
ANSYS
R15.0
DESIGN 41

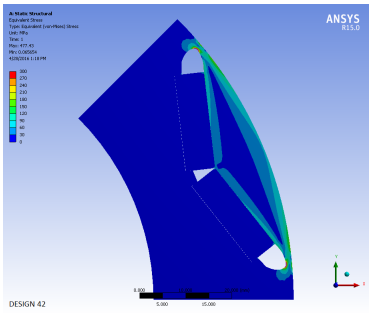
ANSYS
R15.0
DESIGN 42

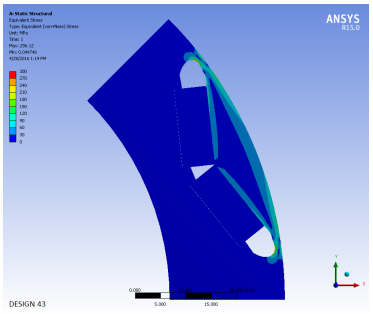
ANSYS
R15.0
DESIGN 43

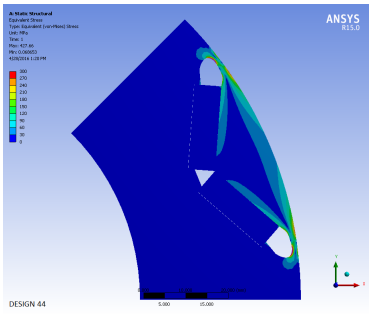
ANSYS
R15.0
DESIGN 44

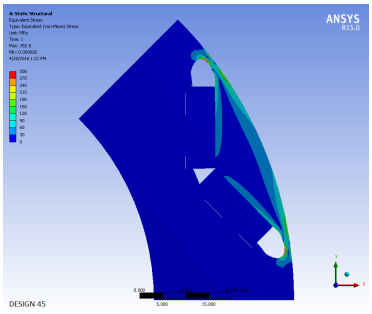
ANSYS
R15.0
DESIGN 45

APPENDIX III

A	Magnetic vector potential (Weber per meter)
ACEEE	American Council for an Energy-Efficient Economy
ADVISOR	Advanced Vehicle Simulator
A_{Fe}	Area of iron per pole (square meter)
α_{pm}	Magnet pole coverage (degrees)
α_s	Slot pitch (mechanical radians)
AMC	Active Material Cost
ANN	Artificial Neural Network
A_{pm}	Area of magnet per pole (square meter)
B	Magnetic flux density (Tesla)
β	Regression coefficients
B_g	Peak air-gp flux density (Tesla)
B_{pm}	Average flux density over magnet piece (Tesla)
B_r	Magnet retentivity (Tesla)
c_i	Coded design variables
CCD	Central Composite Design
CCW	Counterclockwise
CE-FEA	Computationally Efficient-Finite Element Analysis
CEM	Computational Electromagnetics
CMODE	Combined Multi-Objective Optimization with Differential Evolution
COP	Constrained Optimization Problem
C_r	Crossover probability
DE	Differential Evolution
δ	Skin depth (meter)
D_{Fe}	Mass density of iron (kilogram per cubic meter)
DOE	Design Of Experiments

d_{pm}	Magnet burial depth (meter)
D_{pm}	Mass density of magnet (kilogram per cubic meter)
Dy	Dysprosium
EA	Evolutionary Algorithms
EM	Electromagnetic
EMF	Electromotive Force
EPA	Environmental Protection Agency
EPAct	Energy Policy and Conservation Act
η_{2k-1}	Skin effect coefficient
EV	Electric Vehicles
F	Difference scale factor
FC	Fan-Cooled
FD	Finite Difference
FE	Finite Element
FEs	Function Evaluations
FEA	Finite Element Analysis
FEM	Finite Element Method
FSCW	Fractional Slot Concentrated Winding
FSM	Flux Switching Motor
GA	Genetic Algorithm
h_g	Air-gap height (meter)
h_{pm}	Magnet height (meter)
h_y	Yoke height (meter)
HPC	High Performance Computing
HSD	Hybrid Synergy Drive
HWFET	Highway Fuel Economy Test Driving Schedule
I_{CH}	Characteristic current (Ampere)
i_d	D-axis component of armature current phasor (Ampere)
IEC	International Electrotechnical Commission
i_q	Q-axis component of armature current phasor (Ampere)

I_R	Rated current (Ampere)
IPM	Interior Permanent Magnet
J	Electric current density (Ampere per square meter)
J_{PM}	Equivalent electric current density used to represent a permanent magnet excitation (Ampere per square meter)
$k_{d_{pm}}$	Ratio of magnet burial depth to its maximum possible depth
k_h	Lamination hysteresis loss coefficient (Watts per Hertz per square Tesla per kilogram)
k_e	Lamination eddy-current loss coefficient (Watts per square Hertz per square Tesla per kilogram)
$k_{r_{ac}}$	Ratio of ac to dc resistance
k_{si}	Split ratio or the ratio of the stator inner to outer diameter
k_σ	Rotor leakage coefficient
$k_{w_{pm}}$	Ratio of magnet width to its maximum possible width
k_{w_q}	Ratio of q-axis web to its maximum possible width
k_{wt}	Ratio of tooth-stem width to slot-pitch
k_{wtt}	Ratio of tooth-tip-width to slot opening
LA99	Unified Dynamometer Driving Schedule
λ	Instantaneous flux-linkage (Weber)
λ_d	D-axis component of flux-linkage (Weber)
λ_{PM}	Magnet flux-linkage (Weber)
λ_q	Q-axis component of flux-linkage (Weber)
λ_R	Total phase flux-linkage (Weber)
LC	Liquid-Cooled
L_d	D-axis synchronous inductance (Henry)
L_q	Q-axis synchronous inductance (Henry)
m	Mass (kilogram)
μ	Permeability (Henry per meter)
μ_r	Relative permeability
MC	Monte-Carlo
MTPA	Maximum Torque Per Ampere
NC	Naturally Cooled

Nd	Neodymium
NdFeB	Neodymium Iron Boron
NEDC	New European Driving Cycle
NEMA	National Electrical Manufacturers Association
N_p	Population size
NREL	National Renewable Energy Laboratory
ν	Reluctivity (meter per Henry)
ω	Angular frequency (electrical radians per second)
ω_m	Angular frequency (mechanical radians per second)
ORNL	Oak Ridge National Laboratory
p	Number of design parameters
P	Number of poles
PC	Personal Computer
P_{ac}	Ac copper losses (Watts)
P_{dc}	Dc copper losses (Watts)
PEV	Plug-in Electric Vehicles
$\vec{P}_g$	Optimization population vector
P_e	Eddy-current loss (Watt per kilogram)
P_{Fe}	Lamination core losses (Watt)
P_h	Hysteresis loss (Watt per kilogram)
PM	Permanent Magnet
PMSM	Permanent Magnet Synchronous Machine
P_w	Aggregate weighted loss per unit output power
PWM	Pulse Width Modulation
R_{ac}	Ac resistance (Ohm)
ρ	Resistivity (Ohm meter)
R_{dc}	Dc resistance (Ohm)
r_{si}	Stator inner radius (meter)
r_{so}	Stator outer radius (meter)
RSM	Response Surface Methodology
SD	Steepest Descent

SF	Slot Fill
σ_t	Tangential stress (Pascal)
SRM	Switched Reluctance Motor
SyRM	Synchronous Reluctance Motor
T_{avg}	Average torque (Newton meter)
T_{em}	Developed electromagnetic torque profile (Newton meter)
$Temp$	Temperature (degree Celsius)
θ	Angle (electrical radians)
θ_m	Angle (mechanical radians)
THD	Total Harmonic Distortion
T_r	Torque ripple (%)
TRW	Torque Ratio per Weight
TSFE	Time-stepping FE
$\vec{u}$	Trial design members
UDDS	Urban Dynamometer Driving Schedule
US06	Supplemental Federal Test Procedure Driving Schedule
v_{Cu}	Volume of copper (cubic meters)
v_R	Total induced voltage in the stator winding (Volts)
w_{pm}	Width of magnet (meter)
w_q	Width of q-axis web (meter)
w_{so}	Width of slot opening (meter)
w_t	Tooth width (meter)
w_{tip}	Width of tooth tip (meter)
x_p	Coordinate direction in rectangular Cartesian coordinates
x_q	Coordinate direction in rectangular Cartesian coordinates
$\vec{x}$	Design members
$x_{i,\max}$	Upper bound of the design parameters
$x_{i,\min}$	Lower bound of the design parameters
$\vec{x}_g$	Population members
y_p	Coordinate direction in rectangular Cartesian coordinates
y_q	Coordinate direction in rectangular Cartesian coordinates